

BAND-ENGINEERED GERMANIUM
FOR CMOS-COMPATIBLE LIGHT EMISSION

A DISSERTATION
SUBMITTED TO THE DEPARTMENT OF ELECTRICAL ENGINEERING
AND THE COMMITTEE ON GRADUATE STUDIES
OF STANFORD UNIVERSITY
IN PARTIAL FULFILLMENT OF THE REQUIREMENTS
FOR THE DEGREE OF
DOCTOR OF PHILOSOPHY

Devanand Suresh Sukhdeo

June 2015

© 2015 by Devanand Suresh Sukhdeo. All Rights Reserved.
Re-distributed by Stanford University under license with the author.



This work is licensed under a Creative Commons Attribution-Noncommercial 3.0 United States License.

<http://creativecommons.org/licenses/by-nc/3.0/us/>

This dissertation is online at: <http://purl.stanford.edu/fj485gy5370>

I certify that I have read this dissertation and that, in my opinion, it is fully adequate in scope and quality as a dissertation for the degree of Doctor of Philosophy.

Krishna Saraswat, Primary Adviser

I certify that I have read this dissertation and that, in my opinion, it is fully adequate in scope and quality as a dissertation for the degree of Doctor of Philosophy.

James Harris

I certify that I have read this dissertation and that, in my opinion, it is fully adequate in scope and quality as a dissertation for the degree of Doctor of Philosophy.

Jelena Vuckovic

Approved for the Stanford University Committee on Graduate Studies.

Patricia J. Gumport, Vice Provost for Graduate Education

This signature page was generated electronically upon submission of this dissertation in electronic format. An original signed hard copy of the signature page is on file in University Archives.

Abstract

Modern electronics has advanced at a tremendous pace over the course of the last half century due to transistor scaling. However, while scaling a complementary metal oxide semiconductor (CMOS) transistor to smaller dimensions increases speed and reduces power consumption, the opposite is true for scaling down the copper interconnects that link these transistors. CMOS-compatible on- and off-chip optical interconnects offer a promising solution to this new performance bottleneck and several key components such as waveguides, detectors and modulators have already been demonstrated. However, a practical silicon CMOS-compatible light source remains elusive. Germanium has been proposed as a laser gain material due to its inherent compatibility with CMOS technology, but this requires overcoming the limitations imposed by germanium's indirect bandgap. Several techniques had been proposed to overcome this limitation such as n-type doping and band engineering through tensile strain. However, there was limited information about how effective each of these two techniques would be. There was also no truly CMOS-compatible technique for engineering large tensile strains in germanium for optimal band engineering.

In this work we present theoretical and experimental answers to these problems. We begin with a theoretical investigation of the relative merits of n-type doping and band engineering to determine which is more useful. For our theoretical modeling we consider both band engineering in the form of tensile strain and band engineering in the

form of germanium-tin alloys. We then show theoretically that while n-type doping is of limited benefit, using a large amount of band engineering can result in an efficient low-threshold germanium laser. We show this to be true for both the case of tensile strain and the case of tin alloying, and we also compare the relative merits of these two band engineering techniques.

From there we present new CMOS-compatible techniques for experimentally engineering large tensile strains in germanium. Firstly, we improve upon an existing microbridge technique to achieve up to 5.7% uniaxial tensile strain in germanium. This is the highest such strain ever reported and is sufficient to turn germanium into a direct bandgap semiconductor. We further show that the highly localized strain in these microbridge results in “pseudo-heterostructures,” a situation where we can fully recreate the electronic band profiles of traditional multi-material double heterostructures but within a single material. These pseudo-hetreostructures are experimentally shown to provide effective carrier confinement at room temperature and also allow for precise tuning of the band profiles at the nanoscale by simply changing certain lithographic dimensions. Secondly, we present a completely new technique for engineering up to 1.1% biaxial strain in germanium microdisks. This is the largest CMOS-compatible biaxial strain ever reported in germanium, and we further demonstrate an optical cavity integrated with our biaxially strained germanium structure. Finally, we discuss the implications of these theoretical and experimental achievements toward creating an efficient low-threshold germanium laser for use in CMOS-compatible on-chip light emission.

Acknowledgements

My nearly five years at Stanford have been an immensely rewarding time and I have many people to thank for this. Firstly, I would like to express my deepest gratitude to my advisor, prof. Krishna Saraswat. Beyond being an extraordinarily intelligent and savvy engineer, Dr. Saraswat is a fantastic teacher and an exceptional mentor. He is always available to his students and he spares no effort in helping each and every one of us excel. He keeps himself at just the right distance, leaving us all plenty of room to explore new ideas with a great degree of freedom but always making himself available when one of us hits a roadblock or needs a hand in determining the path of our research. Dr. Saraswat has also gone above and beyond with career guidance, helping me navigate potential internships, helping me seek out new opportunities both in the field and beyond, and being completely supportive of my career choices as I follow my own path. I truly could not have asked for a better advisor.

A special mention also goes out to all of my labmates in the Saraswat Group from whom I have learned a great deal, especially Shashank Gupta and Dr. Donguk Nam with whom I have collaborated very closely on this project. Shashank and Dr. Nam are two of the brightest and most hardworking researchers I have ever met, and I have learned immensely from working with them. Dr. Nam deserves a particularly special mention as he provided another layer of guidance in the early years, acting as something of a secondary advisor as I was beginning my doctoral studies, and I look forward to seeing his future accomplishments as he embarks on his new career as a

professor at Inha University in Korea. I would also like to thank the other professors at Stanford with whom I have worked, namely prof. Mark Brongersma, prof. Jelena Vuckovic and prof. James Harris and their students. All of these professors have had a substantial and positive impact on my time at Stanford.

I would also like to thank the many people with whom I have worked during my internships. From my many internships at Advanced Photonic Integrated Circuits (APIC) Corporation, I would like to thank my former colleagues including Dr. Boris Vulovic, Dr. Gerald Miller, Dr. Madeleine Glick and the CEO of APIC Corporation Dr. Birendra (Raj) Dutt. Dr. Dutt in particular has been an invaluable mentor even while I was back at Stanford, and I have learned immensely from his leadership and example. I would also like to thank my former colleagues at Factual, especially Eric Lui, Ben Coppersmith and Salil Subbakrishna. The experience of working in software/data was a refreshing change from academia and the skills I learned at Factual, especially from Ben, have served me well at Stanford and will likely continue to do so for a long time. I would also like to thank my former colleagues at Intel, especially Dr. Pranav Kalavade and Dr. Shyam Raghunathan. Working with Dr. Kalavade and Dr. Raghunathan at Intel was a wonderful experience and I learned a great deal from them about the engineering of actual commercial products.

Last but not least I would like to thank my friends and family for their support during the past five years. I've met many wonderful people on campus and beyond, and they've been the single biggest reason why I've so enjoyed my time in California. I would especially like to thank my father Suresh, my mother Cindy, and my brother

Josh for their unconditional love and support over the past 25 years. Being surrounded by such magnificent people is the greatest blessing that I could ever ask for.

Table of Contents

Abstract.....	iv
Acknowledgements	vi
Table of Contents	ix
List of Figures.....	xiv
Chapter 1: Introduction.....	1
1.1 Motivation	1
1.2 Organization of the Dissertation.....	7
Chapter 2: Background on Band-Engineered Germanium.....	10
2.1 General Background.....	10
2.2 Background on Theory & Modeling	12
2.3 Background on Experimental Band Engineering Techniques.....	13
2.3.1 Uniaxial Strain.....	13
2.3.2 Biaxial Strain.....	15
2.3.3 Alternative Experimental Approaches	19
Chapter 3: Theoretical Modeling for Biaxial Strain and N-Type Doping.....	21
3.1 Band Structure Modeling	21
3.2 General Carrier Statistics Modeling	24

3.2.1	Dependence on Strain and Temperature.....	24
3.2.2	Dependence on Strain and N-Type Doping.....	26
3.3	Light Emitting Diode (LED) Modeling.....	28
3.3.1	Dependence on Strain and N-Type Doping.....	28
3.3.2	Dependence on Material Quality.....	32
3.4	Results – Laser Modeling.....	33
3.4.1	Optical Gain.....	33
3.4.2	Threshold Current.....	42
3.4.3	Slope Efficiency and Optical Cavity Loss.....	56
3.4.4	Ultimate Limit of Biaxial Tensile Strain.....	64
3.5	Limitations of the Model.....	68
3.5.1	Band Structure Accuracy Concerns.....	68
3.5.2	Optical Gain Concerns.....	70
3.5.3	Carrier Lifetime Concerns.....	72
3.6	Summary.....	73
Chapter 4:	Theoretical Modeling for Other Types of Band Engineering.....	77
4.1	Overview.....	77
4.2	Uniaxial Strain (<100> orientation).....	78
4.2.1	Band Structure.....	78
4.2.2	Carrier Statistics.....	79

4.2.3 Light Emitting Diode (LED) Modeling.....	80
4.2.4 Laser Modeling – Threshold Current	82
4.2.5 Laser Modeling – Slope Efficiency.....	87
4.3 Other Strain Orientations.....	90
4.3.1 Overview	90
4.3.2 Uniaxial Strains along Different Orientations.....	91
4.3.3 Biaxial Strains along Different Orientations	95
4.4 Germanium Tin ($\text{Ge}_x\text{Sn}_{1-x}$).....	98
4.4.1 Band Structure	98
4.4.2 Threshold Current.....	100
4.4.3 Slope Efficiency	103
4.4.4 Interaction with Strain	106
4.5 Limitations of the Model.....	110
4.5.1 Overview	110
4.5.2 Tensile Strain Modeling (this Chapter Only)	111
4.5.3 Germanium-Tin Modeling.....	114
4.6 Summary.....	115
Chapter 5: Microbridge Structures for Extremely Large Uniaxial Tensile Strain and Single-Material Pseudo-Heterostructures	118
5.1 Overview	118

5.2 Microbridge Fabrication.....	119
5.2.1 Substrate Fabrication.....	119
5.2.2 Patterning the Structure.....	122
5.2.3 Substrate-Adhered Geometries via Stiction for Improved Heat Sinking.....	123
5.3 Characterization.....	124
5.3.1 Raman Spectroscopy.....	124
5.3.2 Photoluminescence.....	128
5.4 Pseudo-Heterostructures.....	130
5.5 Summary and Discussion.....	136
Chapter 6: Etched Microdisk Structures for Large Biaxial Tensile Strain.....	138
6.1 Overview.....	138
6.2 Microdisk Fabrication.....	140
6.3 Mechanical Simulations.....	143
6.3.1 Overview.....	143
6.3.2 Understanding the Structure.....	144
6.3.3 Effect of the Additional Etch Slits.....	145
6.3.4 Homogeneity of the Strain Distribution.....	146
6.3.5 Corner Stresses.....	147
6.3.6 Optimizing the Number of Main Etch Slits.....	148

6.4 Microdisk Characterization	149
6.4.1 Raman Spectroscopy	149
6.4.2 Photoluminescence	151
6.4.3 Fractured Microdisks	153
6.5 Optical Cavity Integration	156
6.5.1 Optical Mode Leakage from Strained Microdisks	156
6.5.2 Dual-Dielectric Fabrication Process for Vertical Optical Confinement	157
6.5.3 Circular Patterning for Lateral Optical Confinement	160
6.5.4 Raman Characterization of Optical Cavities	163
6.5.5 Photoluminescence from Optical Cavities	164
6.6 Summary.....	166
Chapter 7: Conclusions and Outlook.....	170
Appendix	176
Bibliography.....	232

List of Figures

Figure 1-1: Illustration of interconnect scaling	1
Figure 1-2: Impact of scaling on copper resistivity.....	3
Figure 1-3: Predicted breakdown of power consumption at the 50 nm technology node	3
Figure 1-4: Schematic of a typical optical interconnect.....	5
Figure 1-5: Impact of scaling on interconnect performance	6
Figure 3-1: 2D cross-section of germanium's band structure	22
Figure 3-2: 3D cross-section ($k_z=0$) of germanium's band structure	23
Figure 3-3: Germanium's direct (Γ) and indirect (L) bandgaps vs. biaxial tensile strain according to our tight-binding model	23
Figure 3-4: Fraction of electrons in the direct conduction valley vs. strain for undoped germanium at several different temperatures	25
Figure 3-5: Direct conduction valley occupancy in germanium	27
Figure 3-6: Internal quantum efficiency of a germanium double-heterostructure LED vs. biaxial strain for various n-type doping levels.....	31
Figure 3-7: Internal quantum efficiency of a germanium double-heterostructure LED vs. biaxial strain for various SRH lifetime assumptions	33
Figure 3-8: Optical gain in germanium as a function of steady-state carrier densities	37

Figure 3-9: Optical gain in germanium as a function of doping and steady-state injection	40
Figure 3-10: Optical gain in germanium as a function of doping and bias current density.....	44
Figure 3-11: Threshold and wavelength vs. biaxial strain and n-type doping	46
Figure 3-12: Threshold vs. n-type doping for various biaxial strain values & the optimal doping value vs. biaxial strain.....	48
Figure 3-13: Threshold and wavelength vs. biaxial strain for several doping values .	49
Figure 3-14: Threshold current density vs. biaxial strain and n-type doping, shown for various Shockley-Read-Hall lifetime (τ_{SRH}) values.....	53
Figure 3-15: Impact of SRH lifetime on the threshold response and optimal doping.	54
Figure 3-16: Impact of optical cavity loss on the threshold and slope efficiency (contour plots)	60
Figure 3-17: Impact of optical cavity loss on the threshold and slope efficiency (2D plots).....	62
Figure 3-18: Slope efficiency vs. threshold current density for several biaxial strain and doping combinations.....	64
Figure 3-19: Threshold and slope efficiency vs. biaxial strain and doping for the “ideal” optical cavity loss of 700 cm^{-1} .	65
Figure 3-20: Components of the slope efficiency, computed at 700 cm^{-1} optical cavity loss	68

Figure 4-1: Germanium’s direct (Γ) and indirect (L) bandgap energies vs. $\langle 100 \rangle$ uniaxial tensile strain according to deformation potential theory	79
Figure 4-2: Fraction of electrons in the direct conduction valley vs. $\langle 100 \rangle$ uniaxial strain for undoped germanium at several different temperatures	80
Figure 4-3: Internal quantum efficiency of a germanium double-heterostructure LED for various SRH lifetime assumptions.....	81
Figure 4-4: Threshold and wavelength vs. $\langle 100 \rangle$ uniaxial strain and doping	82
Figure 4-5: Threshold current density vs. uniaxial tensile strain ($\langle 100 \rangle$ orientation) and n-type doping (3D plot)	84
Figure 4-6: Threshold and wavelength vs. uniaxial strain for several doping conditions	86
Figure 4-7: Threshold and slope efficiency vs. uniaxial strain and n-type doping for several optical cavity loss value	87
Figure 4-8: Threshold and slope efficiency vs. optical cavity loss for several strain and doping combinations.....	90
Figure 4-9: Bandgaps of germanium as a function of uniaxial tensile strain for the $\langle 100 \rangle$ orientation, $\langle 110 \rangle$ orientation, and $\langle 111 \rangle$ orientation.....	92
Figure 4-10: Fraction of electrons in the direct (Γ) conduction valley in germanium as a function of uniaxial tensile strain for the $\langle 100 \rangle$ orientation, $\langle 110 \rangle$ orientation, and $\langle 111 \rangle$ orientation	94
Figure 4-11: Bandgaps of germanium as a function of biaxial tensile strain for the	

<100> orientation, <110> orientation, and <111> orientation.....	96
Figure 4-12: Fraction of electrons in the direct (Γ) conduction valley in germanium as a function of biaxial tensile strain for the <100> orientation, <110> orientation, and <111> orientation	97
Figure 4-13: Germanium-tin's direct and indirect bandgap energies vs. tin concentration for unstrained germanium-tin	99
Figure 4-14: Threshold and wavelength vs. tin concentration and n-type doping	101
Figure 4-15: Threshold and wavelength vs. tin concentration for several doping conditions	102
Figure 4-16: Threshold and slope efficiency vs. tin concentration and n-type doping for several optical cavity losses	105
Figure 4-17: Threshold and slope efficiency vs. optical cavity loss for several combinations for tin content and doping	106
Figure 4-18: Threshold and wavelength vs. tin concentration and biaxial strain.....	107
Figure 4-19: Comparison of biaxial strain and tin alloying with respect to threshold minimization.....	108
Figure 4-20: Threshold and slope efficiency vs. biaxial strain and tin concentration for several optical cavity loss values.....	110
Figure 5-1: Schematic illustration of the microbridge structure used for uniaxial stress concentration	119
Figure 5-2: Schematic illustration of how the mismatch in thermal expansion	

coefficients between germanium and silicon results in an initial tensile stress in the germanium layer	120
Figure 5-3: Process flow of the germanium-on-insulator (GOI) fabrication process, showing how the defective layer near the initial silicon/germanium interface is physically removed.....	121
Figure 5-4: Micrographs and mechanical simulations of fabricated microbridge structures.....	122
Figure 5-5: Micrographs confirming adhesion between a microbridge and the underlying substrate by stiction.....	124
Figure 5-6: Dependence of the Raman peak redshift on the excitation laser power for both suspended and substrate-adhered germanium wires with ~4% strain	126
Figure 5-7: Raman spectra for suspended germanium wires with various pad dimensions, showing uniaxial strains from 0.79% to 5.71%	127
Figure 5-8: Photoluminescence from suspended germanium wires with various strains.....	129
Figure 5-9: Illustration of the pseudo-heterostructure.....	131
Figure 5-10: Abrupt and graded pseudo-heterostructures	132
Figure 5-11: Experimental observation of room temperature carrier confinement within a pseudo-heterostructure	134
Figure 6-1: Overview of the proposed stress concentrating microdisk structure	139
Figure 6-2: Microdisk fabrication process flow schematic	141

Figure 6-3: Optical surface profile of a fabricated microdisk structure	142
Figure 6-4: Micrographs of successfully fabricated structures	142
Figure 6-5: Finite element method (FEM) simulations of a 100 μm diameter structure with a 5 μm diameter inner microdisk with and without the additional etch slits.....	145
Figure 6-6: Optimizing the number of main etch slits	149
Figure 6-7: Raman characterization of the microdisks	150
Figure 6-8: Photoluminescence characterization of the microdisks.....	153
Figure 6-9: Micrographs of fractured microdisk structures	154
Figure 6-10: Schematic cross-section of the germanium microdisks, showing optical mode leakage paths in the substrate-adhered microdisk structure	157
Figure 6-11: Process flow schematic for the dual-dielectric fabrication process.....	158
Figure 6-12: Micrographs of a resonator created by post-patterning a microdisk. ...	161
Figure 6-13: Raman area scans of the strain distribution (color scale) in the structure using the dual-dielectric fabrication process shown before optical cavity patterning, after circular resonator patterning, and with ~ 200 nm of post-patterning silicon nitride.....	164
Figure 6-14: Photoluminescence (PL) measurements on the microdisk structures before and after patterning the optical cavity	165
Figure A-1: Optical net gain of germanium under 1.0% biaxial tensile strain as a function of electron and hole concentrations and as a function of doping and steady-state injected carrier density, shown at various wavelengths	177

Figure A-2: Optical net gain of germanium computed at the wavelength of maximum net gain, both given as a function of n-type doping and steady-state injected carrier density, and shown for an extended range of biaxial tensile strain values 186

Figure A-3: Threshold current density and slope efficiency vs. biaxial tensile strain (<100> orientation) and n-type doping, shown for an extended range of optical cavity loss values 197

Figure A-4: Threshold current density and slope efficiency vs. uniaxial tensile strain (<100> orientation) and n-type doping, shown for an extended range of optical cavity loss values 208

Figure A-5: Threshold current density and slope efficiency of an unstrained germanium-tin laser vs. tin concentration and n-type doping, shown for an extended range of optical cavity loss values 216

Figure A-6: Threshold current density (left) and slope efficiency (right) of a biaxially strained (<100> orientation) germanium-tin laser as a function of strain and tin content, shown for an extended range of optical cavity loss values 224

Chapter 1

Introduction

1.1 Motivation

Since the invention of the first transistor nearly 70 years ago [1], transistor scaling has driven tremendous improvements in modern electronics which have touched nearly every facet of modern life [2]. The relentless doubling of transistor count per chip roughly every 18 months, popularly known as “Moore’s Law” [3], has now shrunk transistor dimensions down to only a few tens of nanometers [4]. However, while transistors typically improve in performance as they scale down in size [5], the opposite is true for the copper wires that link these transistors together [6]. As illustrated in Fig. 1-1, scaling down copper interconnects results in wires which have a reduced cross-sectional area, thereby increasing resistance, and which are packed more closely together, thereby increasing capacitance [7]. These two effects conspire to increase delay, reduce bandwidth and increase power consumption [8].

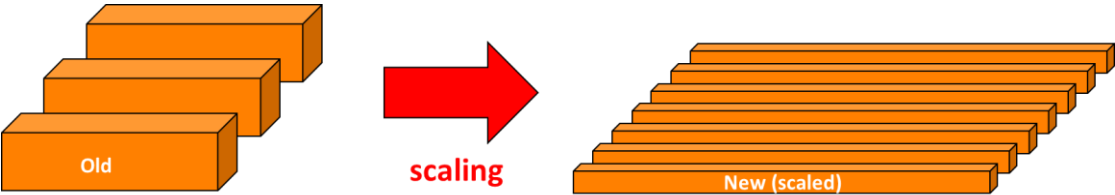


Figure 1-1. Illustration of interconnect scaling.

Even this, however, fails to capture the full scale of the problem. A copper wire is polycrystalline and consists of a multitude of “grains” wherein the resistance is dominated by electron scattering events at the boundaries of these grains [9]. At the nanoscale dimensions of present technology, the cross-sectional area of the wires has become comparable to the grain size. As such, scaling to smaller dimensions introduces more grain boundary scattering by physically reducing the grain sizes and also more surface scattering due to the increased surface-to-volume ratio [10], [11]. Furthermore, copper interconnects typically need a diffusion barrier which usually comes in the form of tantalum, rutherfordium or magnesium based materials [12]. Because the resistivity of these barrier materials is much higher than that of copper, the barrier effectively reduces the useful interconnect cross-section [12]. The result is that the copper material itself becomes less conductive at nanoscale dimensions [13], with an over 6x resistivity increase compared to bulk copper [12] as shown in Figure 1-2 [14]. This makes the problem of increased resistance even more severe and further worsens the delay, bandwidth and power consumption of scaled copper interconnects [12]. Moreover, this is not merely a future problem: even today commercial computer chips are often constrained by latency and power dissipation within the copper wiring [6]. This problem in fact has become so severe that more than 50% of power consumption in a typical integrated circuit is now due to the copper interconnects, as shown in Fig. 1-3 [15], considering both signaling interconnects and interconnects carrying the clock signal [15].

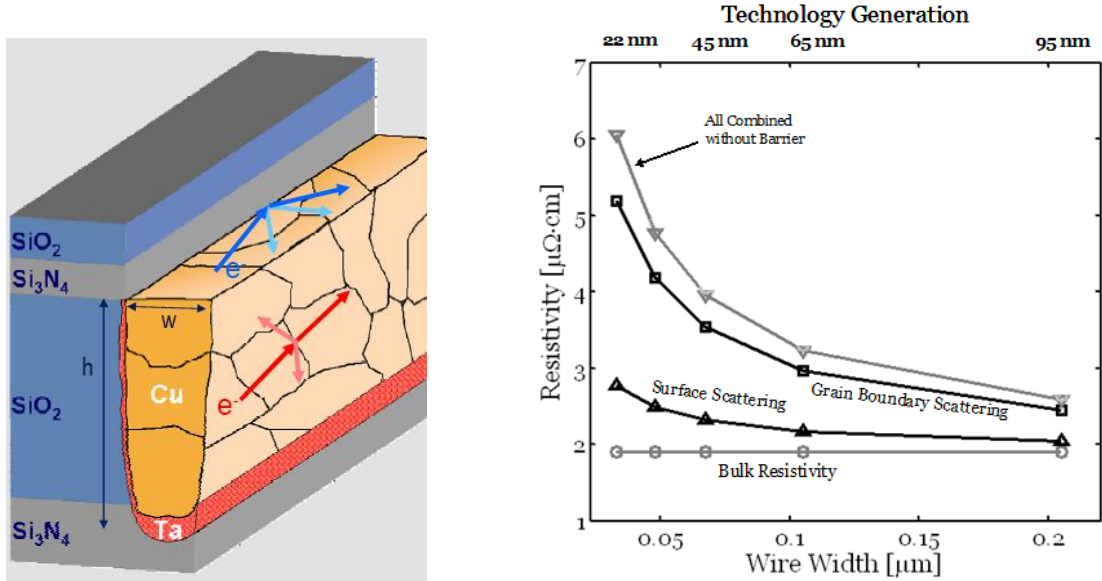


Figure 1-2. Impact of scaling on copper resistivity. (a) Illustrated cross-section of a copper wire showing individual grains with a tantalum barrier layer [14]. (b) Copper resistivity vs. wire width, with and without the effects of surface scattering and enhanced grain boundary scattering. Any additional resistivity due to the barrier layer between copper and surrounding material is ignored [12].

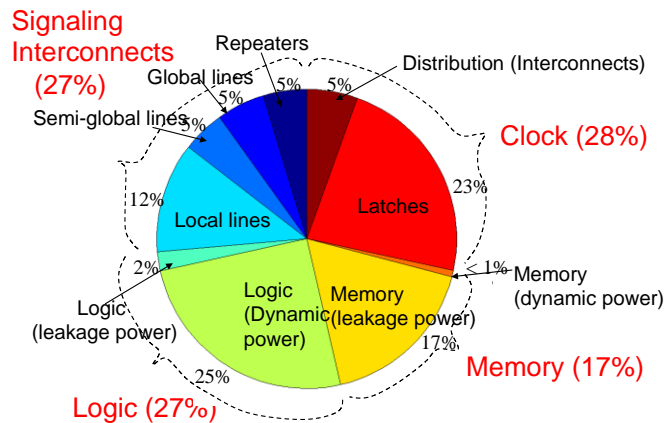


Figure 1-3. Predicted breakdown of power consumption at the 50nm technology node [15].

It therefore appears that copper interconnects have emerged as a critical new performance bottleneck in modern integrated circuits [15], necessitating a superior means of transporting information for intra-chip communication. To this end, researchers have proposed replacing certain copper wires with optical interconnects, particularly for the longer “global” interconnects [6], [7], [16], [17]. Such a system, illustrated in Fig. 1-4, entails a light source in the form of a laser, a modulator to encode the desired signal into the laser light output, a waveguide for transmitting this optical signal over some distance, and photodetector with corresponding receiver circuitry to convert the optical signal back into an electrical one [16]. The motivation for such a scheme is that while there is an overhead in the conversion from an electrical signal into an optical signal and back again, the transmission of the optical signal through a waveguide is so fast and efficient that optics may offer a performance advantage compared to copper wires [6], [7]. This is because sending a signal optically through a waveguide completely eliminates the resistive and capacitive losses and capacitive coupling and cross-talk associated with sending electrical signals through copper wires [17]. In addition, whereas a copper wire can carry only one signal, a single optical waveguide can simultaneously carry many different optical signals by wavelength division multiplexing [18]. As a result, optics can be expected to offer a performance advantage for longer wires where the efficient transmission over a long distance is more important than the overhead of converting the signal between electrical and optical [7], and it logically follows that replacing the longer “global” interconnects with an optical link will go a long way toward alleviating the interconnect performance bottleneck [6]. Researchers have performed extensive

theoretical modeling to compare electrical and optical interconnects and have confirmed that optical interconnects can offer substantial performance improvements over traditional copper interconnects with respect to both energy and latency as shown in Fig. 1-5 for a 10mm wire [7]. As can be seen in Fig. 1-5, optics not only offers superior performance over copper but is also offers a more robust solution as technology continues to scale, particularly with respect to latency where scaling to smaller technology nodes introduces more delay to copper wires but actually improves the performance of optical interconnects due to the improved performance of scaled modulators, detectors, etc. [7]

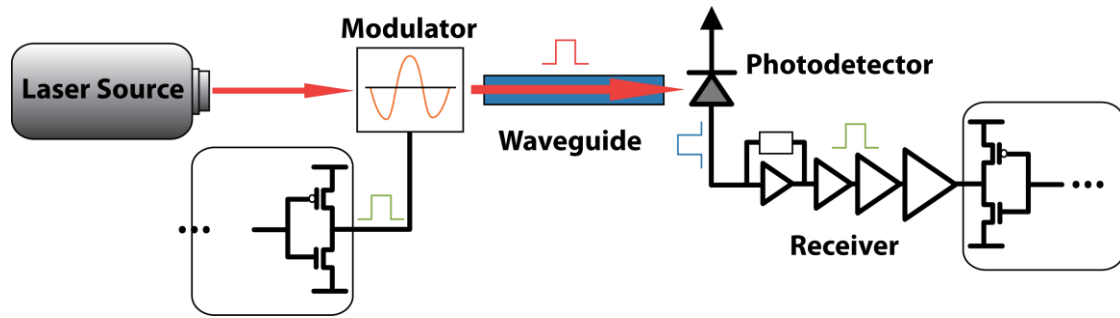


Figure 1-4. Schematic of a typical optical interconnect.

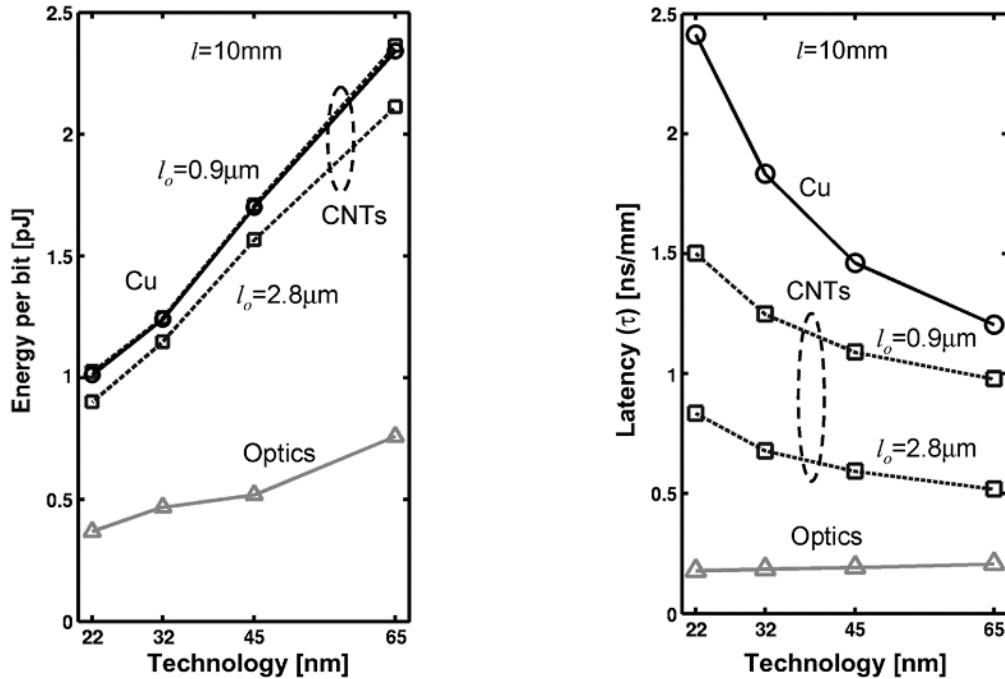


Figure 1-5. Impact of scaling on interconnect performance. (a) Energy per bit vs. technology node, and (b) latency versus technology node. Shown for copper interconnects, carbon nanotube interconnects and optical interconnects [7].

With the advantages of optical interconnects over existing options clearly established, the logical next step would be to physically integrate such optical links with existing silicon CMOS electronics. However, manufacturing such an optical system in a way that maintains compatibility with standard silicon CMOS process technology is a serious challenge [6]. This is largely a materials problem: there are several manufacturing concerns about integrating the optoelectronically useful III-V materials with silicon CMOS integrated circuits [19]. For this reason, researchers are considering the use of Group IV materials [20], in particular germanium [21], for realizing the optoelectronic devices which comprise the optical interconnect of Fig. 1-4. As will be explained in detail in the next Chapter, tremendous progress has been

made in this arena and at present the only component still missing before a practical CMOS-compatible optical interconnect can be realized is an efficient germanium laser. In this dissertation we show band engineering, particularly by means of tensile strain, to be a compelling approach for achieving the efficient light emission from germanium that is necessary to complete a CMOS-compatible optical link.

1.2 Organization of the Dissertation

Chapter 2 discusses the status of previous work on light emission from band-engineered germanium when our own efforts began. We present a broad review firstly of theoretical efforts to understand how various techniques may enhance light emission from germanium and secondly of experimental efforts toward realizing such improvements in practical germanium devices. This sets the stage for our own efforts by explaining where existing techniques were relatively mature and the areas in which there was a compelling research need for greater advances.

Chapter 3 presents a theoretical investigation of how band engineering can enhance light emission from germanium for the specific case of band engineering through biaxial tensile strain. This investigation begins with a brief analysis of how the performance of a germanium LED can be improved before delving into a more thorough theoretical analysis of band engineered germanium lasers. In addition, the improvements available from band engineering are compared to the improvements available from n-type doping, an alternative technique for enhancing germanium light emission. The interaction between strain and doping in particular is carefully examined with respect to improving the performance of germanium optical devices.

Chapter 4 extends this theoretical investigation to other forms of band engineering, specifically uniaxial tensile strain and tin alloying. These additional forms of band engineering are again contrasted with n-type doping in the context of enhancing germanium light emission, and are qualitatively compared with band engineering through biaxial tensile strain which is examined in the preceding chapter. In addition, the interaction between strain and tin alloying is also modeled theoretically, though subsequent chapters reserve experimental realization of strained germanium tin alloys for future works.

Chapter 5 transitions to experimental efforts, specifically a new approach which we present for inducing large uniaxial strains in germanium. Our technique makes use of the small pre-existing biaxial tensile strain that is often present in as-grown germanium and employs a microbridge geometry [22] to convert this small pre-existing biaxial strain into a large localized uniaxial strain, including sufficient strain to make germanium a direct bandgap semiconductor [23]. We further show that this technique creates “pseudo-heterostructures” which makes use of carefully tailored strain non-uniformities to recreate the electronic band profiles of conventional multi-material double heterostructures within our germanium structures [24].

Chapter 6 presents a new technique for engineering large biaxial tensile strains in germanium, again using a stress concentration approach. Just as the approach presented in Chapter 5 makes use of a clever microbridge geometry for inducing a large uniaxial strain, the technique of Chapter 6 involves using a special disk geometry to induce a large biaxial strain. Using this new disk geometry we are able to achieve by the largest CMOS-compatible strain that has ever been reported in germanium [25].

Chapter 7 concludes this dissertation by summarizing the achievements resulting from this research and by discussing potential avenues for future work.

Chapter 2

Background on Band-Engineered Germanium

2.1 General Background

While optical interconnects offer compelling performance advantages over existing copper interconnects [7], manufacturing an optical link in a way that is compatible with existing silicon CMOS technology is a serious challenge [6]. Silicon itself is inherently unsuitable for light emission due to its complete absence of a direct bandgap [26] and there are many manufacturing challenges associated with integrating III-V materials with standard silicon CMOS electronics, though progress is being achieved on the latter issue [27]–[29]. In order to bypass these limitations researchers have sought to use Group IV materials for optoelectronic applications as these materials pose far fewer contamination concerns when integrated with existing silicon CMOS electronics [19], [21]. In this framework germanium-on-silicon has long found use as a detector [30]–[33] and more recently as a modulator [34]. The use of germanium is highly advantageous in this context since germanium can be readily grown on silicon through high-quality heteroepitaxy [35], [36] and because germanium is already widely used in commercial CMOS processing [37], [38]. Moreover, although germanium has an indirect bandgap of 0.667 eV, it also has a direct bandgap of 0.8 eV [39] which can be readily accessed for absorptive applications such as detectors [30]–[33] and modulators [34]. In fact, the marginally indirect

bandgap nature of germanium can actually be helpful for detectors since photo-generated electrons in the direct conduction valley will quickly scatter into the indirect valleys [40] where radiative recombination is suppressed [41], thereby increasing carrier lifetimes which in turn increases the quantum efficiency [42]. For light emission applications, however, the indirect bandgap poses a considerably larger hurdle: over 99.98% of injected electrons will reside in the indirect conduction valleys [43] where they cannot contribute substantially to useful optical processes [41], [44]. This makes building an efficient germanium light emitter, and in particular a germanium laser, quite challenging [19], [45].

As a result of the challenges associated with germanium light emission, most of the initial efforts toward building a Si-compatible laser involved hybrid III-V bonding onto silicon [46], an approach which is still very actively pursued today [47]–[49]. However, in 2007 it was proposed that by employing a few special tricks, germanium could indeed be used as the gain medium for a Si-compatible laser [41], thereby creating an optical link solely within the Group IV materials system and avoiding all of the challenges and complexities associated with hybrid III-V processes. Specifically, these “special tricks” consisted of employing band engineering in the form of a small 0.25% biaxial tensile strain along with heavy n-type doping of the active region to “fill up” states in the indirect conduction valley [41]. At the time this research project began in early 2011, however, there were many open questions about the viability of these proposed techniques from both a theoretical and experimental perspective.

2.2 Background on Theory & Modeling

Interest in band-engineered germanium for light emission took off in 2007 with a theoretical publication [41] which claimed that a combination of a small 0.25% biaxial tensile strain and $7.6 \times 10^{19} \text{ cm}^{-3}$ n-type doping can achieve up to 400 cm^{-1} optical gain in an ideal structure, enough to build a working laser [41]. A follow-up theoretical study [50] from early 2010 provided a somewhat more in-depth investigation of how the optical gain varies with the doping level and steady-state injected carrier density. However, while these studies were both pioneering in the field, they focus primarily on quantifying the achievable net optical gain rather than more critical parameters such as the lasing threshold. The slope efficiency of the proposed Ge laser is never even mentioned. In addition, the scope of these studies did not include any investigation of strain values beyond 0.25%, leaving no information about whether researchers should focus their efforts on achieving higher strain values or heavier doping levels in Ge.

A separate study was done by different authors in 2012 considering not only strain and n-type doping but also band engineering through tin alloying [51]. However, this study restricted the analysis to a wavelength of exactly 1550nm [51]. Since band engineering reduces germanium's bandgap [39], [52], it logically follows that a band engineered germanium laser will operate most efficiently at longer wavelengths; any study that doesn't account for this wavelength shift will not properly quantify the benefits of band engineering [53]. The study of [51] also stopped after calculating a threshold injected carrier density, which is very different from calculating the more relevant threshold current. Converting a steady-state injected

carrier density to a current density is non-trivial since it may depend heavily on the Auger recombination lifetime which depends on the total electron density and, in turn, the concentration of extrinsic electrons from doping [41]. And lastly, rather than using an empirical equation for free carrier absorption as in [41], the study of [51] calculated free carrier absorption using the Drude-Lorenz equation [54] which has since been shown to exclude the inter-valence band transitions which are believed to dominate the actual free carrier absorption [55].

Due to the limitations of these studies there was initially very little information about whether n-type doping or band engineering approaches such as strain would be most useful for realizing an efficient low threshold on-chip germanium laser. There was also very limited information about the interaction of n-type doping and band engineering and how this interaction would affect the performance of a germanium laser. In Chapter 3 we answer these questions through a comprehensive theoretical study of a germanium laser's performance as a function of both n-type doping and band engineering for the specific case of band engineering through biaxial tensile strain. In Chapter 4 we extend this study to other forms of band engineering such as uniaxial tensile strain and alloying with tin to create GeSn.

2.3 Background on Experimental Band Engineering Techniques

2.3.1 Uniaxial Strain

Several approaches have been investigated for engineering large uniaxial tensile strains in Ge. Some of these approaches are decidedly not compatible with Si CMOS device technology, such as the use of an external micromechanical three-point module

to apply up to 1.8% uniaxial tensile strain in Ge [56]. Another approach involved using external silicon nitride stressors on patterned Ge to induce uniaxial strain up to ~1.5% [57]. Although this approach was fully CMOS-compatible it involves a very inhomogeneous strain, and thus a spatially non-uniform bandgap, which would impede any practical device realization because different Ge regions would be optimized for operation at different wavelengths in accordance with the different bandgaps. A separate CMOS-compatible structure, analogous to one mentioned for biaxial strain, achieved up to 0.96% uniaxial tensile strain using a suspended geometry with two silicon nitride stressor beams attached laterally to a pre-patterned Ge region [58]. However, as with the analogous biaxial structure, employing a suspended geometry drastically limits thermal dissipation [59], thus precluding any practical device realization on account of excessive heating. In early 2013 researchers developed a superior structure using suspended all-germanium microbridges [22]. Not only did this new approach achieved a higher uniaxial strain value of 3.1%, but it also eliminated the silicon nitride stressors and thereby simplified the fabrication to a low-cost one-mask process [22].

Here at Stanford, we developed a largely similar microbridge technique in 2013 and showed that the high degree of strain localization reproduced double heterostructure action – a crucial requirement for lasers – within a single material [24]. We investigated this phenomenon through careful optical characterization but, due to the wavelength cutoff of detector, we stopped with devices of only 2.3% uniaxial strain; any attempt to engineer a larger strain would have redshifted the luminescence beyond our detection capabilities due to strain-induced bandgap narrowing [24]. We

then introduced a novel technique that employed stiction to adhere these suspended germanium microbridges to the underlying silicon substrate, thereby solving the thermal dissipation problem but, due to the relative large geometries in that work, we achieved only uniaxial strain of up to 1.6% [60]. This results have all been described in detail in a previous dissertation [61]. However, no attempt was made in that work to engineer the largest possible uniaxial strain for optimal band engineering, a shortcoming which we address in this work. In Chapter 5 we present microbridges with the largest CMOS-compatible uniaxial tensile strains ever reported: up to 4.1% for substrate-adhered microbridges and up to 5.7% in suspended microbridges.

2.3.2 Biaxial Strain

Achieving a large biaxial strain in germanium is known to be physically possible as researchers have achieved beyond 2% biaxial tensile strain in germanium, enough to achieve a direct bandgap, using approaches that were not compatible with Si CMOS technology. Using pseudomorphic growth of germanium by molecular beam epitaxy on a deliberately lattice-mismatched $\text{In}_x\text{Ga}_{1-x}\text{As}$ buffer region supported on a GaAs substrate, researchers have achieved 2.33% biaxial tensile strain in germanium [62]. Other researchers have achieved 2.00% biaxial strain in Ge by applying ~700 kPa of gas pressure to a suspended ultrathin Ge nanomembrane supported on polyimide, thereby inducing a vertical deflection and accompanying strain [63]. Unfortunately these approaches are not compatible with silicon CMOS technology. For the example of lattice-mismatched pseudomorphic growth of Ge on an $\text{In}_x\text{Ga}_{1-x}\text{As}$ buffer, the III-V template not only precludes CMOS compatibility but defeats the entire purpose of

using Ge which is to avoid the presence of any III-V materials. For the example of the gas pressure on a Ge nanomembrane, this approach is not CMOS-compatible because the strain is not permanently sustained: upon release of the gas pressure the strain relaxes. Even if a pressurized gas could somehow be physically manufactured into a commercial CMOS unit, this gas pressure would then become temperature dependent in accordance with Gay-Lussac's law – an unacceptable situation given the wide range of temperatures at which commercial electronics are typically expected to operate. Although not quite a direct bandgap, in 2015 researchers also reported 1.5% biaxial tensile strain in Ge microdisk cavities on Si using a silicon nitride all-around stressor technique [64]. However, the success of this technique relied upon the use of GaAs growth templates for high-quality Ge and also coating the entire Si substrate with gold for the bonding process [64]. While further innovations may – and hopefully will – bring this new all-around silicon nitride technique into the realm of CMOS compatibility, the large quantities of GaAs and gold involved raise serious cost and contamination related concerns at present.

Much prior work has also been done on biaxial strain approaches that are CMOS-compatible at least in principle, however each of the approaches has at least one critical drawback. Perhaps the most common approach is to obtain a small biaxial strain directly from the Ge-on-Si growth process. Heteroepitaxy of Ge on a Si wafer yields relaxed Ge at the 600°C –800°C growth temperature but, upon cooling to room temperature, a small strain of about 0.20%-0.25% accumulates in the Ge due to the dissimilar thermal expansion coefficients between Ge and Si [65]. This strain can be slightly increased by using heavily n-type Ge since n-doping increases Ge's thermal

expansion coefficient [66] and hence the mismatch with Si's coefficient [41], however the observed strain enhancement from heavy n-doping is relatively small [67]. (Note that the change in n-type Ge's thermal expansion coefficient should, in principle, occur for all forms of n-type doping regardless of the specific dopant element employed. This is because the underlying mechanism for the change in thermal expansion coefficient is believed to be free carrier effects from the large extrinsic electron density [68]: it is well understood that free carriers can substantially affect Ge's elastic coefficients [69], [70] and this should logically affect the thermal expansion coefficient as well [68].) Additional techniques are therefore needed in order to achieve larger strains. One such technique involves creating a freestanding Ge membrane supported on a silicon wafer and then depositing a tungsten stressor layer [71]. The tungsten stressor has an initial compressive strain which relaxes upon deposition, thereby causing a vertical deflection technique and inducing up to 1.11% biaxial strain in the Ge membrane [71]. Integration of devices such as photodetectors and LEDs using this technique was also demonstrated, though only up to 0.76% strain was achievable with device integration [71], [72]. However, there are downsides with this approach. Creating the Ge membrane involved backside etching through the entire thickness of the silicon handle wafer which, while technically still CMOS-compatible, is a highly undesirable process for commercial products. The vertical deflection of the membrane also results in a very inhomogeneous strain distribution thereby causing dramatic variations in the Ge bandgap across the membrane; a constant bandgap is essential for practical optical devices operating at a defined wavelength. Lastly, the presence of tungsten metal adjacent to the Ge and the out-of-plane deflection would

compromise any optical cavity design and create large free carrier losses in the metal. Separately, a truly CMOS-compatible structure has been shown by depositing a stressed silicon nitride layer on a Ge stripe to induce an “equivalent biaxial strain” of up to 0.9% [57]. However this strain was not truly biaxial and, critically, was very inhomogeneous in the vertical direction. It is therefore the case that this structure will also lack the spatially constant bandgap necessary for optimal laser operation at a pre-defined wavelength. Yet another CMOS-compatible structure with up to 0.82% biaxial tensile strain was demonstrated using a suspended geometry with four silicon nitride stressor beams attached laterally to a pre-patterned Ge region [58]. However, employing a suspended geometry eliminates the physical contact between the Ge and the underlying Si substrate. This removes the traditional heat conduction pathway and makes it impossible to conduct even a simple photoluminescence experiment without excessive heating [59].

In light of the limitations of these prior techniques, there is a clear need for a new structure that can induce large homogeneous biaxial tensile strains in Ge with full compatibility with existing Si CMOS technology. In order to be a truly effective platform for Ge lasers, this structure must involve no out-of-plane deflections or metal stressor layers that might compromise an optical cavity and must include an efficient means of thermal conduction from the Ge to either the substrate or some form of heat sink. Preferably, such a structure should involve a simple one-mask fabrication process with no exotic materials to limit cost and complexity. In Chapter 6 we present a structure that satisfies all of these criteria.

2.3.3 Alternative Experimental Approaches

Within the context of band engineering, germanium tin alloys have also garnered substantial interest as an alternative to strain [19], [73], [74]. Just as applying a tensile strain to germanium lowers the direct conduction valley relative to the indirect conduction valleys, alloying germanium with tin to create GeSn can also result in a direct bandgap material for use as a laser gain medium [73]. This tin alloying approach was substantially more mature than tensile strain in terms of experimental realization at the time we began our research. Researchers have previously reported compressively strained GeSn alloys with up to 34% tin [75] and unstrained GeSn alloys with 15% tin [76] grown on silicon substrates by molecular beam epitaxy. This is well beyond the ~6.3% tin required for a direct bandgap in relaxed GeSn [77], [78]. Although the material quality suffered from a high dislocation density in those particular works [75], [76], other researchers have made tremendous progress in this arena [74], [79]–[86]. Very recently in 2015, researchers have even demonstrated a direct bandgap GeSn laser, albeit with some severe limitations with regard to threshold and operating temperature [87], which clearly demonstrates the potential of band engineered germanium [88]. Given both the relative maturity of GeSn technology and the large number of researchers working on GeSn [74], [79]–[88] we decided to focus our experimental efforts exclusively on germanium strain engineering rather than GeSn.

Although it is not technically band engineering, n-type doping is another prominent technique to improve the performance of germanium lasers [41], almost always employed in combination with the small ~0.25% biaxial tensile strain [55],

[89]–[93] which results naturally from the germanium growth process [36]. Prior to this work, tremendous advances had been made in the realm of achieving ever-higher n-type doping in germanium [94], [95] and efforts were already underway in applying these advances to germanium light emitters such as light emitting diodes [72], [96]–[100]. In early 2010 researchers demonstrated an optically pumped germanium laser by employing an n-type doping of $1 \times 10^{19} \text{ cm}^{-3}$ [90]. This achievement was followed-up by increasing the doping level to $5 \times 10^{19} \text{ cm}^{-3}$ [93] and then building an electrically-pumped germanium laser [101] which, despite suffering from an unacceptably high threshold of about 280 kA/cm^2 and poor efficiency [101], represented a tremendous breakthrough. However, although n-type doping was the leading candidate for realizing an efficient low threshold germanium laser when this work began, our theoretical modeling in Chapter 3 showed that doping does not in fact represent a viable path to this goal [53]. As such, we decided to focus our experimental efforts exclusively on engineering large strains in germanium rather than achieving ever higher doping levels.

Chapter 3

Theoretical Modeling for Biaxial Strain and N-Type

Doping

3.1 Band Structure Modeling

The first step of any modeling approach is to compute the full bandstructure of germanium over the intended range of strain values [53], as illustrated in Fig. 3-1 for the specific cases of zero strain and 2.0% strain. This can be done using any of several techniques such as $k \cdot p$ [102], tight-binding [53], non-local empirical pseudo-potentials [103], [104], density functional theory [86], or even simple deformation potential theory [39] with parabolic bands [25]. For our modeling on biaxial strain in this chapter, we will use $sp^3d^5s^*$ tight-binding following the approach of Refs [105], [106]. The use of tight-binding allows us to compute not just the bandstructures' 2D cross sections shown in Fig. 3-1 but also the allows energies over a full $200 \times 200 \times 200$ mesh of k -points encompassing the entirety of the first Brillouin Zone. This gives the full 4D bandstructure, i.e. energy as a function of the three wavevector components k_x , k_y and k_z . Using tight-binding allows us to account for the complicated mixing and warping of the valence bands under stain, as can be seen in the bandstructures' 3D cross-sections shown in Fig. 3-2. Lastly, we note that our model assumes germanium will become direct bandgap semiconductor at 2.4% biaxial tensile strain as shown in Fig. 3-3, which means that our model is very conservative in that considerably more

strain is needed to achieve a direct gap in our model than the $\sim 1.7\%$ predicted by most models [39], [52], [107]. This means that our model assumes that biaxial tensile strain reduces the energy difference between the direct and indirect conduction valleys by only 55 meV for every 1% of strain, i.e. the initial 133meV difference between germanium's direct and indirect valleys divided by the 2.4% biaxial strain needed to achieve a direct gap. Meanwhile, models that assume that only $\sim 1.7\%$ biaxial strain is needed to achieve a direct gap implicitly assume that every 1% of biaxial strain causes a much larger 78 meV reduction in the energy difference between the direct and indirect conduction valleys. Since our model underestimates the extent to which biaxial strain reduces the energy difference between the direct and indirect conduction valleys we can expect any of our subsequent modeling results to be quite conservative.

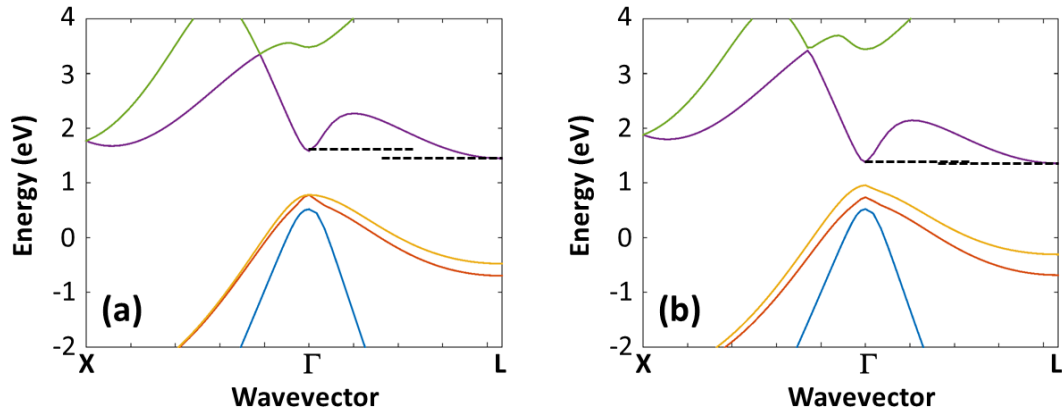


Figure 3-1. 2D cross-section of germanium's band structure computed. Computed by tight-binding and shown at (a) zero strain, and (b) 2.0% biaxial tensile strain. Black dashed horizontal lines are visual aids to help illustrate the reduction in the Γ -L energy separation under tensile strain.

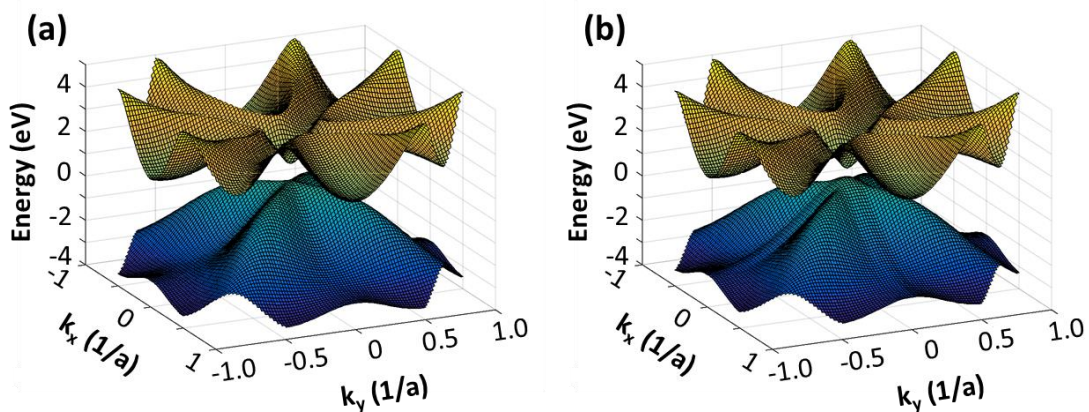


Figure 3-2. 3D cross-section ($k_z=0$) of germanium's band structure. Computed by tight-binding and shown at (a) zero strain, and (b) 2.0% biaxial tensile strain. The x - and y -components of the wavevector (\mathbf{k}) are shown, with units given as multiples of the inverse lattice constant ($1/a$).

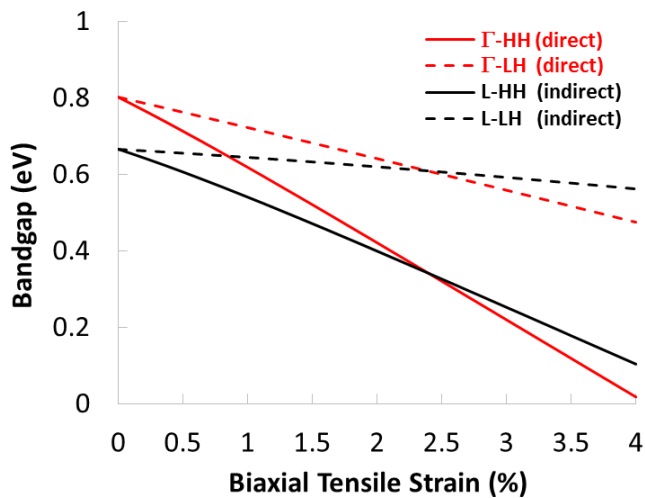


Figure 3-3. Germanium's direct (Γ) and indirect (L) bandgaps vs. biaxial tensile strain according to our tight-binding model. Crossover of the direct gap is visible at 2.4% biaxial strain.

3.2 General Carrier Statistics Modeling

3.2.1 Dependence on Strain and Temperature

The overriding motivation for employing band engineering in germanium, in this case by biaxial tensile strain, is to increase the fraction of electrons that reside in the direct Γ conduction valley as opposed to the indirect L conduction valleys. Using our bandstructure model as described in the preceding section we can directly quantify this phenomenon for undoped germanium. To do this we compute the Maxwell-Boltzmann occupation probability for each allowed k-point and then integrate over the full k-point mesh of allowed energies encompassing the first Brillouin Zone to obtain the carrier concentration in each valley. As shown in Fig. 3-4, we observe a dramatic increase in the percentage of electrons which reside in the direct conduction valley upon applying a tensile strain. Although there is an interesting temperature dependence in Fig. 3-4, we will begin by considering only room temperature (300K). At room temperature only 0.011% of electrons reside in the direct conduction valley in the absence of strain. Applying 1.0% biaxial tensile strain increases this proportion by 8x to 0.087%. Increasing the strain from 1.0% to 2.0% results in another 7x enhancement to 0.62% occupancy, and further increasing the strain to 3.0% yields a further 6x enhancement to 3.7% occupancy. Thus, applying a 3.0% biaxial tensile strain increases the proportion of electrons in the direct conduction valley by more than two orders of magnitude from only 0.011% to about 3.7%.

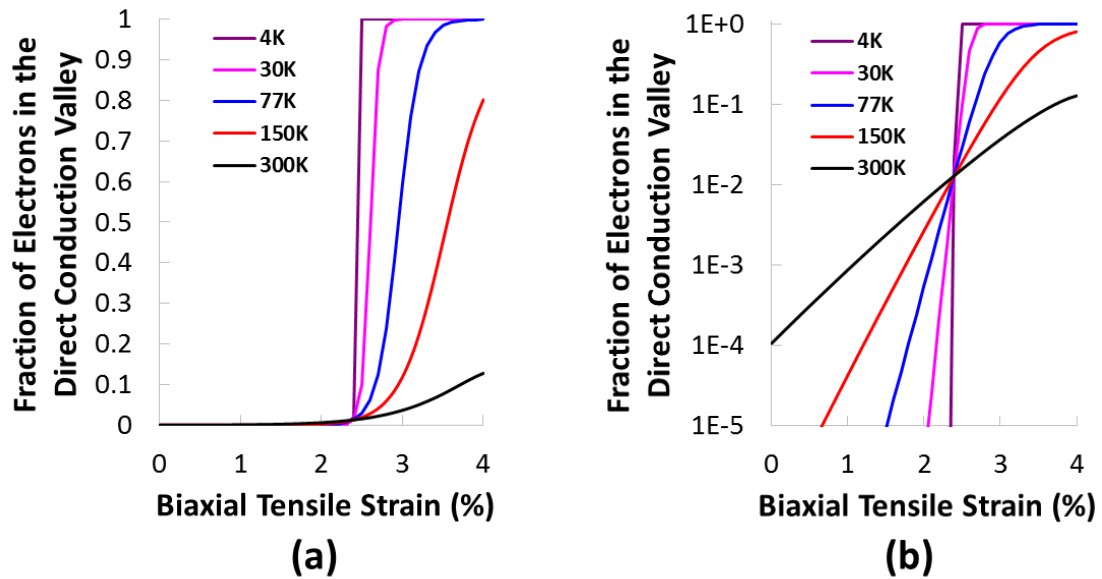


Figure 3-4. Fraction of electrons in the direct conduction valley vs. strain for undoped germanium at several different temperatures. Data shown on (a) linear, and (b) logarithmic scales.

There is another interesting behavior that can be seen from Fig. 3-4: the achievement of a direct bandgap at 2.4% strain is of no particular importance unless extremely low temperatures are employed, for instance the 4K temperature associated with liquid helium. For instance, at 2.4% biaxial strain germanium will become a direct bandgap semiconductor yet only 1.3% of electrons will reside in the direct valley. The reason for this is that the indirect valleys, being 4-fold degenerate and having a much larger effective mass, collectively have a >50x higher effective density of states than the direct valley [108]. (Note that although germanium has 8 equivalent L valleys in the conduction band, each of these valleys is only half contained within the first Brillouin zone thus making the indirect valleys exactly 4-fold degenerate for multiplicity purposes.) Germanium will actually become a negative bandgap material (at ~4.1%

strain as shown in Fig. 3-3) before even 20% of electrons reside in the direct valley at room temperature. Even at the 77K temperature associated with liquid nitrogen it takes a full 3.0% strain, significantly more strain than needed for a direct gap, before a majority of electrons reside in the direct conduction valley. The takeaway of this finding is that there is no special practical relevance to achieving a direct bandgap for room temperature devices or even for liquid nitrogen cooled devices [23], [25]. In fact, as we will show in the next section there is not even a special benefit to having >50% of carriers in the direct valley [25]. To the extent that there is a “critical” strain that researchers should strive to achieve this should be determined by detailed device modeling [25] as we will show in the following sections.

3.2.2 Dependence on Strain and N-Type Doping

Next we can incorporate the effects of n-type doping into our model. In this case Maxwell-Boltzmann statistics are no longer valid and so we must compute the occupancy probabilities using Fermi-Dirac statistics. We first iteratively determine the Fermi level which gives a total electron concentration equal to the assumed doping. (Although only a fraction of the dopants will be ionized when the Fermi level is above the donor level, our model only considers those dopants which have indeed been ionized i.e. the electrically active doping concentration; our model also ignores any interaction between the injected electron density and the proportion of dopants which are ionized.) Knowing the Fermi level we can then compare the relative electron populations inside and outside the direct conduction valley. As shown in Fig. 3-5, n-type doping can deliver some very large enhancements in the percentage of electrons

that reside in the direct conduction valley. For unstrained germanium only 0.011% of electrons will reside in the direct conduction valley in the absence of doping, increasing by 2x to 0.020% at $2 \times 10^{19} \text{ cm}^{-3}$ doping, and increasing by a further 7x to 0.14% at $1 \times 10^{20} \text{ cm}^{-3}$ n-type doping.

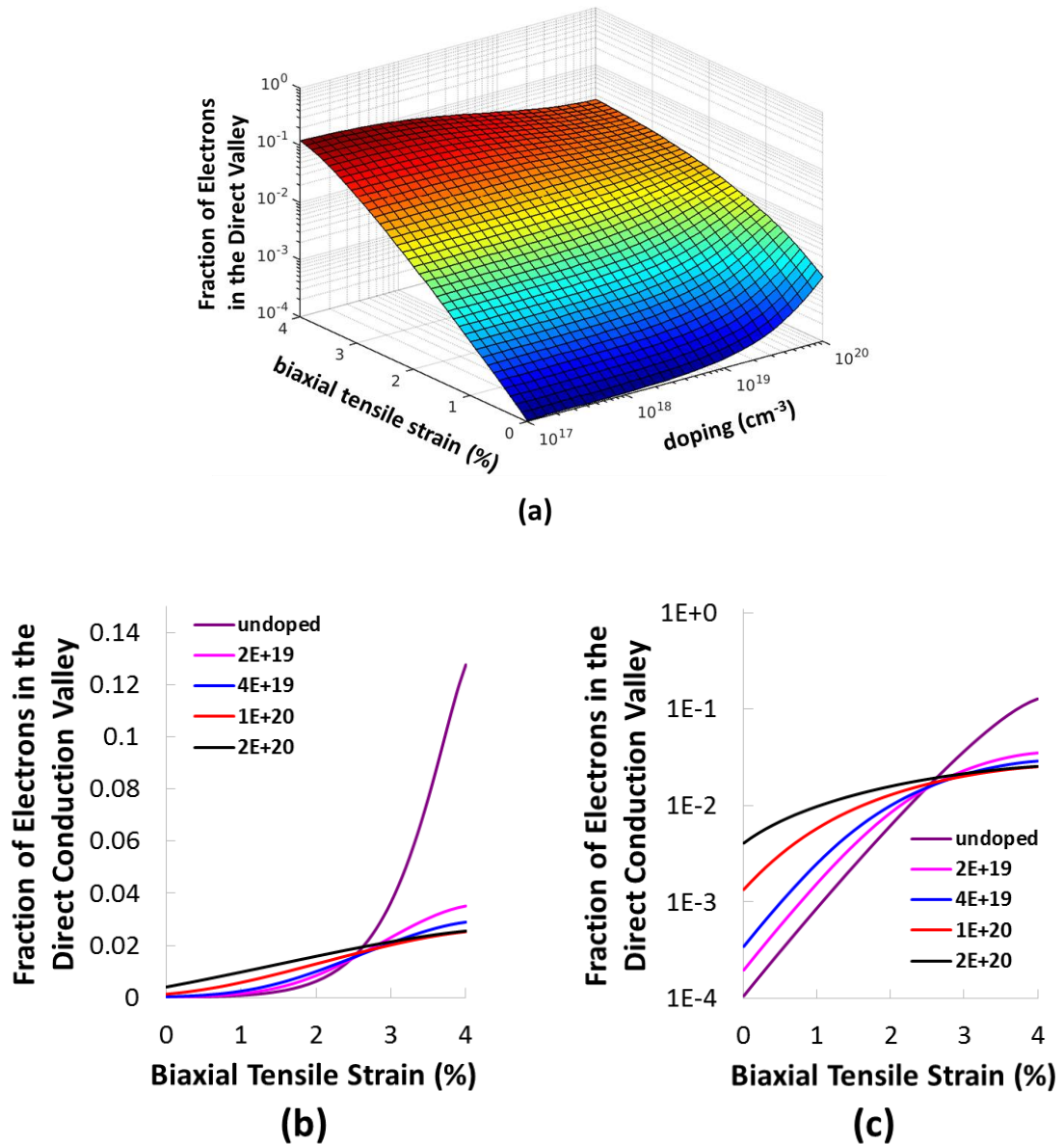


Figure 3-5. Direct conduction valley occupancy in germanium. (a) Fraction of electrons in the direct conduction valley vs. strain and doping at room temperature. (b,c) Fraction of

electrons in the direct conduction valley vs. strain for several different n-type doping levels at room temperature, shown on (b) linear, and (c) logarithmic scales.

Interestingly, there is a negative interaction between strain and doping and, as can be seen in Fig. 3-5, once the strain exceeds $\sim 2.4\%$ n-type doping actually reduces the proportion of electrons in the direct conduction valley. This is because doping causes spillover of electrons from the lower energy conduction valley(s) to the higher energy conduction valley(s). Once a direct bandgap has been achieved, i.e. for biaxial strains larger than 2.4% , the direct valley is the lowest energy valley. Thus, for direct bandgap germanium, i.e. for biaxial strains larger than 2.4% , doping will cause spillover of electrons out of the direct valley into the indirect valleys. Nevertheless, as we will see in the subsequent sections, doping retains some utility for practical devices even once a direct bandgap has been achieved by strain.

3.3 Light Emitting Diode (LED) Modeling

3.3.1 Dependence on Strain and N-Type Doping

Having modeled the carrier statistics for germanium in the presence of biaxial tensile strain and n-type doping in the preceding section it is now straightforward to model the performance of a simple germanium LED. For this modeling we will focus on the internal quantum efficiency (IQE) of a hypothetical germanium LED. Assuming a heterostructure design such that diffusion current is negligible and the injection efficiency will be virtually 100% , something which can be achieved even in a simple Si/Ge/Si double heterostructure LED [89], the IQE will simply be the fraction of

carrier recombination which is radiative. We can compute the radiative and non-radiative recombination rates by using Equation 3-1 and Equation 3-2, respectively. The radiative recombination rate of Equation 3-1 considers spontaneous emission from both the direct and indirect conduction valleys, with the radiative recombination lifetime being much faster in the direct valley, and so strain increases the radiative recombination rate by increasing the $\left(\frac{n_r}{n}\right)$ term. The non-radiative recombination rate of Equation 3-2, meanwhile, is agnostic to whether electrons are in the direct or indirect conduction valley and is therefore independent of strain, at least in the approximations of our model. Then, finally, the IQE is simply the ratio of radiative recombination to total recombination as given in Equation 3-3.

$$\begin{aligned}
U_{\text{radiative}} &= R_L n_L p + R_r n_r p \\
&= R_L (n - n_r) p + R_r n_r p \\
&= R_L n p + (R_r - R_L) n_r p \\
&= R_L n p + (R_r - R_L) n p \left(\frac{n_r}{n}\right) \\
&\cong R_L n p + R_r n p \left(\frac{n_r}{n}\right) \tag{3-1}
\end{aligned}$$

Equation 3-1. Radiative recombination rate ($U_{\text{radiative}}$) in terms of the electron density (n), hole density (p) and fraction of electrons in the direct conduction valley $\left(\frac{n_r}{n}\right)$. The terms n_r and n_L denote the electron concentrations in the direct and indirect valleys, respectively. The recombination coefficients are $R_L=5.1 \times 10^{-15} \text{cm}^3/\text{s}$ and $R_r=1.3 \times 10^{-10} \text{cm}^3/\text{s}$ [41].

$$\begin{aligned}
U_{\text{non-radiative}} &= C_{\text{nnp}}n(np - n_i^2) + C_{\text{ppn}}p(np - n_i^2) + \frac{\min(n, p)}{\tau_{\text{SRH}}} \\
&= C_{\text{nnp}}n(np - n_i^2) + C_{\text{ppn}}p(np - n_i^2) + \frac{p}{\tau_{\text{SRH}}} \quad (3-2)
\end{aligned}$$

Equation 3-2. Non-radiative recombination rate ($U_{\text{non-radiative}}$) in terms of the electron density (n), hole density (p) and defect-limited minority carrier lifetime (τ_{SRH}). Note that since we always presume either undoped or n-type doped material the minority carrier density will always be the hole carrier density (p). The recombination coefficients are $C_{\text{nnp}}=3.0 \times 10^{32} \text{ cm}^6/\text{s}$ and $C_{\text{ppn}}=7.0 \times 10^{-32} \text{ cm}^6/\text{s}$ [41].

$$\text{IQE} = \frac{U_{\text{radiative}}}{U_{\text{radiative}} + U_{\text{non-radiative}}} \quad (3-3)$$

Equation 3-3. Internal quantum efficiency (IQE) in terms of the radiative recombination rate ($U_{\text{radiative}}$) and the non-radiative recombination rate ($U_{\text{non-radiative}}$).

Assuming a 100ns defect-limited minority carrier lifetime (τ_{SRH}) as in Ref [41] and a steady-state carrier injection level of $\Delta n = \Delta p = 10^{17} \text{ cm}^{-3}$, we can compute the IQE of a germanium LED versus strain for several different doping conditions as shown in Fig. 3-6. From this figure we observe that both strain and doping enable tremendous enhancements in IQE for a germanium LED, at least in the assumption that neither strain nor doping affects the defect-limited minority carrier lifetime – a somewhat dubious assumption about doping [109], [110] which we will revisit later in section 3.5.

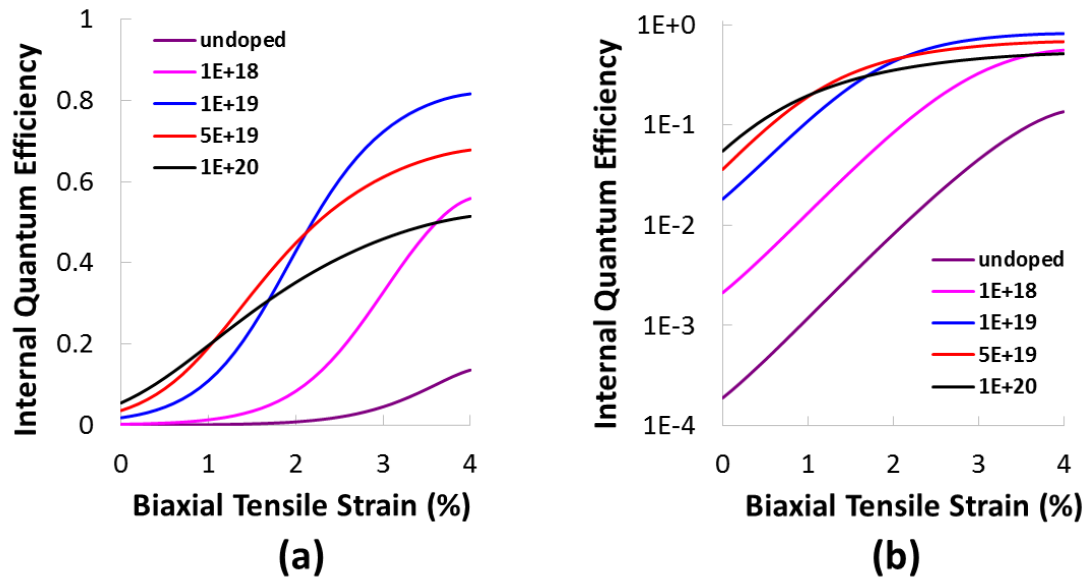


Figure 3-6. Internal quantum efficiency of a germanium double-heterostructure LED vs. biaxial strain for various n-type doping levels. Data shown on (a) linear, and (b) logarithmic scales. Defect-limited Shockley-Read-Hall (SRH) lifetime is assumed to be 100ns.

Interestingly, even once a direct bandgap has been achieved (i.e. for biaxial strains larger than 2.4%) we observe that doping can still enhance the IQE of our hypothetical germanium LED. This is despite the fact that doping actually reduces the fraction of electrons in the direct conduction valley for such high strains as previously shown in Fig. 3-6 and will therefore decrease the $\left(\frac{n_r}{n}\right)$ term in Equation 3-1. The trend is not even monotonic with doping: at 4.0% strain we observe from Fig. 3-6 that the IQE increases as we increase the doping from zero to $1 \times 10^{18} \text{ cm}^{-3}$ and then to $1 \times 10^{19} \text{ cm}^{-3}$, but the IQE then decreases as we further increase the doping to $5 \times 10^{19} \text{ cm}^{-3}$ or $1 \times 10^{20} \text{ cm}^{-3}$. The explanation is that, neglecting the $\left(\frac{n_r}{n}\right)$ term for a moment, the radiative recombination rate in Equation 3-1 is directly proportional to the electron density “n”.

The non-radiative recombination rate in Equation 3-2, on the other hand, has a defect-limited Shockley-Read-Hall (SRH) term P/τ_{SRH} which is independent of n , and an Auger term $C_{\text{nnp}}n(np - n_i^2) \cong C_{\text{nnp}}n^2p$ which is proportional to n^2 . Thus, we find that non-radiative recombination will always dominate at very small electron densities due to the SRH term (P/τ_{SRH}) and at very large electron densities due to the Auger term ($\cong C_{\text{nnp}}n^2p$), and so there will be an optimal electron concentration – and hence an optimal n-type doping – where the “np” terms of the radiative recombination can dominate. From Fig. 3-6 we conclude that this optimal doping is at least $1 \times 10^{20} \text{ cm}^{-3}$ for small strain values and decreases to somewhere in the vicinity of $1 \times 10^{19} \text{ cm}^{-3}$ for larger strain values such as the 2.4% biaxial tensile strain necessary for a direct bandgap. This optimal doping is also likely to be a function of the SRH lifetime, with larger doping being more useful when the SRH lifetime is shorter and less doping being more useful when the SRH lifetime is longer, although this tradeoff will not be explicitly explored in this dissertation in the context of LEDs.

3.3.2 Dependence on Material Quality

We can also consider how the material quality affects the performance of double-heterostructure germanium LEDs, since the defect-limited minority carrier lifetime (τ_{SRH}) is a strong function of material quality [109], [111], [112]. As shown in Fig. 3-7 there is no conceivable level of strain that will result in an efficient germanium LED if the SRH lifetime is less than 1ns. On the other hand, if the SRH lifetime can be greater than 100ns then the IQE can approach 100% for large strain values. Given that

most epitaxially-grown germanium in the present state-of-the art has a minority carrier lifetime of approximately 1ns or faster [111], considerably less than the bulk lifetime values of $>1\mu\text{s}$ [113], there is an acute need for research efforts such as those of Refs [112], [114] which explore innovative ways of improving the material quality and thereby improving the SRH lifetime. Such experimental efforts on material quality, however, are outside the scope of this dissertation.

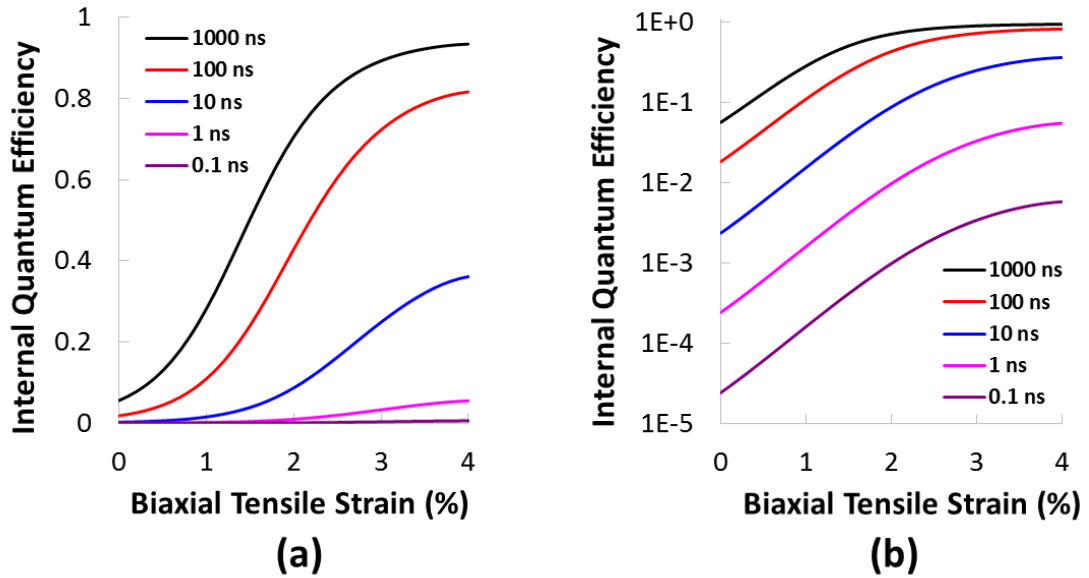


Figure 3-7. Internal quantum efficiency of a germanium double-heterostructure LED vs. biaxial strain for various SRH lifetime assumptions. Data shown on (a) linear, and (b) logarithmic scales. Doping is assumed to be $1 \times 10^{19} \text{ cm}^{-3}$.

3.4 Results – Laser Modeling

3.4.1 Optical Gain

The penultimate goal of using band engineered germanium is to build an efficient low threshold germanium-on-silicon laser for use in on-chip optical interconnects [115]. It

is therefore imperative to investigate theoretically how a germanium laser will perform in the presence of tensile strain and/or n-type doping. Having already computed the band structures of biaxially strained germanium along with basic carrier statistics in the presence of strain and n-type doping, the next step is to model the optical gain. We do this using an empirical absorption coefficient for germanium [116], shown in Equation 3-4, which contains a special modification to account for how the bandgaps change in the presence of strain. This special modification consists of dividing the bulk absorption coefficient into two components, one each for the Γ -LH and Γ -HH transitions, with a proportion given by the relative joint density of states masses for each of these two transitions [116]. We will conservatively ignore transitions from the indirect valley, i.e. the L-LH and L-HH transitions; although contributions from the indirect transitions are helpful they are much weaker and would only add $\sim 100\text{cm}^{-1}$ of gain [41].

$$\alpha_{\Gamma} = 1.9 \times 10^4 \text{ eV}^{0.5} \text{ cm}^{-1} \left(0.682 \sqrt{E_{\text{photon}} - E_g^{\Gamma\text{-HH}}} + 0.318 \sqrt{E_{\text{photon}} - E_g^{\Gamma\text{-LH}}} \right) / E_{\text{photon}} \quad (3.4)$$

Equation 3-4. Empirical absorption coefficient (α_{Γ}) from the direct transitions of strained germanium as a function of photon energy (E_{photon}) as given in Ref [116]. The energy separation between the direct conduction valley and the heavy hole valence band is denoted $E_g^{\Gamma\text{-HH}}$, and the energy separations between the direct conduction valley and the light hole valence band is denoted $E_g^{\Gamma\text{-LH}}$.

With the absorption coefficient and quasi-Fermi levels now determined, we can proceed to compute the optical net gain at various carrier concentrations. For any given wavelength this consists first of multiplying the absorption coefficient by the population inversion factor in accordance with Equation 3-5 [116] to obtain the gain from the direct transition. We can then subtract the free carrier absorption to obtain the net gain [41] as shown in Equation 3-6. This free carrier absorption is given by Equation 3-7 [41] which is an empirical fit to experimental data [117], [118] and therefore agnostic to the underlying free carrier absorption mechanism, thus bypassing any concerns about whether intra-band or inter-band transitions are primarily responsible [55].

$$\gamma_{\Gamma} = \alpha_{\Gamma}(f_c - f_v) \quad (3.5)$$

Equation 3-5. Gain from the direct transition (γ_{Γ}), given in terms of strained germanium's absorption coefficient from the direct transition (α_{Γ}) and the population inversion factor ($f_c - f_v$) [116].

$$\gamma_{\text{net}} = \gamma_{\Gamma} - \alpha_{FCA} \quad (3-6)$$

Equation 3-6. Optical net gain (γ_{net}) as a function of the direct transition gain (γ_{Γ}) and the free carrier absorption (α_{FCA}).

$$\alpha_{FCA} = 3.4 \times 10^{-25} n \lambda^{2.25} + 3.2 \times 10^{-25} p \lambda^{2.43} \quad (3-7)$$

Equation 3-7. Free carrier absorption (α_{FCA}) as a function of electron concentration (N), hole concentration (P) and wavelength (λ), according to the empirical fit computed in Ref [41]. α_{FCA} is in units of cm^{-1} , n is in units of cm^{-3} , p is in units of cm^{-3} and λ is in units of nm.

Having subtracted the free carrier absorption from the direct transition gain, we now have the optical net gain for a particular wavelength, for instance as shown for 1.0% strain in Fig. 3-8(a) at an emission wavelength of 1900 nm or in Fig. 3-8(b) at an emission wavelength of 1500 nm. This net gain calculation is then repeated across all strain values and for all possible emission wavelengths with a 1nm resolution, resulting in the full net gain spectrum for any different combination of strain, electron density and hole density. We then assume that lasing will always occur at the wavelength of peak net gain, giving a result such as the one shown in Fig. 3-8(c), which allows us to remove wavelength as an independent variable to a function of only three variables: strain, electron density and hole density. The information about the emission wavelength is not lost, however, as we can keep track of the wavelength of peak net gain as shown in Fig. 3-8(e). Additional net gain plots for 1.0% strained germanium showing the detailed evolution of the net gain with wavelength are available as Fig. A-1 in the Appendix. Additional net gain plots showing the evolution of the net gain with strain [43] are also included in the Appendix as Fig. A-2.

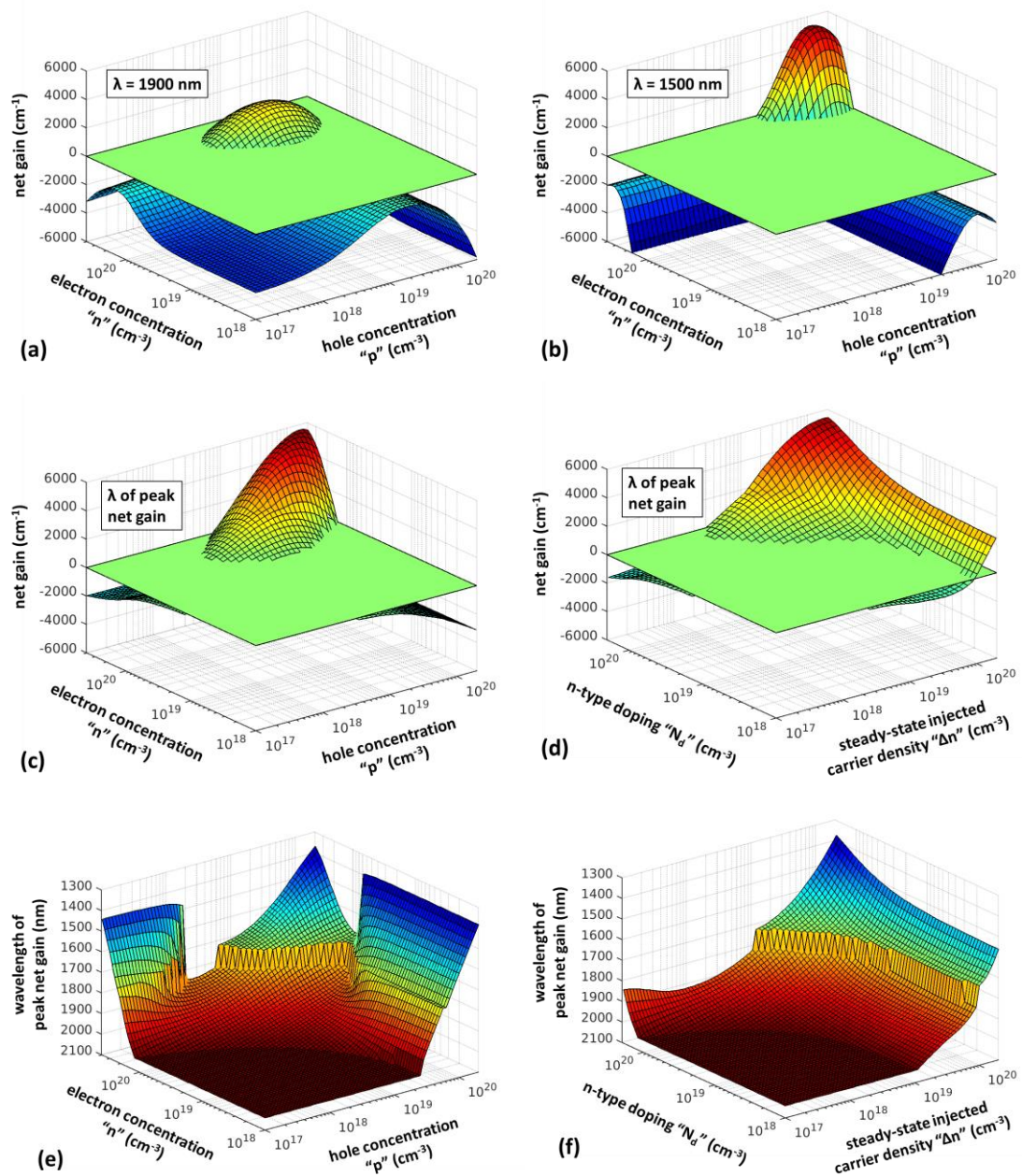


Figure 3-8. Optical gain in germanium as a function of steady-state carrier densities. (a-c) Optical net gain of germanium as a function of electron and hole concentrations, for 1.0% biaxial tensile strain at (a) 1900 nm, (b) 1500 nm, (c) the wavelength of maximum net gain. (d) Optical net gain of germanium as a function of n-type doping and steady-state injected carrier density, for 1.0% biaxial tensile strain at the wavelength of maximum net gain. (e,f) Wavelength of maximum net gain for germanium under 1.0% biaxial tensile strain, shown (e)

as a function of electron and hole concentrations, and (f) as a function of n-type doping and steady-state injected carrier density. The zero-plane (light green) is included in figures a-d to help visualize where the net gain becomes positive.

From there we can convert electron density and hole density to doping concentration and steady-state carrier injection by a straightforward linear mapping. This conversion is done by assuming that all holes come from injection, that the electron density is the sum of the steady-state injection level and the doping level, and that electrons and holes are injected in approximately equal numbers to maintain charge neutrality – an assumption validated by device level simulations [89]. These assumptions, namely that the hole density equals the steady-state injected carrier density and that the electron density equals the sum of the n-type doping and the steady-state injected carrier density, can be written explicitly as Equation 3-8 and Equation 3-9, respectively.

$$p = \Delta n \quad (3-8)$$

Equation 3-8. The hole concentration (p) equals the steady-state injected carrier density (Δn).

$$n = N_d + \Delta n \quad (3-9)$$

Equation 3-9. The electron concentration (n) equals the sum of the n-type doping concentration (N_d) and the steady-state injected carrier density (Δn).

Thus, we set the steady-state carrier injection to equal the hole concentration as shown in Equation 3-10 and then set the doping level to equal the difference between the electron and hole concentrations in accordance with Equation 3-11.

$$\Delta n = p \quad (3-10)$$

Equation 3-10. *The steady-state injected carrier density (Δn) equals the hole concentration (p).*

$$N_d = n - p \quad (3-11)$$

Equation 3-11. *The n-type doping concentration (N_d) equals the difference between the electron concentration (n) and the hole concentration (p).*

For any given strain value, applying this linear transformation to Fig. 3-8(c) gives us the optical net gain versus doping and steady-state injection as shown in Fig. 3-8(d) for the example of 1.0% biaxial strain. We can also keep track of how the assumed emission wavelength, i.e. the wavelength of maximum net gain changes, by applying the same linear mapping to Fig. 3-8(e) in order to obtain a result such as Fig. 3-8(f) which now gives the assumed emission wavelength as a function of doping and steady-state injected carrier density. We can then repeat this peak net gain versus doping and injection calculation for additional strain values as shown in Fig. 3-9 for the example cases of zero strain and 2.0% biaxial tensile strain. (Results for an extensive range of strain values are available in Fig. A-2 in the Appendix.) From these figures we observe that tensile strain dramatically enhances the optical gain, not only

increasing by $\sim 2x$ the maximum possible net gain but also reducing by $\sim 10x$ the injected carrier density needed to achieve positive net gain.

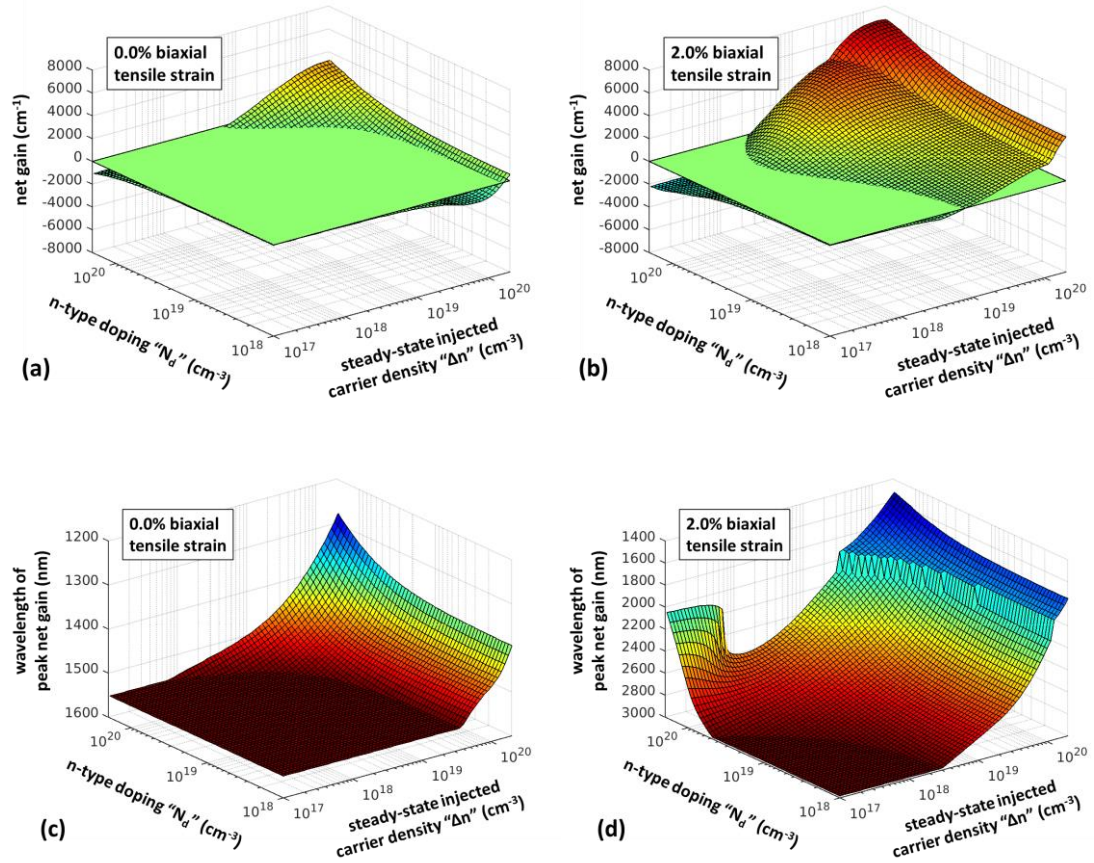


Figure 3-9. Optical gain in germanium as a function of doping and steady-state injection. (a,b) Maximum optical net gain as a function of n-type doping and steady-state injected carrier density, computed at (a) zero strain, and (b) 2.0% biaxial tensile strain. The zero-plane (light green) is included to help visualize where the net gain becomes positive. (c,d) Wavelength of maximum net gain as a function of n-type doping and steady-state injected carrier density, computed at (a) zero strain, and (b) 2.0% biaxial tensile strain. Figures (a) and (b) where computed using the wavelength of figures (c) and (d), respectively.

There are also some interesting aspects regarding how the net gain responds to strain. For the low-doping low-injection region of Fig. 3-9 we observe that the optimal wavelength corresponds to an energy just below germanium's bandgap. This is because in this region the gain from the direct transition is negative so photons with more than the bandgap energy will experience a strong absorption, meanwhile very long wavelengths will result in a large free carrier absorption (Equation 3-7), and so the absorption (negative gain) can be minimized for a photon energy just below the bandgap. From Fig. 3-9(c,d) we also find that, regardless of strain level, injecting a large number of carriers blueshifts the wavelength of maximum net gain; this is a typical behavior in lasers due to the larger joint density of states for higher energy optical transitions. However, the behavior for the 2.0% strained case (Fig. 3-9(d)) is markedly different than the behavior for the unstrained case (Fig. 3-9(c)). For one thing, at higher strain values we observe a blueshift of the optimal wavelength at high doping even without substantial carrier injection. In this heavy-doping low-injection region the large electron density due to extrinsic carriers has pushed the electron quasi-Fermi level high enough into the conduction band that the absorption from the direct transition has been bleached. Positive gain in this low injection region is not possible due to the relative lack of holes, but with the absorption from the direct transition bleached the net gain can now become less negative at shorter wavelengths where free carrier absorption is weaker (Equation 3-7). However, this is not particularly relevant to achieving a positive net gain.

A more important feature of Fig. 3-9 is that there are two distinct regimes for the 2.0% strained case (Fig. 3-9(b,d)) but not for the unstrained case (Fig. 3-9(a,c)).

For the 2.0% strain case, once the injected carrier density exceeds about $\sim 10^{20} \text{ cm}^{-3}$ there is an abrupt jump (redshift) in wavelength (Fig. 3-9(d)) and the net gain starts experiences a kink and increases much more dramatically (Fig. 3-9(b)). This is due to the LH/HH in the valence band that occurs under strain: at low-moderate injected carrier densities the only top (HH) valence band can contribute to the gain, but at higher injected carrier densities the hole quasi-Fermi level will be pushed below the top of the second (LH) valence band and both the HH and LH bands can contribute positive to the net gain. At this point an abruptly blueshifted wavelength becomes optimal such that the photon energy now exceeds the Γ -LH energy separation. Since both the Γ -HH and Γ -LH transitions contribute to the optical gain is new regime we observe a kink in the net gain (Fig. 3-9(b)) and much larger net gains become achievable. This LH/HH splitting effect will be particularly important to the threshold calculations of the next section.

3.4.2 Threshold Current

Having computed the optical gain in germanium at arbitrary strain values, the next step is to compute the threshold current to determine the utility of biaxial tensile strain and n-type doping. From where we left off in Fig. 3-8(d,f) with the net gain and optimal wavelength as functions of n-type doping and steady-state carrier injection we can do another mapping, this time a non-linear mapping, to convert the “steady state injected carrier density” axis into “drive current density” as shown in Fig. 3-10(a). This is done assuming a 100% injection efficiency by using the rate equation (Equation 3-12) which assumes the amount of pumping per unit volume to equal the

amount of recombination from all sources, including defect-assisted SRH recombination, radiative recombination from the direct transition, radiative recombination from the indirect transition, and both forms of Auger recombination. The recombination coefficients for these processes were taken to be the same as those used in Ref [41].

$$\begin{aligned}
 J &= t_{active} \times U_{total} \\
 &= t_{active} \times (U_{radiative} + U_{non-radiative}) \\
 &= t_{active} \times \left(R_L np + (R_I - R_L) np \left(\frac{n_r}{n} \right) + C_{nnp} n (np - n_i^2) + C_{ppn} p (np - n_i^2) + P / \tau_{SRH} \right)
 \end{aligned}
 \tag{3-12}$$

Equation 3-12. Current density (J) expressed in terms of the active region thickness (t_{active}), electron density (n), hole density (p), defect-limited minority carrier lifetime (τ_{SRH}), and fraction of electrons in the direct conduction valley ($\frac{n_r}{n}$). The terms $U_{radiative}$, $U_{non-radiative}$ and U_{total} represent the radiative, non-radiative and total recombination rates, respectively. The recombination coefficients are $R_L=5.1 \times 10^{-15} \text{ cm}^3/\text{s}$, $R_I=1.3 \times 10^{-10} \text{ cm}^3/\text{s}$, $C_{nnp}=3.0 \times 10^{-32} \text{ cm}^6/\text{s}$ and $C_{ppn}=7.0 \times 10^{-32} \text{ cm}^6/\text{s}$ [41].

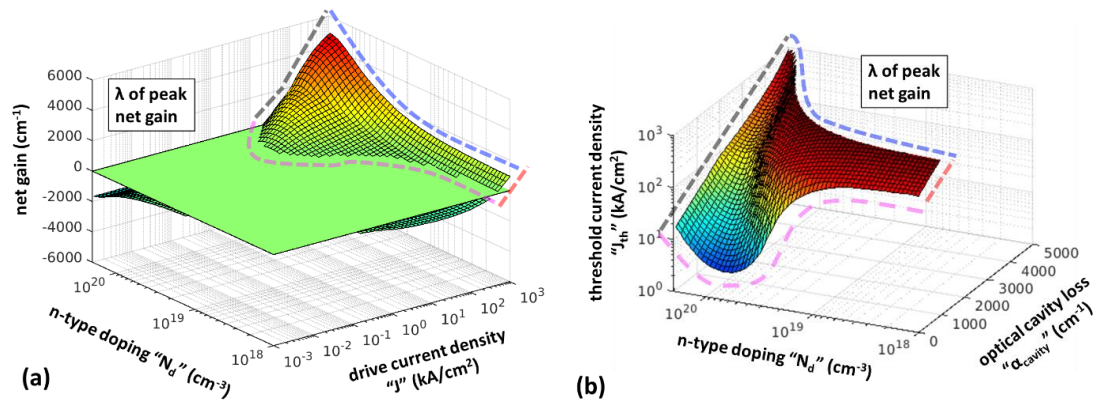


Figure 3-10. Optical gain in germanium as a function of doping and bias current density. (a) Optical net gain of 300nm-thick germanium slab as a function of n-type doping and applied current density, for 1.0% biaxial tensile strain at the wavelength of maximum net gain. The zero-plane (light green) is included to help visualize where the net gain becomes positive. (b) Threshold current density of a 300nm-thick germanium laser as a function of n-type doping and optical cavity loss, for 1.0% biaxial tensile strain assuming a perfect double heterostructure, a 100% optical confinement factor and lasing at the wavelength of maximum net gain. Dashed colored lines are visual aids to help identify each edge for the transformation (swapping the x- and z-axes) that relates figure b to figure a.

The next step then is to actually determine the threshold current density. In our model we assume that lasing occurs when the unsaturated gain, i.e. the net gain which we have computed in accordance with the preceding paragraphs, equals the loss of the particular optical cavity which we are modeling. This amounts to simply relabeling the axes of Fig. 3-10(a) such that “net gain” becomes “optical cavity loss (per unit length)” and “drive current density” becomes “threshold current density,” and then treating the threshold current as the dependent variable as shown in Fig. 3-10(b). Visual aids are included in Fig. 3-10 to help show how Fig. 3-10(b) is simply an

isometric transformation (reflection & rotation) of Fig. 3-10(a). At this point we have successfully computed the threshold current density versus doping and optical cavity loss for a given strain value, and so it simply becomes a matter of repeating this mapping over the desired range of strain values.

An important side note is that we have not specified any particular type of optical cavity when considering the optical cavity loss: we have simply used the generic loss per unit length. Indeed, in this Chapter and also in the next Chapter we will always abstract away the physical details of the optical cavity by only considering the resonator's loss per unit length, meaning that our results are applicable to all conceivable optical cavities such as longitudinal Fabry-Perot cavities, micro-ring resonators, or any other design. In addition, this optical cavity loss is presumed to consist solely of useful out-coupling of light rather than parasitics such as imperfect reflections at a back mirror or optical scattering.

Having now finished all the relevant calculations, we can directly examine how the threshold varies with strain as shown in Fig. 3-11(a) assuming a double heterostructure with a 300nm thick germanium active region and a perfectly lossless optical cavity. From this figure we clearly see that employing 3.0% biaxial strain can reduce the threshold to just a few hundred A/cm^2 compared to over 1000 kA/cm^2 for the undoped and unstrained case. Due to the strain-induced bandgap narrowing, we expect and indeed observe a large redshift in the emission wavelength with strain as shown in Fig. 3-11(b), with 3.0% strain redshifting the emission wavelength from approximately 1550 nm to nearly 5000 nm. This is unfortunate since the 1550 nm emission associated with unstrained germanium corresponds to the C-band for low-

loss transmission over conventional erbium-doped optical fiber [50], [119]. Our modeling further suggests that the threshold is quite sensitive to the emission wavelength, and so it does not appear possible to combine the benefits of large tensile strains with an output wavelength in the vicinity of 1550 nm. However, while 1550 nm is important because it corresponds to the C-band minimum loss window for long-distance transmission in erbium-doped fiber, this is not particularly critical for short-distance transmission since there exist waveguides and short-range optical fibers with reasonable transparency in these wavelength ranges [19], [120]. Moreover, if a Ge light emitter can be strained to redshift its emission wavelength then a Ge modulator or photodetector can also be strained to similarly redshift its operating wavelength, and highly strained Ge photodetectors with a redshifted detection cutoff have already been demonstrated [71]. Thus, while it is not possible for a highly strained Ge laser to efficiently operate near 1550 nm this is not a major cause for concern given that solutions exist for modulation, transmission and detection at these redshifted wavelengths.

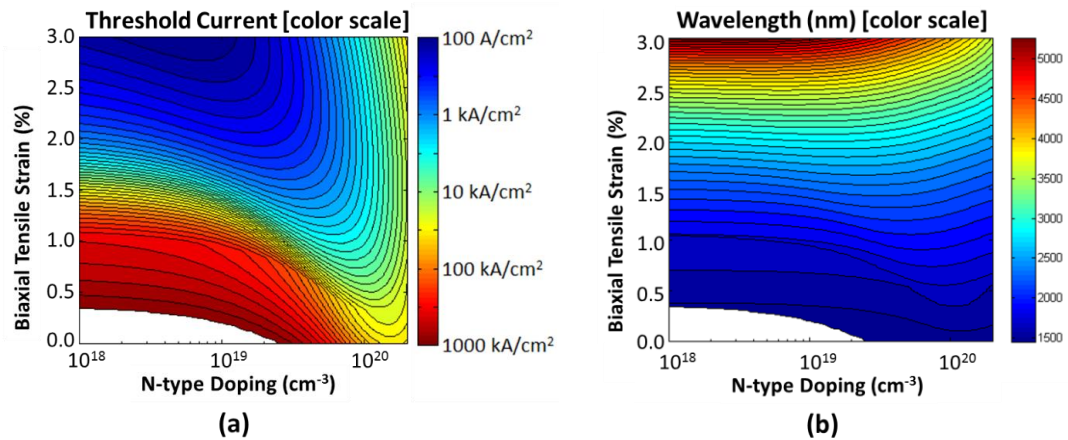


Figure 3-11. Threshold and wavelength vs. biaxial strain and n-type doping. (a) Threshold current density of a double heterostructure germanium laser (color scale) vs. biaxial tensile

strain and n-type doping. (b) Emission wavelength (color scale) vs. biaxial tensile strain and n-type doping. Germanium thickness is assumed to be 300nm with an optical cavity loss of zero and $\tau_{SRH}=100ns$. The blank region in the bottom left corner is due to the cutoff of the simulation bounds, i.e. thresholds greater than 1000 kA/cm^3 .

Returning to the more critical issue of how the threshold varies with biaxial tensile strain and n-type doping, it is clear from Fig. 3-11(a) that strain offers considerably greater benefits than doping. Whereas thresholds well below 1kA/cm^3 can be achieved with strain in the absence of doping, using only doping without strain would only unlock threshold current densities of about 30kA/cm^3 which is still far too high to be useful in practical devices. There is also a negative interaction between tensile strain and n-type doping with respect to achieving a low threshold. In fact, we plainly observe that applying too much n-type doping can actually cause the threshold to increase quite dramatically. Furthermore, the maximum achievable enhancement from doping becomes considerably smaller at large strain values. These two phenomena are shown explicitly in Fig. 3-12(a). From this figure we further observe that the critical doping, i.e. the maximum useful doping before which the threshold starts to increase, is itself a strong function of strain. As shown in Fig. 3-12(b) we find that the maximum useful doping decreases very dramatically with strain. Whereas up to about $1.5 \times 10^{20} \text{ cm}^{-3}$ of n-type doping would be useful for unstrained germanium, at 3.0% biaxial tensile strain the maximum useful doping has decreased to merely $6 \times 10^{18} \text{ cm}^{-3}$. This means that combining large tensile strain with ultra-heavy n-type doping is fundamentally detrimental to the performance of a germanium laser, and so one

approach must be chosen over the other [53]. Given that the largest reductions in threshold are only available at large strains, it logically follows that researchers must aim to combine a large tensile strain with only moderate n-type doping if a low threshold germanium laser is desired. Notably, 5×10^{19} n-type doping has already been employed in experimental germanium laser devices [93], [101]. This doping level is larger than the critical value for strains exceeding about 1% and so it will actually be necessary to reduce the doping from present levels for optimal performance once larger strains are reached., whereas there is a very fundamental need for techniques which can induce a large tensile strain in germanium for the sake of low threshold operation [53].

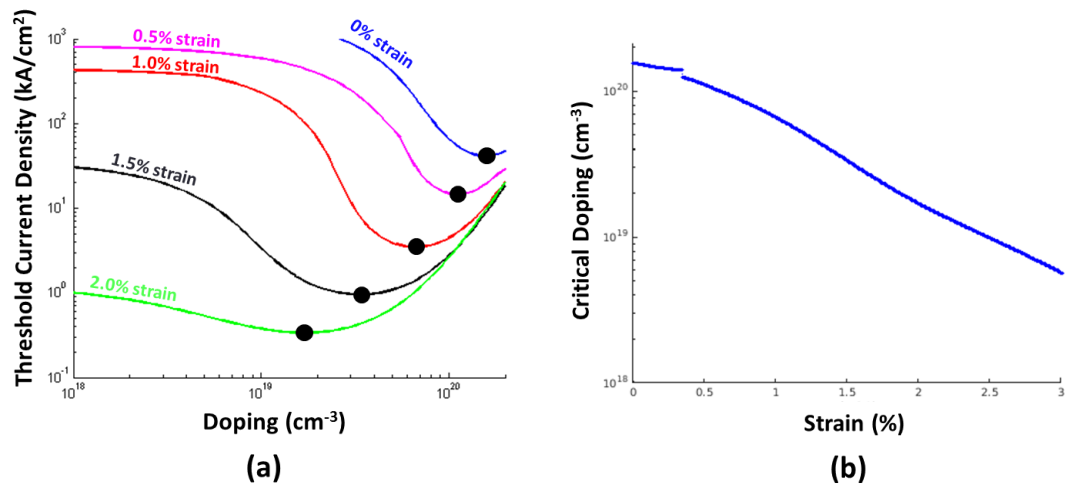


Figure 3-12. Threshold vs. n-type doping for various biaxial strain values & the optimal doping value vs. biaxial strain. (a) Threshold current density of a 300nm-thick double heterostructure germanium laser vs. n-type doping for different amounts of biaxial strain. Optimal doping is indicated by a black dot. (b) Optimal doping value vs. biaxial tensile strain. In all cases the optical cavity loss is assumed to be zero with $\tau_{SRH}=100ns$.

Another important aspect of Fig. 3-11(a) is that, upon careful inspection, there are two regimes with strain. The boundary between these regimes is about 1% strain for low doping and about 0.5% strain for heavy doping. Below this boundary the contour lines in Fig. 3-11(a) are spaced far apart indicating a relatively gradual change in threshold with strain, but immediately above this boundary the contour lines become packed very close together indicating a very steep change in threshold with strain. This is shown explicitly in Fig. 3-13(a) where a kink can be seen in the threshold vs. strain plot, and this kink occurs at somewhat smaller strain values in the presence of heavy doping. Concurrent with this kink in the threshold response is a discontinuity in the wavelength, as seen in Fig. 3-13(b). From Fig. 3-13(b) we also observe that the wavelength redshifts much more sharply with strain once the kink/discontinuity has been exceeded.

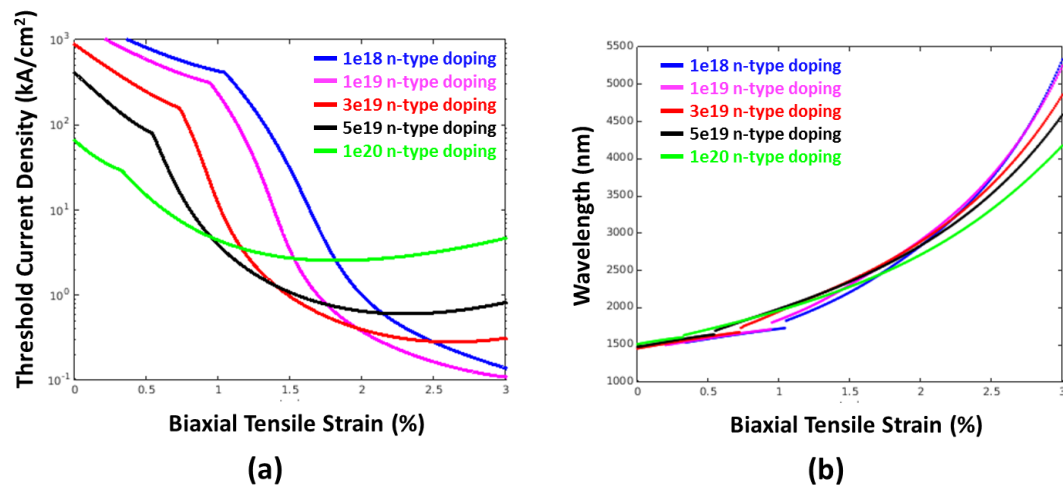


Figure 3-13. Threshold and wavelength vs. biaxial strain for several doping values. (a)

Threshold current density of a germanium laser vs. biaxial tensile strain for different doping conditions. (b) Emission wavelength of a germanium laser vs. biaxial tensile strain for

different doping conditions. In all cases a double heterostructure design with a 300nm thick germanium active region and $\tau_{SRH}=100ns$ is assumed.

The explanation for this behavior has to do with the LH/HH splitting of the valence bands under strain. For a biaxial tensile strain the heavy-hole (HH) band rises above the light-hole (LH) band. Although the HH band has a >50x larger density of states (DOS) than the LH band [108], the joint density of states (JDOS) for the Γ -HH and Γ -LH transitions differs only by about 2x (as evidenced in Equation 3-4 [116]) since the JDOS calculation involves a harmonic mean of the respective valence band (HH or LH) mass with the very small Γ mass in the conduction band. As such, the Γ -LH contribution represents a significant addition to the optical gain despite the small DOS mass of the LH band. Under low strains the LH/HH splitting is small and the gain from the top of the HH band alone is insufficient to overcome free carrier absorption, making it necessary to push the hole quasi-Fermi level down into the LH band where the combined contributions of the Γ -HH and Γ -LH transitions makes lasing possible. In this regime a marginal increase in LH/HH splitting is harmful as it adds unnecessary states at the top of the valence band, thereby requiring more carriers for population inversion and counteracting some of the benefits from strain's effect on the conduction band. Thus, in this first regime strain has a beneficial effect on the conduction band which is mitigated by a harmful effect on the valence band. Beyond a certain critical splitting (and hence beyond a critical strain), however, it becomes possible to exceed the free carrier absorption using only gain from the Γ -HH transition. In this new regime a marginal increase in the LH/HH splitting is now

beneficial in that it pushes the states in the LH band (which do not contribute to gain in this regime) down to lower energies where they will contain fewer carriers, thereby reducing the required concentration of injected holes for optical gain. (This can also be seen in Fig. A-2 in the Appendix.) In this second regime strain has a beneficial effect on the conduction band which is supplemented by another beneficial effect on the valence band. Thus there is a kink in the threshold response at the boundary of these two regimes along with a sudden jump in the wavelength. Furthermore, upon careful analysis of both Fig. 3-13(b) and Fig. 3-3 we observe that in the first (i.e. low strain) regime the predicted germanium laser emission wavelength changes in line with the Γ -LH bandgap, and in the second (i.e. high strain) regime the emission wavelength changes in line Γ -HH bandgap, with the boundary between these two regimes being the discontinuity in Fig. 3-13(b). From a practical standpoint, what this means is that strain will become disproportionately beneficial at large values, and building prototypes with only small tensile strains will vastly undersell the potential benefits of tensile strain. As such, researchers should focus their efforts on realizing the largest possible strain in germanium before attempting to build prototype strained germanium lasers.

While the modeling shown so far has answered some critical questions such as the relative merits of tensile strain and n-type doping, another important variable is the defect-limited minority carrier lifetime (τ_{SRH}). In section 3.3.2 we showed that maximizing τ_{SRH} , presumably through improved material quality [112], is critically important to the performance of a germanium LED. Unsurprisingly, we find that maximizing the SRH lifetime is also very important to achieving a low threshold

germanium laser. As shown in Fig. 3-14 there is no combination of strain and doping that gives a useable threshold for the case of a defect-limited minority carrier lifetime below 1ns. On the other hand, improving the SRH lifetime to 100 ns (our assumption in all previous figures) makes it possible to achieve thresholds as low as 100 A/cm^3 . These benefits appear to have fully saturated once the SRH lifetime reaches about 1 μs . Given that most epitaxial germanium today has a lifetime of only about 1ns or less [111], this means that it is absolutely imperative to improve the material quality if an efficient germanium laser is ever to be realized. Fortunately, this should be within the realm of possibility given that the bulk lifetime of germanium exceeds $1\mu\text{s}$ [113], at which point our modeling suggests that the maximum possible benefit would be achieved. We reiterate, however, that such experimental efforts on material quality are outside the scope of this dissertation.

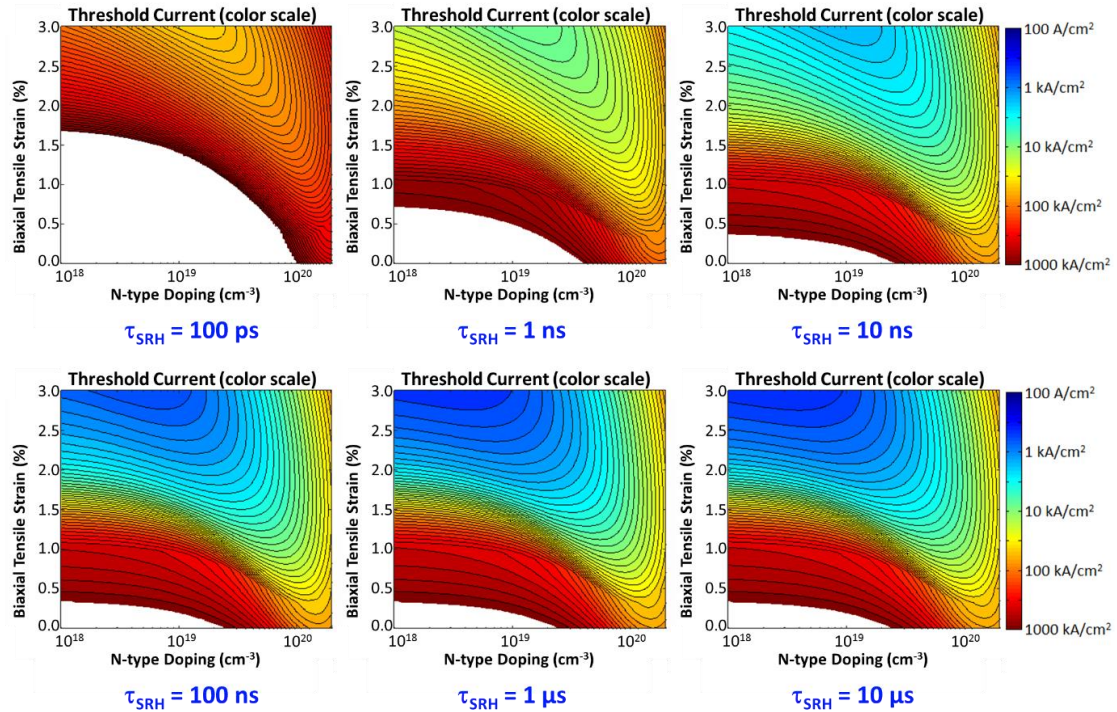


Figure 3-14. Threshold current density vs. biaxial strain and n-type doping, shown for various Shockley-Read-Hall lifetime (τ_{SRH}) values. In all cases a double heterostructure design with a 300nm thick germanium active region and zero optical cavity loss is assumed.

Another interesting observation from Fig. 3-14 is that improving the SRH lifetime appears to offer the most benefit for strain & doping combinations that give the smallest threshold. This is shown more explicitly in Fig. 3-15(a) by plotting the threshold versus strain for several different SRH lifetimes, assuming $5 \times 10^{18} \text{ cm}^{-3}$ n-type doping. For strains below 1.0% there is almost no difference between the curves for SRH lifetimes of 10ns or greater. At 1.5% strain the 10ns curve shows a noticeably higher threshold than the 100ns–10 μ s curves, and at 2.0% strain even the 100ns curve has started to diverge from the 1 μ s–10 μ s curves. The explanation for this phenomenon is that improving the SRH lifetime is only helpful when the carrier

lifetime is limited by the SRH process as opposed to other mechanisms such as spontaneous emission or, in particular, Auger recombination. In the high threshold regime the Auger-limited lifetime is about 1ns or less, and so it makes little difference whether the defect-limited SRH lifetime is 1 μ s or 10ns. In the low threshold regime, however, the Auger-limited lifetime may be closer to 300ns. In this case reducing the SRH lifetime from 1 μ s to 10ns will dramatically reduce the net carrier lifetime and thus increase the threshold by more than an order of magnitude. The key takeaway of this result is that while material quality is already important to improving the performance of germanium lasers, it will become even more important as techniques such as band engineering and n-type doping start to enable lower lasing thresholds.

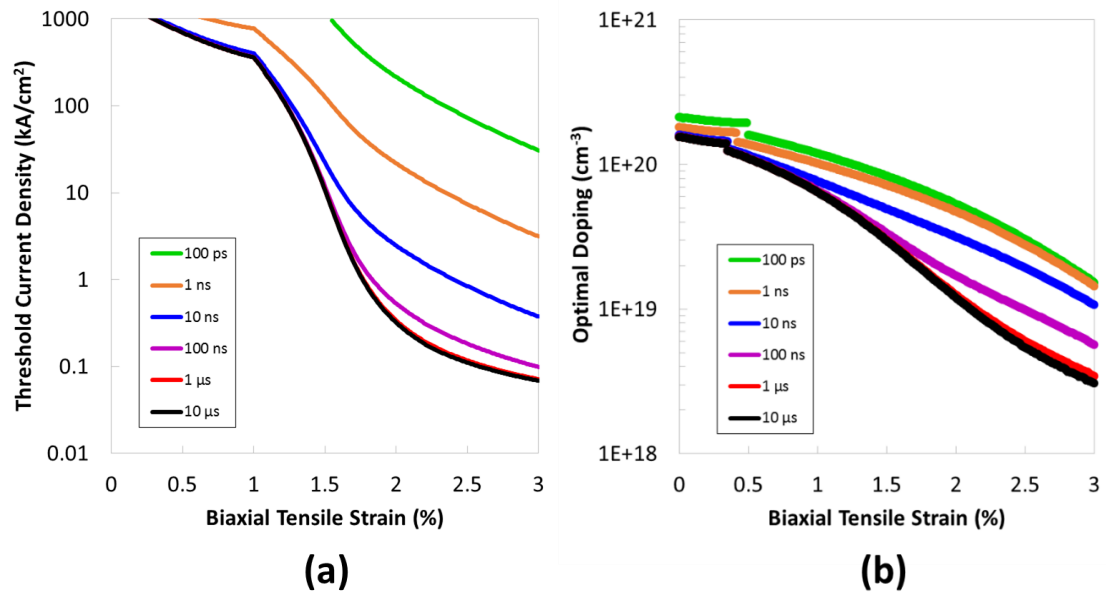


Figure 3-15. Impact of SRH lifetime on the threshold response and optimal doping. (a) Threshold current density vs. biaxial strain assuming a 300nm thick germanium active region with $5 \times 10^{18} \text{ cm}^{-3}$ n-type doping, shown for various Shockley-Read-Hall lifetime (τ_{SRH}) values.

(b) Optimal doping vs. biaxial strain, shown for various Shockley-Read-Hall lifetime (τ_{SRH}) values. In all cases a double heterostructure design with zero optical cavity loss is assumed.

One more observation from Fig. 3-14 is that the SRH lifetime seems to affect the optimal doping level. This is shown explicitly in Fig. 3-15(b) where we observe that the critical doping value is lower when the SRH lifetime is higher. The explanation for this phenomenon lies in the nature of why an optimal doping value exists. While n-type doping is useful in that it fills up excess states in the indirect conduction valley, it can also be harmful by means of two mechanisms. First, the extrinsic electrons from doping cause unwanted free carrier absorption in accordance with Equation 3-7. Second, the extrinsic electrons contribute to unwanted Auger recombination in accordance with Equation 3-2 (see also Equation 3-12). In the regime where the carrier lifetime is limited by the Auger process (i.e. when τ_{SRH} is large) both of these harmful mechanisms are at play and so the optimal doping is comparatively low. On the other hand, in the regime where the carrier lifetime is limited instead by the SRH process (i.e. when τ_{SRH} is small) then only the first harmful mechanism (unwanted free carrier absorption from extrinsic electrons) is at play and so the optimal doping is comparatively a bit higher. This explains why we see in Fig. 3-15(b) an upper bound given approximately by the 100ps and 1ns curves (i.e. the small τ_{SRH} regime) and a lower bound given by the 1 μ s and 10 μ s curves (i.e. the large τ_{SRH} regime), with the 10ns and 100ns curves being somewhere in the middle. On a practical level what this means is that while doping may have some utility now that SRH lifetimes are quite

low [121], it will be necessary to improve this SRH lifetime and once this SRH lifetime has been improved n-type doping will become even less useful.

3.4.3 Slope Efficiency and Optical Cavity Loss

While the threshold is one particularly critical figure of merit for realizing a practical germanium laser, another key parameter is the slope efficiency which is defined as the differential power efficiency of the proposed laser just above threshold [122]. Given that our modeling is for a highly ideal cavity there are only two mechanisms which we consider to be limiting the slope efficiency, though in practice there will of course be additional parasitics. The first mechanism is due to the fact that while many of the photons generated by stimulated emission will leave the cavity as useful light emission, some will be lost to free carrier absorption thereby limiting the quantum efficiency [53]. Thus, the differential quantum efficiency of our hypothetical laser will be given by the ratio of the optical cavity loss to the sum of optical cavity loss and free carrier absorption (Equation 3-12). Note that our model assumes that this optical cavity loss consists exclusively of useful out-coupling of light from the cavity, for example transmission through the mirror in a Fabry-Perot resonator. (Note that while Auger recombination plays a very major role in worsening the threshold current, it plays absolutely no role in determining slope efficiency in our model because our model assumes abrupt and total gain clamping at threshold. The Auger process involves only electrons and holes, not photons, and hence has no bearing on the probability that any given photon will exit the cavity as useful light emission; the

Auger process only determines how much pumping is needed to achieve the steady-state carrier density required for positive net optical gain.)

$$\text{differential quantum efficiency} = \frac{\alpha_{\text{cavity}}}{\alpha_{\text{cavity}} + \alpha_{\text{FCA}}} \quad (3-12)$$

Equation 3-12. *Differential quantum efficiency as a function of optical cavity loss (α_{cavity}) and free carrier absorption (α_{FCA}).*

The next and final step is to convert this differential quantum efficiency to a differential power efficiency, which involves multiplying by the ratio of the photon energy to the energy required to send an electron through the system. To determine the electron energy we need to know the voltage applied to the laser device. In our ideal model where we ignore contact resistance and other parasitics such as resistance of any barrier layers, this total voltage will simply be the active region voltage which is given by the quasi-Fermi level separation divided by the electron charge (Equation 3-13). From there the electron energy is simply the elementary charge times the voltage (Equation 3-14).

$$V_{\text{active}} = \frac{E_{fn} - E_{fp}}{q} \quad (3-13)$$

Equation 3-13. *Active region voltage (V_{active}) as a function of the electron quasi-Fermi level (E_{fn}) and the hole quasi-Fermi level (E_{fp}). The term q is the elementary charge.*

$$E_{\text{electron}} = qV_{\text{active}} = E_{f_n} - E_{f_p} \quad (3-14)$$

Equation 3-14. Energy expended to send a single electron through the device (E_{electron}) as a function of the electron quasi-Fermi level (E_{f_n}) and the hole quasi-Fermi level (E_{f_p}). The term q is the elementary charge and V_{active} denotes the active region voltage.

Next, the photon energy can be computed from the wavelength in accordance with Equation 3-15. Knowing both the electron and photon energies, we are now also able to compute the photon-to-electron energy ratio (Equation 3-16).

$$E_{\text{photon}} = hc/\lambda \quad (3-15)$$

Equation 3-15. Photon energy (E_{photon}) as a function of wavelength (λ). The term h denotes the Planck constant and c is the speed of light.

$$E_{\text{photon}}/E_{\text{electron}} = \frac{hc/\lambda}{E_{f_n} - E_{f_p}} \quad (3-16)$$

Equation 3-16. Ratio of photon energy to electron energy ($E_{\text{photon}}/E_{\text{electron}}$) as a function of wavelength (λ) and quasi-Fermi level separation ($E_{f_n} - E_{f_p}$). The term h denotes the Planck constant and c is the speed of light.

This ratio of photon energy to electron energy will always be strictly less than unity in order to achieve a population inversion factor greater than zero, thus representing the second loss mechanism for slope efficiency. Finally, knowing both the differential quantum efficiency (Equation 3-12) and the photon-to-electron energy ratio (Equation

3-16), we can simply multiply these two quantities together to obtain the slope efficiency as shown in Equation 3-17.

$$\begin{aligned} \text{slope efficiency} &= \text{differential quantum efficiency} \times \left(\frac{E_{\text{photon}}}{E_{\text{electron}}} \right) \\ &= \frac{\alpha_{\text{cavity}}}{\alpha_{\text{cavity}} + \alpha_{\text{FCA}}} \times \frac{hc/\lambda}{E_{fn} - E_{fp}} \end{aligned} \quad (3-17)$$

Equation 3-17. Slope efficiency as a function of optical cavity loss (α_{cavity}), free carrier absorption (α_{FCA}), wavelength (λ) and quasi-Fermi level separation ($E_{fn} - E_{fp}$). The term h denotes the Planck constant and c is the speed of light.

Having calculated the slope efficiency, we can now plot it versus strain and doping, but we must now explicitly consider the optical cavity loss. While all of the preceding figures were computed in the assumption of zero optical cavity loss, an optical cavity loss of zero always results in a slope efficiency of exactly zero in accordance with Equation 3-17. We must therefore set the optical cavity loss to some non-zero value in order to observe some slope efficiency, with higher slope efficiencies typically expected for optical cavities with more loss. This is indeed the case, as shown in Fig. 3-16, however we also find that introducing more optical cavity loss has a detrimental effect on the threshold, representing a typical tradeoff in laser design [123].

(Threshold and slope efficiency plots for an extended range of strain values are available as Fig. A-3 in the Appendix.) Moreover, the slope efficiency of these germanium lasers is unusually low: 100 cm^{-1} is a substantial amount of optical cavity loss, and yet with 100 cm^{-1} of out-coupling loss the slope efficiency can never exceed about 15% even in our highly ideal model. Even increasing the out-coupling loss to an

absurdly high 1000 cm^{-1} results in a maximum slope efficiency of less than 60%. This is somewhat surprising since we might naively expect the slope efficiency to be primarily limited by parasitics such as scattering at the optical cavity surfaces which our model explicitly excludes; the optical cavity loss in our ideal model is assumed to consist exclusively of useful out-coupling of light and, as explained previously and in accordance with Equation 3-17, is completely unaffected by the large Auger recombination in our model. The explanation for this unusually low slope efficiency is that free carrier absorption is considerably more problematic in germanium than in typical III-V lasers due to the large carrier densities, particularly in the indirect conduction valleys, needed to achieve lasing.

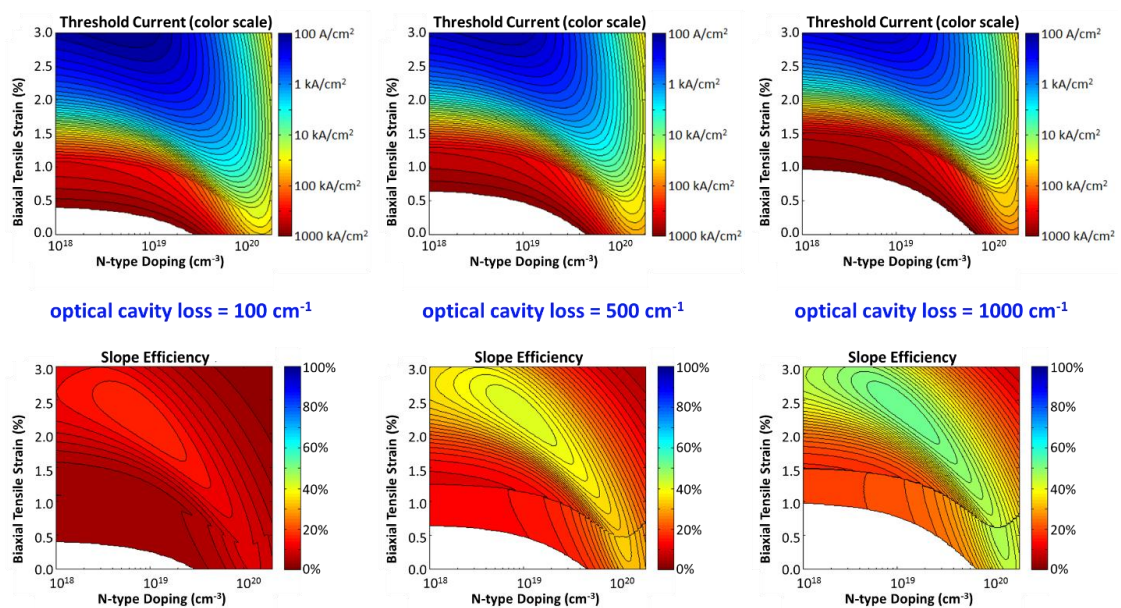


Figure 3-16. Impact of optical cavity loss on the threshold and slope efficiency (contour plots). Threshold current density (top) and slope efficiency (bottom) are shown for optical cavity losses of 100 cm^{-1} (left), 500 cm^{-1} (middle) and 1000 cm^{-1} (right). In all cases a double

heterostructure design with a 300nm thick germanium active region and $\tau_{SRH}=100ns$ is assumed. (Threshold and slope efficiency plots for an extended range of strain values are available as Fig. A-3 in the Appendix.)

Looking at the trend of slope efficiency with respect to strain and doping reveals that there is a band of strain and doping combinations shaped like an arc in Fig. 3-16 where the best slope efficiencies are achievable. As was the case with minimizing threshold, for maximizing slope efficiency there is a “critical” or “optimal” doping for any given strain value and this optimal doping value decreases in the presence of strain. As before, the explanation for why there exists an optimal doping is that while doping is useful in that it fills up excess states in the indirect conduction valley, too much doping results in a large number of excess carriers which introduce harmful free carrier absorption and thereby reduce the differential quantum efficiency in accordance with Equation 3-12. Unlike the optimal doping for threshold, however, recombination mechanisms such as Auger plays no role in determining the slope efficiency as can be seen in Equation 3-17 and therefore Auger recombination does not play any role whatsoever in determining the optimal doping for slope efficiency in our model. Nevertheless, the optimal doping for minimum threshold and the optimal doping for maximum slope efficiency are very close. The conclusion is therefore that while doping is useful for slope efficiency, it is only useful to a point. Too much doping will degrade the slope efficiency and in the presence of strain doping will be less useful to the point that, at about 1.1% strain it will actually become necessary to reduce the n-type doping from presently-favored value of $5 \times 10^{19} \text{ cm}^{-3}$ [93], [101].

We can also directly investigate the behavior of threshold and slope efficiency by plotting these quantities versus optical cavity loss in Fig. 3-17. This confirms explicitly that introducing more out-coupling loss increases both the threshold and the slope efficiency. From Fig. 3-17(a) we observe a monotonic increase in threshold with optical cavity loss as expected. Interestingly, we observe in Fig. 3-17(b) that too much optical cavity loss can occasionally be harmful to the slope efficiency. This is because at large optical cavity losses a very large material gain is required which in turn necessitates very large carrier densities. This means that increasing the out-coupling loss too much can sometimes cause the free carrier absorption to start rise faster than the out-coupling loss itself, thereby reducing the differential quantum efficiency and with it the slope efficiency. As shown in Fig. 3-17, these conclusions hold across large range of strain and doping values.

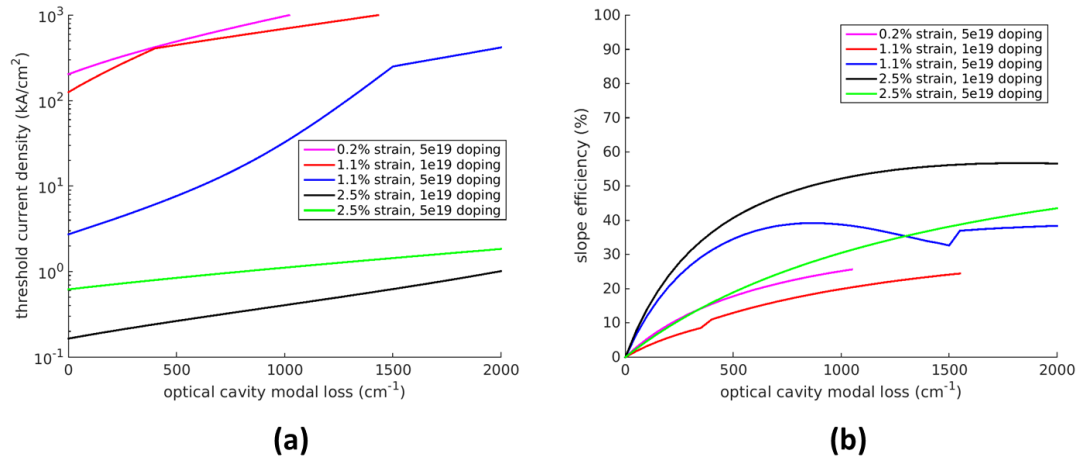


Figure 3-17. Impact of optical cavity loss on the threshold and slope efficiency (2D plots). (a) Threshold current density vs. optical cavity loss, shown for several strain and doping combinations, (b) Slope efficiency vs. optical cavity loss, shown for several strain and doping combinations

combinations. In all cases a double heterostructure design with a 300nm thick germanium active region and $\tau_{SRH}=100ns$ is assumed.

It is therefore clear that there is a tradeoff to be had between a low threshold and a high slope efficiency as is the case for virtually any laser [123], though the rather low achievable slope efficiency makes this tradeoff particularly acute for germanium lasers. We can examine this tradeoff explicitly in Fig. 3-18 which shows directly how the slope efficiency relates to threshold as the optical cavity loss is increased. The x-axis of Fig. 3-18 is simply the y-axis of Fig. 3-17(a) and the y-axis of Fig. 3-18 is simply the y-axis of Fig. 3-17(b). From Fig. 3-18 we observe that increasing the threshold by a factor of two (accomplished by introducing the requisite amount of out-coupling loss) can increase the slope efficiency from zero to about 30-50%. From Fig. 3-17 this means that we will want to introduce about 700 cm^{-1} of optical cavity loss for this tradeoff optimization. Since we are looking to change the threshold by many orders of magnitude by modulating the strain level and the doping, this factor of two increase in threshold for slope efficiency optimization should be eminently tolerable.

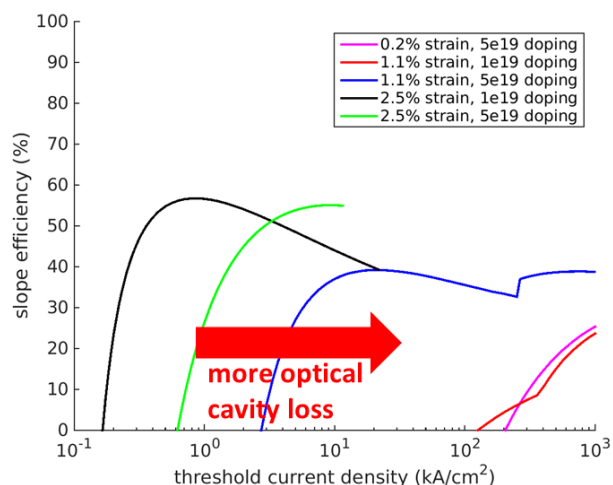


Figure 3-18. Slope efficiency vs. threshold current density for several biaxial strain and doping combinations. This explicitly shows the tradeoff that results from varying the optical cavity loss – increasing the optical cavity loss involves moving to the right along any curve in this figure. A double heterostructure design with a 300nm thick germanium active region and $\tau_{SRH}=100ns$ is assumed.

3.4.4 Ultimate Limit of Biaxial Tensile Strain

A final question, then, is to determine the “ultimate limit” of biaxial tensile strain. Just as n-type doping is only useful up to point, we might expect that there similarly exists a maximum useful level of strain [124]. To investigate this question we have extended our modeling up to biaxial tensile strains of 4.0% and re-plotted the threshold current density and slope efficiency, as shown in Fig. 3-19 assuming 700 cm^{-1} optical cavity loss. It is quite likely that some of the assumptions of our model, for instance the assumption that the free carrier can be modeled by the relation of Equation 3-7 even at very long wavelengths, will cease to be valid as the strain approaches 4.0%. At this 4.0% strain the bandgap has shrunk to under 0.02eV as shown in Fig. 3-3 and at 4.1%

strain germanium becomes a negative bandgap material according to our tight-binding model. In addition, once the bandgap has shrunk such that the direct bandgap approximately equals the energy separation between the top valence band (HH) and the split-off hole band (SO) we would expect the free carrier absorption to spike dramatically due to direct intervalence band HH-SO absorption [55] while the Auger recombination coefficient would also degrade dramatically due to CHSH Auger process [125]. Nevertheless, it is instructive to see what ultimately limits the usefulness of strain even if some of the underlying assumptions of the model have started to breakdown. As shown in Fig. 3-19, our model predicts that the ideal combination of strain and doping for minimum threshold is $\sim 3.7\%$ biaxial tensile strain with $\sim 2 \times 10^{18} \text{ cm}^{-3}$ n-type doping. At this combination of 3.7% strain and $2 \times 10^{18} \text{ cm}^{-3}$ n-type doping we expect a threshold of only $\sim 80 \text{ A/cm}^2$, a reduction of $>5000\times$ compared to the $\sim 600 \text{ kA/cm}^2$ threshold that our model predicts for state-of-the-art germanium laser values of 0.2% and $5 \times 10^{19} \text{ cm}^{-3}$ n-type doping.

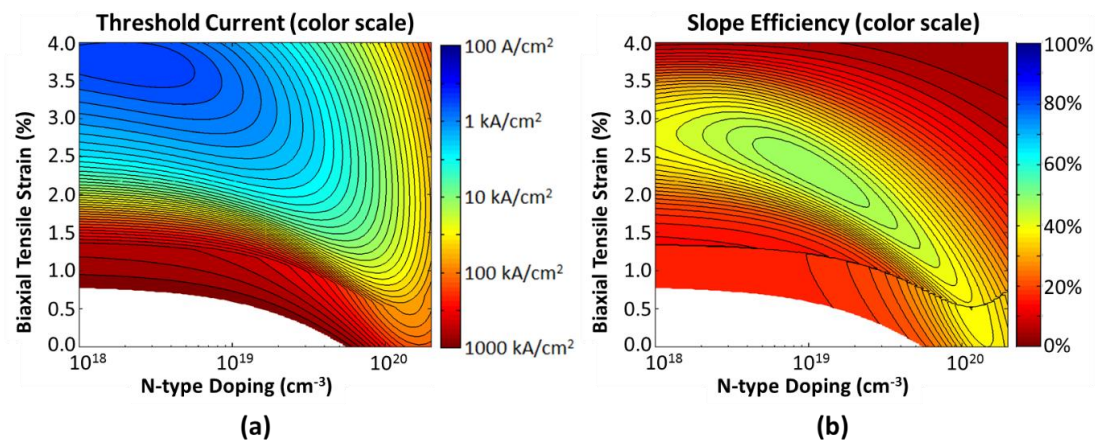


Figure 3-19. Threshold and slope efficiency vs. biaxial strain and doping for the “ideal” optical cavity loss of 700 cm^{-1} . (a) Threshold current density vs. biaxial tensile strain and n-

type doping at 700 cm^{-1} optical cavity loss, shown for an extended range of strain values assuming a 300nm thick germanium active region with $\tau_{SRH}=100\text{ns}$. (b) Slope efficiency vs. biaxial tensile strain and n-type doping at 700 cm^{-1} optical cavity loss, shown for an extended range of strain values. In all cases a double heterostructure design is assumed.

While the minimum threshold occurs at $\sim 3.7\%$ it would be unwise to actually implement such a strain as it would result in a slope efficiency of only about 15% even before considering parasitics. As shown in Fig. 3-19(b) the maximum slope efficiency occurs at a markedly smaller strain of $\sim 2.3\%$ with $\sim 1 \times 10^{19} \text{ cm}^{-3}$ n-type doping. Interestingly, this is slightly less than the 2.4% strain that our model assumes is necessary for a direct bandgap, meaning that germanium performs most efficiently when the band gap is still slightly indirect. Most likely this is not an indictment of the benefits of making the bandstructure direct but instead simply a coincidence in light of the analysis of section 3.2 which showed that there is no abrupt change in carrier distribution once a direct bandgap has been reached, at least for room temperatures such as the one considered here. In any event, at this 2.3% strain and $1 \times 10^{19} \text{ cm}^{-3}$ doping combination the slope efficiency is $\sim 47\%$ before parasitics with a threshold of only $\sim 500 \text{ A/cm}^2$. While this threshold is about 6x higher than what might be achieved at 3.7% strain (at the expense of very poor slope efficiency) it still represents a $>1000\text{x}$ threshold reduction compared to the present state-of-the-art germanium laser parameters of 0.2% biaxial strain and $5 \times 10^{19} \text{ cm}^{-3}$ n-type doping.

It is also worthwhile to consider the mechanism by which the slope efficiency is constrained to this ultimate limit. From Equation 3-17 we know that the slope

efficiency consists of two components that combine multiplicatively: the differential quantum efficiency (Equation 3-12) and the photon energy to electron energy ratio (Equation 3-16). By computing each of these components separately in Fig. 3-20 we find that slope efficiency is almost exclusively limited by the differential quantum efficiency rather than by the photon-to-electron energy ratio. In fact, except for a small region in the upper right portion of Fig. 3-20(b), i.e. when the doping is anyway much larger than its optimal value, the photon energy to electron ratio is consistently about 85-90% across all strain and doping values. The differential quantum efficiency (Fig. 3-20(a)) on the other hand shows a strong dependence on the strain and doping, with a 52% differential quantum efficiency at ~2.3% strain and $\sim 1 \times 10^{19} \text{ cm}^{-3}$ n-type doping that decreases rapidly if the strain is further increased. Since the differential quantum efficiency is the limiting factor of the slope efficiency it logically follows that this ultimate limit for slope efficiency is governed by free carrier absorption, specifically the fact that emission wavelength redshifts from strain (Fig. 3-11(b)) will increase the free carrier absorption in accordance with Equation 3-7. Since the free carrier absorption appears directly in the equation for slope efficiency (Equation 3-17) but only indirectly affects the equation for threshold (Equation 3-12, affected indirectly via Equation 3-6), this likely explains why the “ultimate limit” for slope efficiency occurs at just 2.3% biaxial tensile strain whereas threshold continues to benefit from strain up until 3.7% biaxial tensile strain.

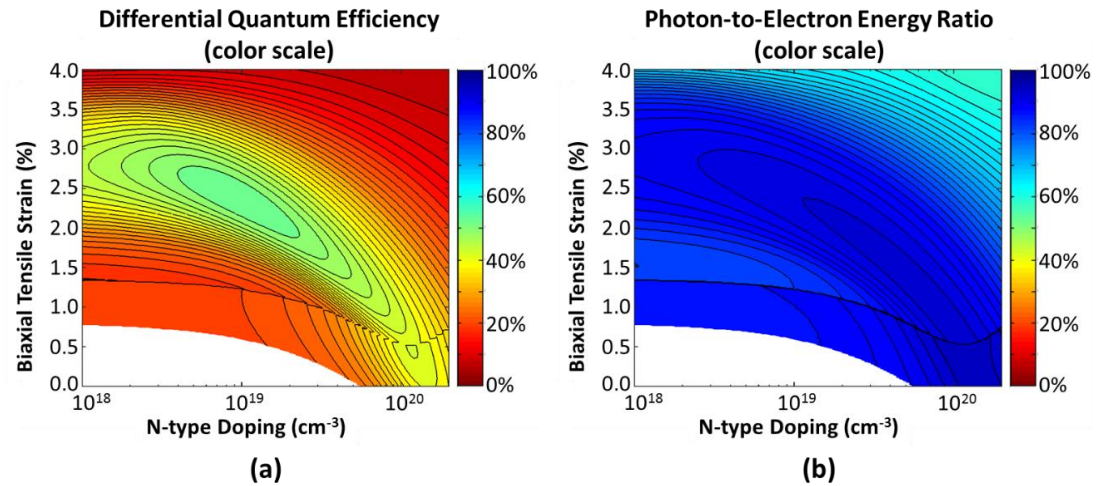


Figure 3-20. Components of the slope efficiency, computed at 700 cm^{-1} optical cavity loss. (a) Differential quantum efficiency, (b) ratio of the output photon energy to the input electron energy. In all cases a double heterostructure design is assumed.

3.5 Limitations of the Model

3.5.1 Band Structure Accuracy Concerns

As with any model, a few simplifying assumptions have been made which may introduce some uncertainties to the results. Some of these uncertainties are related to the band structure computation. The first uncertainty is that there is some controversy regarding exactly how much strain is required to achieve a direct bandgap in germanium, with theoretical estimates ranging from 1.7% to 2.5% biaxial strain [52], [73], [103], [107]. Since our assumption of a direct gap crossover at 2.4% strain is essentially the worst possible case – in particular since it has now been definitively shown that the crossover occurs before 2.33% strain [62] – this means that our model is quite conservative in estimating the potential enhancements from biaxial tensile strain. An analogous uncertainty exists with regard to precisely how much valence

band splitting occurs under strain. A final uncertainty in the band structure calculations of our model is that we have ignored the bandgap narrowing which occurs with heavy doping, and which has been shown to be ~ 33 meV narrowing of both the direct and indirect gaps at $5 \times 10^{19} \text{ cm}^{-3}$ [126]. This is not particularly important since the direct and indirect gaps are believed to be similarly affected, and thus the Γ -L energy separation should not be affected by doping-induced bandgap narrowing [126], [127]. The only effect of doping-induced bandgap narrowing is therefore to redshift the gain from the direct transition to a longer wavelength thereby making the free carrier absorption a bit more problematic and slightly increasing the threshold. This means that the practical implication of doping-related bandgap narrowing is to make heavy n-type doping a slightly less attractive proposition for germanium lasers, particularly at large strains where the bandgap has already become quite small. There are of course separate device concerns that arise once the bandgap has been narrowed so dramatically; these concerns will be addressed in the following sections.

As a side note, while we explicitly do not consider quantum wells [128] in this work, we expect quantum wells to be something of a double-edged sword. Specifically, quantum wells tend to increase the bandgap with the change in any given band or valley's energy inversely correlated with its effective mass. Since the direct conduction valley has a much smaller effective mass than the indirect conduction valleys [108], we would naturally expect quantum wells to raise the direct conduction valley relative to the indirect valleys. This is an undesirable change which directly opposes the benefits offered by tensile strain (and other forms of useful band

engineering). Thus, the question of whether quantum wells will be helpful or harmful is a very complex one which requires further investigation.

3.5.2 Optical Gain Concerns

We have also made some simplifying assumptions when computing the optical gain from the direct transition. Most importantly, our model does not incorporate polarization which has been shown theoretically [129], [130] and experimentally [60], [130] to be important, particularly in the presence of a non-hydrostatic strain due to the complicated splitting and mixing of the valence bands [63]. Since we have simply used the absorption coefficient for unpolarized light, it is plausible that our model is somewhat conservative as we would typically expect at least one polarization to be equal to or better than the unpolarized value. We have also assumed that the absorption coefficient for unstrained germanium still applies in the case of strain, with only a simple correction for how the direct gap energy separations (Γ -HH and Γ -LH) change. This implicitly assumes that the joint density of states and optical matrix elements for the two transitions (Γ -HH and Γ -LH) remain constant with strain. (The density of states changes under strain are however included when computing carrier densities and quasi-Fermi level locations). Given that experimental investigations of how germanium's absorption coefficient changes between 0.0% and 0.2% strain showed the pre-factor of Equation 3-4 to increase by about 5% [41], it is likely that our model slightly underestimates the absorption coefficient – and hence the optical gain – of germanium in the presence of strain. This means that strain is likely even more useful than our model predicts.

Another concern is that we have assumed that the free carrier absorption relation of Equation 3-7 is valid at all wavelengths, and that this relation does not change with strain. These are all somewhat dubious assumptions which were necessary on account of the lack of available information; there is also some disagreement in the research community regarding how exactly the free carrier absorption should be modeled [45]. With regard to the validity of Equation 3-7 at longer wavelengths, the free carrier absorption is theoretically expected to increase with λ^2 [51], however the empirical fit of Equation 3-7 dictates that the free carrier absorption increases even faster: $\sim\lambda^{2.25}$ to $\sim\lambda^{2.43}$. This means that our empirical fit may overestimate the free carrier absorption at very long wavelengths, i.e. for wavelengths outside the range used for the empirical fit, meaning that very large tensile strains (which dramatically redshift the emission wavelength) likely deliver even more of a performance enhancement than our model predicts. The issue of how strain will directly affect Equation 3-7, however, is much more complex and uncertain. Inter-valence band transitions are believed to dominate the free carrier absorption from holes [55] and, due to the strain-induced splitting and mixing of the valence bands, it is almost certain that strain will have a noticeable effect on this inter-valence band absorption [131]. Whether this effect will be positive or negative for the particular case of germanium is a complex question to which the answer is not presently known. However, for the specific cases when the strain level is such that the direct bandgap is approximately equal to the energy separation between any pair of valence bands we would expect an extremely problematic spike in the free carrier absorption from holes due to intervalence band transitions [55]. Thus we might expect certain “dead zones”

in the strain response, i.e. an abrupt drop in laser slope efficiency around a small number of precise strain values – an effect not accounted for in our models.

3.5.3 Carrier Lifetime Concerns

Another issue is whether or not the assumed recombination rates remain valid across different strain and doping conditions. One particularly dubious assumption, mentioned briefly in Section 3.3, is the assumption that the defect-limited minority carrier lifetime is independent of doping. In practice, introducing dopants – especially in large quantities – has a very adverse effect on the defect density and hence on the lifetime [109], [110]. We have deliberately excluded this effect from our model for two reasons. Firstly, this allows us to isolate τ_{SRH} as an independent variable in Sections 3.3 & 3.4.2 and secondly because the precise relation between doping is a strong function of the particular doping and passivation scheme [114]. However, the reality that n-type doping almost universally decreases τ_{SRH} [109], [110], [121] means that n-type doping will be even less useful than our model suggests.

There are, of course, more contributors to the recombination than simply the defect-mediated SRH process: there is also spontaneous emission from both the direct and indirect conduction valleys and especially Auger recombination. The coefficients for these processes (Equation 3-12) may vary with strain – an effect which our model ignores. This is of particular concern for the Auger process since the Auger process tends to be stronger for very narrow bandgap materials [132], and strain can cause very substantial bandgap narrowing (Fig. 3-3). On the other hand, the dominant Auger process in unstrained germanium is phonon-assisted [133]–[135], which suggests that

the Auger coefficient would instead be independent of strain [136]. Most likely what this ultimately means is that the Auger coefficient would initially be roughly independent of strain for low strain values, but would start to counteract the beneficial effects of band engineering once the strain becomes too large. Thus, with respect to this particular mechanism of a potentially strain-dependent Auger coefficient, it would appear that our model likely overestimates the maximum possible utility of strain somewhat. This is particularly true given that the CHSH Auger process [125] would likely increase dramatically once the direct bandgap equals the HH-SO energy separation between the valence bands, or for the other corresponding Auger processes whenever the direct bandgap approximately equals the energy separation between any pair of valence bands. We therefore expect that the “dead zones” for slope efficiency around a small number of precise strain values, explained at the end of Section 3.5.2, will be problematic on account of threshold too.

3.6 Summary

To summarize the results of this chapter, we have modeled the carrier statistics, LED and laser performance of germanium under biaxial tensile strain with n-type doping. From the carrier statistics we find that strain and doping can both enhance the percentage of electrons in the direct conduction valley dramatically but that strain is more useful, offering three orders of magnitude enhancement in the direct conduction valley occupation compared to an enhancement of only one order of magnitude from doping. Moreover, there is a negative interaction between strain and doping such that doping becomes less useful at high strain values: doping can actually decrease the

fraction of electrons in the direct conduction valley for very highly strained germanium. Another key point is that there is no special benefit to achieving a direct gap unless extremely low temperatures ($<30\text{K}$) are employed. Due to the $>50\text{x}$ larger density of states in the indirect valleys, only $\sim 1.3\%$ of electrons will reside in the direct valley even when the strain becomes just sufficient to achieve a direct gap. For room temperature devices the percentage of electrons in the direct valley will continue to increase exponentially with strain even for strains beyond the direct bandgap crossover.

With regard to strained n-type doped germanium LEDs we find similar results: biaxial tensile strain and doping can both yield dramatic increases in the internal quantum efficiency of a germanium double heterostructure LED (for example an $\text{n}^+\text{-Si/n}^+\text{-Ge/p}^+\text{-Si}$ LED [89]). However there is again an optimal doping which decreases with strain, indicating a negative interaction between these two approaches. Our modeling shows that it is also critically important to improve the defect-limited minority carrier lifetime in order to achieve a high efficiency LED, indicating that much work is needed on improving material quality [112]. Given that state-of-the-art epitaxial germanium has a defect-limited carrier lifetime of only $\sim 1\text{ ns}$, our modeling suggests that improving this lifetime would improve the efficiency of a germanium LED by more than two orders of magnitude. This makes lifetime improvements even more critical to LED device performance than band engineering such as biaxial strain.

For the penultimate goal of building an efficient low-threshold germanium laser, our modeling shows that band engineering through biaxial tensile strain is a very promising route, offering threshold reductions of 3-4 orders of magnitude. N-type

doping is also a somewhat useful technique, but only to a point and too much doping will be actively harmful. Our modeling suggests that for strains beyond 1% the maximum useful doping is less than $5 \times 10^{19} \text{ cm}^{-3}$, and for strains beyond 2% the maximum useful doping is less than $1 \times 10^{19} \text{ cm}^{-3}$. Given that germanium lasers to date have used $5 \times 10^{19} \text{ cm}^{-3}$ n-type doping with only $\sim 0.25\%$ strain [101], this means that further efforts to achieve high n-type doping concentration will not be helpful. Instead, it will actually become necessary to reduce the doping from present levels once larger strains become practical. On the other hand, there is a clear need for large tensile strain in order to achieve low threshold; strain will remain useful up to 2.4-3.7% depending on whether threshold minimization or slope efficiency maximizing is more critical to the particular application intended. More importantly, due to valence band splitting effects we find that strain becomes disproportionately beneficial at large values, showing a sudden increase in utility once the strain value exceeds about $\sim 1\%$. This means that researchers should focus first on achieving the largest possible tensile strains, as we will do in this dissertation, before attempting to create device prototypes. In addition, as was the case for our LED modeling, our germanium laser modeling suggests that it is necessary to improve germanium's defect limited minority carrier lifetime to several hundred nanoseconds, presumably by improving the material quality [112]. This need to achieve longer defect-related carrier lifetimes will become particularly acute for large strain values. And lastly, due to an unusually strong contribution from free carrier absorption it will be necessary to employ optical cavities with much more out-coupling loss than is typical for III-V lasers, probably in the vicinity of $\sim 700 \text{ cm}^{-1}$ of out-coupling loss. Incorporating such a large out-coupling

loss, however, will only increase the threshold by about a factor of two while enabling slope efficiencies of about 30-60% before parasitics. These parasitics will pose a substantial challenge in their own right, particularly with regard to achieving a large gain overlap with the active region and minimizing electrical and optical losses in the metal contacts [101]. However, since overcoming parasitics is a problem of device structure optimization rather than a fundamental limit we expect further research to ultimately provide viable solutions with regard to designing a practical device structure given that our model shows the fundamental material properties of band engineered germanium to be sufficient.

Chapter 4

Theoretical Modeling for Other Types of Band Engineering

4.1 Overview

In the previous Chapter we thoroughly investigated how band engineering through $\langle 100 \rangle$ biaxial tensile strain enhances light emission from germanium. We also considered how n-type doping enhances light emission from germanium and, in particular, the interaction between band engineering and n-type doping for the specific case of band engineering through $\langle 100 \rangle$ biaxial strain. We naturally expect other types of band engineering to give somewhat similar results, provided that such alternative means of band engineering also reduce the Γ -L energy separation such that the band structure becomes more direct. However, it is worth investigating how other forms of band engineering differ from $\langle 100 \rangle$ biaxial tensile strain with respect to enhancing light emission and the cause of any such differences where they exist. In this Chapter we will investigate band engineering by $\langle 100 \rangle$ uniaxial strain and also band engineering through tin alloying to form $\text{Ge}_x\text{Sn}_{1-x}$, using our previous investigation of $\langle 100 \rangle$ biaxial strain as a point of reference. We will also provide a casual analysis of other strain orientations such as $\langle 110 \rangle$ and $\langle 111 \rangle$ and their implications to germanium light emission.

4.2 Uniaxial Strain (<100> orientation)

4.2.1 Band Structure

Uniaxial strain changes the band structure in much the same way as biaxial strain. We can directly model these changes to germanium's bandstructure under <100> uniaxial strain using deformation potential theory [39] as shown in Fig. 4-1. Comparing Fig. 4-1 with Fig. 3-3 from the preceding chapter we immediately notice two distinctions between uniaxial and biaxial strain. First, whereas it takes a mere ~2.4% biaxial strain to achieve a direct bandgap according to our tight-binding model [53], [105], [106], or even just ~1.7% biaxial strain according to deformation potential theory [39], a considerably larger 4.6% uniaxial strain [39] is required to accomplish the same feat. The second difference concerns the valence band splitting that occurs under strain. Whereas for <100> biaxial tensile strain the top valence band retains a mostly heavy hole (HH) character, under <100> uniaxial strain the LH/HH splitting is such that the top valence band retains a mostly light hole (LH) character [137], [138]. This latter distinction concerning valence band splitting will play a particularly major role in section 4.2.4 when we model how uniaxial strain affects the threshold current.

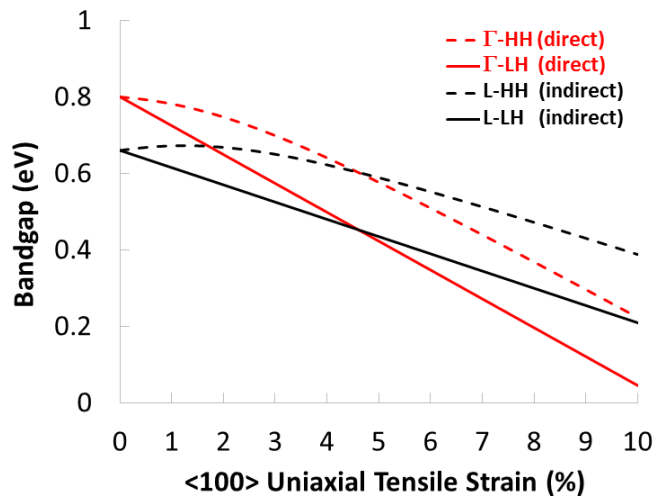


Figure 4-1. Germanium's direct (Γ) and indirect (L) bandgap energies vs. $\langle 100 \rangle$ uniaxial tensile strain according to deformation potential theory [39]. Crossover of the direct gap is visible at 4.6% uniaxial strain.

4.2.2 Carrier Statistics

Having computed the band edge locations, we can now investigate how uniaxial strain enhances the carrier population in the direct conduction valley as shown in Fig. 4-2. Comparing Fig. 3-4 ($\langle 100 \rangle$ biaxial strain) with Fig. 4-2 ($\langle 100 \rangle$ uniaxial strain) shows that in both cases strain causes an exponential increase in the percentage of electrons in the direct valley, except whereas every additional 1% of $\langle 100 \rangle$ biaxial strain causes a $\sim 8x$ enhance we find that every 1% of $\langle 100 \rangle$ uniaxial strain causes only a $\sim 3x$ enhancement. This is because it takes about twice as much uniaxial strain to achieve a direct bandgap, and so every 1% of uniaxial strain will be less effective. To the extent that any other differences in electron carrier statistics between $\langle 100 \rangle$ biaxial and $\langle 100 \rangle$ uniaxial strains are observed the explanation is that our tight-binding model for

biaxial strain accounts for effective mass changes whereas our deformation potential theory model for uniaxial strain does not; effective mass changes are a decidedly secondary effect compared to band edge changes.

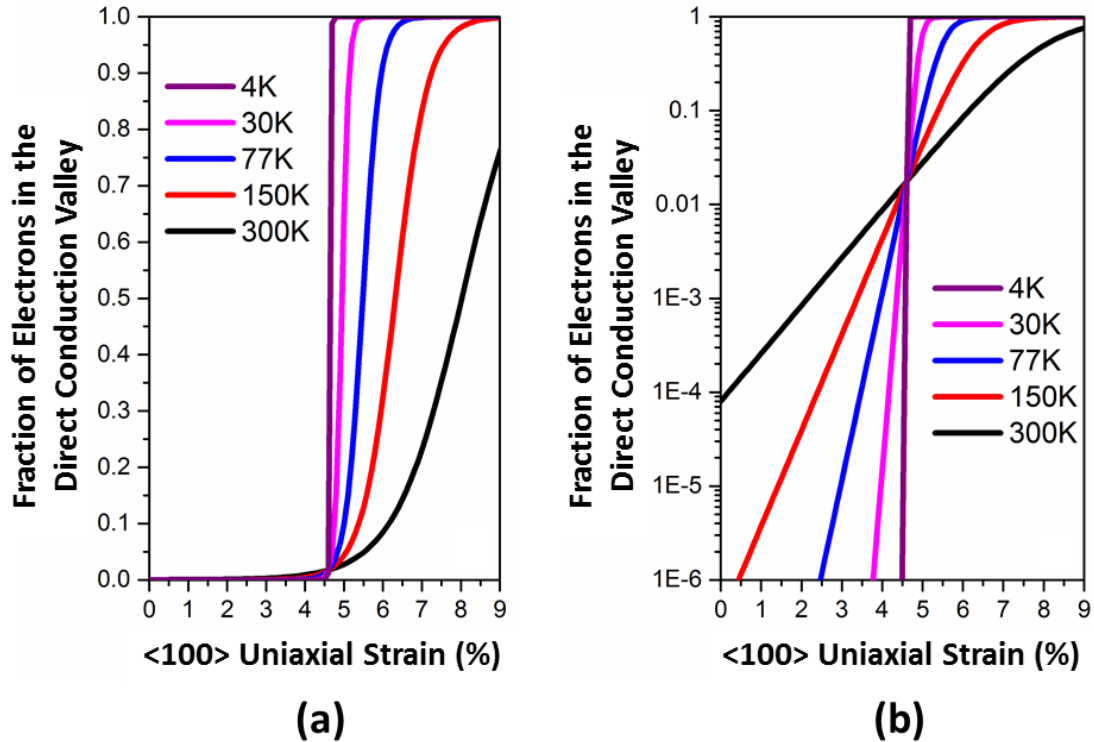


Figure 4-2. Fraction of electrons in the direct conduction valley vs. $\langle 100 \rangle$ uniaxial strain for undoped germanium at several different temperatures, shown on (a) linear, and (b) logarithmic scales. [23]

4.2.3 Light Emitting Diode (LED) Modeling

Having computed the carrier statistics for germanium under $\langle 100 \rangle$ uniaxial tensile strain, we can now continue to basic LED modeling. As was done in Section 3.3 in the previous chapter, we will consider simply the internal quantum efficiency of a

hypothetical double-heterostructure germanium LED using Equation 3-3. As shown in Fig. 4-3 we find that $\langle 100 \rangle$ uniaxial tensile strain can dramatically enhance the efficiency of a germanium LED: assuming a 1 μs Shockley-Read-Hall (SRH) lifetime we find that applying 7.5% uniaxial strain will increase the internal quantum efficiency from only $\sim 5\%$ to $\sim 95\%$. However, at the ~ 1 ns nanosecond lifetimes which are commonly reported in epitaxial germanium [112], [121] the results become vastly less promising: even employing 7.5% uniaxial strain would only result in a $\sim 10\%$ internal quantum efficiency. These results are therefore qualitatively the same as we found for $\langle 100 \rangle$ biaxial strain (Fig. 3-7) in the preceding Chapter, with the conclusion in both cases being that tensile strain can dramatically improve the internal quantum efficiency of a germanium LED but that it is even more imperative to improve the material quality so as to achieve a longer SRH lifetime.

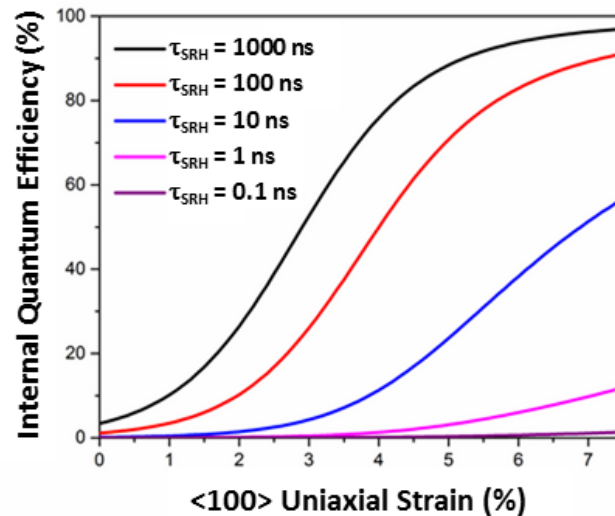


Figure 4-3. Internal quantum efficiency of a germanium double-heterostructure LED for various SRH lifetime assumptions [23]. Doping is assumed to be $1 \times 10^{19} \text{ cm}^{-3}$.

4.2.4 Laser Modeling – Threshold Current

Having already extensively modeled the threshold of a biaxially strained germanium laser, we can now repeat this analysis using our deformation potential model for uniaxial strain. As was the case in the preceding chapter, we presume a double heterostructure design with 300nm-thick germanium active region that always lases at the wavelength of maximum net gain. By applying this same approach can readily compute the threshold current density and emission wavelength as a function of $\langle 100 \rangle$ uniaxial tensile strain and n-type doping as shown in Fig. 4-4.

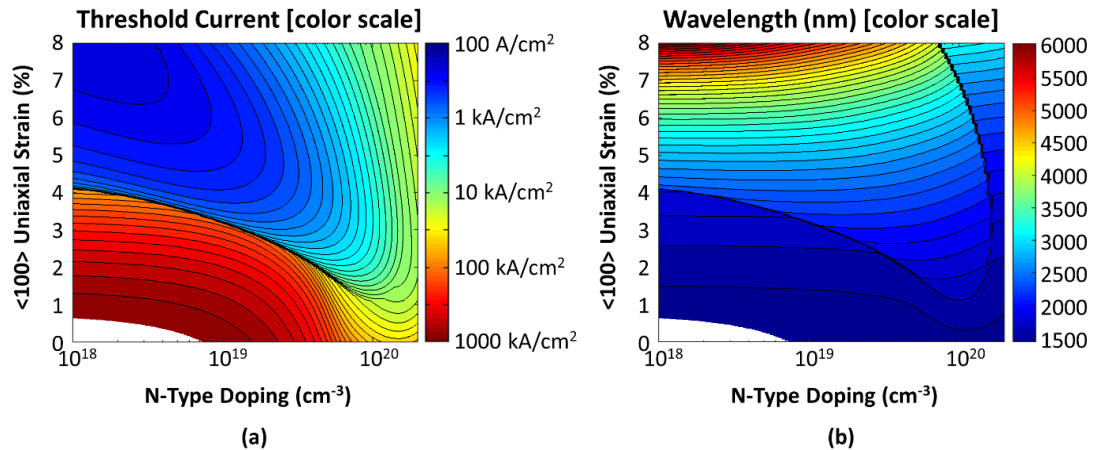


Figure 4-4. Threshold and wavelength vs. $\langle 100 \rangle$ uniaxial strain and doping. (a) Threshold current density of a double heterostructure germanium laser (color scale) vs. uniaxial tensile strain ($\langle 100 \rangle$ orientation) and n-type doping. (b) Emission wavelength (color scale) vs. uniaxial tensile strain ($\langle 100 \rangle$ orientation) and n-type doping. Germanium thickness is assumed to be 300nm with an optical cavity loss of zero and a defect-limited minority carrier lifetime of $\tau_{SRH}=100ns$. The blank region in the bottom left corner is due to the cutoff of the simulation bounds, i.e. thresholds greater than 1000 kA/cm^3 .

From Fig. 4-4 ($\langle 100 \rangle$ uniaxial strain) we observe many similarities with the $\langle 100 \rangle$ biaxial strain scenario of Fig. 3-11. Both forms of strain, for instance, exponentially reduce the threshold current of a germanium laser and dramatically redshift the preferred emission wavelength. These enhancements with strain continue even after a direct bandgap has been achieved at 2.4% biaxial or 4.6% uniaxial strain, and we observe no special benefit to achieving a direct bandgap with respect to laser performance. Furthermore, we again observe the presence of an “optimal doping” which decreases in the presence of strain, with qualitatively similar results for uniaxial and biaxial strains along $\langle 100 \rangle$. And lastly, we observe two distinct regimes for both uniaxial and biaxial strain due to LH/HH splitting in the valence bands: after about 0.5-1.0% biaxial strain or 2-4% uniaxial strain it becomes possible to achieve particularly dramatic reductions in threshold coupled with an abrupt jump in wavelength. This two-regime phenomenon, however, is also a major point of distinction between uniaxial and biaxial strain. Whereas for biaxial strain we found that exceeding a certain critical value causes the threshold reductions to suddenly accelerate, for uniaxial strain we find that exceeding a certain critical value causes an abrupt and immediate drop in the threshold itself. This phenomenon can be seen more clearly in Fig. 4-5, which is a 3D surface plot of Fig. 4-4(a). This is a very important distinction, since this sudden drop in threshold can exceed two orders of magnitude depending on the doping level.

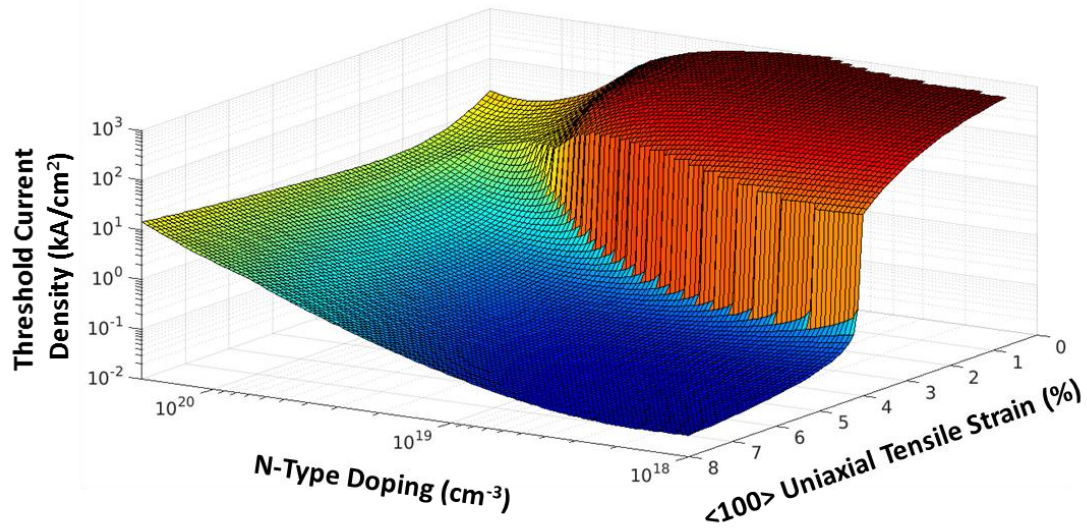


Figure 4-5. Threshold current density vs. uniaxial tensile strain (<100> orientation) and n-type doping (3D plot). A double heterostructure design with a 300nm-thick germanium active region and zero optical cavity loss is assumed.

The explanation for why only uniaxial strain allows for this sudden and abrupt drop in threshold at a critical value has to do with the details of the LH/HH splitting in the valence bands. For biaxial strain the top valence band retains a mostly heavy hole (HH) character which, due to its larger density of states, means that there is less immediate benefit when the splitting is sufficiently large to allow lasing from just to top valence band transition. In addition, due to the large joint density of states for the Γ -HH transition we find that this transition alone becomes sufficient for lasing at a relatively small biaxial strain of 0.5-1.0%, which is not even halfway to achieving a direct bandgap. For uniaxial strain, on the other hand, the top valence band retains a mostly light hole (LH) character. (Or in our simplified deformation potential model simply *is* the light hole band.) This means that when the valence band splitting does

become sufficiently large to allow lasing using only the Γ -LH transition the threshold will be dramatically smaller due to the much smaller density of states in the LH band. In addition, due to the smaller joint density of states for the Γ -LH transition it can take up to ~4.1% uniaxial strain – nearly enough for a direct bandgap – before this regime change occurs. Because this regime change to lasing with just the top valence band only happens at larger strains there is a much larger accumulated benefit that is instantly realized upon reaching this regime change, which also explains the discontinuity in threshold. As shown in Fig. 4-6 for $\langle 100 \rangle$ uniaxial strain (compare to Fig. 3-13 for $\langle 100 \rangle$ biaxial strain), employing a heavier doping allows this regime change to happen at smaller strain values whereupon the discontinuity is less pronounced. At $1 \times 10^{20} \text{ cm}^{-3}$ n-type doping the regime change occurs at ~1.1% strain and there is no discontinuity, just a kink. At $5 \times 10^{19} \text{ cm}^{-3}$ doping the regime change occurs at ~1.8% strain and there is a discontinuity whereupon the threshold abruptly drops by ~5x. At $1 \times 10^{19} \text{ cm}^{-3}$ doping the regime change occurs at ~3.2% strain and there is a discontinuity whereupon the threshold abruptly drops by ~200x. This supports the hypothesis that the discontinuity is due to the fact that larger uniaxial strains are required to reach the regime where only the top valence band contributes to lasing, and that the needed for larger strains means that there is a larger accumulated benefit that is abruptly realized.

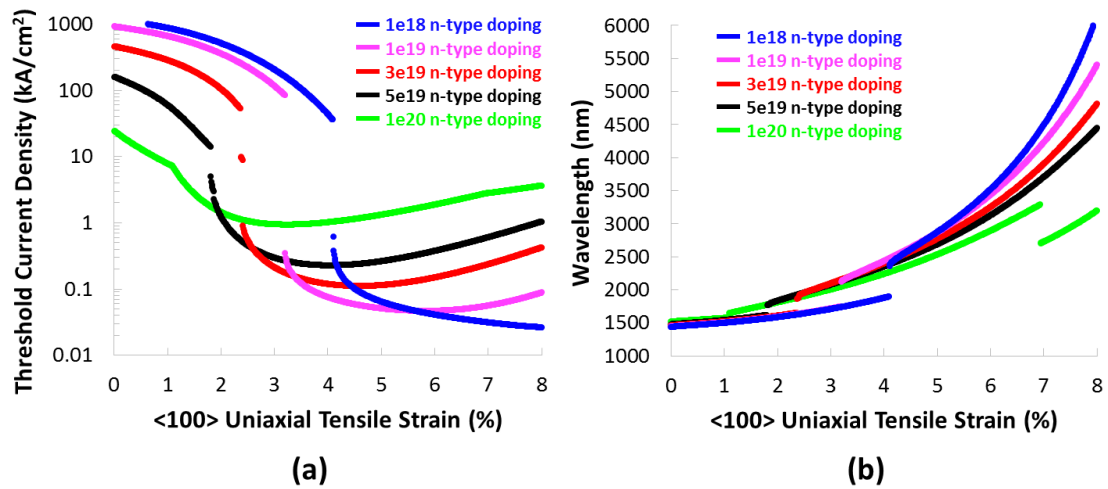


Figure 4-6. Threshold and wavelength vs. uniaxial strain for several doping conditions. (a) Threshold current density of a germanium laser vs. uniaxial tensile strain (<100> orientation) for different doping conditions. (b) Emission wavelength of a germanium laser vs. uniaxial tensile strain (<100> orientation) for different doping conditions. In all cases a double heterostructure design with a 300nm thick germanium active region, zero optical cavity loss, and a defect-limited minority carrier lifetime of $\tau_{SRH}=100ns$ is assumed. The outlier data points in the discontinuity region of figure (a) are artifacts from linear interpolations in the vicinity of the discontinuity.

From a practical perspective what this means is that it is even more essential to reach this critical strain for uniaxial strain than it was for biaxial strain. Whereas for biaxial this critical strain represents a soft boundary where the threshold shows faster improvements beyond a certain strain, for uniaxial this critical strain represents a hard boundary between a very high threshold regime and a very low threshold regime. For the case of $1 \times 10^{19} \text{ cm}^{-3}$ n-type doping this critical strain is about 3.2% along the <100>

direction which is considerably smaller than the 4.6% $\langle 100 \rangle$ uniaxial strain needed to achieve a direct bandgap.

4.2.5 Laser Modeling – Slope Efficiency

Having investigated the threshold we can now consider the slope efficiency of a $\langle 100 \rangle$ uniaxially strained germanium laser. As explained in Section 3.4.3 of the preceding Chapter, it is necessary to introduce some optical cavity loss due to out-coupling of light in order to achieve a non-zero slope efficiency. We further expect, and indeed observed for biaxial strain, that introducing more optical cavity loss will generally be helpful to slope efficiency but detrimental to threshold. As shown in Fig. 4-7 this is indeed the case for uniaxially-strained n-type doped germanium lasers.

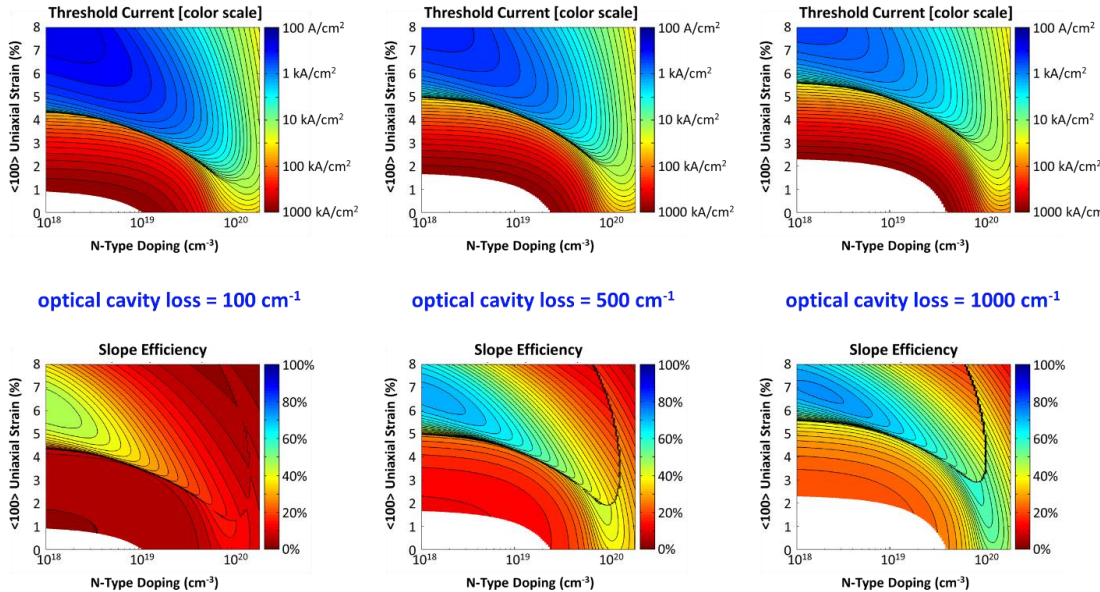


Figure 4-7. Threshold and slope efficiency vs. uniaxial strain and n-type doping for several optical cavity loss values. Threshold current density (top) and slope efficiency (bottom) are shown for optical cavity losses of 100 cm⁻¹ (left), 500 cm⁻¹ (middle) and 1000 cm⁻¹ (right). In

all cases a double heterostructure design with a 300nm thick germanium active region and $\tau_{SRH}=100ns$ is assumed. (Threshold and slope efficiency plots for an extended range of optical cavity loss values are available as Fig. A-4 in the Appendix.)

From Fig. 4-7 we also find that the slope efficiency responds to $\langle 100 \rangle$ uniaxial strain in much the same way that it responds to $\langle 100 \rangle$ biaxial strain (Fig. 3-16). In both cases we observe that strain enhances the slope efficiency and that, as with threshold, there is an optimal doping that decreases with strain. There are, however, two notable differences between the uniaxial results of Fig. 4-7 and the biaxial results of Fig. 3-16 in the preceding Chapter. The first difference has to do with the ultimate limit of strain with respect to enhancing slope efficiency. For biaxial strain the ultimate limit occurs for around 2.4% strain which is the same as required to achieve a direct bandgap and considerably less than the 3.7% strain corresponding to the ultimate limit for threshold. In contrast, we find that uniaxial strain remains useful for slope efficiency at up to 6-7% strain – noticeably more than the 4.6% strain required to achieve a direct gap and much closer to the 7-8% strain which corresponds to the ultimate limit for threshold in the uniaxial case. The likely explanation for this difference again has to do with the fact that uniaxial strain results in the top valence band having a light hole character with a small density of states. This means that there are far fewer holes in the low threshold region for the uniaxially strained case, which is important because holes cause much more free carrier absorption than holes at the longer wavelengths associated with highly strained germanium in accordance with Equation 3-7. As a result of this reduced hole concentration at threshold, uniaxially strained germanium

offers a greater performance robustness against the redshifts that accompany strain and we find that uniaxial strain is capable of offering a larger maximum benefit for slope efficiency purposes than biaxial strain.

The second point of distinction between biaxial and uniaxial strains along $\langle 100 \rangle$ is that the maximum slope efficiency is noticeably higher for the uniaxial case, particularly for smaller optical cavity losses. For an optical cavity loss of 100 cm^{-1} , for instance, only about 15% slope efficiency is possible using biaxial strain (Fig. 3-16) but approximately 50% slope efficiency is possible using uniaxial strain (Fig. 4-7). For a 500 cm^{-1} cavity a maximum slope efficiency of about 50% using biaxial strain can be obtained compared to about 65% slope efficiency using uniaxial strain. This is again due to the greatly reduced hole concentration at threshold when employing a large uniaxial strain, which in turn can be explained by the fact that the top valence band under uniaxial strain is the light hole band for density of states purposes. We can also directly examine how the optical cavity loss affects the threshold and slope efficiency for the case of $\langle 100 \rangle$ uniaxial strain as shown in Fig. 4-8.

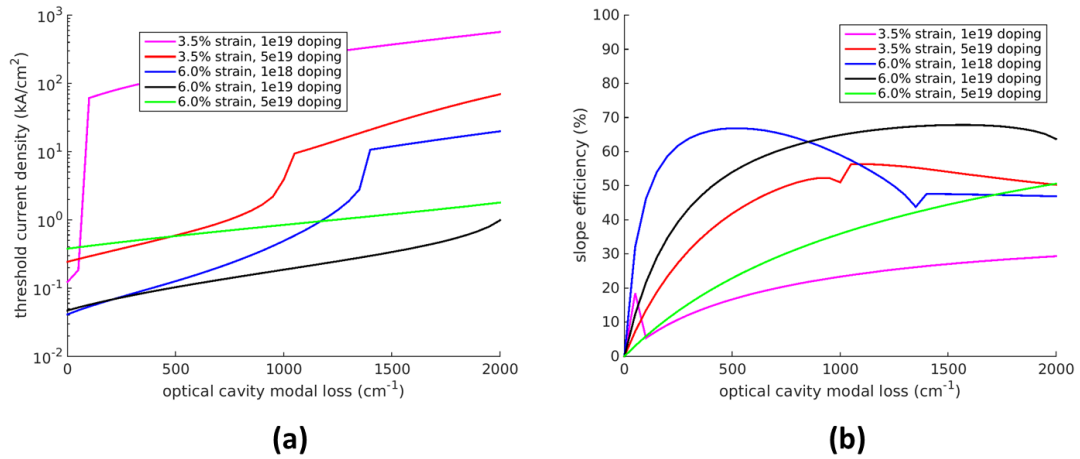


Figure 4-8. (a) Threshold current density vs. optical cavity loss, shown for several strain and doping combinations, (b) Slope efficiency vs. optical cavity loss, shown for several strain and doping combinations. In all cases a double heterostructure design with a 300nm thick germanium active region and a defect-limited minority carrier lifetime of $\tau_{\text{SRH}}=100\text{ns}$ is assumed. All strains are uniaxial strains oriented along $\langle 100 \rangle$.

4.3 Other Strain Orientations

4.3.1 Overview

Having investigated both biaxial and uniaxial strains along $\langle 100 \rangle$ in the preceding Chapter and the preceding Section, respectively, we can also consider strains along the $\langle 110 \rangle$ and $\langle 111 \rangle$ orientations. For these analyses we will limit our investigation to the how the bandstructure changes under such strains and how this affects the proportion of electrons in the direct conduction valley. While our previous analyses it is clear that device-level results will depend on some subtleties beyond just the proportion of electrons in the direct valley, the overriding motivation for band

engineering is to increase this proportion and so it remains a valid proxy for at least determining whether a particular type of band engineering will be helpful or harmful.

4.3.2 Uniaxial Strains along Different Orientations

We will begin with uniaxial strain. As shown in Fig. 4-9, strains along $\langle 110 \rangle$ and $\langle 111 \rangle$ break the symmetry between the four previously degenerate L valleys. Note that there are actually eight L valleys in the conduction band, each of which is only half within the first Brillouin Zone. Furthermore, there is an unbreakable symmetry between four pairs of antiparallel L valleys, $\langle 111 \rangle$ & $\langle -1-1-1 \rangle$, $\langle 11-1 \rangle$ & $\langle -1-11 \rangle$, $\langle 1-11 \rangle$ & $\langle -11-1 \rangle$, $\langle 1-1-1 \rangle$ & $\langle -111 \rangle$, and each of these L valleys pairs will be labelled L_1 , L_2 , L_3 , L_4 respectively for this dissertation. We further observe from Fig. 4-9(b) that for $\langle 110 \rangle$ uniaxial strain the Γ - L_1 and Γ - L_2 energy separations rapidly decrease with increasing strain, however the Γ - L_3 and Γ - L_4 energy separations actually increase as a tensile $\langle 110 \rangle$ strain is applied. This means that strain will serve primarily to enhance the proportion of electrons in the L_3 and L_4 conduction valleys rather than in the Γ valley. Meanwhile, the proportion of electrons in the L_1 and L_2 valleys would decrease under the application of a $\langle 110 \rangle$ tensile strain.

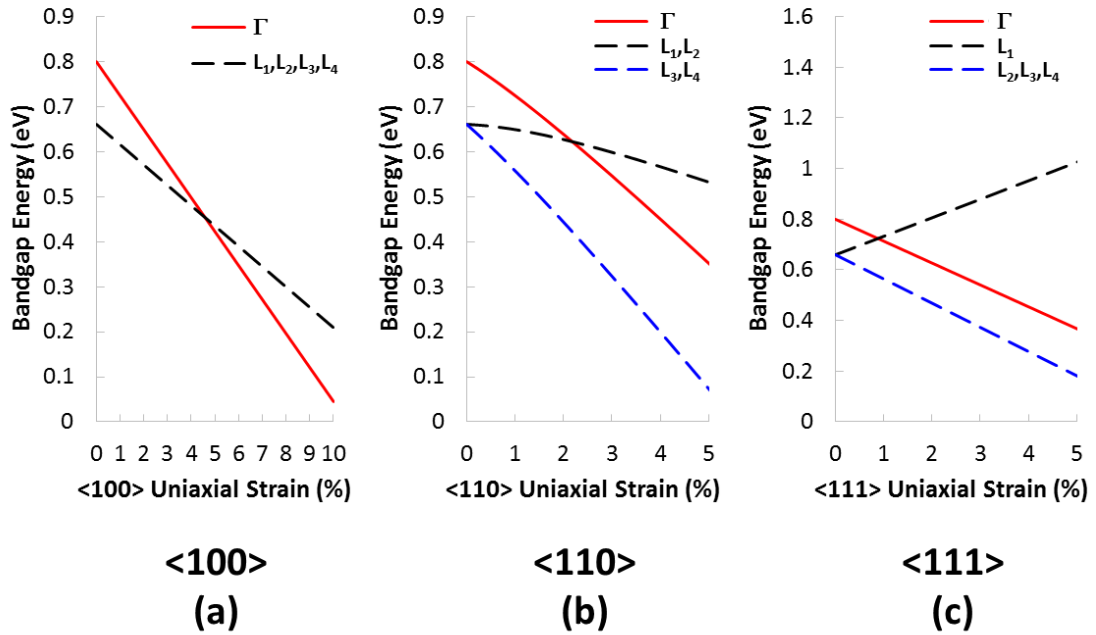


Figure 4-9. Bandgaps of germanium as a function of uniaxial tensile strain for the (a) <100> orientation, (b) <110> orientation, and (c) <111> orientation.

We can observe this phenomenon quantitatively by computing the proportion of electrons in the Γ conduction valley for each strain orientation in Fig. 4-10. From Fig. 4-10(b) we observe that <110> strain initially offers a small benefit due to carrier spillover from the L₁ and L₂ valleys, but <110> strain quickly becomes harmful due to spillover of electrons out of the Γ valley and into the L₃ and L₄ valleys and the proportion of electrons in the Γ never exceeds 0.01%. A similar phenomenon is observed for the <111> strain orientation. As shown in Fig. 4-9(c), the Γ -L₁ energy separation decreases under the application of <111> tensile strain but the Γ -L₂, Γ -L₃ and Γ -L₄ energy separations all increase which is problematic. As shown in Fig. 4-

10(c), $\langle 111 \rangle$ is also slightly helpful initially before becoming extremely harmful and again the proportion of electrons in the direct conduction valley never exceeds 0.01%. We can therefore conclude that for uniaxial strain only the $\langle 100 \rangle$ orientation is helpful whereas the $\langle 110 \rangle$ and $\langle 111 \rangle$ orientations are actually quite harmful for germanium light emission.

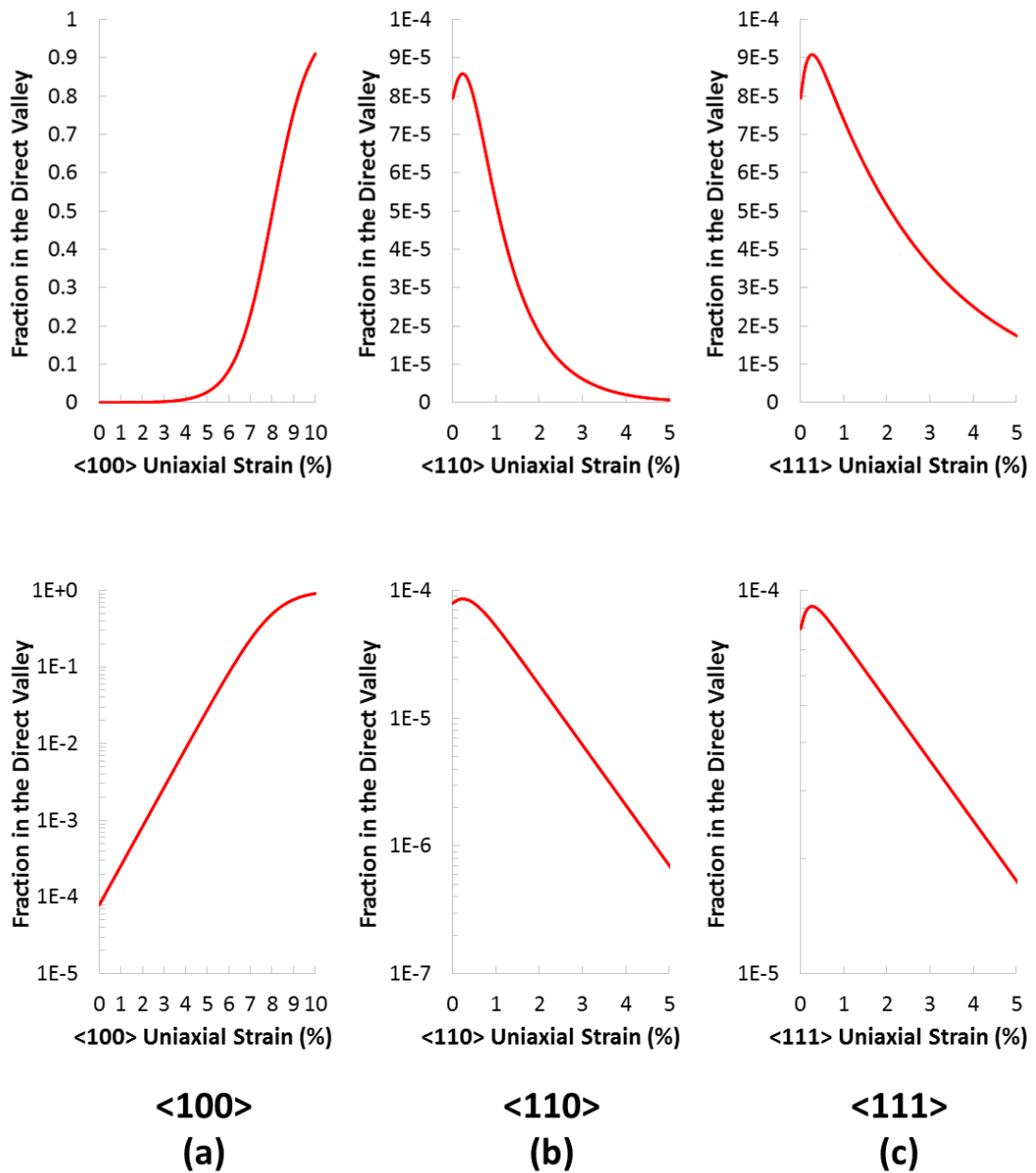


Figure 4-10. Fraction of electrons in the direct (Γ) conduction valley in germanium as a function of uniaxial tensile strain for the (a) $\langle 100 \rangle$ orientation, (b) $\langle 110 \rangle$ orientation, and (c) $\langle 111 \rangle$ orientation. Results are shown on both linear (top) and logarithmic (bottom) scales.

We note that this conclusion differs dramatically from Ref. [139] which claimed that $\langle 110 \rangle$ and $\langle 111 \rangle$ strain orientations would be extremely useful for converting germanium into a direct bandgap semiconductor. This is almost certainly because Ref. [139] completely neglected the breaking of the L valley degeneracy and therefore erroneously concluded that all L valleys were at the L_1 energy level indicated in Fig. 4-9. A similar point can be made for biaxial strain along different orientations when comparing the results of Ref. [139] to our modeling in Fig. 4-11 of the next Section.

4.3.3 Biaxial Strains along Different Orientations

We can now repeat this analysis for biaxial strain along different orientations. As shown in Fig. 4-11, for biaxial strain we find that $\langle 100 \rangle$ and $\langle 110 \rangle$ orientations are both promising in that the Γ -L energy separation decreases under strain for all the L valleys, whereas the $\langle 111 \rangle$ orientation seems to be unappealing since the Γ - L_1 energy separation increases under $\langle 111 \rangle$ biaxial strain. This is indeed confirmed in Fig. 4-12 where we find that the proportion of electrons in the Γ valley increases exponentially with both $\langle 100 \rangle$ and $\langle 110 \rangle$ biaxial strain. In contrast, we find in Fig. 4-12(c) that the proportion of electrons in the Γ valleys initially increases very slightly under $\langle 111 \rangle$ biaxial strain before rapidly decaying. Thus, we conclude that $\langle 111 \rangle$ biaxial strain is not an appealing approach just as we previously concluded for $\langle 110 \rangle$ and $\langle 111 \rangle$ uniaxial strains. Lastly, while we find that $\langle 110 \rangle$ biaxial strain is helpful, from Fig. 4-12(a,b) we find that $\langle 100 \rangle$ biaxial strain offers more benefit for the same amount of strain. Considering that Young's modulus is larger along the $\langle 110 \rangle$ axis than along

the $\langle 100 \rangle$ axis in germanium [140], this discrepancy becomes even larger when comparing $\langle 110 \rangle$ stress with $\langle 100 \rangle$ stress rather than comparing strains. Thus, while $\langle 110 \rangle$ biaxial is a beneficial band engineering technique, we expect $\langle 100 \rangle$ to be the optimal strain orientation for biaxial tensile strain.

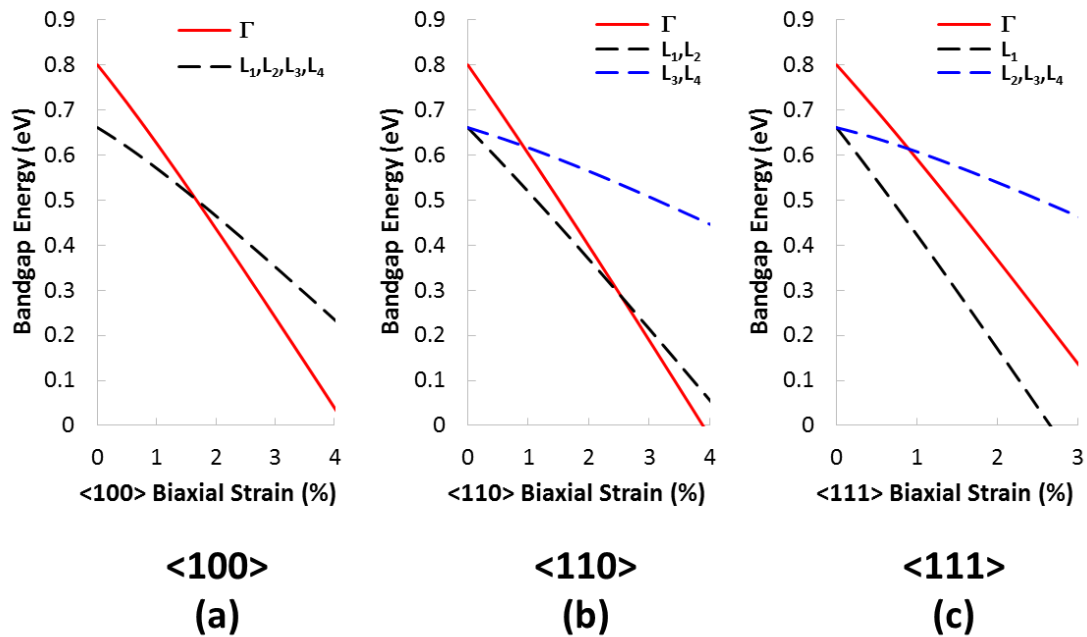


Figure 4-11. Bandgaps of germanium as a function of biaxial tensile strain for the (a) $\langle 100 \rangle$ orientation, (b) $\langle 110 \rangle$ orientation, and (c) $\langle 111 \rangle$ orientation.

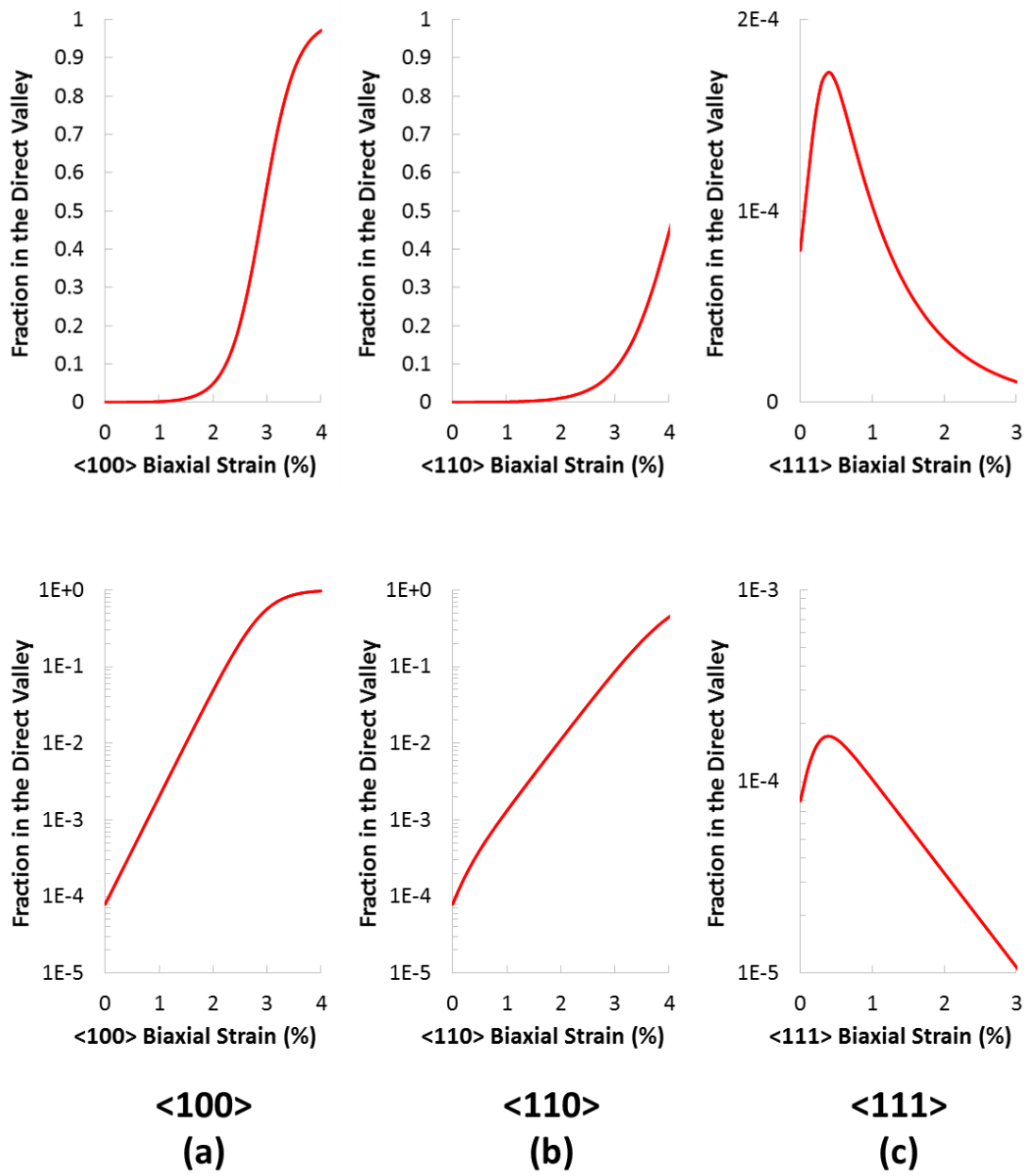


Figure 4-12. Fraction of electrons in the direct (Γ) conduction valley in germanium as a function of biaxial tensile strain for the (a) <100> orientation, (b) <110> orientation, and (c) <111> orientation. Results are shown on both linear (top) and logarithmic (bottom) scales.

4.4 Germanium Tin (Ge_xSn_{1-x})

4.4.1 Band Structure

An alternative technique for germanium band engineering is to alloy the germanium with tin to form a germanium-tin (Ge_xSn_{1-x}) alloy. As was the case with applying a tensile strain, increasing the tin content (i.e. decreasing “x” in Ge_xSn_{1-x}) has the effect of shrinking both the direct and indirect bandgaps, but to shrink the direct bandgap noticeably faster than the indirect gap such that employing about 6.55% tin (i.e. $Ge_{0.9345}Sn_{0.0655}$) will result in a direct bandgap [84], [141]. The effect of tin alloying on the bandstructure can be modeled in a number of ways such as density functional theory [86], tight-binding [142] or empirical pseudo-potentials [141]; in all cases the virtual crystal approximation with disorder effects [86], [141], [142] can be used to account for the combination of two dissimilar elements. In this work we will instead employ a “hack” wherein we reuse the conduction band structures which we have computed for biaxially strained germanium along with the valence band structures for unstrained germanium. This represents the assumption that germanium tin changes the conduction band in the same way as tensile strain, i.e. reducing the direct gap relative to the indirect gap, but without substantially altering the valence band, i.e. without the LH/HH splitting that occurs under biaxial and uniaxial tensile strain. Assuming that a direct gap occurs at either 6.55% tin [141] or 2.40% biaxial tensile strain ($\langle 100 \rangle$ orientation) [53], we take every 1% tin to equal 0.3664% biaxial strain for the purposes of the conduction band. We then combine the conduction bands from our tight-binding model for the appropriate strain level with the valence bands for unstrained germanium and then, following the example of the scissor operator [143]

commonly used in density functional theory, we manually raise or lower the conduction bands such that the bandgap is forced to the correct value in accordance with Ref. [82]. This results in a bandgap dependence on tin concentration as shown in Fig. 4-13 which is in good agreement with accepted models and experimental results for tin concentrations smaller than about 10% [82], [84], [141], [144].

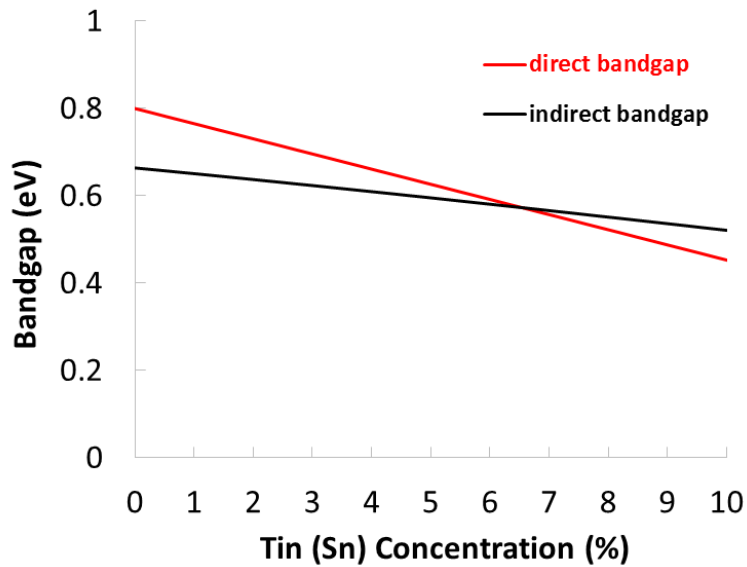


Figure 4-13. Germanium-tin’s direct and indirect bandgap energies vs. tin concentration for unstrained germanium-tin. Crossover of the direct gap is visible at 6.55% tin.

Although there are some drawbacks to this approach, which will be explained in detail in Section 4.5, the fact that this approach reuses the biaxial strain band structures from our tight-binding model is necessary for investigating the interaction between biaxial tensile strain and tin alloying (Section 4.4.4) in a computationally feasible way.

Computing a full 4D bandstructure for any given strain value is very time consuming,

and even computing these band structures over a range of strains can take several days. To compute the bandstructures for every possible combination of strain and tin alloying would be completely impractical using our present approach. Thus, while the approach we have used for tin alloying is somewhat unconventional it is necessary for a proper exploration of the interaction between tensile strain and n-type doping and, critically, is scientifically sound since the computed band edges in the presence of tin alloying (Fig. 4-13) are in good agreement with accepted models and experiments (Fig. 1 of Ref [141]) and the effect of strain is also in agreement with accepted literature [53].

4.4.2 Threshold Current

Having computed the bandstructure of germanium-tin the next step is to model how tin alloying affects the performance of a germanium laser. As shown in Fig 4-14, we find that band engineering through tin alloying up to 10% can reduce the threshold of a germanium-based laser by over two orders of magnitude while redshifting the emission wavelength beyond 2.5 μm . This assumes that the germanium-tin gain medium is completely unstrained. Furthermore, from Fig. 4-14(a) there is again an “optimal doping” that decreases with increased tin alloying, and it appears that at 10% tin we have still not reached the “ultimate limit” with respect to threshold minimization. Compared to the previous results for biaxial or uniaxial strains ($\langle 100 \rangle$ orientation), however, this represents a comparatively smaller reduction in threshold and a smaller redshift. This is despite the fact that 10% tin is about 1.5x the amount of

tin required for a direct bandgap, just like 3.5% biaxial strain (<100> orientation) is about 1.5x the amount of biaxial strain required for a direct bandgap, and yet 3.5% biaxial strain would result in a germanium with double the emission wavelength and about a tenth the threshold current density.

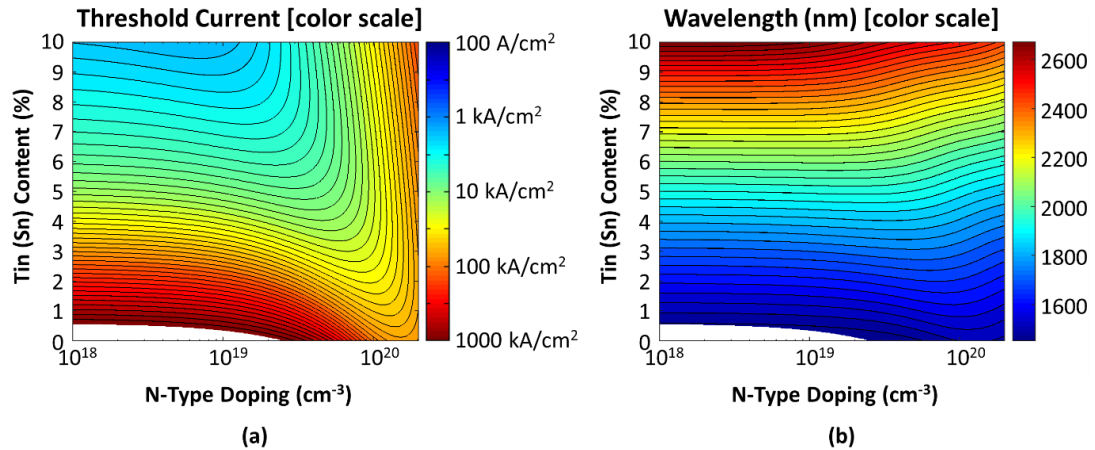


Figure 4-14. Threshold and wavelength vs. tin concentration and n-type doping. (a) Threshold current density of an unstrained double heterostructure germanium tin (Ge_xSn_{1-x}) laser (color scale) vs. tin (Sn) content and n-type doping. (b) Emission wavelength (color scale) vs. tin (Sn) content and n-type doping. GeSn thickness is assumed to be 300nm with an optical cavity loss of zero and a defect-limited minority carrier lifetime of $\tau_{SRH}=100ns$. The blank region in the bottom left corner is due to the cutoff of the simulation bounds, i.e. thresholds greater than 1000 kA/cm^3 .

The explanation for this discrepancy is that tin alloying does not cause any splitting or mixing of the valence bands. This splitting/mixing of the valence bands, which happens under both uniaxial and biaxial strain but not in unstrained germanium-tin alloys (e.g. Fig. 4-14), reduces the density of states at the top of the valence band and

therefore further reduces the threshold current. In addition, because the top valence band moves upward under valence band splitting which further reduces the bandgap, thus explaining the greater emission redshifts that occur under strain. A corollary of this absence of valence band splitting is that whereas both uniaxial and biaxial strains yielded two regimes, a low strain regime where strain is somewhat helpful and then a high strain regime where marginal strain suddenly becomes extremely helpful, no such two-regime behavior is observed for the case of tin alloying in Fig. 4-14. Furthermore, looking more closely at the threshold and wavelength response with tin alloying in Fig. 4-15 we observe that there is no kink or discontinuity in either the threshold or wavelength response, marking a major point of contrast compared to biaxial and uniaxial tensile strain.

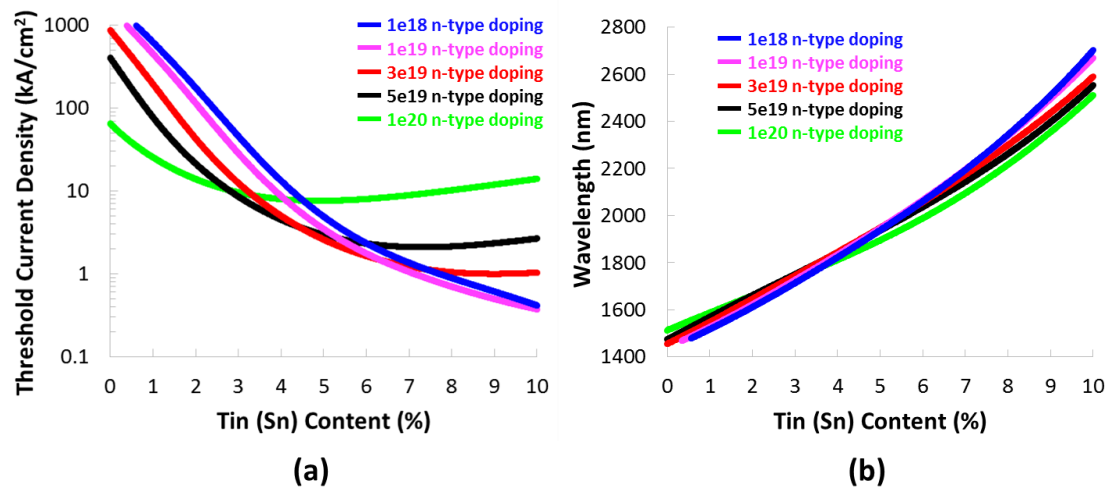


Figure 4-15. Threshold and wavelength vs. tin concentration for several doping conditions.

(a) Threshold current density of a germanium-tin (Ge_xSn_{1-x}) laser vs. tin (Sn) content for different doping conditions. (b) Emission wavelength of a germanium-tin (Ge_xSn_{1-x}) laser vs. tin (Sn) content for different doping conditions. In all cases a double

heterostructure design with a 300nm thick germanium-tin active region and a defect-limited minority carrier lifetime of $\tau_{SRH}=100ns$ is assumed.

4.4.3 Slope Efficiency

We can also model the slope efficiency of germanium-tin laser in Fig. 4-16. As was previously observed for the case of tensile strain, for germanium-tin lasers we need to introduce some out-coupling loss to the optical cavity in order to achieve a non-zero slope efficiency. However, while increasing the (non-parasitic) optical cavity loss improves the slope efficiency it worsens the threshold, and this tradeoff is shown more explicitly in Fig. 4-17. In most respects these results are qualitatively similar to those previously observed when modeling biaxially and uniaxially strained germanium lasers, except without the phenomenon of having two regimes, i.e. a low-strain regime and a high-strain regime. The key difference for germanium-tin is that we do not observe an “ultimate limit” for tin alloying even up to 10% tin, which is nearly 1.5x the amount of band engineering required to achieve a direct gap. (There may however be still be an ultimate limit due to effects not included in our model, particularly when the direct bandgap becomes almost exactly equal to the energy separation between the top valance band and the split-off band, as explained in Section 4.5.1.) In addition, the maximum achievable slope efficiency at 100 cm^{-1} optical cavity loss using tin alloying is about 30-40% which is considerably better than we found to be the case for biaxial strain but less than for uniaxial strain. The explanation for this phenomenon is that tin alloying causes less bandgap reduction and hence less emission redshift (Fig. 4-15(b)) than strain does (Fig. 3-13(b) & Fig. 4-6(b)). Because free carrier absorption increases

superlinearly with wavelength (Equation 3-7), thereby limiting the differential quantum efficiency (Equation 3-12) which is the limiting factor for slope efficiency (Fig. 3-20), this smaller redshift results in a major performance advantage for germanium-tin compared to biaxial strain. However, because tin alloying does not introduce valence band splitting the heavy hole (HH) band remains the top valence band which results in lower slope efficiency than for uniaxial strain where the light hole band dominates the hole population. As previously explained in Section 4.2.5, because the heavy hole (HH) band has a $\sim 21\times$ larger density of states than the light hole (LH) band based on the effective masses [108], and because the joint density of states for the Γ -HH transition is only about $\sim 2.1\times$ larger than the joint density of states for the Γ -LH transition (Equation 3-4 [116]), the heavy hole band introduces much more free carrier absorption relative to gain than the light hole band. Thus, we find that $\langle 100 \rangle$ uniaxial strain offers the best slope efficiency, tin alloying offers the second best slope efficiency, and biaxial strain is the least effective for improving slope efficiency, comparatively speaking.

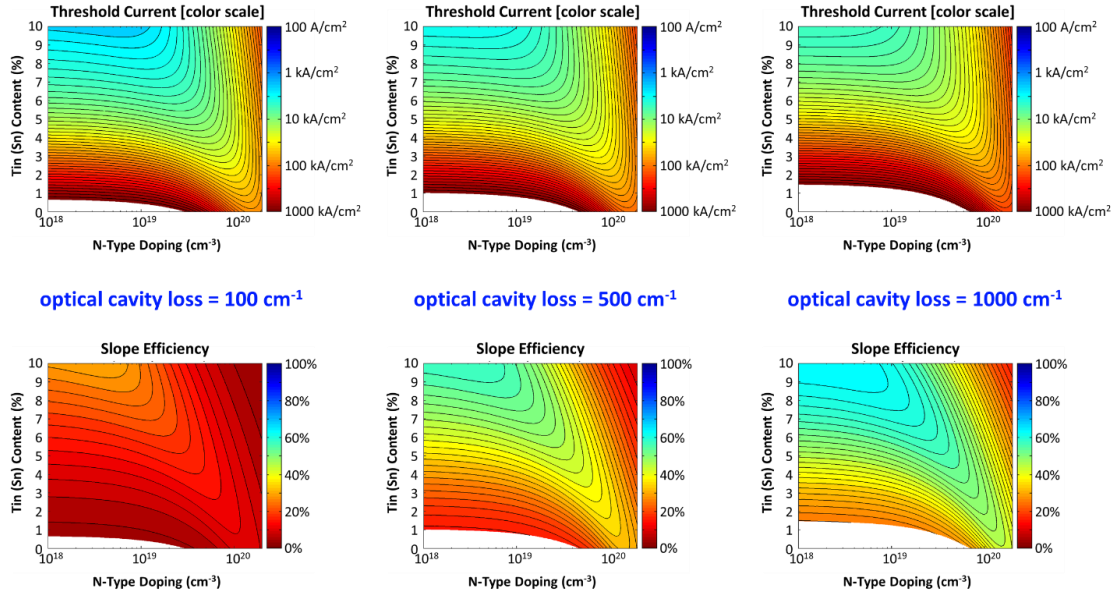


Figure 4-16. Threshold and slope efficiency vs. tin concentration and n-type doping for several optical cavity losses. Threshold current density (top) and slope efficiency (bottom) shown for optical cavity losses of 100 cm⁻¹ (left), 500 cm⁻¹ (middle) and 1000 cm⁻¹ (right). In all cases a double heterostructure design with a 300nm thick germanium tin (Ge_xSn_{1-x}) active region and $\tau_{SRH}=100ns$ is assumed. (Threshold and slope efficiency plots for an extended range of optical cavity loss values are available as Fig. A-5 in the Appendix.)

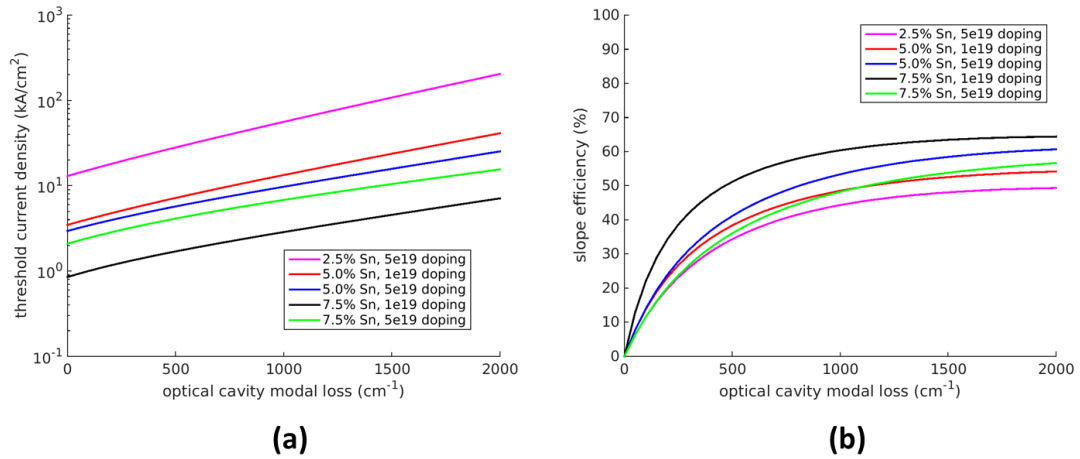


Figure 4-17. Threshold and slope efficiency vs. optical cavity loss for several combinations for tin content and doping. (a) Threshold current density vs. optical cavity loss, shown for several combinations of n-type doping and tin (Sn) content, (b) Slope efficiency vs. optical cavity loss, shown for several combinations of n-type doping and tin (Sn) content. In all cases a double heterostructure design with a 300nm thick germanium tin (Ge_xSn_{1-x}) active region and a defect-limited minority carrier lifetime of $\tau_{SRH}=100ns$ is assumed.

4.4.4 Interaction with Strain

A final point to consider for germanium tin is how tin alloying interacts with tensile strain with an eye toward tensile strained germanium tin lasers. Even in the context of electronics, researchers have expressed interested in combining tensile strain and tin alloying to realize the benefits of both techniques [86], [145]. However, it is not a given that any two techniques for enhancing germanium light emission can be combined in a useful manner. Both strain and tin alloying separately showed a negative interaction with n-type doping for instance: n-type doping offered comparatively smaller benefits in the presence of tensile strain and/or tin alloying. We

are therefore interested to know if there is any interaction between tensile strain and tin alloying in the context of germanium-based laser device and, if any interaction exists, whether the interaction is positive or negative. As shown in Fig. 4-18 we find that tensile strain and tin alloying can indeed be combined to achieve a very useful result and reduce the threshold by more than three orders of magnitude when combining 2% biaxial strain ($\langle 100 \rangle$ orientation) with 5% tin. If anything, we find that alloying with tin reduces the amount of strain needed to reach the “high strain” regime where outsized reductions in threshold become possible, as can be seen in both Fig. 4-18 and Fig. 4-19. We therefore conclude that tensile strain and tin alloying can indeed be effectively combined for a low threshold laser, i.e. a tensile strained germanium-tin laser.

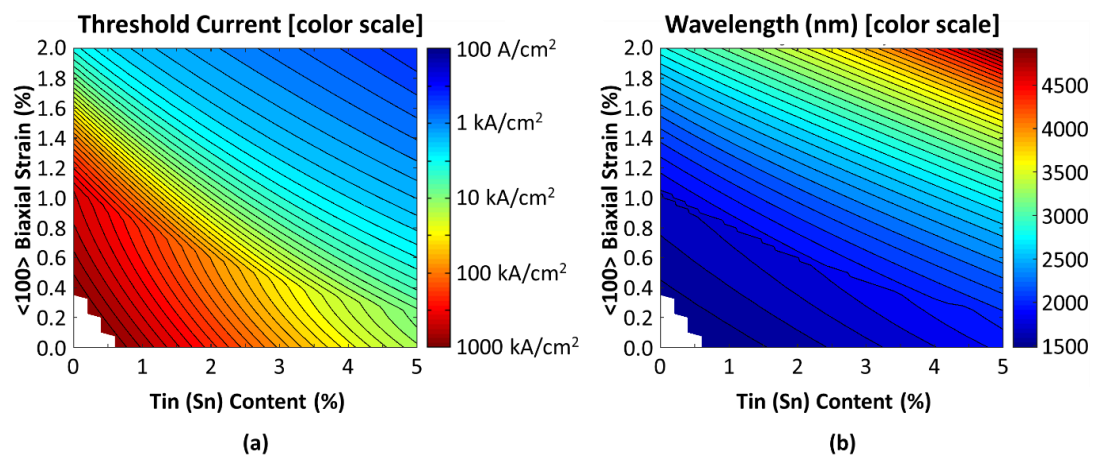


Figure 4-18. Threshold and wavelength vs. tin concentration and biaxial strain. (a) Threshold current density of a double heterostructure germanium tin ($\text{Ge}_x\text{Sn}_{1-x}$) laser (color scale) vs. $\langle 100 \rangle$ biaxial tensile strain and tin (Sn) content. (b) Emission wavelength (color scale) vs. $\langle 100 \rangle$ biaxial tensile strain and tin (Sn) content. GeSn thickness is assumed to be 300nm with

an optical cavity loss of zero, 1×10^{18} n-type doping, and a defect-limited minority carrier lifetime of $\tau_{SRH} = 100$ ns. The blank region in the bottom left corner is due to the cutoff of the simulation bounds, i.e. thresholds greater than 1000 kA/cm^2 .

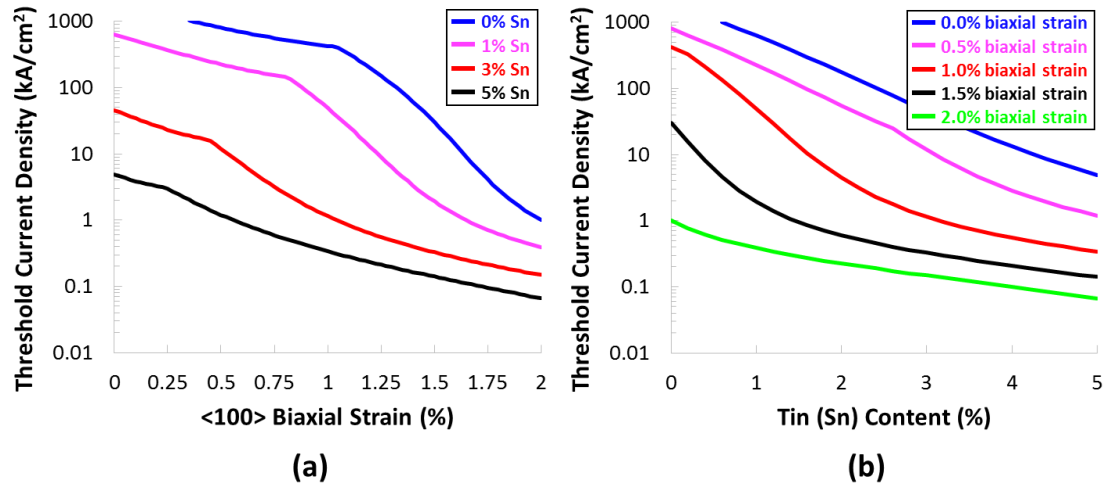


Figure 4-19. Comparison of biaxial strain and tin alloying with respect to threshold minimization. (a) Threshold current density of a germanium-tin laser vs. biaxial tensile strain (<100> orientation) for different amounts of tin alloying. (b) Emission wavelength of a germanium laser vs. biaxial tensile strain (<100> orientation) for different amounts of tin alloying. In all cases a double heterostructure design with a 300nm thick germanium active region, 1×10^{18} n-type doping, zero optical cavity loss, and a defect-limited minority carrier lifetime of $\tau_{SRH} = 100$ ns is assumed.

Having established that tensile strain and tin alloying can indeed be combined to achieve a low threshold germanium-based laser, the next question is whether or not such a combination would result in a useful slope efficiency. As shown in Fig. 4-20,

we find that combining tensile strain with tin alloying does indeed result in a useful slope efficiency. If anything, by comparing Fig. 4-20 with Fig. 3-16 we find that combining $\langle 100 \rangle$ biaxial strain with germanium tin, for instance a combination of 1.5% strain and 5% tin, allows for larger slope efficiencies than can be achieved using only biaxial strain. This is in line with our finding in Section 4.4.3 that tin alloying is typically superior for the purposes of maximizing slope efficiency. Interestingly, for the case of 5% tin we do observe an “ultimate limit” of about 1.5% biaxial strain whereupon increasing the strain further degrades the slope efficiency, indicating that tin alloying does have greater maximum potential than biaxial strain. Nevertheless, the overall finding is that comparatively large slope efficiencies are indeed possible when combining tensile strain with tin alloying, and thus a tensile strain germanium-tin laser is a very promising route to achieving both a low threshold and a reasonable slope efficiency.

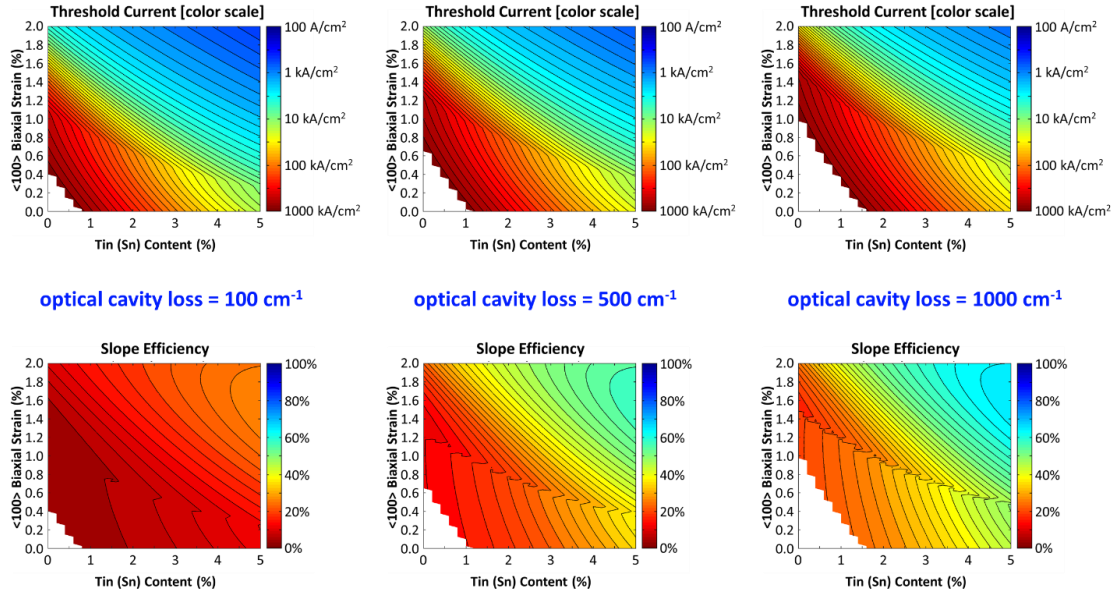


Figure 4-20. Threshold and slope efficiency vs. biaxial strain and tin concentration for several optical cavity loss values. Threshold current density (top) and slope efficiency (bottom) for a biaxially strained germanium-tin laser, shown for optical cavity losses of 100 cm⁻¹ (left), 500 cm⁻¹ (middle) and 1000 cm⁻¹ (right). In all cases a double heterostructure design with a 300nm thick germanium tin (Ge_xSn_{1-x}) active region with 1×10^{18} cm⁻³ n-type doping and $\tau_{SRH} = 100$ ns is assumed, with the biaxial strain oriented along the $\langle 100 \rangle$ axis. (Threshold and slope efficiency plots for an extended range of optical cavity loss values are available as Fig. A-6 in the Appendix.)

4.5 Limitations of the Model

4.5.1 Overview

In general, the uncertainties of our models for uniaxially strained germanium and for germanium-tin are the same as those described for the case of biaxial strain described in Section 3.5 of the preceding Chapter: uncertainties about precisely how much band

engineering is required to achieve a direct gap, and uncertainties about how band engineering affects a broad array of things such as the free carrier absorption equation (Equation 3-7), the recombination coefficients, the optical matrix element for the direct transition, etc. We also would again expect there to be “dead zones” of abruptly degraded laser performance for a few precise strain values where the direct bandgap is approximately equal to the energy separation between any pair of valence bands (heavy hole, light hole, split-off hole), an effect not accounted for in our models. A key difference in this Chapter, however, is that we have diverged from our previous approach of straightforward $sp^3d^5s^*$ tight-binding in favor of a deformation potential approach in order to model the bandstructures in the presence of uniaxial strains, the bandstructures for strains along different orientations, and the bandstructures of germanium-tin. There are therefore a few new uncertainties which arise for our models in this Chapter.

4.5.2 Tensile Strain Modeling (this Chapter Only)

For the case of strain modeling in Sections 4.2 and 4.3 of this Chapter, i.e. for modeling uniaxial strain and for strain along different orientations, we used deformation potentials with parabolic bands [39]. This introduces a new source of error in that non-parabolicities are not accounted for, which means that our model slightly underestimates the number of carriers required to push the electron quasi-Fermi level far enough above the L valley edge to “fill up” the indirect valleys. This makes our model slightly underestimate the lasing threshold, particularly for the low

strain case where non-parabolicities are more important, and overestimate how much n-type doping would be ideal. The use of deformation potentials also means that we have ignored how the effective masses change with strain; in reality tensile strain tends to decrease the relevant effective masses [137], [138] and hence reduce the density of states in all bands somewhat. This is therefore a beneficial effect that our model neglects, meaning that our model slightly underestimates the extent to which uniaxial tensile strain can improve the performance of a germanium laser.

A more pernicious omission for Section 4.2 is that using deformation potentials, as we have done, accounts for the splitting of the valence bands but not the complex mixing and warping of the valence bands under tensile strain. This limitation is inherent to any model that relies on deformation potentials with isotropic bands. While our model presumes that the light hole and heavy hole masses remain unchanged under strain, the reality is that the top two valence bands become a mix of light hole and heavy hole. Very roughly speaking, under sufficiently large biaxial or uniaxial tensile strain ($\langle 100 \rangle$ orientation) the top valence band will retain a heavy hole mass along the axis (or axes) of strain with a light hole mass along the other axis (or axes). The second valence band will then retain a light hole mass along the axis (or axes) of strain with a heavy hole mass along the other axis (or axes). Thus, under a large $\langle 100 \rangle$ biaxial tensile strain the top valence band is mostly heavy hole (since two axes are under strain) but has something resembling the light hole mass along the axis perpendicular to the strain plane (i.e. $\langle 100 \rangle$) with the converse being true for the second valence band [137], [138]; this mixing is fully accounted for in our tight-binding model of the preceding Chapter [53]. Meanwhile, under a large $\langle 100 \rangle$

uniaxial tensile strain the top valence band is mostly light hole (since only one axis is under strain) but nevertheless retains something resembling the heavy hole mass along the strain axis (i.e. $\langle 100 \rangle$) with the converse again being true for the second valence band [137], [138]; this effect is completely ignored in our modeling in Section 4.2. Qualitatively what this means is that uniaxial strain will be somewhat less useful than our model predicts because the density of states at the top of the valence band will not be reduced quite as dramatically. However, we have diligently investigated this issue by repeating our modeling and forcing the valence band masses to be mixed in the 2:1 ratio described above. Such a model, i.e. one that assumes full 2:1 mixing of the valence band masses, is more accurate for high strains where the mixing is very strong but less accurate for low strains where the mixing is virtually non-existent. Ultimately, such modeling showed extremely similar qualitative behavior, with a discontinuity rather than a kink separating the high strain and low strain regimes for $\langle 100 \rangle$ uniaxial tensile strain and, as a result, considerably better thresholds and slope efficiencies possible than for the case of $\langle 100 \rangle$ biaxial strain. Of course, none of these concerns are applicable to Section 4.3 which concerns itself solely with conduction band effects.

As a further note, although we explicitly do not consider quantum wells [128] in this work, there may be an unwanted effect from quantum wells in we expect quantum wells to lower the light hole band relative to the heavy hole band on account of their effective masses. This directly opposes the beneficial effect of raising the light hole band relative to the heavy hole band that results from $\langle 100 \rangle$ uniaxial tensile strain. This adds another layer to the complex question, discussed previously in Section 3.5.1,

of whether quantum wells will be helpful or harmful to the performance of a band engineered germanium laser.

4.5.3 Germanium-Tin Modeling

Our modeling for germanium-tin is much more similar to the tight-binding approach of the preceding Chapter, and in fact even reuses those same band structures. The only particular issue here is that the effective masses may be slightly off: our approach assumes that the conduction band masses change in the same way as biaxial tensile strain and that the valence band masses do not change at all. This has the likely effect of overestimating the valence band masses somewhat and underestimating the conduction band masses somewhat; both of these effects are insignificant compared to how the band edges move. There is of course an uncertainty regarding precisely how much tin is needed to achieve a direct gap [73], [82], [84], [86], [146], [147], but this is an inherently unavoidable issue and our model is in agreement with many published works [82], [84], [144]. Most importantly, similar modeling has been performed using empirical pseudopotentials [141], [148], i.e. using a completely different method of computing the bandstructure, and those works reached extremely similar conclusions with regard to how tin alloying can improve the performance of a germanium-based lasers [141] and also how tin alloying compares with $\langle 100 \rangle$ biaxial tensile strain [148].

4.6 Summary

In summary, we have extended the modeling of the preceding Chapter to several additional types of germanium band engineering such as uniaxial strain, strains along different orientations, and tin alloying. For strains along different orientations we find that uniaxial strains along $\langle 110 \rangle$ and $\langle 111 \rangle$ as well as biaxial strain along $\langle 111 \rangle$ are simply not usable for significantly enhancing light emission from germanium: applying large amounts of any of these particular strains would actually decrease the proportion of electrons in the direct conduction valley and therefore inhibit light emission from germanium. For biaxial strains although the $\langle 110 \rangle$ orientation does offer some utility we find that the $\langle 100 \rangle$ orientation, which we modeled in detail in the preceding Chapter, is by far the most promising route. This can broadly be taken to mean that the L-valley splitting that occurs under $\langle 110 \rangle$ and $\langle 111 \rangle$ strain is extremely harmful to light emission from germanium, and any experimental efforts on strain engineer should therefore focus on the $\langle 100 \rangle$ strain orientation.

We have also performed in-depth modeling of uniaxial strain ($\langle 100 \rangle$ orientation). This modeling suggests that uniaxial strain is even more effective than biaxial strain with respect to improving the performance of germanium lasers. This discrepancy can be attributed to the fact that under uniaxial tensile strain the top valence band retains a mostly light hole character whereas under biaxial tensile strain the top valence band retains a mostly heavy hole character. This means that uniaxial strain is dramatically more effective than biaxial strain at reducing the density of states at the top of the valence band. (As a side note quantum wells, which we do not explicitly consider in this work, may counteract this benefit somewhat by lowering the

light hole band relative to the heavy hole band). As a result, we find that the threshold drops much more dramatically with uniaxial strain than with biaxial strain, and uniaxial strain also unlocks much higher slope efficiencies too. As was the case for biaxial strain, we find that there is again an optimal doping that decreases with uniaxial strain, and so we find that combining heavy n-type doping [93], [149] with large tensile strain [23], [25] is not a winning proposition regarding of whether the strain is biaxial or uniaxial. Lastly, while for biaxial strain we found that there was a kink in the threshold response such that the performance enhancements from biaxial strain accelerate as the strain increases beyond ~1%, for uniaxial strain this is a discontinuity such that the threshold abruptly drops (and the slope efficiency abruptly increases) when the strain passes ~4%. Thus, while it is still important for to reach large strains for the biaxial case, it is even more imperative to employ a very large tensile strain for the uniaxial case since the performance enhancements are overwhelmingly determined by whether the uniaxial strain is above or below the critical value.

Lastly, we have extended our modeling to germanium-tin lasers. As expected, band engineering by means of tin alloying is qualitatively similar to band engineering by means of tensile strain. In both cases a very large reduction in threshold is possible and a negative interaction with n-type doping is observed. However, there are a few differences that arise from the lack of valence band splitting for the case of tin alloying. Firstly, whereas for tensile strain there were always two regimes, a high-strain regime and a low-strain regime with a kink or discontinuity at the boundary, for tin alloying there is only one regime and thus we find that the benefits from tin

alloying do not depend quite as disproportionately on realizing large tin concentrations. Another key effect from the lack of valence band splitting is that the bandgap does not shrink as much in the presence of tin alloying as it does in the presence of tensile strain. While this is important in its own right since the redshifts from band engineering are typically unwanted in that it moves germanium away from the 1550 nm operating wavelength that corresponds to the C-band communication window [50], [119], any redshift also directly impacts the laser performance since these redshifts exacerbate the free carrier absorption problem. Because tin alloying causes smaller redshifts, it is more helpful to the slope efficiency than biaxial strain. (However, tin alloying is not as beneficial to slope efficiency as uniaxial strain because such strains effectively get rid of the heavy hole band with its much larger density of states). As such, we find that whereas biaxial tensile strain would reach its “ultimate limit” for slope efficiency at approximately the same level as required to achieve a direct bandgap, tin alloying remains helpful to slope efficiency up to at least 10% tin which is ~50% more than is needed to achieve a direct gap. Thus, we find that germanium tin is more useful than biaxial strain for slope efficiency, but still less useful than uniaxial strain. In addition, we have investigated the interaction between biaxial tensile strain and tin alloying in the context of germanium lasing. Our findings indicate that, unlike the case for n-type doping, tensile strain and tin alloying can indeed be effectively combined to achieve dramatic improvements in laser performance. This raises the possibility of a tensile strained germanium-tin laser for low threshold high efficiency operation.

Chapter 5

Microbridge Structures for Extremely Large Uniaxial Tensile Strain and Single-Material Pseudo-Heterostructures

5.1 Overview

As explained in Chapter 2, there is an acute need for experimental techniques that induce the largest possible uniaxial tensile strain in germanium while maintaining full CMOS-compatibility. Previous research efforts have shown stress concentration approaches to be very promising in this regard, particularly the microbridge design [22], [150] illustrated in Fig. 5-1 which offers a simple and elegant fabrication process. However, in those previous efforts the maximum reported uniaxial strain was only about 3.1% [22]. In this Chapter we dramatically improve upon these previous microbridge efforts and present germanium wires, supported on silicon substrates, with uniaxial tensile strains as high as 5.7% along the $\langle 100 \rangle$ axis [23]. These wires were fabricated in a manner similar to the technique of Ref [22], but using high quality germanium-on-insulator (GOI) substrates with hyperbolic tapering of certain key features to increase the maximum achievable strain before material fracture. In addition, we will show that these structures constitute “pseudo-heterostructures” which allow us to create, within a single material, the carrier confinement needed for

efficient lasing at room temperature [24], [151]. Furthermore, our technique allows us to tune the band profiles with nanoscale precision using lithography such that dissimilar heterojunctions can be fabricated side-by-side in a simple mask process for unprecedented design flexibility [24], [151].

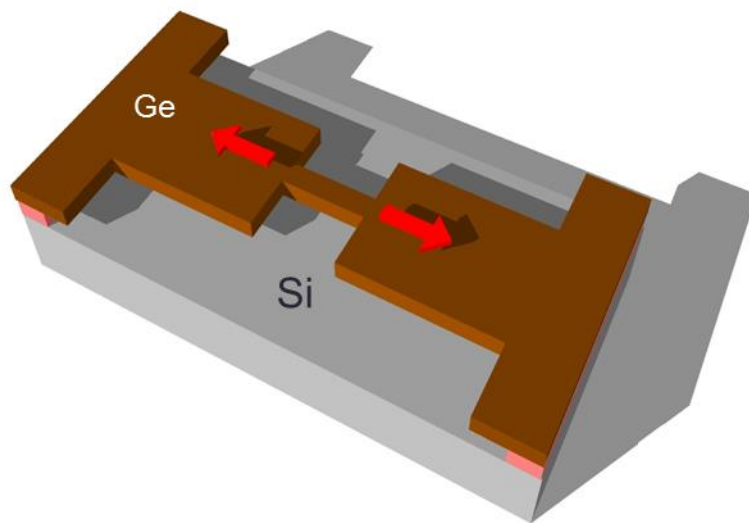


Figure 5-1. Schematic illustration of the microbridge structure used for uniaxial stress concentration. Brown is germanium, pink is silicon dioxide, grey is silicon, and red arrows indicate the tensile stress.

5.2 Microbridge Fabrication

5.2.1 Substrate Fabrication

To begin, a germanium-on-insulator (GOI) substrate is fabricated using the method of Ref [152]. The germanium was originally grown heteroepitaxially on silicon, which

results in baseline tensile strain of $\sim 0.2\%$ after cooling down from growth temperatures due to a mismatch of the thermal expansion coefficients [119] as illustrated in Fig. 5-2. This tensile strain remains after bonding onto a silicon/silicon-dioxide wafer to create the GOI substrate [24], [152]. The use of GOI provides substantial benefits over using germanium-on-silicon as in Ref [22] because, as illustrated in Fig. 5-3, the use of GOI eliminates the original germanium/silicon interface [152] which is known to be highly defective due to the lattice mismatch between germanium and silicon [153]. Not only is the material quality important from a carrier lifetime and device performance perspective [112], but material defects such as threading dislocations are known to reduce material strength and hence reduce the maximum achievable strain before material fracture [154]. We therefore hypothesize that the use of GOI is the key reason why we observe substantially more strain than other researchers who employed a similar technique [22].

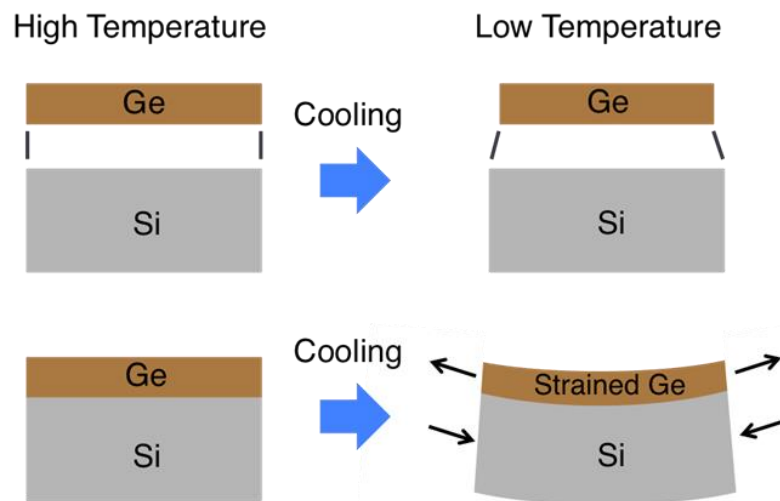


Figure 5-2. Schematic illustration of how the mismatch in thermal expansion coefficients between germanium (Ge) and silicon (Si) results in an initial tensile stress in the germanium

layer. Top: when cooling from the germanium growth/anneal temperature (~825°C [43], [61], [155]) to room temperature the germanium layer would, if freestanding and unattached, shrink by a larger ratio than the silicon layer. Bottom: if the germanium is instead attached to the large silicon substrate the result after cooling to room temperature is that a tensile stress is imparted to the thin germanium layer, while a negligibly small compressive stress is imparted to the thick silicon substrate to compensate.

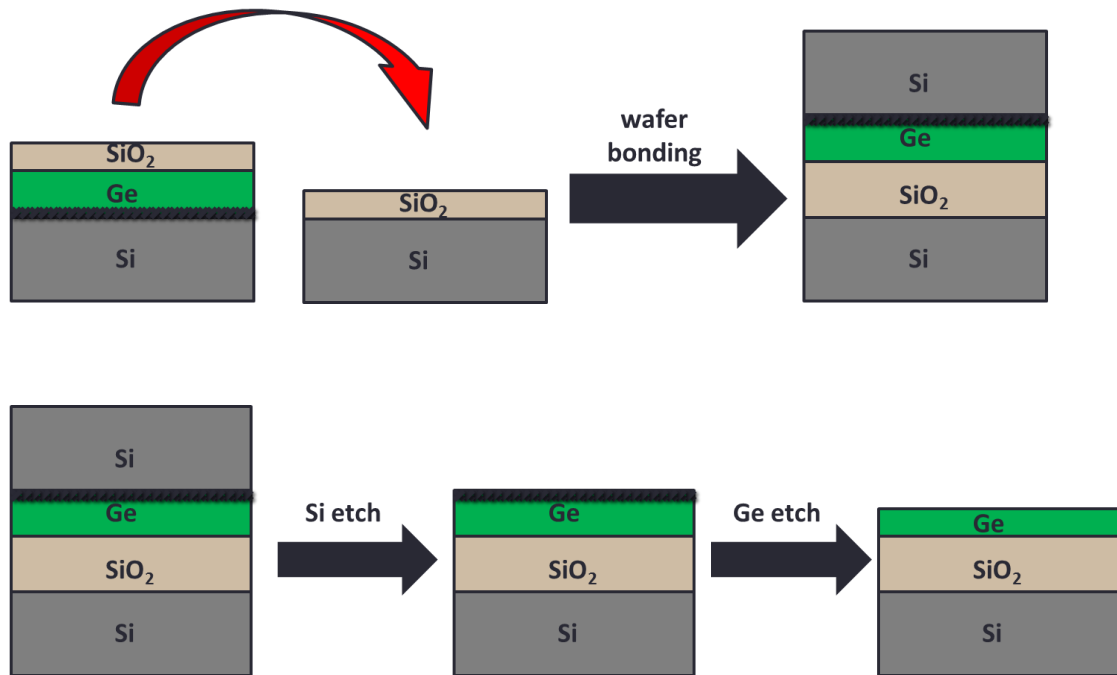


Figure 5-3. Process flow of the germanium-on-insulator (GOI) fabrication process, showing how the defective layer near the initial silicon/germanium interface is physically removed. Grey is silicon (Si), beige is silicon dioxide (SiO_2), and green is germanium (Ge). Defects are indicated as the black region near the germanium/silicon interface. Top: the initial Si/Ge/ SiO_2 substrate is flipped over and bonded to a Si/ SiO_2 substrate, given a material stack of Si/ SiO_2 /Ge/Si with the defects now at the top of the germanium layer. Bottom: the top silicon region is physically wet etched away in tetramethylammonium hydroxide (TMAH) solution,

leaving the defective region now exposed at the top surface where it is subsequently removed by a partial germanium wet etch in aluminum etchant. [156]

5.2.2 Patterning the Structure

Using this GOI, a pad and nanowire geometry similar to the microbridges of Refs [22], [24] was patterned using e-beam lithography and dry etching in SF₆ and CHClF₂ (Freon-22) plasma [23]. The underlying oxide was then etched in HF vapor, releasing the structure to give a suspended germanium wire attached on either side to suspended germanium pads as shown in Fig. 5-4(a). Typical wire dimensions were ~4.5 μm x ~200 nm, as shown in Fig. 5-4(b). Once the entire structure is released the initial ~0.2% tensile strain redistributes such that the germanium pads relax slightly while the strain in the germanium wire increases, as confirmed by COMSOL finite element method modeling in Fig. 5-4(c).

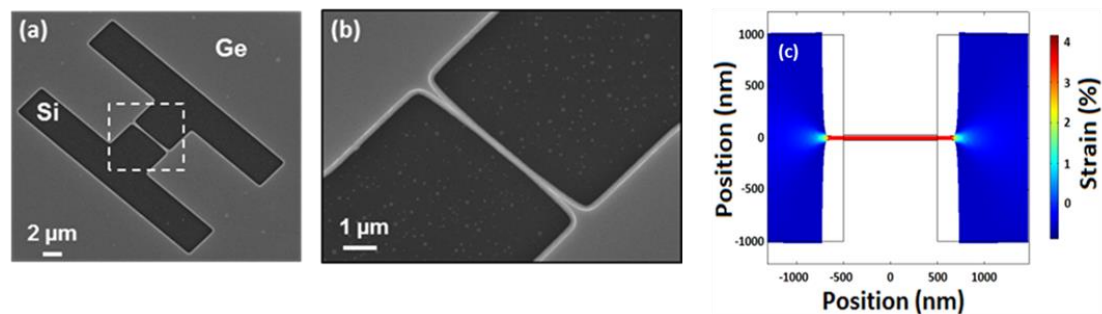


Figure 5-4. Micrographs and mechanical simulations of fabricated microbridge structures.

(a) Scanning electron micrograph (SEM) of a suspended strained germanium wire attached to suspended germanium pads. (b) Zoomed-in SEM of the region indicated in Fig. (a). (c) COMSOL simulation of the strain distribution in a suspended germanium wire attached to suspended germanium pads. [23]

5.2.3 Substrate-Adhered Geometries via Stiction for Improved Heat Sinking

While using HF vapor etch successfully yields a suspended germanium wire under high tensile strain, this suspended geometry results in poor thermal conduction since there is no direct heat conduction path from the wire to the substrate. We have since shown that replacing the HF vapor etch of the underlying oxide with a liquid HF etch induces post-release stiction that adheres the germanium wire and pads to the substrate [60], as shown in Fig. 5-5. This change does not reduce the strain induced in the wire – if anything we would expect this to increase the strain slightly but the release layer is so thin that the resulting change is typically too negligible to observe. However, placing the germanium wire in thermal contact with the substrate creates an efficient heat conduction path, which in turn drastically reduces any heating effects while maintaining the desired strain distribution [60].

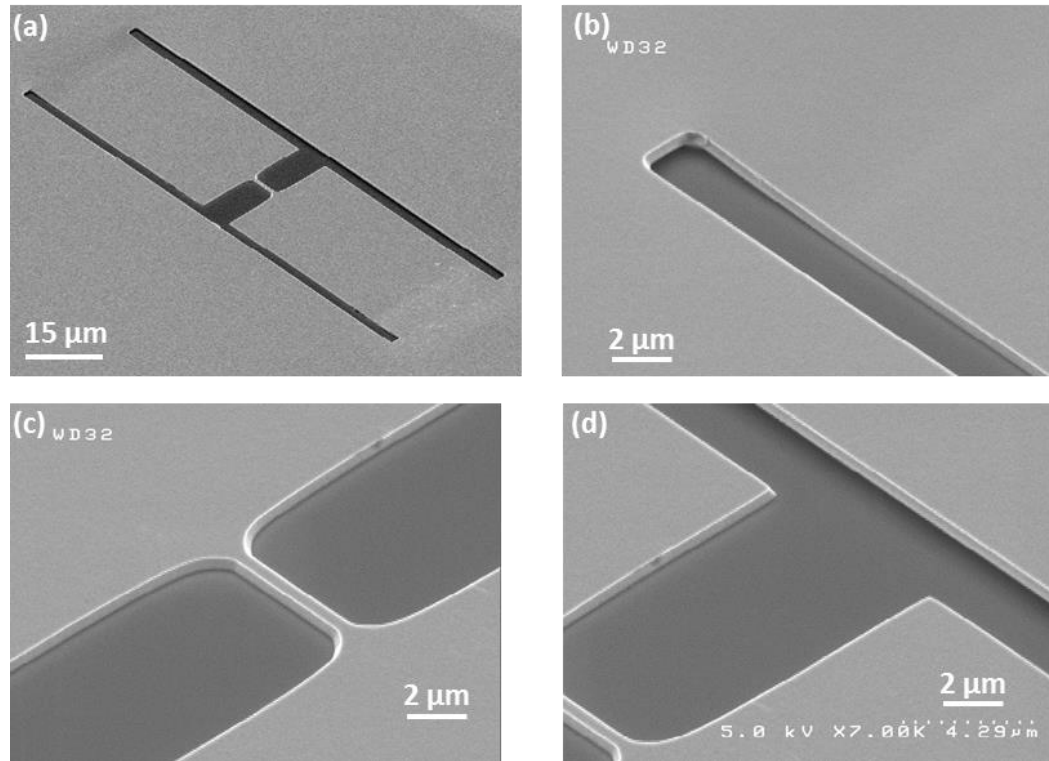


Figure 5-5. Micrographs confirming adhesion between a microbridge and the underlying substrate by stiction. (a) Tilted scanning electron micrograph (SEM) of a substrate-adhered strained germanium wire and pads. (b) Zoomed-in tilted SEM of the edge of a pad, showing deflection due to stiction. (c) Zoomed-in tilted SEM of the substrate-adhered germanium wire. (d) Zoomed-in tilted SEM showing of a substrate-adhered germanium wire and pads next to an overhang of suspended germanium. [23]

5.3 Characterization

5.3.1 Raman Spectroscopy

The strain in the fabricated germanium wires was experimentally determined using Raman spectroscopy. Under tensile strain, the Raman peak of 301 cm^{-1} for relaxed germanium becomes redshifted to shorter wavenumbers: every 1% $\langle 100 \rangle$ uniaxial tensile strain redshifts the Raman peak by 1.52 cm^{-1} [22], [157]. (As a side note, and

as previously explained in Ref [23], using this strain-shift coefficient of 1.52 cm^{-1} for $\langle 100 \rangle$ uniaxial strain corrects two previous works, namely Refs [24] and [156], where the wrong coefficient was used. As a result of that error, all $\langle 100 \rangle$ uniaxial strains in Refs [24] and [156] were underreported by $\sim 25\%$.) For all of our Raman measurements we used a 514nm wavelength excitation laser which limits our strain measurements to the sample's top surface. However, we can safely assume that the strain was uniform along the vertical axis because our suspended structures showed no vertical deflections (a hallmark of vertical strain gradients) and also because finite element method COMSOL simulations indicated that no vertical strain gradients were to be expected.

While the strain is a simple linear function of the Raman peak redshift, care must be taken to ensure that no significant heating occurs due to the excitation laser since temperature increases are also known to redshift the Raman peak. It is therefore critical to ensure that any observed Raman redshift corresponds to tensile strain rather than heating effects [157]. To this end, we have measured how the Raman peaks of both a suspended and a substrate-adhered germanium wire change with the Raman excitation laser power, as shown in Fig. 5-6. These wires had nominally identical dimensions and both exhibited approximately $\sim 4\%$ strain based on the observed Raman shifts of about $5.9\text{-}6.2 \text{ cm}^{-1}$ as shown in Fig. 5-6. Note that while there is a slight difference in the observed strain at low power this discrepancy can be readily explained by the fact that each sample was fabricated in a separate run. The amount of lateral underetching at the pad boundaries varied slightly from one run to another and this lateral underetching distance noticeably affects the strain in the wire [150]. This,

coupled with the uncertainty resulting directly from the Raman measurement and fitting, easily explains the small observed discrepancy. In reality this stiction has a negligible impact on the strain distribution because the thickness of the sacrificial layer is very small compared to the total device diameter and this was apparent over a larger informal sample of structures.

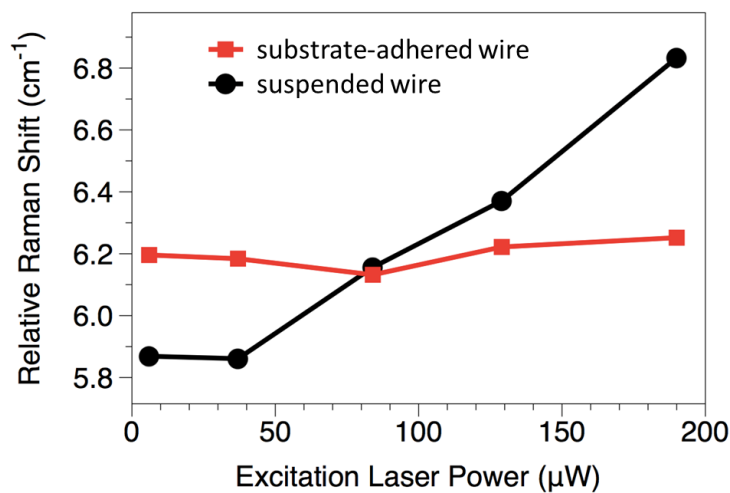


Figure 5-6. Dependence of the Raman peak redshift on the excitation laser power for both suspended and substrate-adhered germanium wires with $\sim 4\%$ strain. Both curves are the difference between the wire's Raman peak location and the Raman peak location of relaxed bulk germanium. [23]

It is clear from Fig. 5-6 that Raman excitation laser powers below $\sim 40 \mu\text{W}$ produce no significant heating effect in our suspended germanium wires. A laser excitation power of $\sim 6 \mu\text{W}$ was therefore used in all subsequent Raman measurements, which is a factor of ~ 6.5 less than the maximum acceptable excitation power to avoid heating effects. Due to time constraints and competing research priorities, we have yet to fabricate

substrate-adhered wires with more than the ~4% strain shown in Fig. 5-6. However, our work on suspended wires is more mature and we have observed substantially larger strains in these wires. Raman spectra of suspended wires with varying pad dimensions, shown in Fig. 5-7, reveal Raman peak locations as low as 292.37 cm^{-1} , compared to the Raman peak of 301.05 cm^{-1} for relaxed germanium. The observed redshifts of up to 8.68 cm^{-1} of the Raman peak correspond to uniaxial strains of up to 5.71% using the 152 cm^{-1} Raman strain-shift coefficient [22], [157]. According to the deformation potentials for germanium [39], this largest observed strain of 5.71% corresponds to a direct bandgap of 0.369 eV and an indirect bandgap of 0.403 eV. This means that the bandgap of this 5.71%-strained germanium wire is direct.

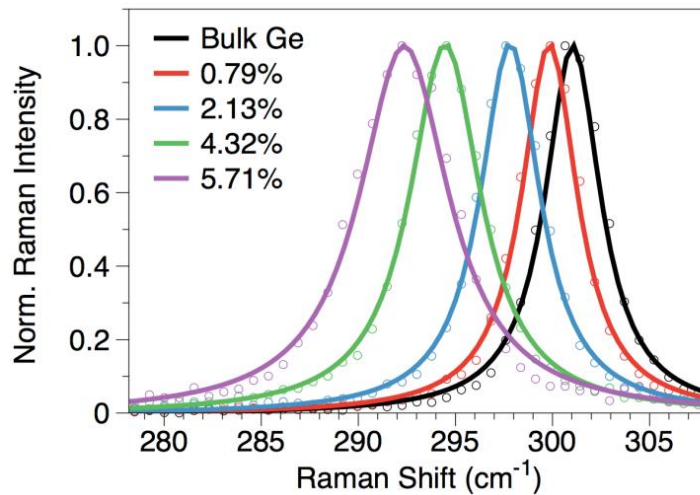


Figure 5-7. Raman spectra for suspended germanium wires with various pad dimensions, showing uniaxial strains from 0.79% to 5.71%. [23]

5.3.2 Photoluminescence

We have also characterized our samples using photoluminescence (PL) measurements with a 532 nm pump wavelength operated at a power of 20 mW for substrated-adhered samples. This excitation power was low enough to preclude any significant heating effects in our substrate-adhered structures due to the extremely effective heat sinking providing by the silicon substrate. The lowest possible PL power was used when measuring suspended structures. Germanium's optical absorption length at this pump wavelength is only ~20 nm deep, indicating that carriers are only generated within the top ~20 nm of the sample, whereas the thickness of all our samples in this dissertation was approximately 500 nm. However, the diffusion length our germanium is several microns (as will be experimentally confirmed later in Fig. 5-11) and so all of the photogenerated carriers will diffuse very quickly along the vertical axis. As a result, we expect the carrier density to be approximately uniform along the vertical axis before any substantial the recombination can take place, and hence our PL measurements can be considered as measurements of uniformly excited germanium. The relative contributions of surface recombination and bulk recombination in these germanium samples has been discussed by research collaborators in a separate work [112].

In terms of optical properties, PL measurements on the suspended wires confirm that strain causes both a redshift of the emission wavelength due to the bandgap reduction and an enhancement of the PL intensity due to increased occupation of the direct conduction valley, as shown in Fig. 5-8. In fact, the PL intensity enhancement with strain is actually greater than the theoretical predictions of

Fig. 4-2 in the preceding Chapter due to pseudo-heterostructure effects [24] between the pads and the wires as will be explained in Section 5.4. This redshift and enhancement of the PL confirms that the strain is indeed affecting germanium's optical properties as expected.

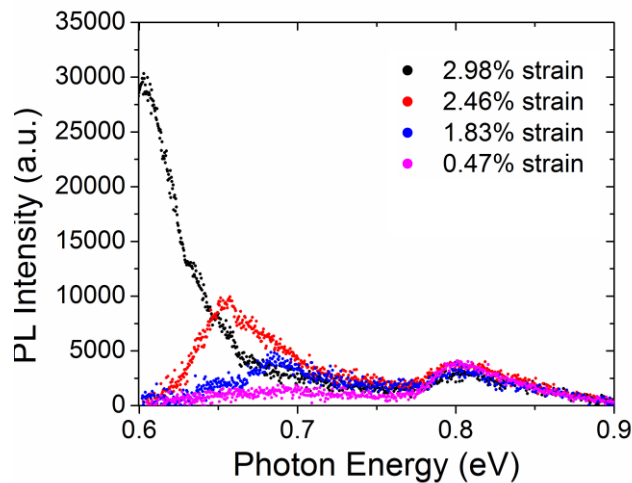


Figure 5-8 Photoluminescence from suspended germanium wires with various strains. The peak near 0.8 eV represents emission from the unstrained pad regions and is therefore invariant with the measured strain in the nanowire. PL on suspended wires used the lowest possible excitation power due to the poor heat sinking associated with suspended geometries. [23]

Due to the limitations of our detection setup, PL from wires with strains beyond ~3% could not be measured because the emission was redshifted beyond the detector cutoff of ~2060 nm (0.6eV photon energy) in our micro-PL setup. From Fig. 5-8 it is clear that even the 2.98% strained wire has been largely redshifted beyond this detection limit. Since only germanium wires with >4.6% strain have a direct bandgap, no optical

measurements were possible on our direct bandgap germanium samples. We must therefore reserve such measurements for a future work.

5.4 Pseudo-Heterostructures

While these highly strained wires are indeed desirable because of how uniaxial strain improves germanium's optical properties, there is an additional utility that results from the fact that the highly strained wire is connected to germanium pad regions that are essentially relaxed. As has been discussed in-depth in a previous dissertation [61], these microbridge structures actually recreate the electronic band profiles of traditional semiconductor double-heterostructure but within a single material. Semiconductor heterostructures are an indispensable part of modern photonics, in particular semiconductor lasers [128], [158]. However, creating semiconductor heterostructures typically involves vertical heteroepitaxy of multiple materials [158], drastically limiting the number of dissimilar heterojunctions that can be fabricated on a single wafer. Here we bypass this limitation by creating pseudo-heterostructures that are homo-compositional but whose electronic band profiles and behavior are indistinguishable from traditional multi-material double heterostructures. This is achieved within our microbridge structures because they employ a lithographically-determined tensile strain to selectively and controllably narrow the bandgap in a highly localized region of a single semiconductor [24], namely germanium in this work. If we consider the axis of the nanowire, indicated by a dotted green line in Fig. 5-9(a) [156], we have a region of tensile strained germanium (the nanowire) sandwiched between two regions of relaxed germanium (the pads). From Fig. 4-1 in

the preceding Chapter, we know that the tensile strained region will have a smaller bandgap than the relaxed regions. Thus, if we draw the band diagram along the axis of the nanowire, shown in Fig. 5-9(b) [151], the result is unmistakably the band profile of a double heterostructure.

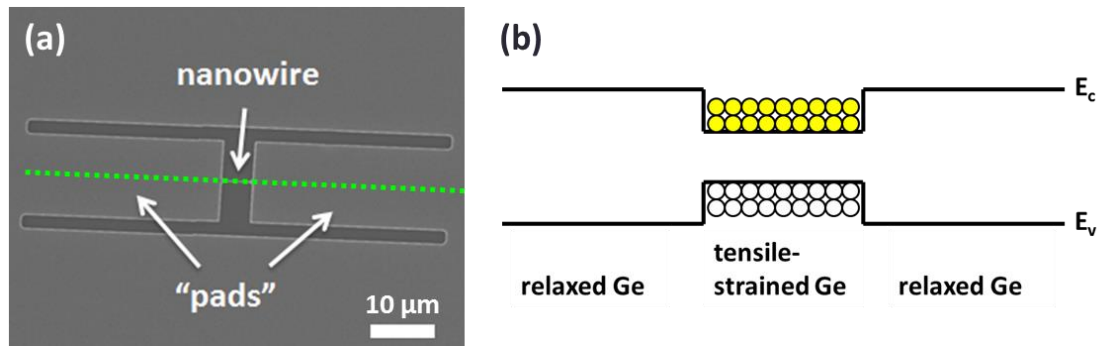


Figure 5-9. Illustration of the pseudo-heterostructure. (a) The axis of the pseudo-heterostructure, indicated as a dotted green line, (b) illustrated of the band diagram along the axis of the pseudo-heterostructure, showing electrons (yellow circles) and holes (empty circles) being confined in the region of highly strained germanium (Ge).

In addition, arbitrary well shapes can be created by considering the fact that the strain in any cross-section of the structure will, to first order, be inversely proportional to the width of that cross-section. For an abrupt double heterostructure this is simple: we simply fabricate an abrupt microbridge as shown in the scanning electron micrograph of Fig. 5-10(a). The resulting strain distribution therefore involves an abrupt increase in the nanowire relative to the pads, as shown in the Raman area scan of Fig. 5-10(b). Because the strain changes abruptly, so too does the band diagram exhibit an abrupt change as illustrated in Fig. 5-10(c). For graded heterostructures it is only slightly more complicated to compute the necessary geometry: one must simply add a taper

between the pads and the nanowire, and the width of this taper must vary with the reciprocal of the intended strain distribution. For the example of a linearly graded heterostructure we require a linearly varying strain between the barriers (pads) and the potential well (nanowire). Since the reciprocal of a linear function is a hyperbolic function, we have fabricated a microbridge with a hyperbolic taper between the pads and the nanowire as shown in the scanning electron micrograph of Fig. 5-10(d). A Raman area scan, shown in Fig. 5-10(e), experimentally confirms that the resulting strain distribution is indeed linear, and thus we have a linearly graded heterostructure as illustrated in Fig. 5-10(f). Naturally, the abrupt and linearly graded heterostructures shown in Fig. 5-10 are only two examples of the possible designs and much more complex band profiles can be realized with relative ease: it is possible to create essentially arbitrary heterostructures using our technique. For heterostructures in which the band profiles are to be graded in a more complex manner, for instance in the case of a graded index separation and confinement heterostructure “GRINSCH” laser [159], the required taper dimensions are again determined by simply having the taper width vary as the reciprocal of the desired strain distribution.

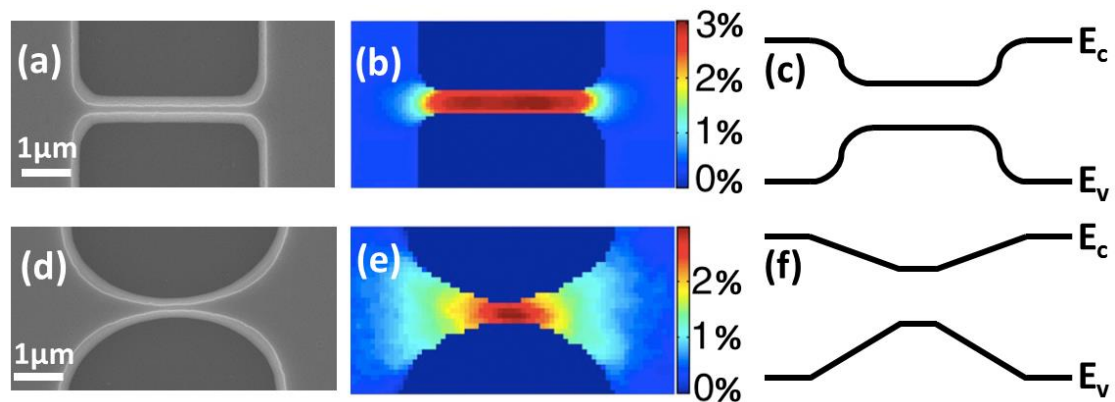


Figure 5-10. Abrupt and graded pseudo-heterostructures. (a) Zoomed-in SEM of an abrupt pseudo-heterostructure. (b) Uniaxial strain distribution of an abrupt pseudo-heterostructure from Raman spectroscopy. (c) Approximate band diagram for an abrupt pseudo-heterostructure. (d) Zoomed-in SEM of a linearly-graded pseudo-heterostructure. (e) Uniaxial strain distribution of a linearly-graded pseudo-heterostructure from Raman spectroscopy. (f) Approximate band diagram for a linearly-graded pseudo-heterostructure. [151]

As explained in Section 5.3.1 and shown in Fig. 5-7, a uniaxial strain of up to 5.71% was observed. Using the deformation potentials of [39], these strains correspond to a bandgap as low as 0.369 eV in the germanium potential well, considerably less than the 0.667 eV bandgap in the relaxed pad regions. This bandgap reduction of nearly 300 meV in the potential well is much larger than the thermal energy kT (~ 26 meV) and thus more than sufficient for room-temperature carrier confinement. Further investigation using a self-consistent Poisson solver to compute the precise band bending in such structures confirms that the energy barrier for electrons and the energy barriers for holes are both well above the thermal energy kT [24]. In fact, due to a very strong tendency for the bands to tend toward charge neutrality, the total bandgap reduction in the potential well is nearly evenly split between providing an energy barrier to electrons and providing an energy barrier to holes, further reinforcing the theoretical suitability of these pseudo-heterostructures for strong and effective carrier confinement at room temperature [24].

In addition to the above theoretical investigation, we also present compelling experimental evidence in the form of room-temperature micro-photoluminescence

(micro-PL) measurements which confirm that these pseudo-heterostructures are capable of room-temperature carrier confinement just like traditional multi-material heterostructures. As shown in Fig. 5-11 for a nanowire under 2.98% strain, there is always a strong signal from the highly-strained nanowire, even when the excitation spot is more than 20 μm away from the nanowire. This means that carriers diffusing away from the excitation spot are captured and confined in the potential well even at room temperature. The wavelength of the photoluminescence emission also confirms a localized bandgap reduction with strain. As shown in Fig. 5-8, applying strain up to 2.98% redshifts the nanowire emission from ~ 0.8 eV (~ 1550 nm) to the detector cutoff of ~ 0.6 eV (~ 2070 nm), a ~ 500 nm range. This pseudo-heterostructure platform may therefore be suitable for accessing a greater range of optical wavelengths than would normally be possible on a single wafer.

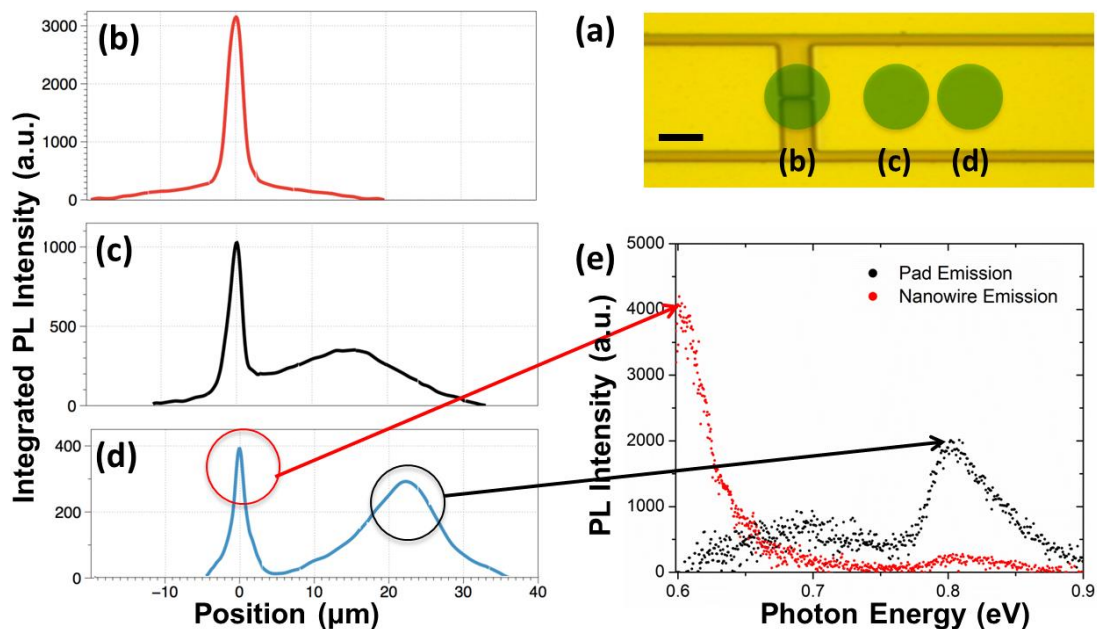


Figure 5-11. Experimental observation of room temperature carrier confinement within a pseudo-heterostructure. Counter-clockwise from top-right: (a) Optical micrograph of

nanowire and pad barriers for the 2.98% strain case, with green circles indicating approximate excitation locations. Scale bar, 5 μm . (b-d) Integrated PL as a function of position along the pseudo-heterostructure for (b) excitation directly at the nanowire, (c) excitation $\sim 15 \mu\text{m}$ away from the nanowire, and (d) excitation $\sim 22 \mu\text{m}$ away from the nanowire. (e) PL spectra for excitation $\sim 22 \mu\text{m}$ away from the nanowire, measured at the nanowire itself (black) and near the excitation location in the pad (red). [151]

While this work has focused exclusively on Ge, the pseudo-heterostructure approach can be readily applied to any arbitrary semiconductor with an initial tensile stress. Lithographically controlled strain amplification has already been demonstrated in suspended silicon for instance [150]. For the case of other semiconductors, the range of accessible bandgaps would be solely a function of that semiconductor's deformation potentials and the maximum strain that can be realized before material fracture. By enabling arbitrary strain distributions to be precisely tailored by lithography, this platform enables a new degree of freedom for photonic device integration by allowing band profiles to be strongly customized from one device to another on the same die, with sufficient carrier confinement for room temperature operation. Potential applications include expanded wavelength-division multiplexing by accessing a wider range of bandgaps, and reduced-cost lateral-injection lasers by removing expensive heteroepitaxy process steps.

5.5 Summary and Discussion

By employing germanium-on-insulator (GOI) substrates we have achieved a record $\langle 100 \rangle$ uniaxial tensile strain of 5.7% in suspended germanium wires. Since 4.6% strain is believed to transform germanium into a direct bandgap semiconductor [39] as indicated in Fig. 4-1 in the preceding Chapter, these highly strained germanium wires represent a direct bandgap Group IV semiconductor integrated on silicon. This strain was measured by Raman spectroscopy, and great care was taken to ensure that the observed Raman shifts were not due to heating effects. Micro-photoluminescence (PL) measurements confirmed that the germanium wires with strains up to $\sim 3\%$ exhibited enhanced and redshifted emission as expected due to the lowering of the direct conduction valley relative to the indirect valley and the overall bandgap narrowing. Germanium wires with $>3\%$ strain are also expected to show continued redshifts and enhancements of the PL, however for strains beyond $\sim 3\%$ the PL emission is redshifted beyond our present detection capabilities. Optical measurements on our most highly-strained germanium wires, including those with $>4.6\%$ strain which we infer to have a direct bandgap, must therefore be reserved for future efforts.

In addition to achieving the highest CMOS-compatible uniaxial tensile strain even reported in germanium, we have also introduced an entirely new paradigm for creating heterostructures without the expense or complexity of multi-material heteroepitaxy. We have shown experimental evidence of strong carrier confinement in our pseudo-heterostructures and theoretical calculations indicate that we have realized band offsets well in excess of the thermal energy kT at room temperature.

Furthermore, our technique makes it possible to create arbitrary band profiles, whether

abrupt or graded, with nanoscale precision by simply choosing the correct lithographic dimensions for the desired result. Moreover, because the band profiles are lithographically determined, it is trivial to create any number of unique heterojunctions side-by-side on the same die using a simple one mask process.

Chapter 6

Etched Microdisk Structures for Large Biaxial

Tensile Strain

6.1 Overview

In the previous Chapter we presented very substantial advances in realizing large uniaxial strains in germanium using nanowire and micro-bridge structures, including a maximum reported uniaxial strain of 5.7% along the $\langle 100 \rangle$ axis which represents direct bandgap germanium-on-silicon [23]. In this Chapter we will present analogous advances in biaxially strained germanium-on-silicon. This is important because biaxial strain is best suited to the radial symmetry of microdisk and microgear resonators which combine high Q factors and compact form factors. While researchers have been actively pursuing ways of inducing large biaxial strains in germanium, these previous approaches were typically not CMOS-compatible [62], [63], [160] or else would hinder the final laser cavity design due to issues such as strain inhomogeneities [57], [102], out-of-plane deflections [71], [72], [161], and/or metals that would introduce large optical losses [71]. Very recently, researchers have demonstrated a biaxial strain technique which could in principle become CMOS-compatible [64], but at present that technique still involves III-V materials and large quantities of gold in the fabrication process. There was therefore a need for a CMOS-compatible structure that induces large homogeneous biaxial tensile strains in germanium-on-silicon that can truly be an

effective platform for germanium lasers. Here we present such a structure, illustrated conceptually in Fig. 6-1, which concentrates and amplifies a small pre-existing strain biaxially, and we report experimentally measured biaxial tensile strains up to 1.11% using this structure [25]. Our structure consists of an ultrathin germanium disk with several slits etched in a radially symmetric pattern as shown in the simplified schematic of Fig. 6-1(a) which helps visualize the stress concentration process intuitively. As shown in the finite element method mechanical modeling of Fig. 6-1(b), which will be explored in greater detail in Section 6.3, etching this pattern of slits concentrates the initial strain into the central microdisk region where it is localized and amplified to a larger value. This strain can be conveniently customized from one device to another by lithographically modifying the dimensions of each structure, thereby allowing multiple strains – and therefore multiple bandgaps – to be realized across a single wafer in a simple one-mask process [25].

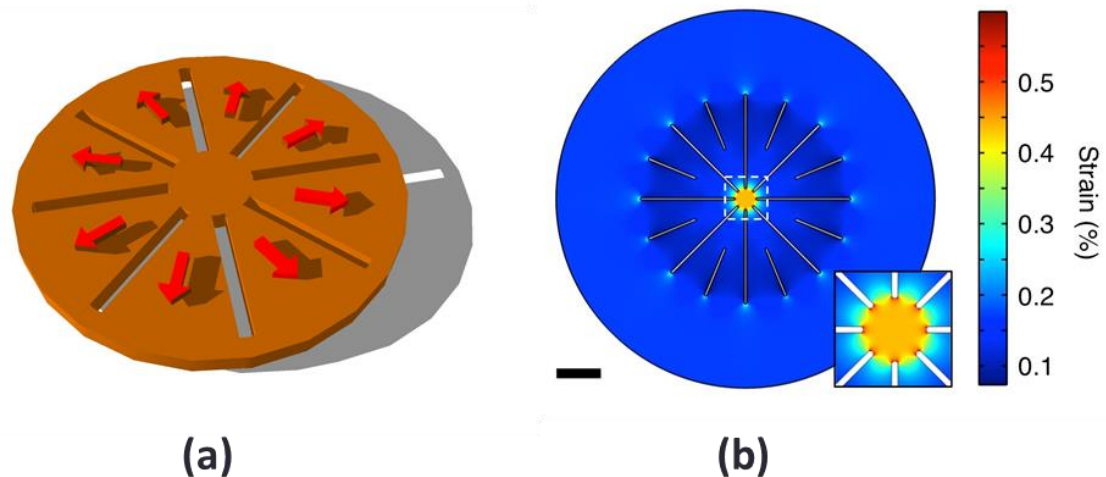


Figure 6-1. Overview of the proposed stress concentrating microdisk structure. (a) Conceptual illustration of the proposed microdisk structure to be employed for stress

concentration. The structure consists of several radially symmetric slits emanating outward from a circular central region. (b) Biaxial strain distribution in the disk structures as computed by finite element method (FEM) COMSOL simulations for the case of a 5 μm inner microdisk diameter and a 50 μm outer (total) diameter, with 20 μm of lateral under-etching. Scale bar, 10 μm . Inset: Zoomed-in view of the central region. [25]

6.2 Microdisk Fabrication

To begin, a Si/SiO₂/Ge substrate was created by wafer bonding a 0.2% strained germanium layer onto an Si/SiO₂ substrate using the technique of Ref [112] as illustrated in Fig. 6-2(a). This approach results in very high quality germanium and the 0.2% strain remains after wafer bonding [112]. Then, using electron-beam lithography and anisotropic dry etching, the top germanium layer of our Si/SiO₂/Ge substrate is patterned into a disk with many slits as shown in Fig. 6-2(b-c). Finally, during the last fabrication step, the oxide from the material stack is removed using a wet etch in liquid hydrofluoric acid. Toward the end of this step, after the oxide has been fully etched away but while the sample is still immersed in the liquid etchant, there is a very brief moment where the germanium layer is suspended. During this brief moment where the germanium is suspended, the small pre-existing tensile stress redistributes and concentrates in the microdisk at the center of each structure. The small microdisks with diameters of 5.0-7.5 μm therefore become very highly strained, while most of the remaining germanium in the structure relaxes somewhat to compensate. During the removal of this final liquid hydrofluoric acid etchant, each entire structure was deflected downward by capillary forces and then permanently adhered to the

underlying silicon substrate by stiction [60] as described in Section 5.2.3 in the preceding Chapter. This permanent downward deflection due to stiction is illustrated in the cross-section schematic of Fig. 6-2(d) and is evidenced experimentally in the measured surface profile of the fabricated structure shown in Fig. 6-3. The stiction has a negligible impact on the strain distribution because the thickness of the sacrificial layer is very small compared to the total device diameter. Having now successfully completed the microdisk fabrication, top-view micrographs showing the resulting structure are provided in Fig. 6-3.

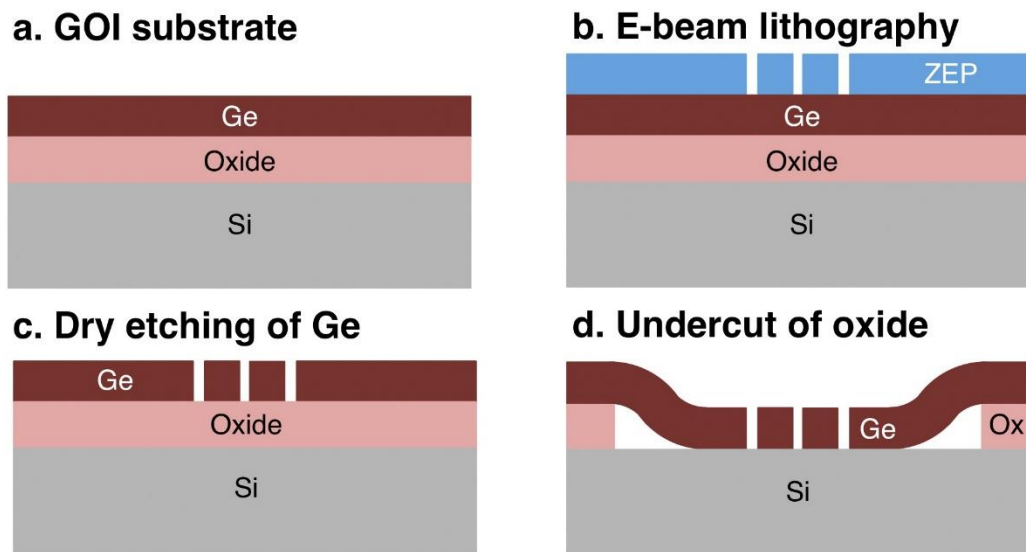


Figure 6-2. Microdisk fabrication process flow schematic. (a) The initial germanium-on-insulator (GOI) substrate. (b) E-beam lithography for resist patterning. (c) Dry etching of the germanium (Ge) layer. (d) Undercut of the sacrificial oxide layer. [25]

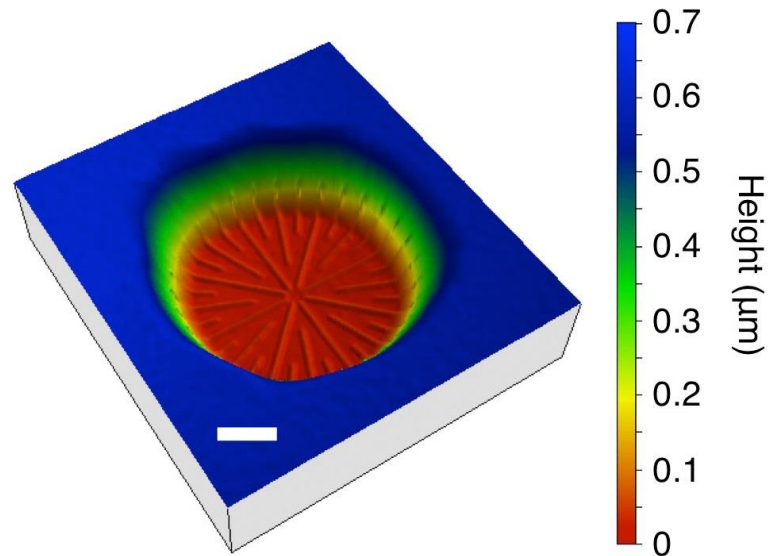


Figure 6-3. Optical surface profile of a fabricated microdisk structure, confirming that the structure is indeed deflected downward due to stiction. Note that the etched lines appear raised due to limitations of the optical interferometer setup; in reality these etch features are ~ 300 nm deep valleys in the profile rather than ~ 40 nm high raised features. Scale bar, $20 \mu\text{m}$. [25]

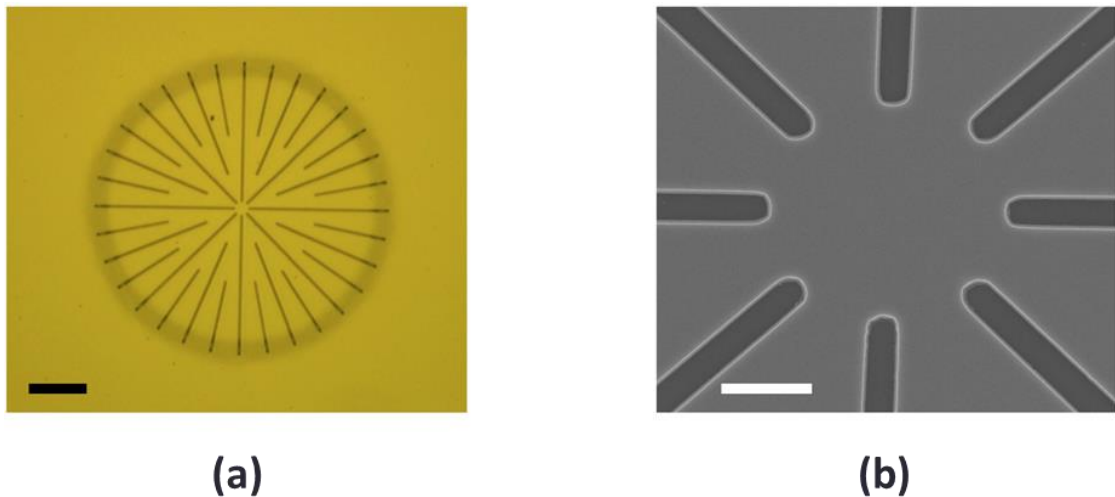


Figure 6-4. Micrographs of successfully fabricated structures. (a) Optical micrograph of the entire structure. Scale bar, $20 \mu\text{m}$. (b) Scanning electron micrograph of the central region of the structure. Scale bar, $2 \mu\text{m}$. [25]

An important feature of our new biaxial strain structure is that the strain in the inner microdisk is purely a function of the initial stress in the germanium and the ratio of the inner microdisk diameter to the total structure diameter. The initial stress in the germanium is usually fixed at $\sim 0.2\%$ which arises from the mismatch in the thermal expansion coefficient between germanium and silicon during the epitaxial growth of germanium on silicon [36], leaving the ratio the total diameter to the inner microdisk diameter as the most meaningful design parameter. By varying this ratio, the strain in the microdisk can be varied lithographically from device to device. For instance, if the inner microdisk diameter is held constant, then the strain in the inner microdisk can be increased simply by making the total (outer) diameter of the structure larger. By varying this ratio of outer diameter to inner microdisk diameter, it is also possible to make the strain arbitrarily large, limited only by material fracture of the Ge.

6.3 Mechanical Simulations

6.3.1 Overview

In addition to physically fabricating these structures, we have performed finite element method (FEM) modeling of the stress distributions to better understand the underlying physics and to optimize our design. All of our FEM simulations were performed using commercial software, namely COMSOL Multiphysics version 4.4. The “fine” mesh size in COMSOL was used in all FEM simulations. The germanium was assumed to have a 0.2% initial strain, and germanium’s Young’s modulus and Poisson ratio were taken to be 103 GPa and 0.26, respectively. Assuming a constant value for Young’s modulus implies that all anisotropies in Young’s modulus are ignored in our FEM

simulations, even though in reality this anisotropy is quite large for germanium [140]. Nevertheless, given the radial symmetry this omission of the modulus anisotropy should not substantially affect our overall results except to perhaps introduce some small and consistent systematic error in any corner stresses.

6.3.2 Understanding the Structure

The first takeaway from our FEM modeling is that, as shown in Fig. 6-1(b), is that our structure is theoretically expected to indeed concentrate strain into the central region. However, it is also worth considering exactly how and why this structure works to concentrate the pre-existing stress. A first point is that our FEM studies assumed perfectly flat suspended geometries, thus establishing that the observed strain enhancement is overwhelmingly due to the patterned etch slits as opposed to other mechanisms such as the deflection from the final stiction step. In terms of the mechanism by which our structure's etch slits concentrate strain, this can be understood by considering only the eight etch slits which touch the central microdisk region; all of the additional etch slits in Fig. 6-1 (i.e. all slits other than the eight touching the inner microdisk) were present only to facilitate the lateral etching of the underlying oxide by exposing more of this oxide for removal in the final fabrication step. These additional slits could just as well have been a series of holes or any other shape that would reduce the maximum distance between exposed areas in order to facilitate lateral etching. By considering a structure with only the main eight etch slits, shown in the FEM simulation of Fig. 6-5(a) we see that the slits create eight of

germanium “wedges” which are all pulling on the central microdisk region.

Considering any given pair of opposing germanium wedges reveals a structure qualitatively similar to the uniaxial microbridges of the preceding Chapter: a wide slab of germanium tapers down to a narrow region in the middle where the stress is concentration. However, because there are germanium wedges pulling on the central regions from all directions, which is in contrast to the microbridge design of the previous Chapter, the resulting strain is biaxial.

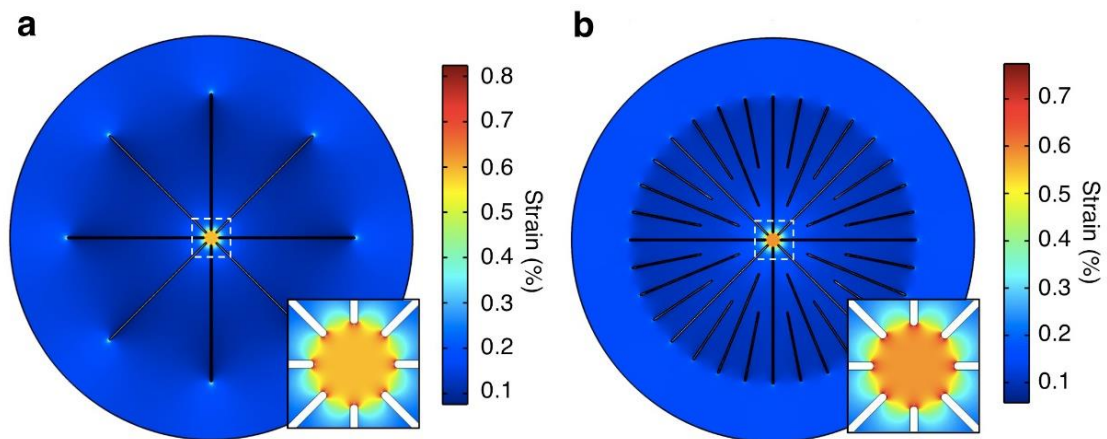


Figure 6-5. Finite element method (FEM) simulations of a $100\ \mu\text{m}$ diameter structure with a $5\ \mu\text{m}$ diameter inner microdisk (a) without the additional etch slits, and (b) with the additional etch slits. [25]

6.3.3 Effect of the Additional Etch Slits

Having established that only the eight etch slits which touch the central region are responsible for the stress concentration, it is worth ascertaining what impact the

“additional” etch slits have on the strain distribution. In order to investigate the effect of these additional slits we have performed two FEM simulations, shown in Fig. 6-5. Both of these FEM simulations are for a 5 μm inner microdisk diameter and a 100 μm total structure diameter, with 20 μm between the total structure dimensions and the fixed boundary. This 20 μm approximates the outward etching of the sacrificial oxide during the final fabrication step. All etch slits were taken to be 500 nm wide with rounded tips on each end, in accordance with our experimental design parameters. In the first FEM simulation, shown in Fig. 6-5(a), only the eight main etch slits have been included. In the second FEM simulation, shown in Fig. 6-5(b), additional etch slits have been included as they were in our actual devices. It can be readily seen that the stress distribution remains qualitatively extremely similar. Looking at the zoomed-in views of the microdisk region, we find that the simulation without additional etch slits resulted in a 0.590% biaxial strain at the microdisk center, whereas the simulation with the additional etch slits resulted in a 0.582% biaxial strain at the microdisk center. In both cases the maximum biaxial strain in the corner regions was approximately $\sim 0.88\%$. Thus, we conclude that the only substantive effect of adding additional etch slits is to very slightly reduce the strain at the microdisk center without otherwise altering the overall strain distribution.

6.3.4 Homogeneity of the Strain Distribution

By carefully observing Fig. 6-1(b) and Fig. 6-5, we find that resulting strain in these structures is exceedingly homogeneous. For instance, the biaxial strain at the center of the inner microdisk (inner 5 μm diameter region) of Fig. 6-1(b) is 0.435%, and

remains constant to the third decimal place over an area of $>10 \mu\text{m}^2$. This represents a negligible variation over a substantial area, indicating an extremely homogeneous strain. This variation remains negligible according to our FEM simulations even as the total diameter, and hence the strain in the inner microdisk, is increased. Although already negligible, this variation can also be further reduced by increasing the number of etch slits touching the inner microdisk, as shown by additional FEM simulations in the Supporting Information.

6.3.5 Corner Stresses

These FEM simulations also point to the expected failure mechanism for very highly strained disks: corner stresses near the inner edges of the main eight etch slits. This is plainly seen in the zoomed-in FEM simulations of Fig. 6-1(b). For this particular simulation, the biaxial strain, to be the average of ϵ_x and ϵ_y for the purposes of FEM simulations, reaches as high as 0.60%, even though the center of the inner microdisk is under only 0.435% biaxial strain, indicating a fracture risk near the corners. Thus, for devices with dimensions yielding larger strains than germanium can tolerate given the present material quality, we expect failure of these devices to occur by material fractures originating near these corner regions. Such mechanical failure was indeed observed experimentally and will be discussed in Section 6.4.3 but the key takeaway is simply that we wish to minimize these corner stresses while maximizing the strain at the center of the microdisk.

6.3.6 Optimizing the Number of Main Etch Slits

Lastly, while our fabricated devices all had exactly eight “main” etch slits touching the inner microdisk, we have nevertheless performed FEM simulations to investigate how the stress distribution would be affected by changing the number of etch slits which touch the inner microdisk. For these simulations, shown in Fig. 6-6, we have fixed the inner microdisk diameter to 5 μm , the total structure diameter to 50 μm , and assumed a constant 20 μm between the total structure dimensions and the fixed boundary to approximate the outward etching of the sacrificial oxide. All etch slits were again taken to be 500 nm wide with rounded tips on each end, in accordance with our experimental design parameters. Meanwhile, the number of main etch slits was varied from 3 to 20. It is immediately clear from Fig. 6-6(a) that increasing the number of main etch slits drastically increases the spatial homogeneity of the strain in the microdisk. The relationship between the number of etch slits and the microdisk strain and the corner strain, shown in Fig. 6-6(b) is more complex. For the design parameters used in this series of FEM simulations it would appear that somewhere between 10 and 15 main etch slits offers the optimal combination of relatively high microdisk strain and relatively low corner strain, though we expect this number to change significantly if the microdisk diameter is changed and/or the width of the etch slits is changed. Nevertheless, this suggests that changing the number of main etch slits may be another avenue to further improve this structure in a future work.

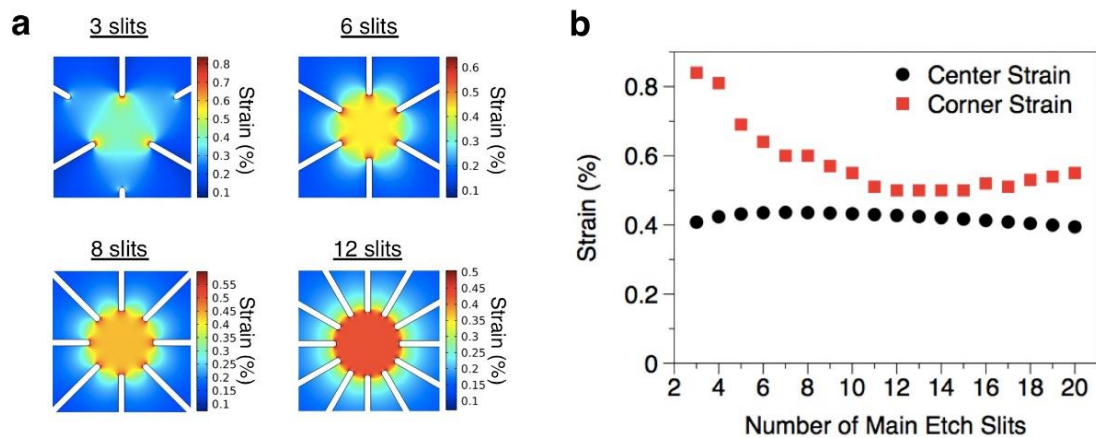


Figure 6-6. Optimizing the number of main etch slits. (a) Finite element method (FEM) simulations of the structure with different numbers of main etch slits. (b) Biaxial strains at the microdisk center and in the corner regions as a function of the number of main etch slits. [25]

6.4 Microdisk Characterization

6.4.1 Raman Spectroscopy

The strain in successfully fabricated structures was then measured by Raman spectroscopy, where a strain-shift coefficient of 390 cm^{-1} was used following the method of Ref [162]. As was the case in the preceding Chapter, a 514nm wavelength excitation laser was used for all Raman measurements. Although this nominally limits our strain measurements to the sample's top surface, we can again safely assume that the strain was uniform along the vertical axis because our suspended structures showed no vertical deflections (a hallmark of vertical strain gradients) and also because finite element method COMSOL simulations again indicated that no vertical strain gradients were to be expected. According to the observed Raman spectra of Fig.

6-7(a), the observed biaxial strains in the structures' inner microdisks ranged from 0.2% to 1.11%; the lower bound of 0.2% strain represents the residual germanium strain in the absence of patterning. The relationship between the observed strain and the outer diameter is shown in the inset of Fig. 6-7(a) for a series of devices fabricated side-by-side in the same run. From the inset of Fig. 6-7(a) it is clear that the measured strain has not saturated even for our largest unbroken sample (130 μm outer diameter), and FEM simulations predict no hard limit on the achievable strain if fracturing is ignored. Thus if the material fractures can be eliminated, perhaps by reducing the initial defect density in the Ge or by alleviating the corner stresses from which the fractures originate, even larger biaxial strains may be within reach with larger dimensions.

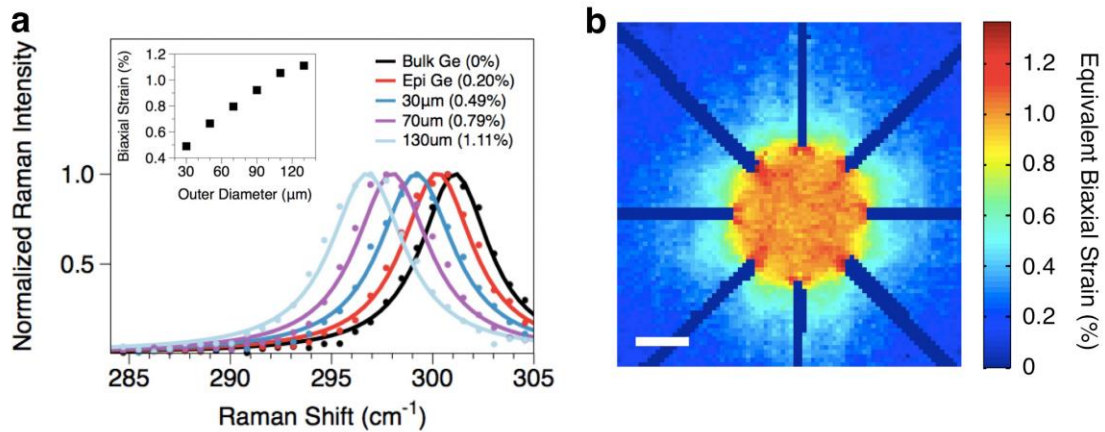


Figure 6-7. Raman characterization of the microdisks. (a) Raman spectra for various structure diameters. Inset: observed strain vs. outer diameter. (b) Biaxial strain distribution in the structure, measured by a Raman area scan. Scale bar, 2 μm . [25]

Another important advantage of our structure is that the biaxial strain is very homogenous over a large area, as suggested by our FEM modeling in Fig. 6-1(b) and Fig. 6-5. Vertical homogeneity of the strain distribution, which we expect theoretically, was inferred experimentally from the complete absence of any noticeable out-of-plane deflections since such deflections inevitably accompany vertical strain gradients. To confirm the strain's lateral homogeneity we have performed a Raman area scan and converted the measured Raman shifts to an "equivalent biaxial strain" by following the example of Ref [162]. As shown in Fig. 6-7(b), the observed strain is nearly constant over a large area in the inner microdisk, indicating excellent strain uniformity except for some sharp increases near the corner regions. While the use of "equivalent biaxial strain" here is imperfect for the very strongly non-biaxial strains in the corner regions, this is a non-issue over most of the central region where the strain is observed to be quite homogenous except for small variations which we ascribe to noise in the Raman measurements. This confirms that our structure achieves a uniform strain over a large area in practice as well as in theory.

6.4.2 Photoluminescence

Finally, the biaxially strained structures were characterized by photoluminescence (PL) measurements, as shown in Fig. 6-8(a), taken at the center of the inner microdisks. As explained in Section 5.3.2 of the preceding Chapter, although the 532 nm PL excitation laser is absorbed near the top surface of our samples, the photogenerated carriers rapidly diffuse along the vertical axis before recombining. As

a result, we can safely assume a vertically uniform carrier distribution for the purposes of our PL measurements. In order to preclude any significant heating effects the PL excitation laser power of 20 mW was again used for measuring germanium samples that were directly adhered to the silicon substrate, except in Section 6.5 where a lower power of 5 mW (and correspondingly longer integration times) was used due to a somewhat reduced heat sinking capability associated with a design change in that section. The structures characterized by PL had a relatively larger inner microdisk diameter of 7.5 μm to accommodate the finite spot size of the excitation laser, and the use of substrate-adhered germanium structures in this work precludes any significant heating effects from the 12 mW laser excitation [23] as evidenced in Fig. 5-6 of the preceding Chapter. Biaxial strain is well understood to enhance germanium's luminescence by increasing the fraction of electrons in the direct conduction valley [45], [53], [71], [72], [163], and we observe this phenomenon in our PL measurements. As shown explicitly in the inset of Fig. 6-8(b), the integrated intensity of the PL emission from our Ge structures increases by a factor of $\sim 2.3\text{x}$ as the strain increases from zero to 0.98%. This is somewhat smaller than the enhancement in direct (Γ) valley occupancy expected from our tight-binding model, shown in Fig. 3-4 of Chapter 3, however this discrepancy can be explained by the fact that valence band splitting and polarization selection rules favor in-plane emission over out-of-plane emission as the biaxial strain increases [63]. Moreover, the presence of a large and uniform strain in the disks is unambiguously confirmed by analyzing how the wavelength of the PL emission changes with strain, and by confirming that the redshifts follow the energy separations between the Gamma (Γ) valley and the two

separate valence bands, the heavy hole (HH) and light hole (LH) bands, as has been observed in previous works [60], [164]. As shown in Fig. 6-8(b), employing larger strains does indeed redshift the PL emission in accordance with the narrowing of the Γ -HH and Γ -LH bandgaps predicted by theory.

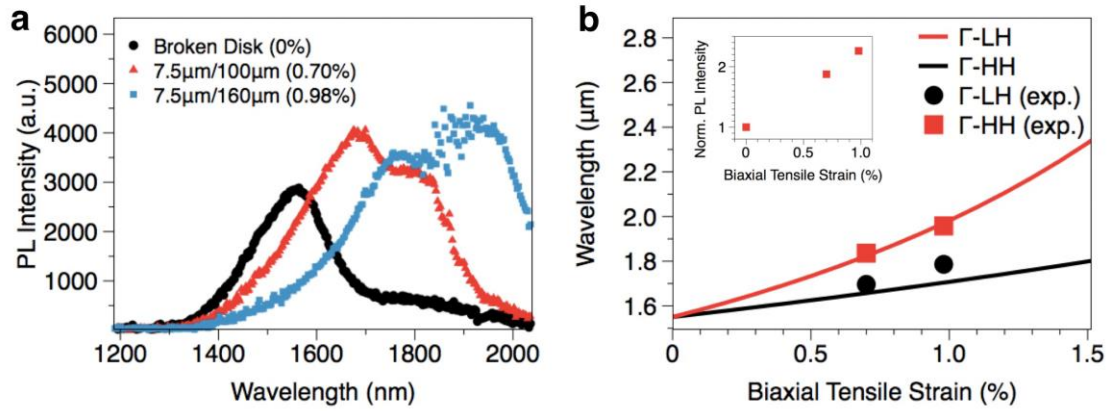


Figure 6-8. Photoluminescence characterization of the microdisks. (a) Photoluminescence (PL) spectra at various strain levels. (b) PL wavelength vs. strain. Inset: PL intensity vs. strain. [25]

6.4.3 Fractured Microdisks

A key point reiterated several times thus far is that our approach enables arbitrarily large biaxial strains, limited only by material fracture. In this section we will investigate this material fracture and how it inhibits us from achieving even larger strains. For the specific case of a structures with an inner diameter of 5 μm, structures were successfully fabricated with outer (total) diameters ranging from 30–130 μm, but structures with outer diameters of 140 μm or larger failed due to material fracture as

shown in Fig. 6-9. As expected from the FEM simulations of Fig. 6-1(b) and Fig. 6-5, we find that the fracture lines typically emanate from the corner regions – an effect plainly visible in Fig. 6-9. A study of several failed devices also revealed a strong tendency of the fracture lines to be aligned with the $\langle 110 \rangle$ cleavage planes, i.e. the standard cleavage planes for face-center cubic crystalline materials such as germanium and Si [165].

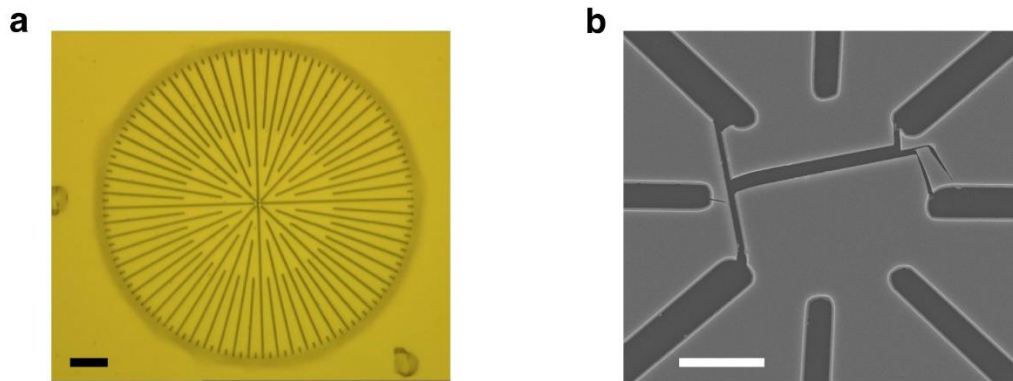


Figure 6-9. Micrographs of fractured microdisk structures. (a) Optical micrograph. Scale bar, 20 μm . (b) Scanning electron micrograph. Scale bar, 2 μm . [25]

Since the structures fail when the strain exceeds our germanium's fracture limit, it is worth considering exactly what this limit is. For our results in this work we can infer that material fracture occurs approximately when the “equivalent biaxial strain,” i.e. the average of the x- and y-components of the strain tensor, exceeds about $\sim 1.7\%$. This is a crude estimate based on the FEM modeling in Fig. 6-6 which shows that the equivalent biaxial strain in the corner region is $\sim 50\%$ larger than the central region strain, and so

we very roughly assume the equivalent biaxial strain at material fracture to be ~50% larger than the maximum achievable strain in the central region which was found to be 1.11%. Although theoretically this fracture limit occurs when a uniaxial strain exceeds ~18% anywhere in the sample, in practice any defects present have a tendency to dramatically reduce this maximum strain limit by increasing crack formation and propagation [166], thus explaining the much smaller value of ~1.7% which we just inferred. This means that, in practice, the fracture tolerance that limits the achievable strain is highly dependent upon the germanium material quality rather than being a fundamental material property of germanium [166]. The n-doped germanium-on-insulator substrates we have used are of comparatively high quality with a carrier lifetime known to be approximately ~3.1 ns [112] which is much better than simple n-doped germanium-on-Si material stacks which exhibit carrier lifetimes of only ~0.4 ns [121] due to the high defect density associated with the lattice-mismatched heteroepitaxy. However, bulk germanium is known to show carrier lifetimes as high as 500 μ s [113], indicating that there remains considerable room to reduce defects and improve the material quality of our germanium. Since the fracture limit is a strong function of the germanium defect density, it logically follows that if independent research advances make it possible to create higher quality germanium-on-insulator substrates then the fracture limit would increase and considerably larger strains could be achievable using our biaxial stress concentration technique.

6.5 Optical Cavity Integration

6.5.1 Optical Mode Leakage from Strained Microdisks

Having successfully fabricated germanium microdisks with large and homogeneous CMOS-compatible biaxial tensile strains, the next step toward realizing a tensile strained germanium is to integrate an optical cavity into our strained microdisks such that the optical mode is confined in the highly strained central region. As indicated in Fig. 6-10, there are currently two paths through which the optical mode can leak out of the active region. First, the optical mode can leak straight down into the substrate as illustrated in Fig. 6-10(a). The fact that our stiction process brings the germanium into direct contact with the underlying silicon substrate was highly desirable in that it greatly helps with heat sinking by allowing very efficient thermal dissipation from the germanium into the silicon, however this contact between germanium and silicon also allows the optical mode to easily leak into the substrate due to the low refractive contrast between germanium and silicon. While we could solve this problem by employing suspended geometries, i.e. forgoing the stiction by replacing the liquid hydrofluoric etch with an isotropic vapor etch, this is undesirable because suspended geometries tend to suffer heating problems at high powers as shown in Fig. 5-6 in the preceding Chapter. We therefore require a solution that will combine the vertical optical mode confinement of suspended geometries with the efficient thermal dissipation of stiction-based germanium-on-silicon geometries. In Section 6.5.2 we will present such a solution by employing a novel dual-dielectric fabrication process. The second problem is the optical mode can leak out laterally away from the active region within the germanium as illustrated in Fig. 6-10(b). We must therefore

somehow prevent this lateral mode leakage without substantially degrading the strain distribution. In Section 6.5.3 we will present an additional patterning step which prevents this lateral mode leakage, along with some tricks for maintained the large and homogeneous biaxial strain that we require in the active region.

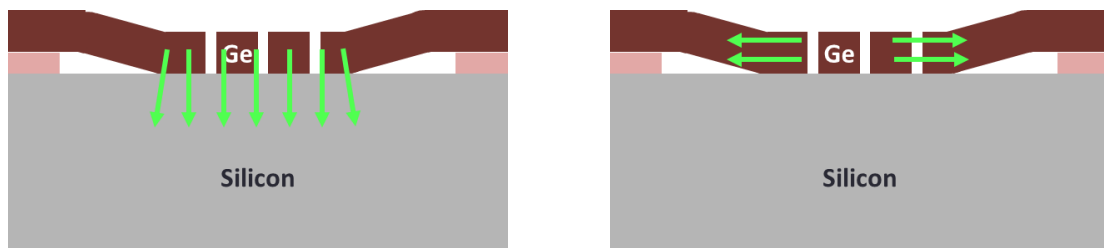


Figure 6-10. Schematic cross-section of the germanium (Ge) microdisks, showing optical mode leakage paths in the substrate-adhered microdisk structure. (a) Vertical optical mode leakage path directly into the silicon substrate, and (b) lateral optical mode leakage path within the germanium microdisk. Optical mode leakage is indicated by light green arrows.

6.5.2 Dual-Dielectric Fabrication Process for Vertical Optical Confinement

As explained in the previous section, we would like to combine strong vertical confinement of the optical mode, normally associated with suspended geometries due to the large refractive index contrast between germanium and air, with efficient thermal dissipation, normally associated with stiction-based germanium-on-silicon geometries due to the large thermal conductivity of silicon. To meet these requirements we must have germanium ultimately in contact with a material that is reasonably thermally conductive, or at least more thermally conductive than air, and that also offers a large

refractive index contrast to germanium. To this end, we have developed a revised fabrication process, shown in Fig. 6-11, that has two dielectric layers, aluminum oxide and silicon dioxide, sandwiched between germanium and the silicon substrate in the starting material stack. Whereas the silicon dioxide is thermally grown, this new layer of aluminum oxide is deposited by atomic layer deposition and is only a few nanometers thick.

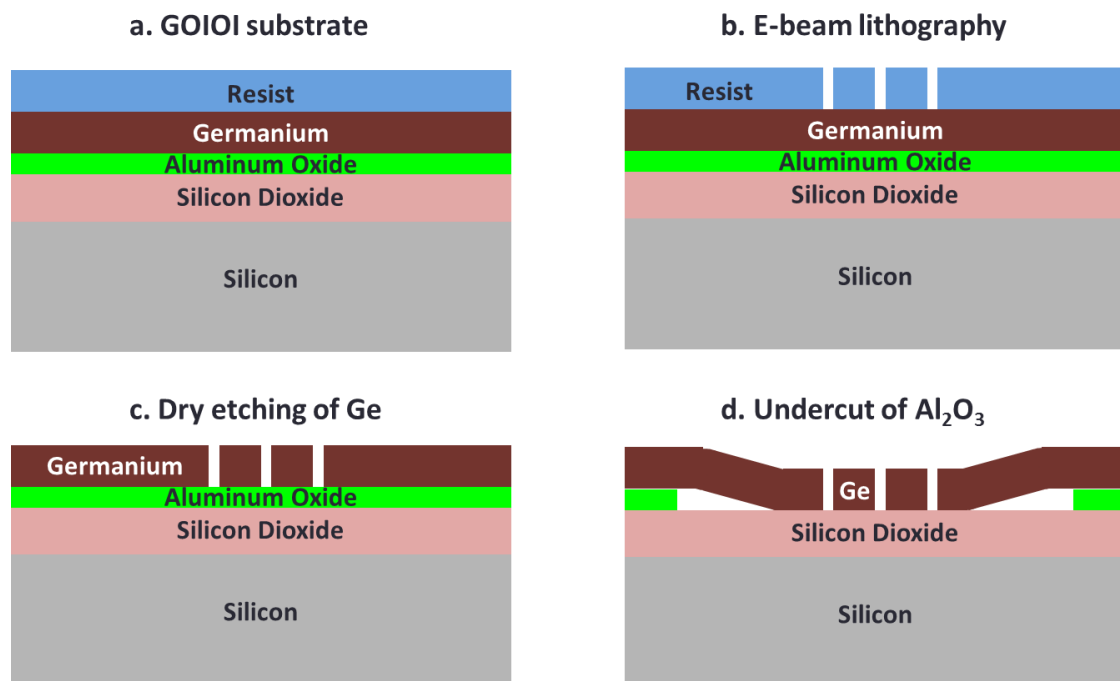


Figure 6-11. Process flow schematic for the dual-dielectric fabrication process. (a) The initial germanium-on-insulator-on-insulator (GOIOI) substrate showing the two dielectric layers: aluminum oxide and silicon dioxide. (b) E-beam lithography for resist patterning. (c) Dry etching of the germanium (Ge) layer. (d) Selective undercut of the sacrificial aluminum oxide (Al_2O_3) layer, leaving germanium/silicon-dioxide/silicon as the final material stack.

As shown in the Fig. 6-11, this dual-dielectric process is essentially the same as before (Fig. 6-2), but now with a layer of aluminum oxide between the germanium and the silicon dioxide. This aluminum oxide now acts as the sacrificial layer which, as illustrated in Fig. 6-11(d), can be isotropically and selectively removed in a wet potassium hydroxide (KOH) etch. This KOH etch leaves the silicon dioxide layer intact so that in the final stiction step germanium is now permanently adhered to the ~800 nm thick silicon dioxide layer, resulting a final material stack of germanium/silicon-dioxide/silicon as shown in Fig. 6-11(d). This now provides good optical confinement due to the large refractive index contrast between germanium and the ~800 nm thick silicon dioxide layer while also providing an efficient thermal dissipation path from germanium downward through the silicon dioxide into the underlying silicon substrate. While silicon dioxide may not be a particularly good thermal conductor it is a dramatic improvement over the previous air gap, and this is borne out in our experimental observations. For suspended geometries (i.e. with an air gap) we found that PL excitation laser powers of ~5 mW would cause the samples to melt. By replacing the air gap with the silicon dioxide layer in our dual-dielectric process, our SiO₂-adhered structures could tolerate up to ~50 mW of PL excitation laser power before melting. This is not quite as thermally resilient as those structures which were directly adhered to silicon and could tolerate excitation powers beyond 100 mW, but the SiO₂-adhered samples of from our dual-dielectric process nevertheless represent a tenfold improvement over the suspended geometries with respect to thermal dissipation. We also found, by modulating the PL pump power, that a full 5 mW of excitation power could be used without significant heating the SiO₂-adhered

samples. (Although 5 mW is a full 10% of the power required to melt the sample the heating at this power is indeed minimal; the melting occurs in a thermal runaway process and so the temperature changes non-linearly, and spikes very abruptly, as the melting excitation power is approached). Thus, our dual-dielectric fabrication process not only fully resolves the issue of vertical confinement of the optical mode but also maintains adequate heat sinking since.

6.5.3 Circular Patterning for Lateral Optical Confinement

There remains the issue of the optical mode leaking away from the active region laterally through the layer. At first glance this may seem like a more fundamental challenge since our stress concentration approach requires the highly strained active region to be physically connected to the rest of the structure, as shown in Fig. 6-12(a-b), in order for the initial stress from the entire structure to be transferred to the central region. However, after the germanium in our structure is briefly released and then permanently adhered to the underlying material by stiction, we find that the stress redistribution has already taken place and the germanium is now fixed in place by its bottom surface. We therefore hypothesized that perhaps we could dry etch the active region into a more traditional circular resonator, about 3.5 μm in diameter as shown in Fig. 6-12(c-d), that is laterally surrounded by air on all sides. This virtually eliminates any lateral leakage of the optical mode and should, at least in principle, enable an efficient optical resonator with whispering gallery modes.

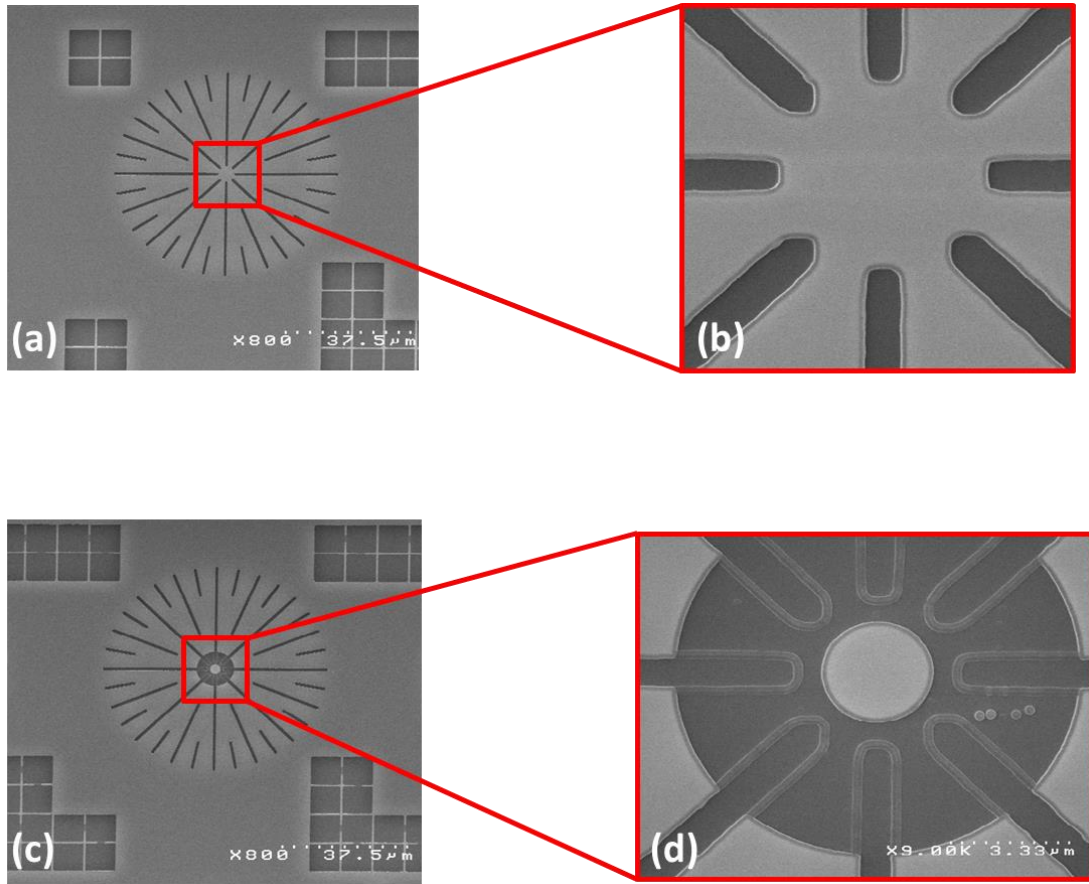


Figure 6-12. Micrographs of a resonator created by post-patterning a microdisk. (a) Scanning electron micrograph of a microdisk before optical cavity patterning, (b) Zoomed-in view of the region of Fig. (a) indicated by the red box, (c) Scanning electron micrograph of a microdisk after optical cavity patterning, (d) Zoomed-in view of the region of Fig. (c) indicated by the red box.

There were two concerns in creating these circularly-patterned optical cavities. First, there was a concern that the germanium may delaminate from the underlying substrate if the adhesion from Van der Waals forces (i.e. due to stiction) is too weak. In our previous work [71], [72], [161] using highly strained silicon nitride we observed a

tendency of the nitride to delaminate if the nitride's strain was too high and the layer was too thick. If our germanium active region were to delaminate it would become completely unusable. To pre-emptively address this issue, we have always performed an anneal at $\sim 400^\circ\text{C}$ for ~ 2 hours before patterning the circular resonator. Our hope was this anneal would create covalent bonds between germanium and the underlying silicon dioxide layer, and that this bonding would be strong enough to prevent delamination of the highly strained germanium resonator. As shown in Fig. 6-12(c-d), we successfully prevented any delamination of the germanium despite the large strain.

A second concern was that removing the lateral connection to the rest of the germanium would result in strain relaxation at the top surface, particularly near the outer perimeter of the top surface. This is common phenomenon in situations such as ours where the strain is maintained solely from the bottom surface. Thinking ahead, we proposed resolving this problem, should it arise, by depositing a compressively stressed silicon nitride layer on top of the entire structure. This is essentially the approach favored by Capellini *et al.* who showed that depositing compressively stressed silicon layers on germanium will impart tensile strain to germanium, but with a large inhomogeneity such that considerably more stress is imparted to the edge regions of the top surface than to the rest of the structure [162]. Since we are concerned about strain relaxation in these outer edges of the top surface, we propose using a silicon nitride stressor layer technique to compensate any strain losses at the top surface perimeter that may be observed in the next section.

6.5.4 Raman Characterization of Optical Cavities

Having fabricated these new circular resonators, the first question is whether or not the large and spatially uniform biaxial strain remains. As shown in Fig. 6-13(a), even before patterning the circular resonator we find that our new dual-dielectric fabrication process has caused some reduction in the strain homogeneity compared to our single-dielectric process (Fig. 6-7(b)). We suspect that this may be due to the annealing step, but the strain still retains a usable degree of homogeneity. However, after patterning the circular resonator we find that the strain has become severely inhomogeneous. As shown in Fig 6-13(b), while the initial strain of about 0.8% remains at the center, the outer edges are almost completely relaxed. If this were the final result, our microdisks would be potentially unusable for laser applications. However, as explained in Section 6.5.3, we anticipated this effect and have attempted to correct for this inhomogeneity by depositing about ~200 nm of compressively strained silicon nitride. As shown in Fig. 6-13(c), this post-patterning nitride deposition completely restores the desired strain inhomogeneity. In fact, this nitride deposition has not only completely compensated for the strain inhomogeneity that results from patterning the circular resonator (Fig. 6-13(b)) but it has also perfectly corrected for the initial unexplained inhomogeneity in Fig. 6-13(a) that resulted from our new dual-dielectric process and/or the annealing. Thus, we have fabricated circular optical cavities while maintaining nearly perfect spatial uniformity of the strain distribution, while of course maintaining efficient thermal dissipation for heat sinking too.

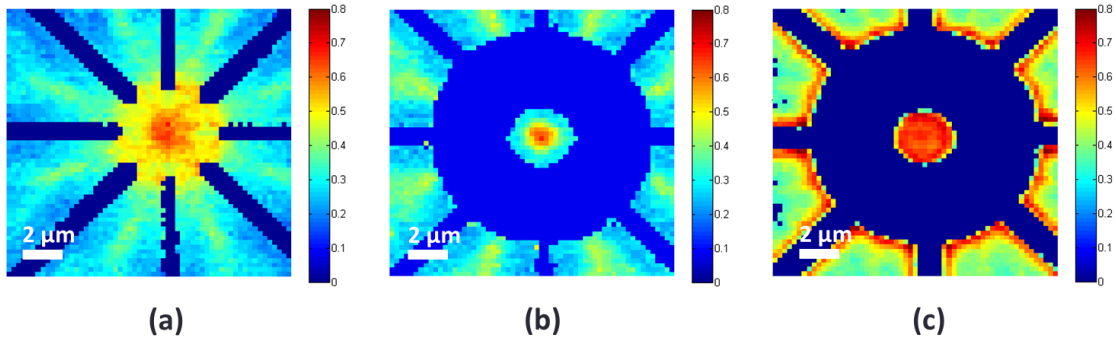


Figure 6-13. Raman area scans of the strain distribution (color scale) in the structure using the dual-dielectric fabrication process shown (a) before optical cavity patterning, (b) after circular resonator patterning, and (c) with ~ 200 nm of post-patterning silicon nitride.

6.5.5 Photoluminescence from Optical Cavities

Having confirmed that our optical cavities maintain the desired strain distribution, the next step is to demonstrate the presence of optical resonances in the light emission. We have done that by measuring the photoluminescence from two microdisks, one with 0.42% strain and another with 0.67% strain, before and after patterning our optical cavity in each case. As can be seen in Fig. 6-14, optical resonances are clearly visible when comparing patterned vs. unpatterned curves for any given strain value. The resonances are not particularly sharp, likely due to nitride surface roughness which may be improved with future optimizations, but establish a clear proof of concept that we have indeed integrated an optical cavity into our germanium microdisks while preserving the large homogeneous biaxial strain.

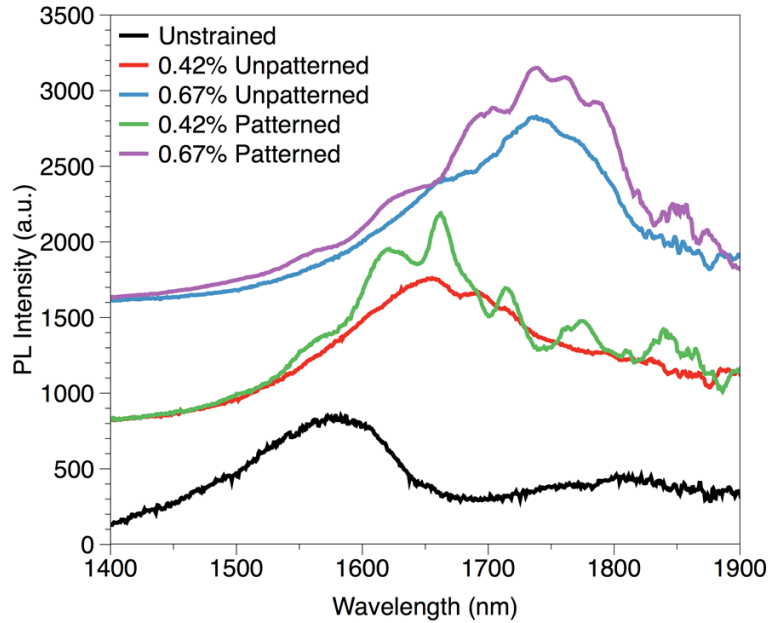


Figure 6-14. Photoluminescence (PL) measurements on the microdisk structures before and after patterning the optical cavity. Note that all patterned structures (i.e. structures with optical cavities) included a ~ 200 nm silicon nitride stressor layer to restore the original strain homogeneity. The PL excitation laser power was reduced to ~ 5 mW for the measurements shown in this figure, coupled with longer integration times, in order to minimize heating effects in these SiO_2 -adhered structures.

We can also infer whether the resulting optical modes are from longitudinal modes along the diameter or whispering gallery modes along the circumference by analyzing the spacing of the observed optical modes. Taking germanium's refractive index to be about 4.35 [71], [167] and assuming a final patterned diameter of $3 \mu\text{m}$, we find an optical path length of about $13 \mu\text{m}$ for the longitudinal modes (diameter) and $41 \mu\text{m}$ for the whispering gallery modes (circumference). For the longitudinal modes, where modes must have a wavelength that can be evenly divided into twice the optical path

length (26 μm), the mode spacing would be $\sim 110 \mu\text{m}$ for resonant wavelengths near 1700nm. For the whispering gallery modes we expect resonances at wavelengths that evenly divide the circumference (41 μm) and thus we would have a mode spacing of $\sim 70 \mu\text{m}$. From Fig. 6-14 we find the observed mode spacing to be about $\sim 60 \mu\text{m}$ for resonances in the vicinity of 1700nm. This observed mode spacing is much closer to the expected value for whispering gallery modes than for longitudinal modes, indicating that the observed resonances are indeed whispering gallery modes along the circumference of the microdisk.

6.6 Summary

In summary, we have experimentally achieved large biaxial strains of up to 1.11% in microdisks fabricated in germanium nanomembranes. Unlike previous works on highly-strained germanium [57], [62], [63], [71], our strain satisfies all the conditions of being permanently-sustained, vertically and laterally homogenous over arbitrarily large volumes, and integrated directly on a silicon substrate while preserving full CMOS-compatibility. Our process has the further advantage of reduced cost and simplicity since it involves only one lithography step and does not require external stressor layers or out-of-plane deflections [63], [71], [160]. The amount of strain in our structures and the lateral homogeneity of the strain distributions were experimentally determined using Raman spectroscopy, and found to be in good agreement with FEM simulations. Vertical homogeneity of the strain distribution was presumed since the geometry is purely in-plane with no relevant vertical features. Red-shifted, enhanced PL spectra from the strained disks offer further confirmation of the high strain levels in these

germanium structures, validating the Raman spectroscopy results. Additionally, the permanent stiction between the germanium nanomembrane and the Si substrate provides excellent thermal conductivity and eliminates heating problems which have traditionally plagued other membrane approaches [23].

The strained germanium structures presented herein also offer an extraordinary level of design flexibility. The size of the structures can also be scaled up or scaled down almost arbitrarily, since the strain is determined almost exclusively by the ratio of the inner microdisk diameter to the total structure diameter. This is important for enabling versatile resonator design if the structures are further patterned into micro-disk or micro-gear resonators. For instance, if some lasers in a final system layout need to have a particularly large light output then they could be made from physically larger resonators for improved heat sinking whereas lasers requiring a smaller light output could be made from resonators with a smaller and more compact form factor, provided that an appropriate inner diameter to outer diameter ratio is maintained when patterning the microdisks for such resonators. Additionally, since a resonator must always have dimensions optimized for the intended operating wavelength, the ability to scale the size up or down means that it will always be possible to create a resonator of the desired size without compromising the strain distribution. The actual design of such resonators, however, is a task which we leave for a future work. Most importantly, the strain can be customized lithographically by changing certain specific dimensions of the structure, specifically the inner diameter to outer diameter ratio. This means that multiple strains, and thus multiple bandgaps, can be realized across a single die using a simple one mask process. The presence of multiple bandgaps means that a much wider range of

wavelengths can be accessed for emission, modulation and detection, thus raising the possibility of employing these structures in extended wavelength-division multiplexing systems for on-chip optical interconnects. This functionality may find applications not only using germanium but also III-V materials, and our approach should be highly transferable to any arbitrary material system provided that the active material begins with some initial tensile stress.

Lastly, we have integrated an optical cavity into our germanium microdisks by patterning circular resonators with whispering gallery modes. This provides lateral confinement of the optical mode, with vertical confinement provided by a layer of silicon dioxide between the germanium resonator and the underlying silicon substrate. This silicon dioxide also provides an efficient heat conduction path, ensuring efficient thermal dissipation which will provide effective heat sinking for practical laser device applications. While patterning this cavity might seem to be detrimental to the homogeneity of the strain distribution, we have shown that employing a final silicon nitride stressor layer deposition can ensure that the spatial uniformity of the large biaxial strain is nearly perfect. We also have experimental evidence of optical resonances from photoluminescence measurements on these highly-strained germanium optical resonators. This represents a critical step toward realizing a highly strained germanium laser on silicon. Another element which we have not considered in this dissertation is that electrical contacts must eventually be incorporated such that these structures can be electrically pumped. This is a significant challenge in that incorporating metal electrodes can severely degrade the quality of an optical cavity, a problem which is already plaguing research efforts in germanium lasers [101]. However, substantial

progress has been recently made in demonstrating tensile strained germanium optical cavities with electrical injection [168]. Given that our work on integrating optical cavities is still in the very early stages, we expect future efforts to deliver considerable improvements toward all of these goals.

Chapter 7

Conclusions and Outlook

Throughout this dissertation we have presented concrete achievements on the road toward realizing an efficient low threshold CMOS-compatible laser using band engineered germanium. In the first part of this dissertation we discussed the motivation for this work. More specifically, in Chapter 1 we leaned on previous research to present the case for on-chip and off-chip optical interconnects in the general sense, to show that a CMOS-compatible laser remains the “missing link” for realizing an on-chip optical link, and to explain why an efficient germanium light source is such a tantalizing prospect. In Chapter 2 we then reviewed the existing research to explain some critical gaps on both the theoretical and experimental fronts. On the theoretical side, there was simply no comprehensive model of band engineering germanium lasers. It was completely unknown, for instance, whether tensile strain or n-type doping, the prevailing technique when we began this work, would offer more promising performance enhancements. It was also unknown whether or not band engineering and n-type doping could be employed together in a useful and effective way. Meanwhile, on the experimental side there were simply no viable techniques for engineering very large tensile strains in germanium, whether uniaxial or biaxial, in a way that is both CMOS-compatible and that can be feasibly integrating with an optical cavity to build a laser. These theoretical and experimental deficiencies in the existing literature are what we have sought to address in this dissertation.

With regard to the theoretical concerns, we have presented in Chapters 3 and 4 of this dissertation the first comprehensive model of how band engineering and n-type doping affect the performance of germanium lasers. We have considered band engineering by means of biaxial and uniaxial strains along all three major orientations as well as band engineering through tin alloying, and we have investigated the particularities of each with respect to germanium's laser performance, including subtleties related to the valence band splitting that occurs under strain. Most importantly, we have presented the first detailed theoretical investigation of the interaction between band engineering and n-type doping: whereas most experimental efforts up to 2010 focused on n-type doping, our models plainly show band engineering, whether by tensile strain or tin alloying, to be the superior approach. We have further shown that there is a negative interaction between all forms of band engineering and n-type doping. In fact, too much n-type doping is decidedly harmful and, if a more useful band engineering approach is employed, it will actually become necessary to reduce the doping from present levels. Meanwhile, our model shows that there is no negative interaction between tensile strain and tin alloying, indicating that tensile strained germanium tin alloys are a very promising route to an efficient CMOS-compatible laser. Lastly, our model is the first to consider the slope efficiency of a germanium laser, which we find to be unexpectedly low even for a very ideal design due to a large amount of free carrier absorption from indirect valley electrons. As such, it will be necessary to employ much more lossy optical cavities than one might typically expect, even though this will come at the expense of threshold and thus necessitate even more band engineering for efficient overall operation.

From there we pivoted to experimental realization of large strains. In Chapter 5 we presented germanium wires with up to 5.7% uniaxial tensile strain using microbridge structures – enough to turn germanium into a direct bandgap semiconductor – while maintaining full CMOS compatibility. We characterized these wires using both Raman spectroscopy and photoluminescence and observed enhanced and redshifted emission from these strained wires. Beyond the singular achievement of a large uniaxial strain, we have also introduced the concept of single material pseudoheterostructures using a spatially varying strain. Since tensile strain modulates germanium’s bandgap, and since our technique allows very precise tailoring of the strain profiles, we are able to deliberately and locally tailor germanium’s bandgap so as to reproduce the electronic band profiles of traditional multi-material heterostructures even though only one material (i.e. germanium) is employed. This opens up an entirely new paradigm for creating custom-designed heterostructures with control of the band profiles at the nanoscale – and without the expense or complexity of heteroepitaxy. Moreover, because the strain – and hence the bandgap – is determined lithographically, our technique makes it possible to access a larger range of wavelengths for extended wavelength division multiplexing. In Chapter 6 we presented an analogous etched microdisk structure for biaxial strain, with up to 1.1% strain observed, which offers the exact same degree of design flexibility: the strain is again precisely tunable by changing certain dimensions at the lithography stage. These structures were also characterized using Raman spectroscopy and photoluminescence which confirmed enhanced and redshifted light emission as expected. In addition, we have fabricated optical cavities using these biaxial microdisks, and we have

demonstrated optical resonances while maintain an extremely spatially homogeneous strain distribution.

Taken together, these achievements represent very tangible theoretical and experimental progress toward realizing an efficient CMOS-compatible laser using band engineered germanium. We now have a vastly improved theoretical understanding of how a band engineered germanium laser will behave, and we now have simple and elegant techniques for achieving this band engineering in practice through both uniaxial and biaxial tensile strain. We have shown enhancements in the light emission, and also a first pass realization of an optical cavity. Looking forward, this represents all the necessary tools for realizing an efficient CMOS-compatible germanium laser and we leave the final push, i.e. building this laser, to future researchers.

The question then remains of how we expect band-engineered germanium to progress in the coming years. One major deficiency that needs to be addressed is the small amount of experimental data, even simple material gain studies, available to validate existing theoretical models. With techniques for achieving large tensile strains and GeSn alloys with very high tin content finally coming to fruition within the past few years [22], [23], [25], [81], [82], [84], [87], more such optical gain demonstrations are a logical next step. The very recent demonstration of an electrically pumped direct bandgap GeSn laser [87] is evidence of the present vitality of this field as it progresses toward a viable CMOS-compatible light source. With direct bandgap Group IV semiconductors on silicon now a reality [23], [87], and having still not yet tapped the possibility of combining tensile strain with GeSn [86], it would appear that the most

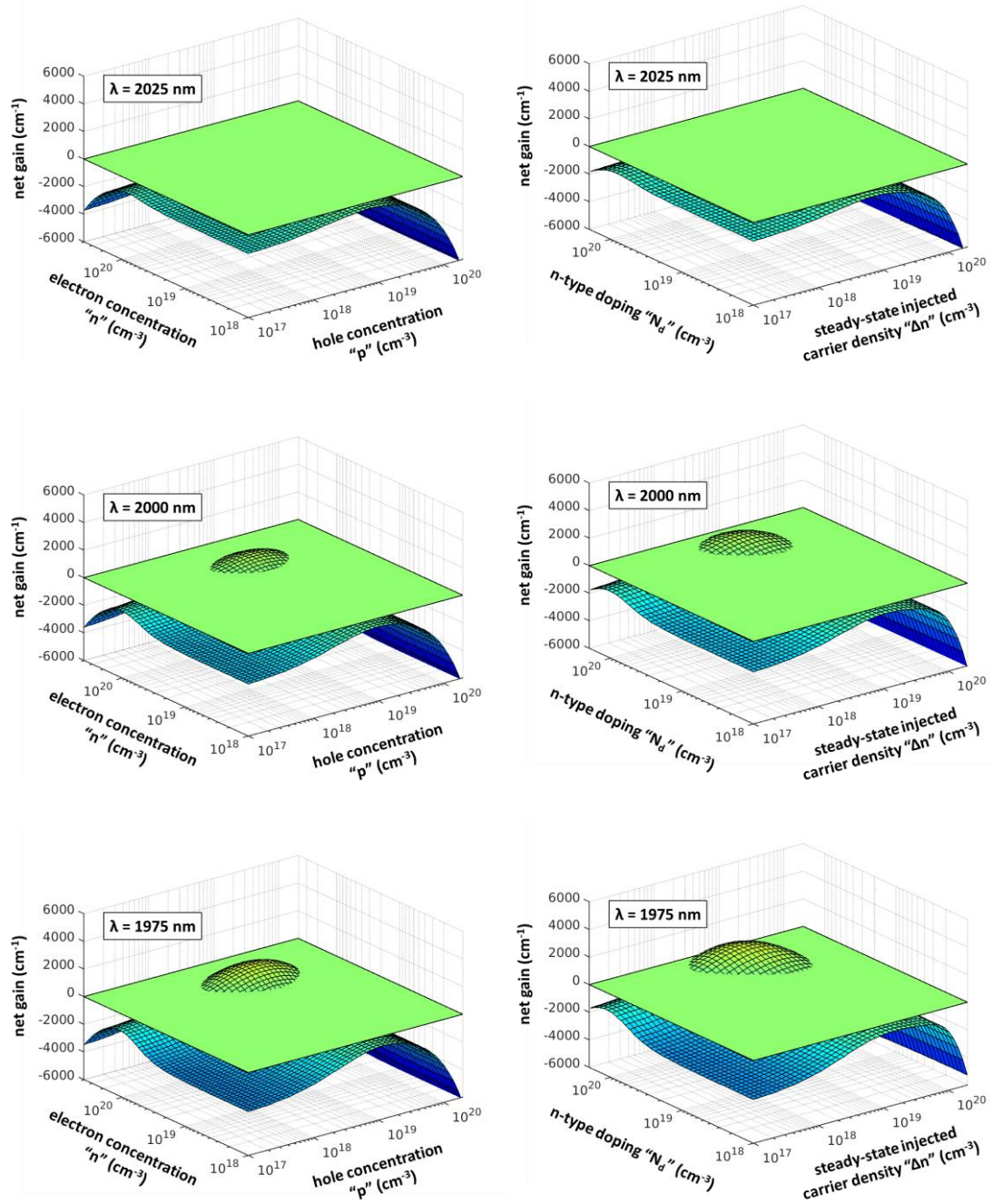
fundamental material challenges have been mostly overcome. (Continued efforts on reducing material defects, though, would certainly be welcome [112], [121]). With practical techniques now beginning to emerge for optical cavity integration, we expect the next few years to be decisive in proving whether or not band-engineered germanium can ultimately be a suitable material for efficient CMOS-compatible light emission.

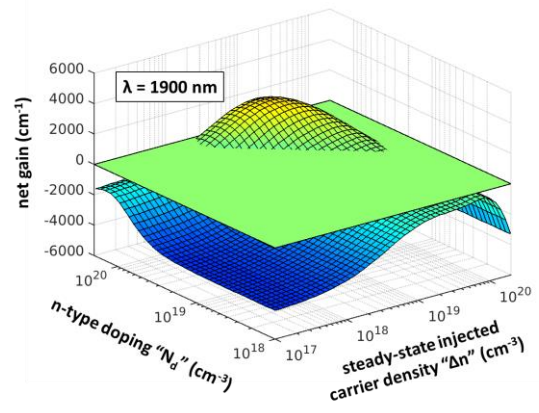
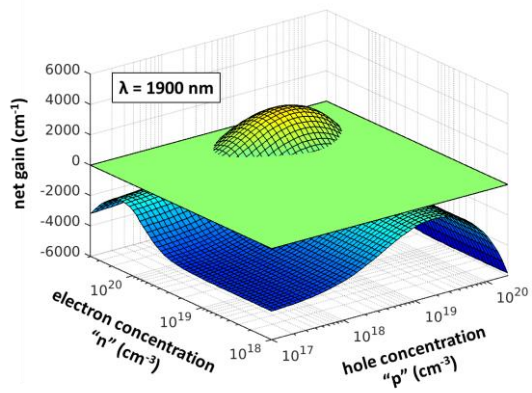
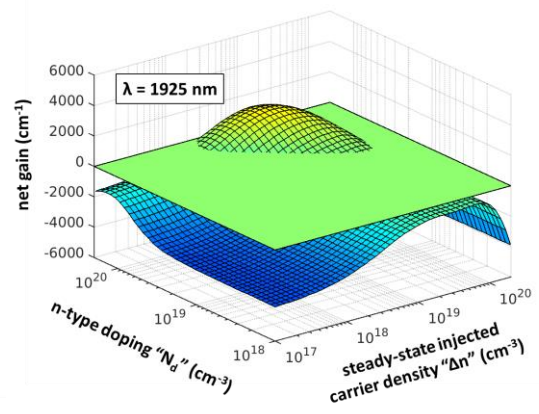
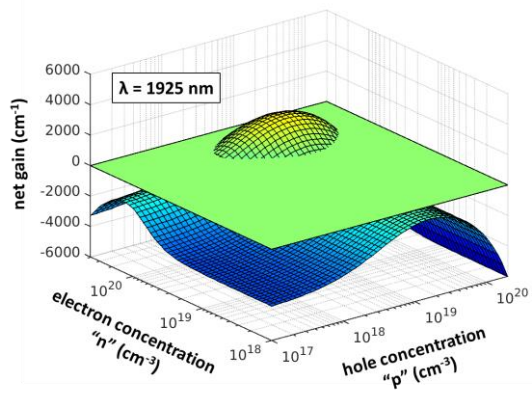
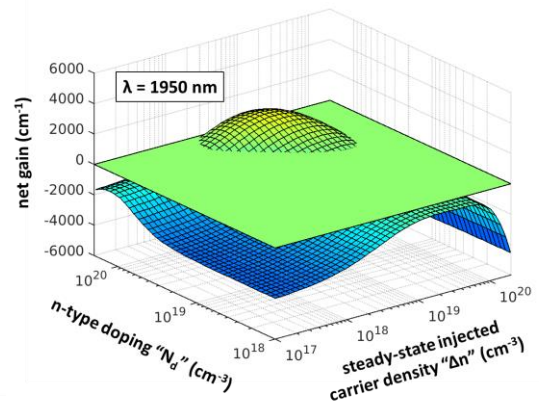
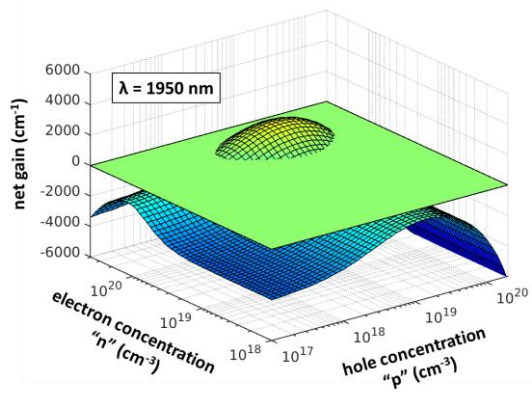
On the subject of optical gain demonstrations, one particularly frustrating hurdle we encountered was the lack of economical detectors that can operate at the redshifted wavelengths associated with our heavily band engineered germanium. Indeed, we were completely unable to measure the optical properties of the direct bandgap strained germanium nanowires that we fabricated [23]. This represents a potentially game-changing yet underexplored application for band engineered germanium as a mid-infrared light emitter and, especially, a detector. While we have hitherto treated the emission and detection redshifts that accompany our proposed band engineering as nuisances to be mitigated for the application of optical interconnects, by pushing germanium's operating wavelength from 1.55 μm into the mid-infrared we have actually developed a material which may be used for thermal imaging. This potentially opens up a large number of military, sensing and medical applications: the CMOS-compatibility of band engineered germanium-on-silicon makes it a very compelling candidate to deliver highly economical optical components in the mid-infrared which could compete very favorably with the costly existing technologies. Thus, while we have focused exclusively on optical interconnect applications in this dissertation and such applications are indeed promising, the

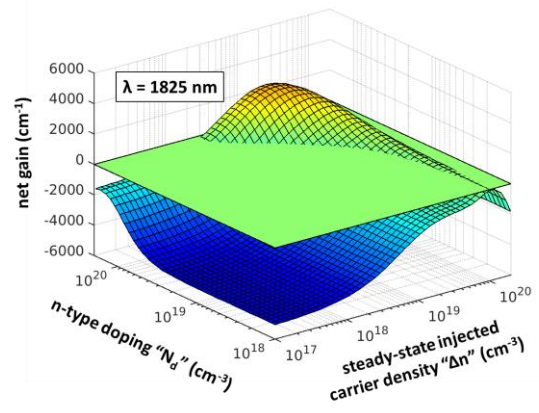
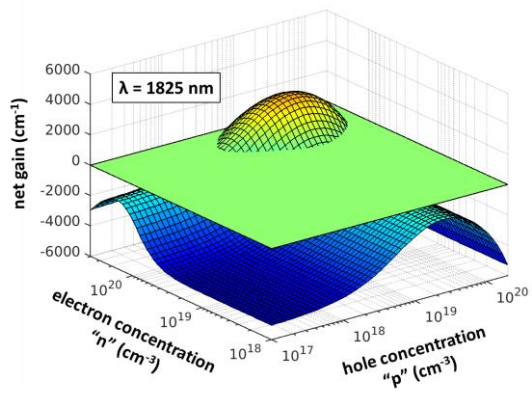
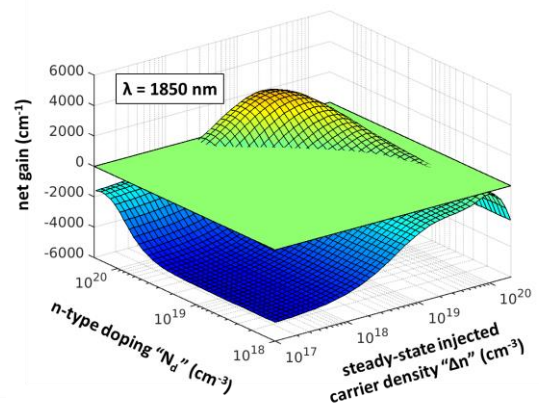
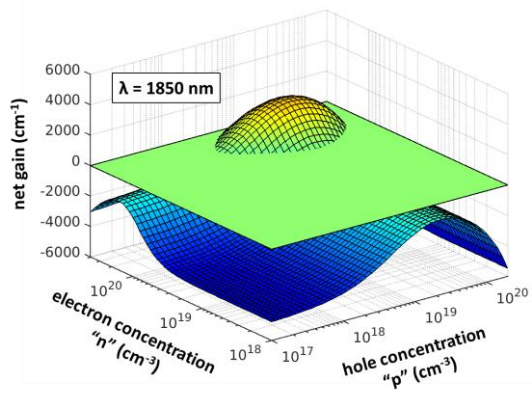
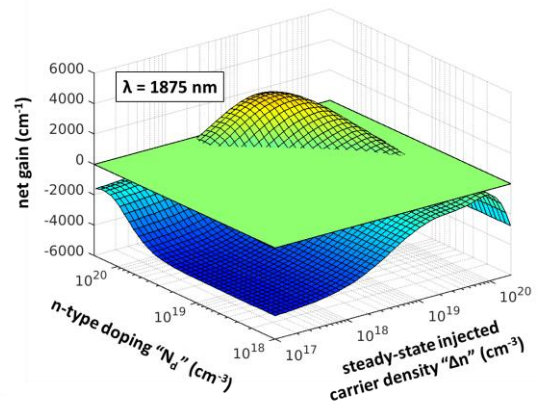
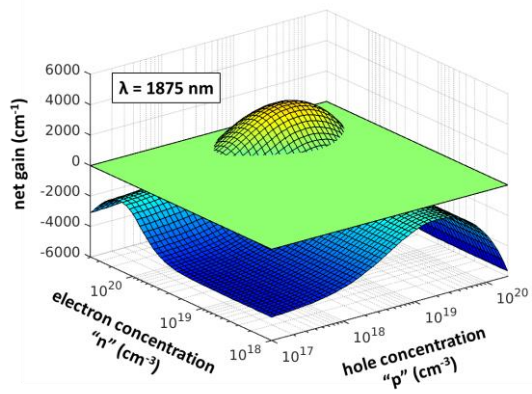
materials we have developed may also find very compelling military, sensing and life sciences applications if researchers are willing to think slightly outside of the box.

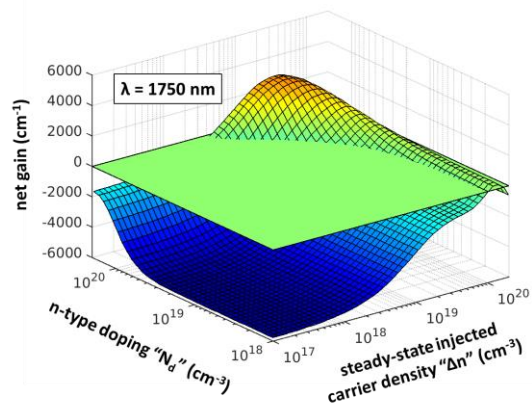
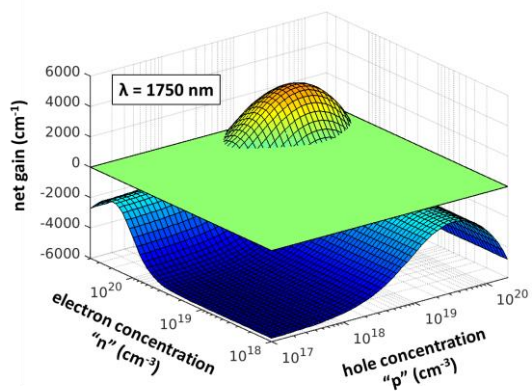
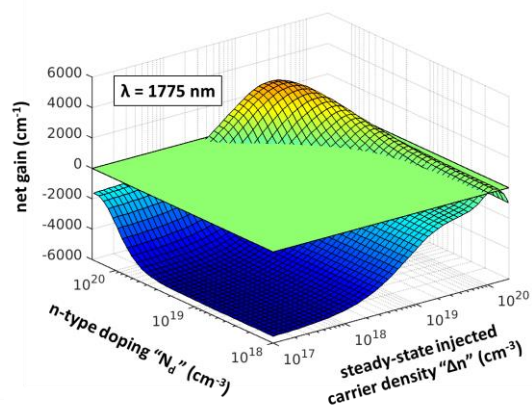
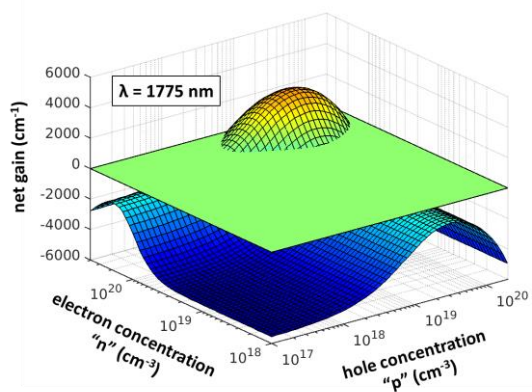
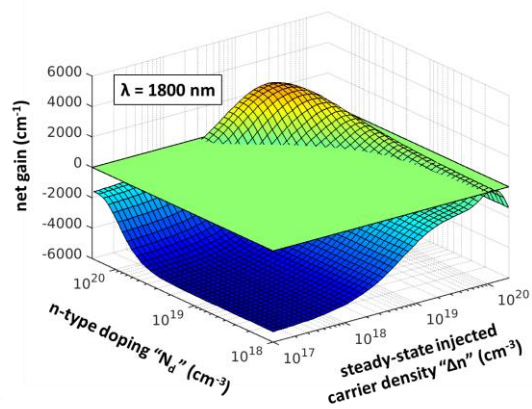
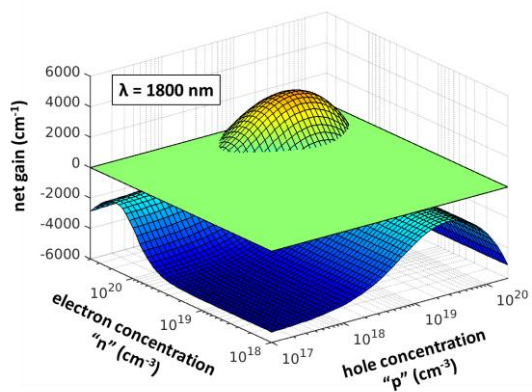
Appendix

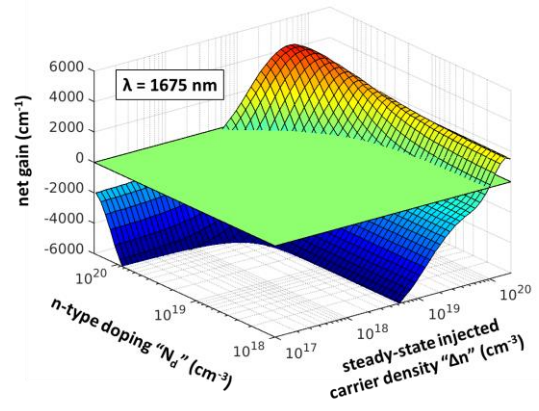
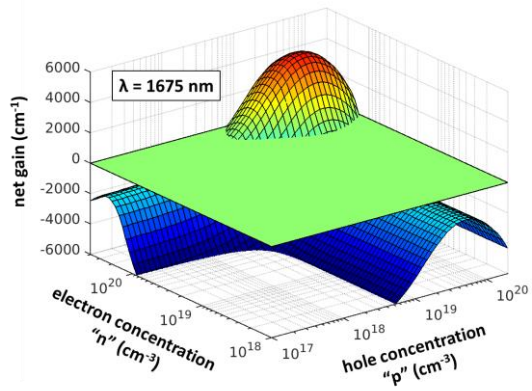
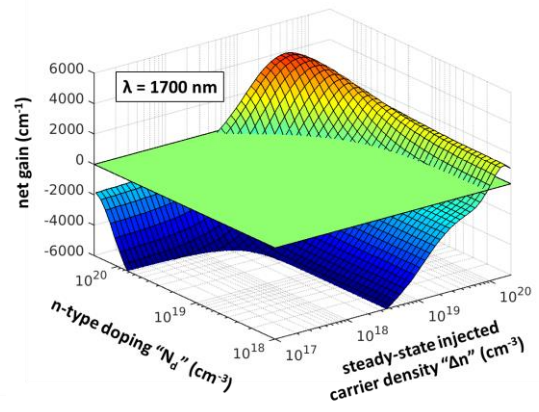
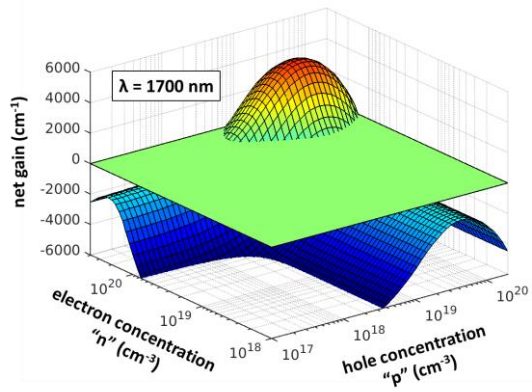
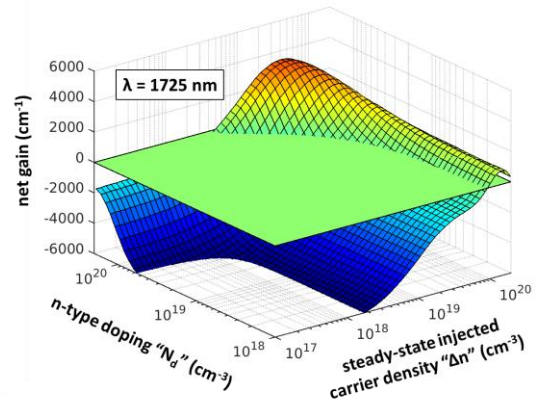
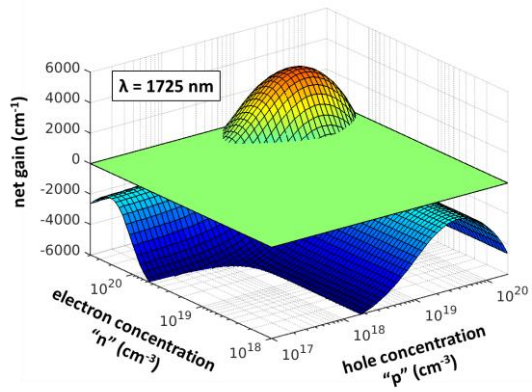
Figure A-1. Optical net gain of germanium under 1.0% biaxial tensile strain as a function of electron and hole concentrations (left) and as a function of doping and steady-state injected carrier density (right), shown at various wavelengths.

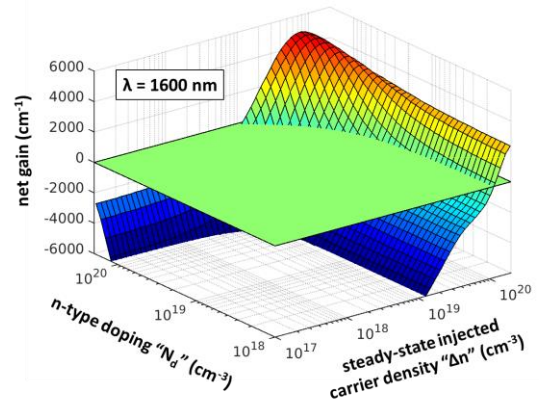
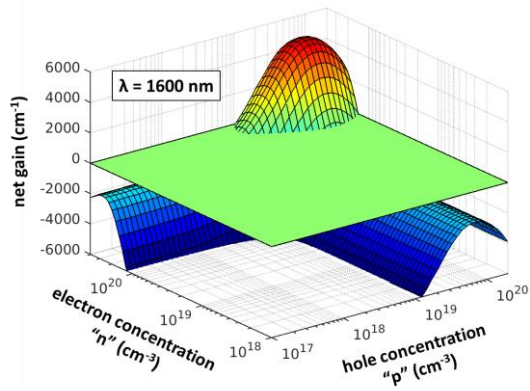
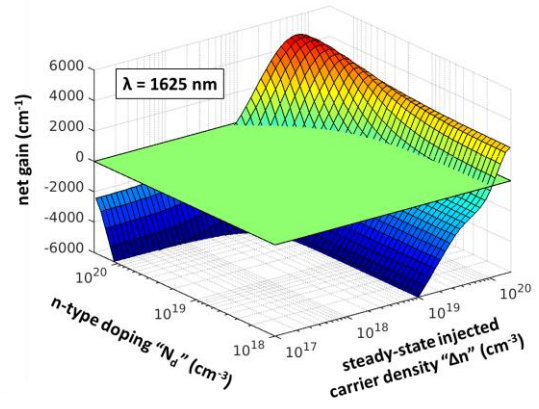
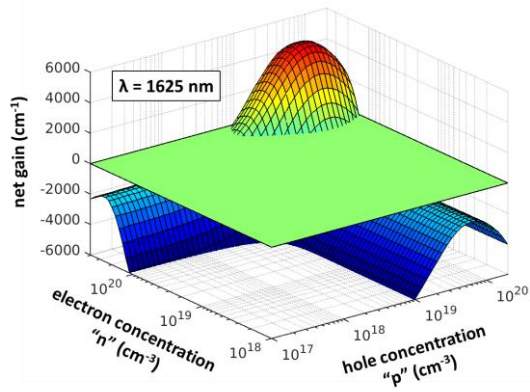
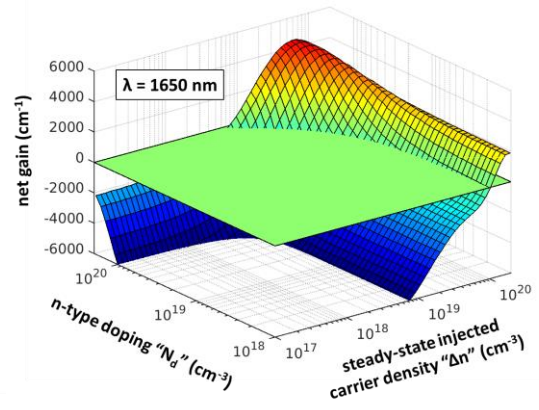
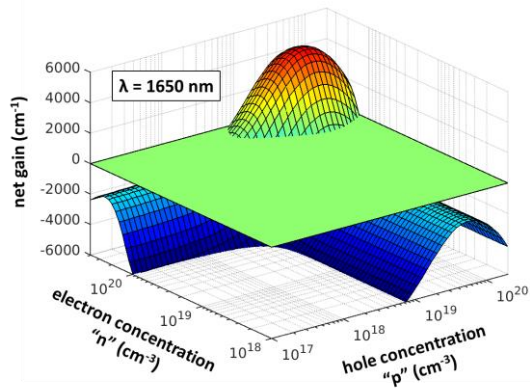


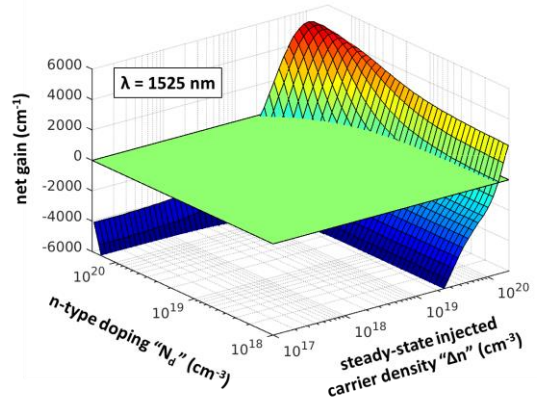
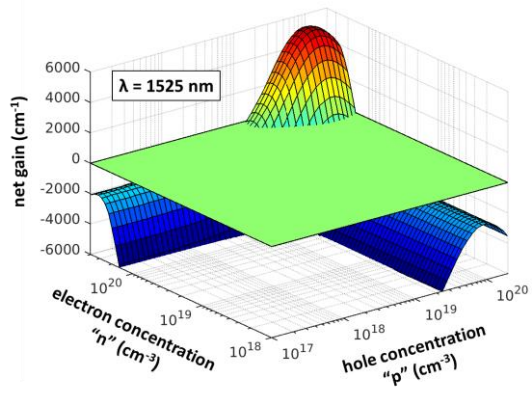
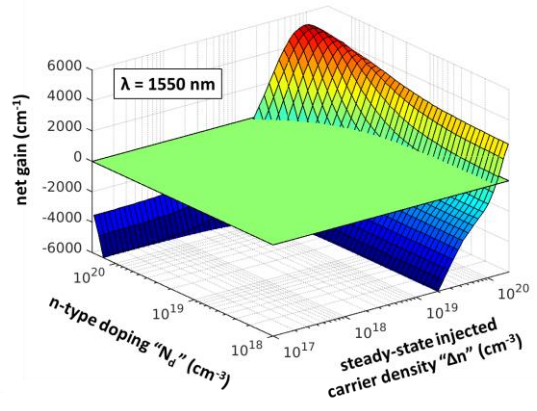
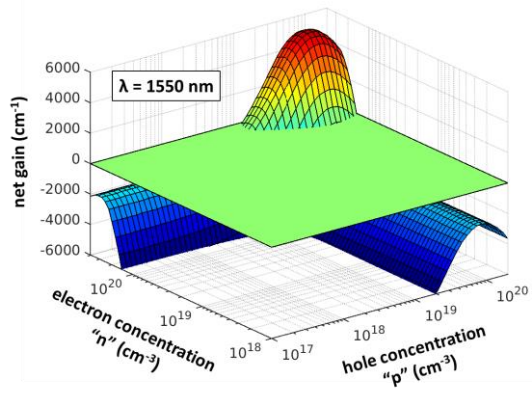
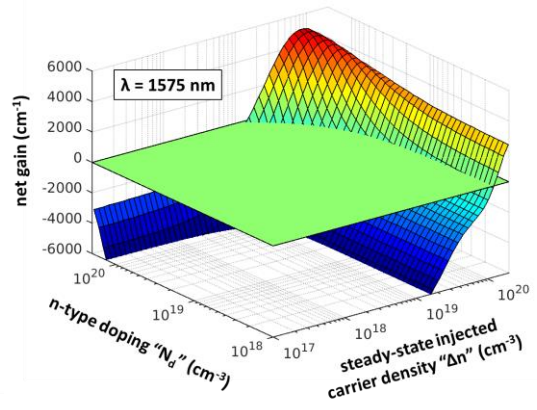
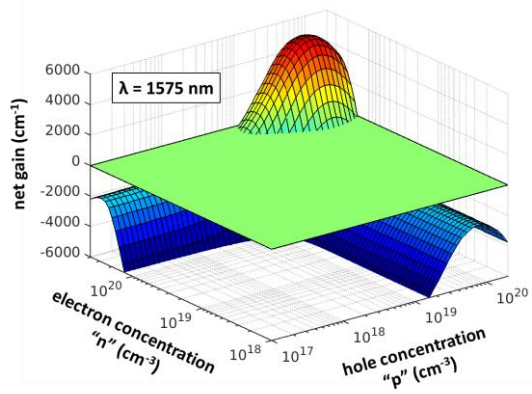


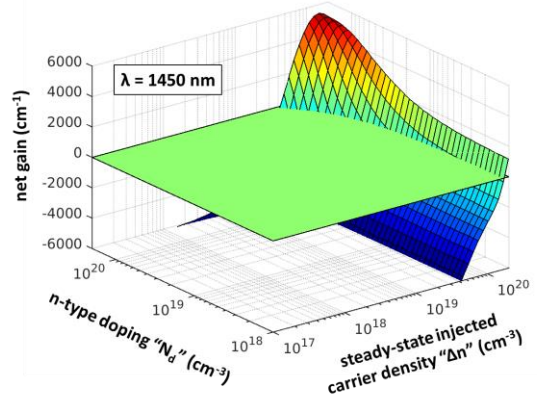
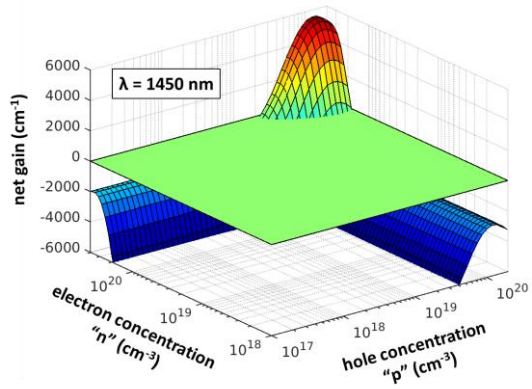
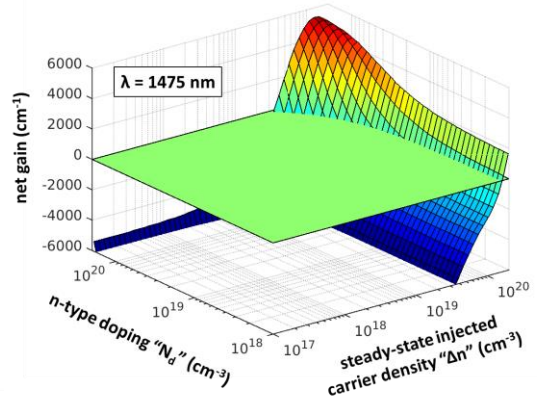
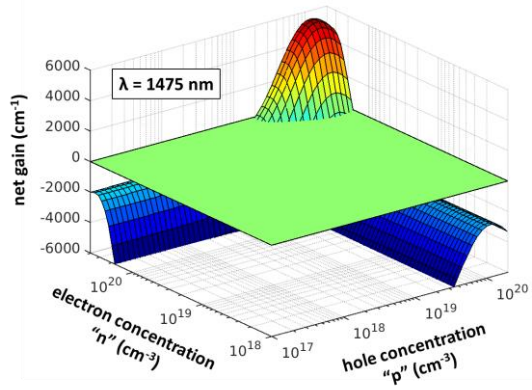
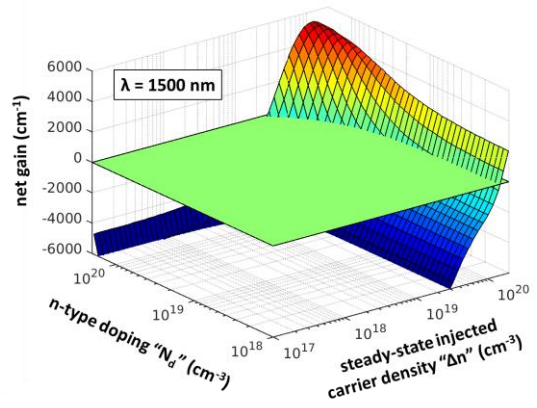
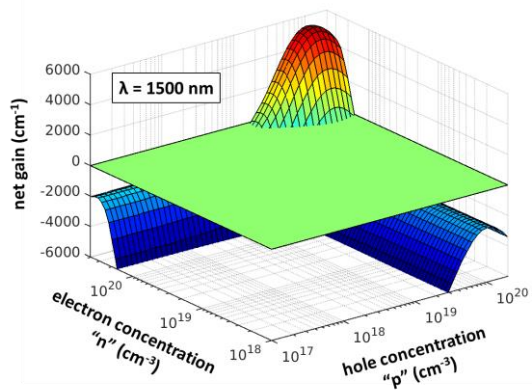












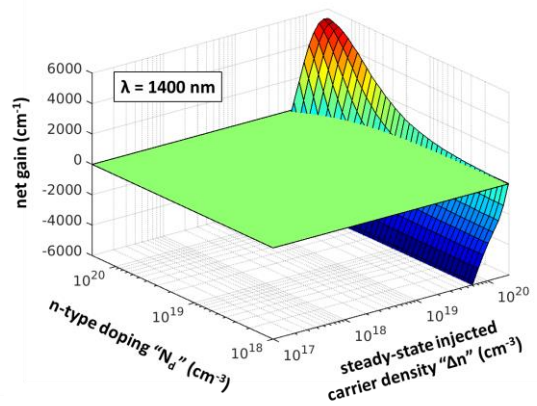
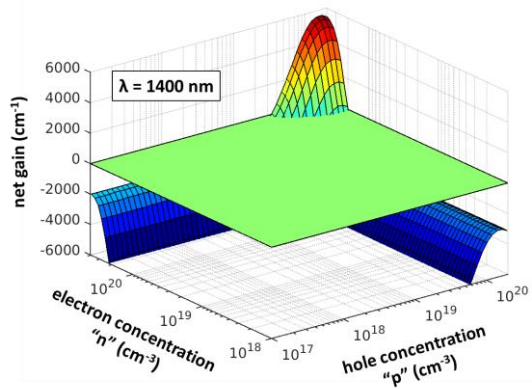
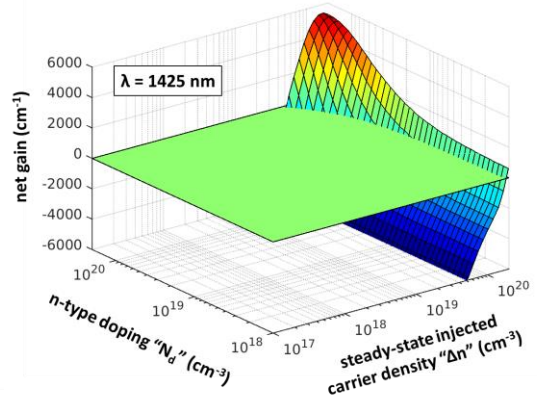
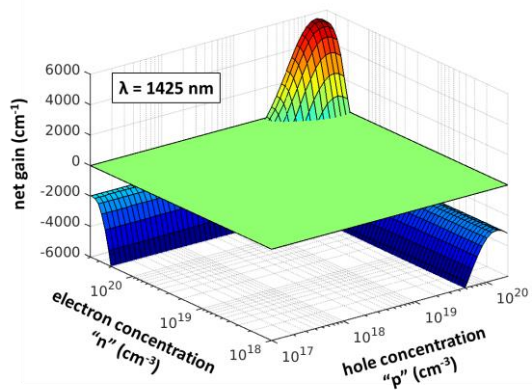
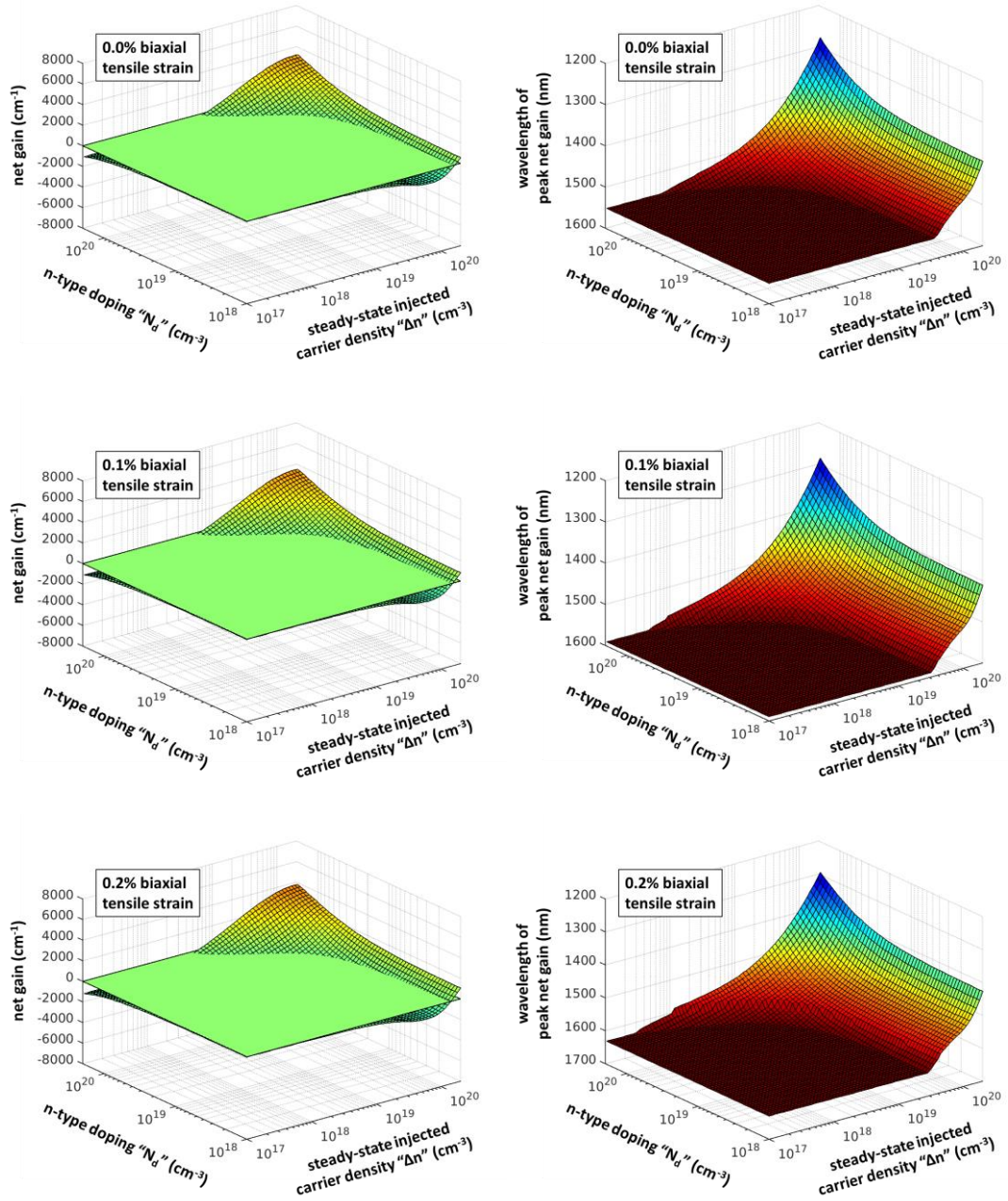
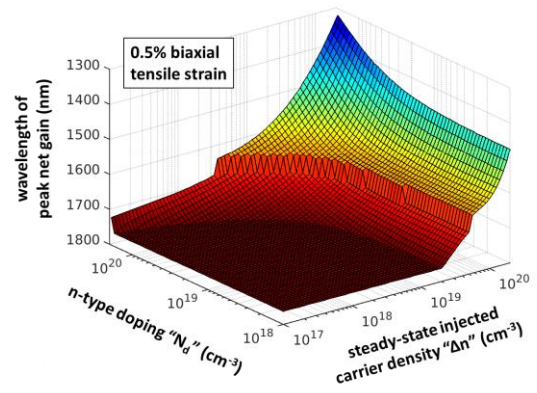
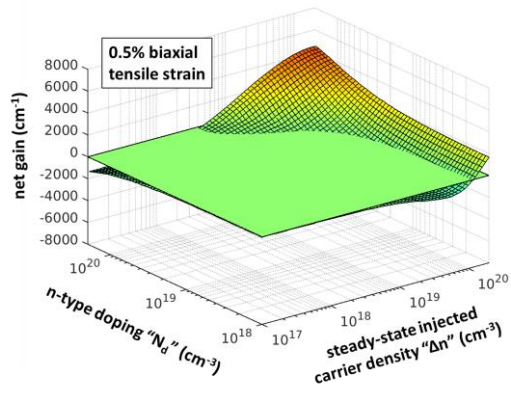
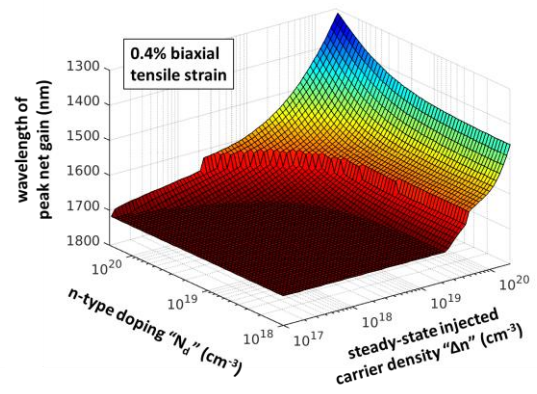
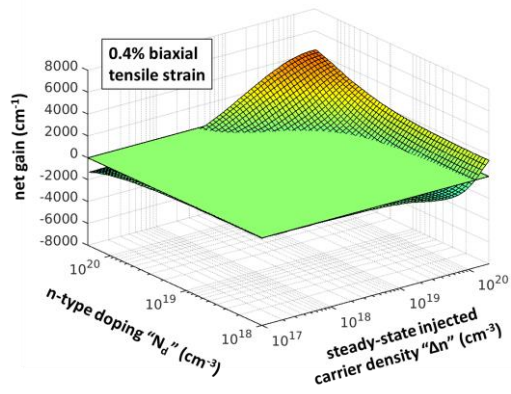
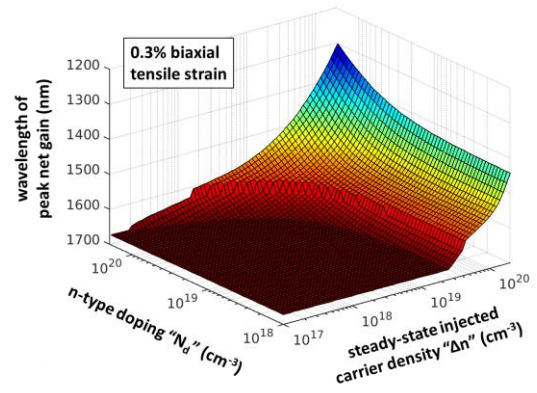
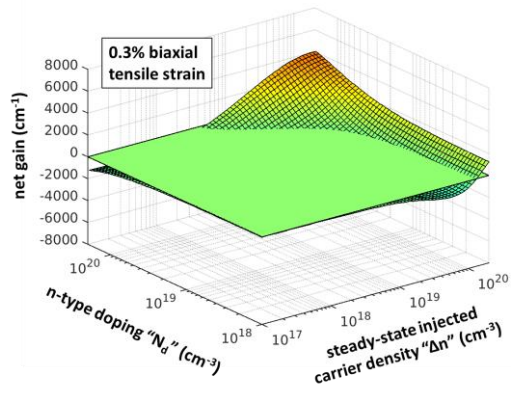
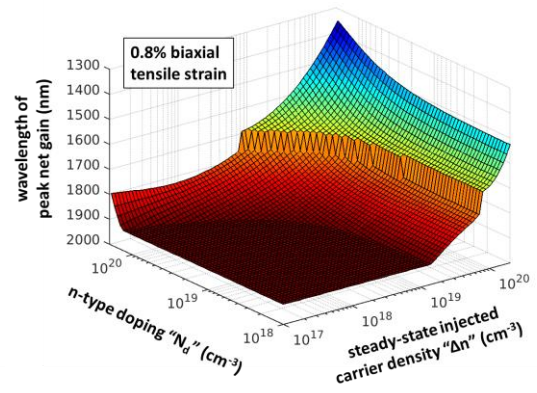
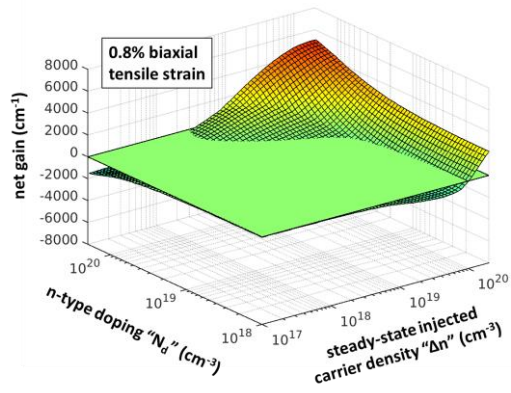
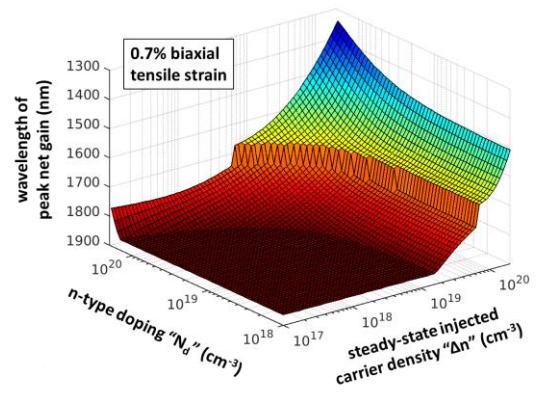
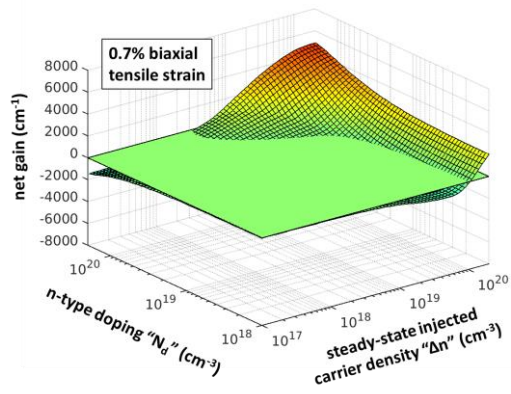
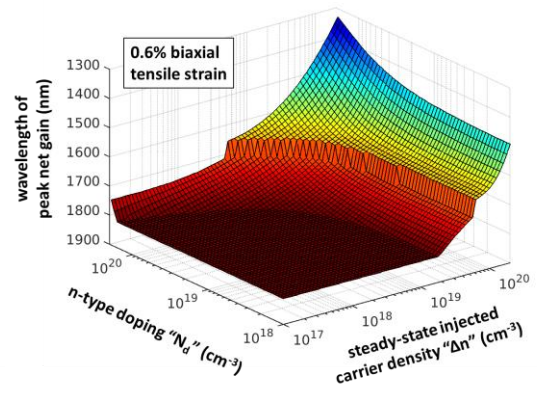
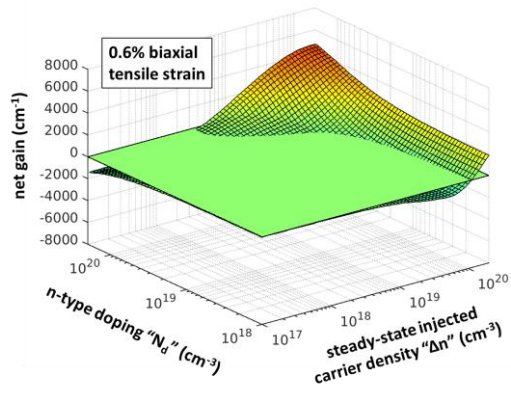
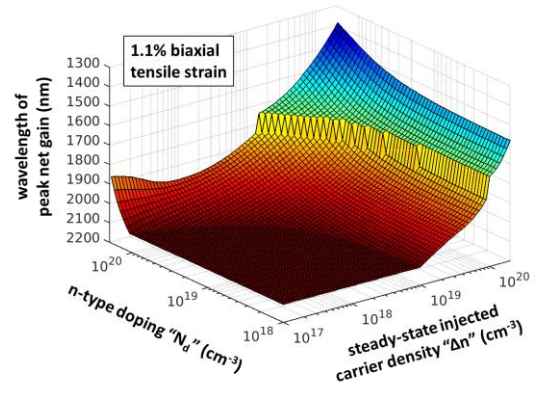
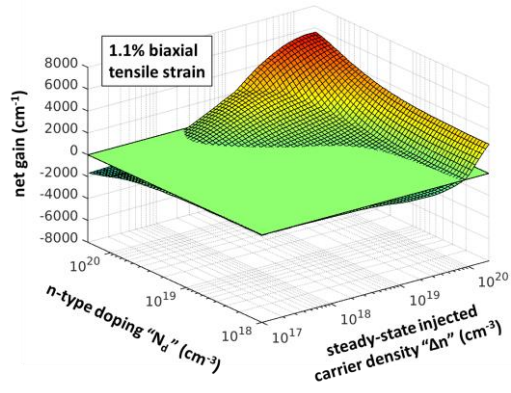
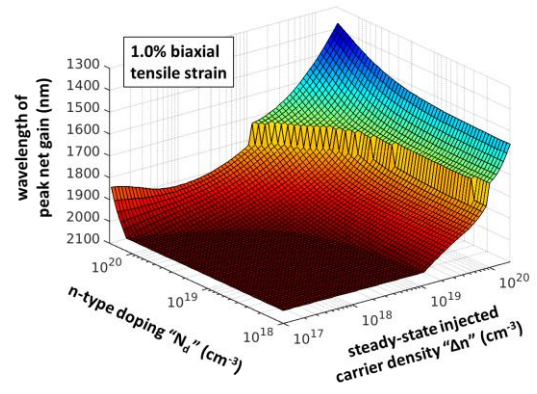
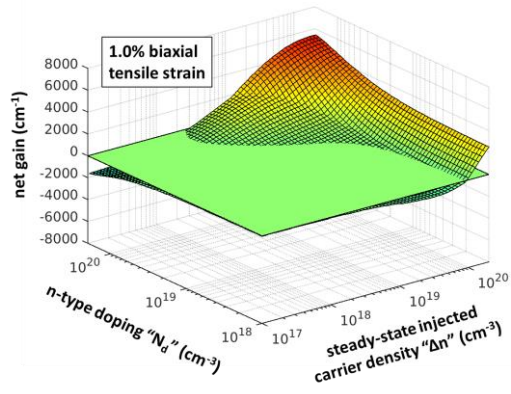
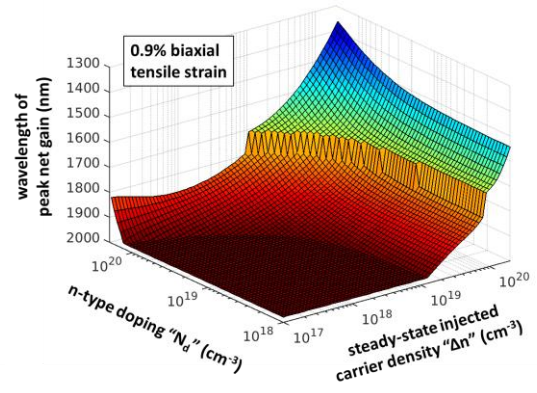
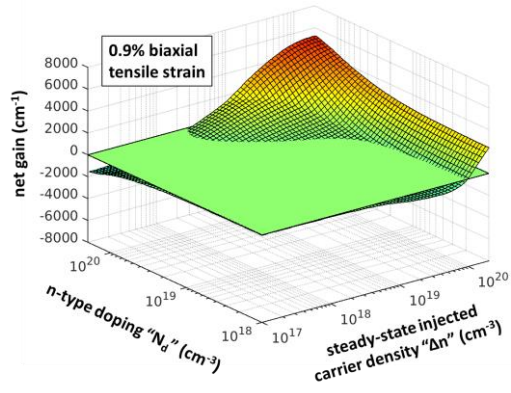


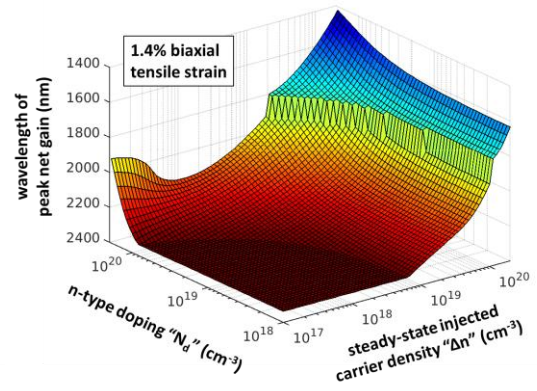
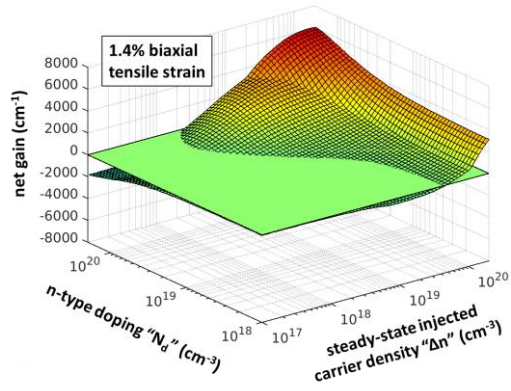
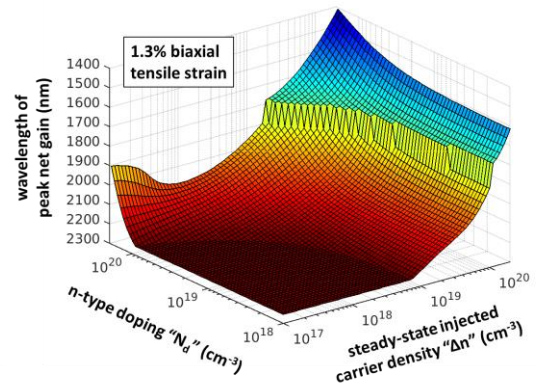
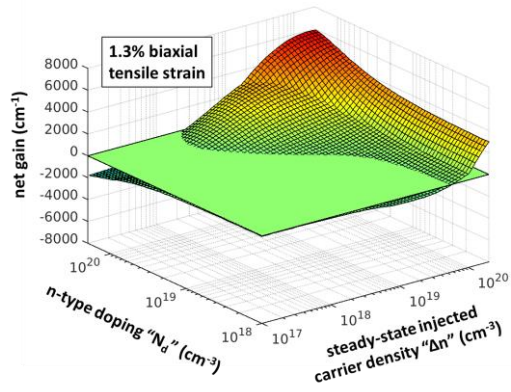
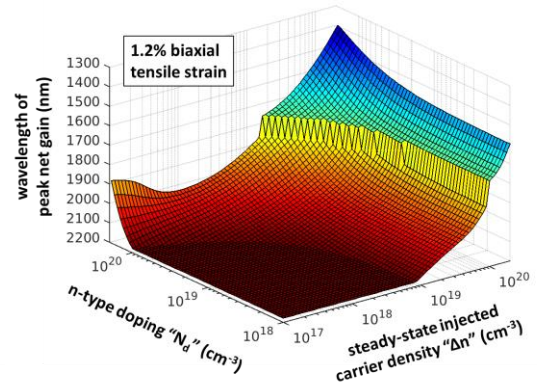
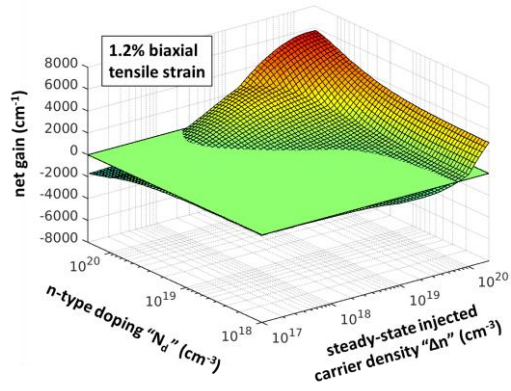
Figure A-2. Optical net gain of germanium (left) computed at the wavelength of maximum net gain (right), both given as a function of n-type doping and steady-state injected carrier density, and shown for an extended range of biaxial tensile strain values.

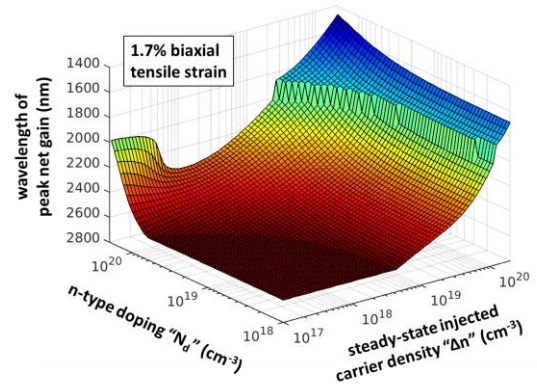
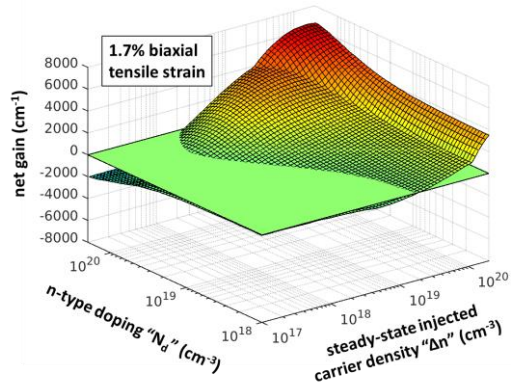
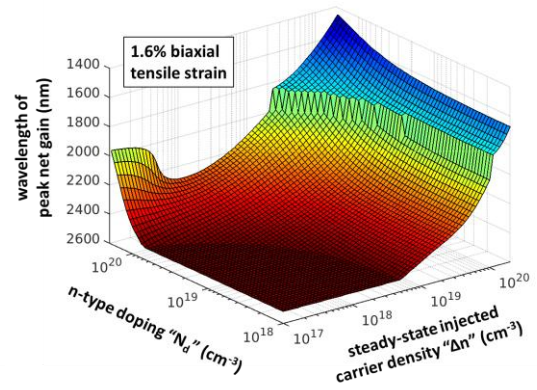
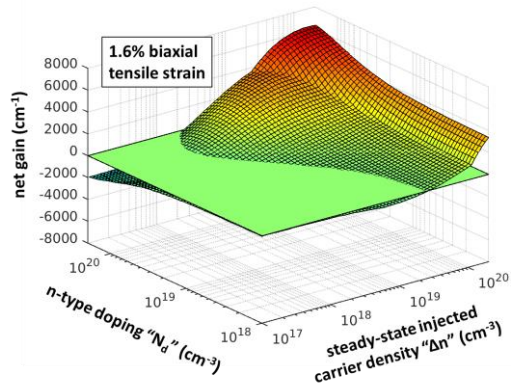
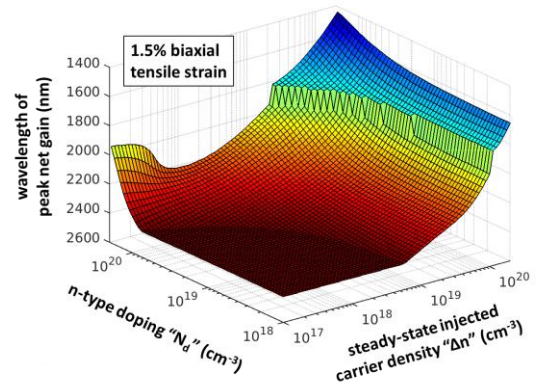
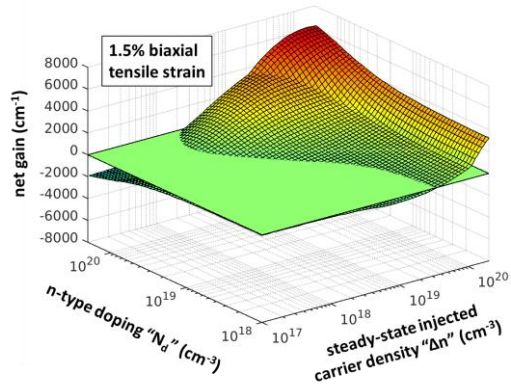


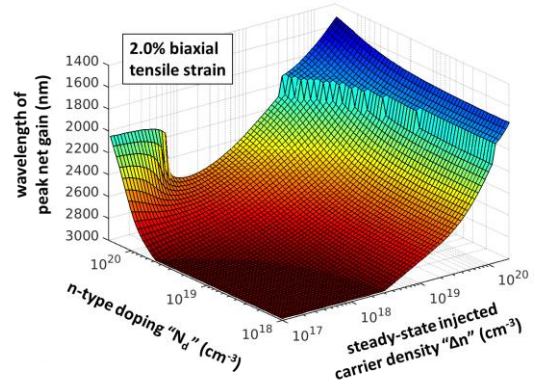
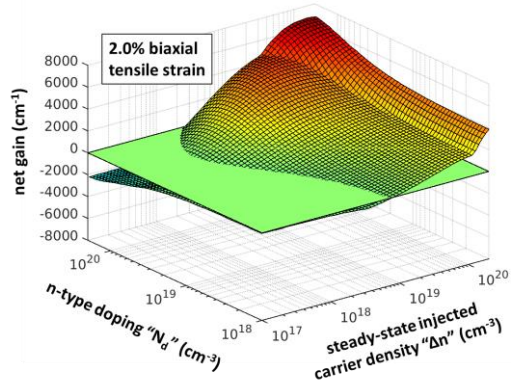
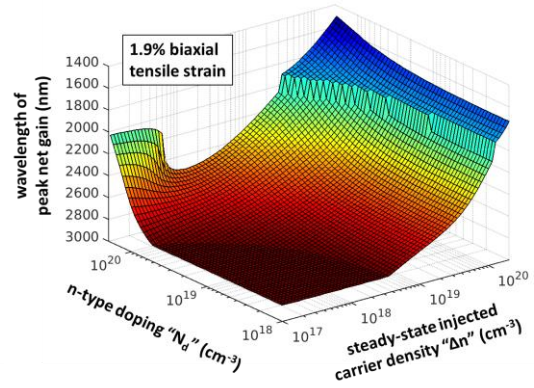
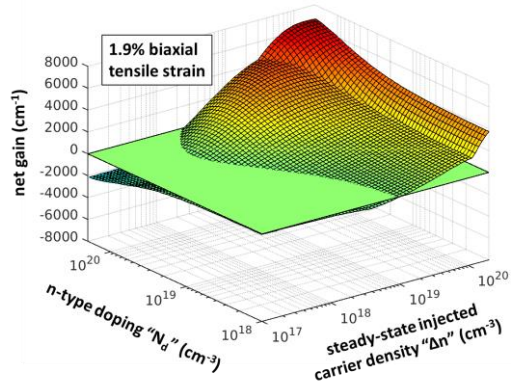
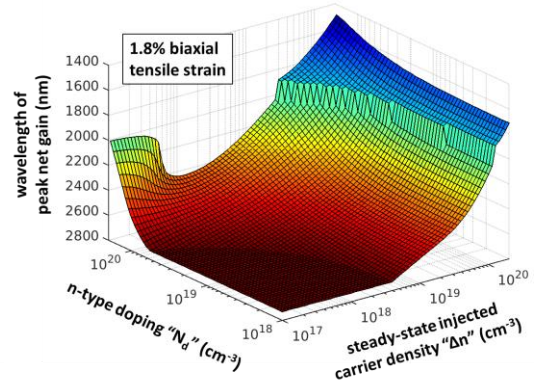
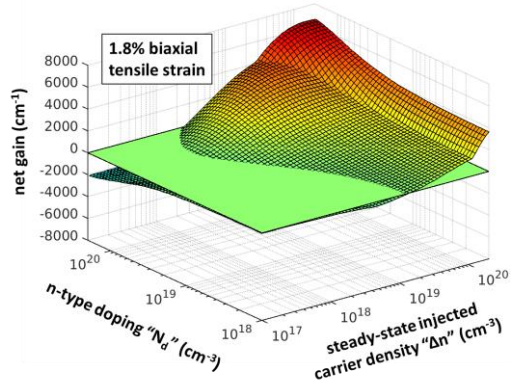


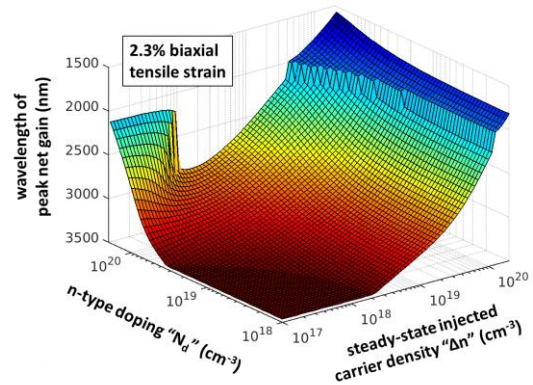
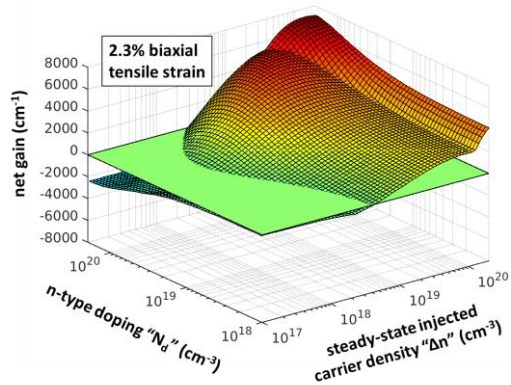
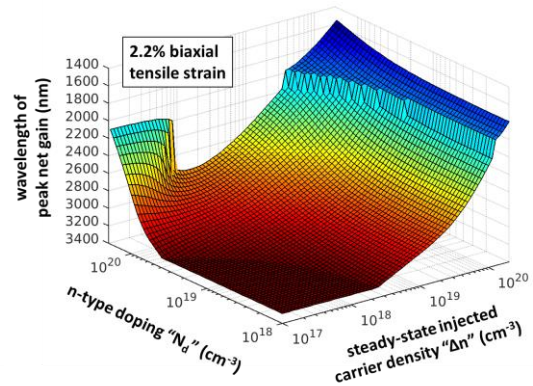
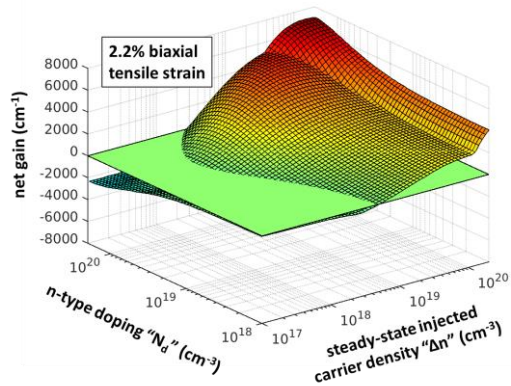
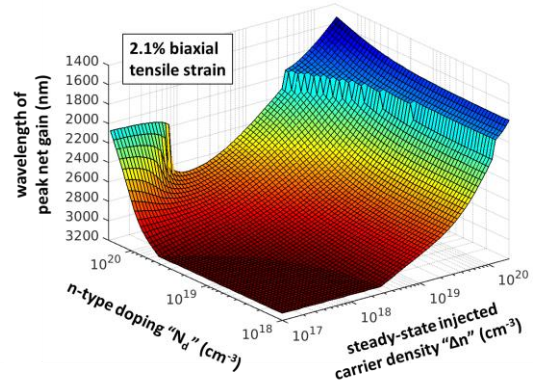
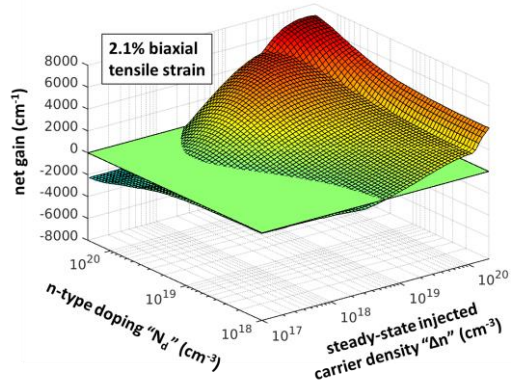


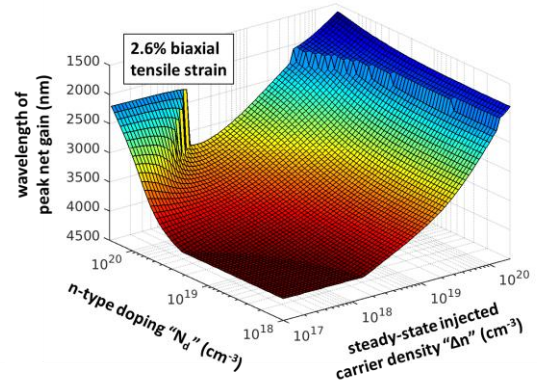
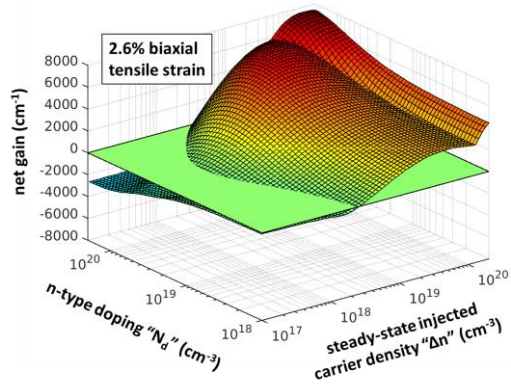
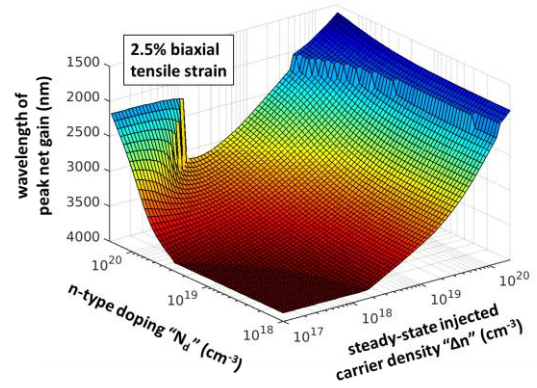
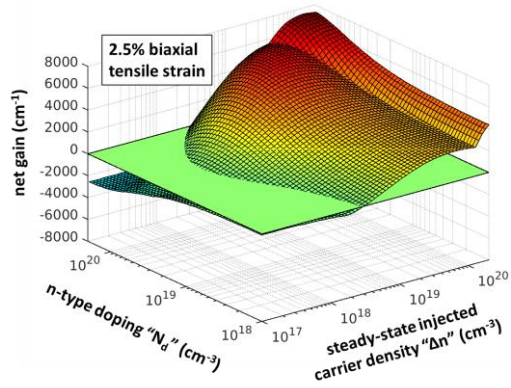
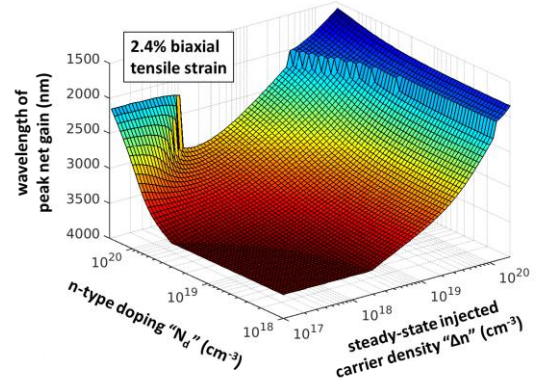
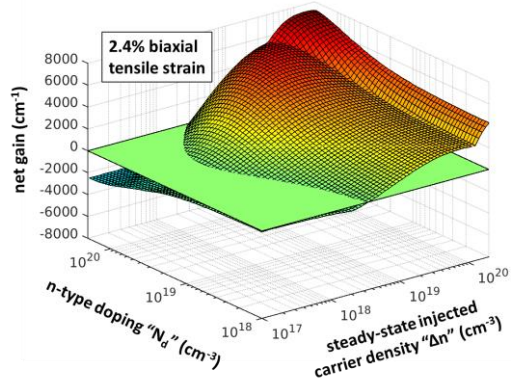


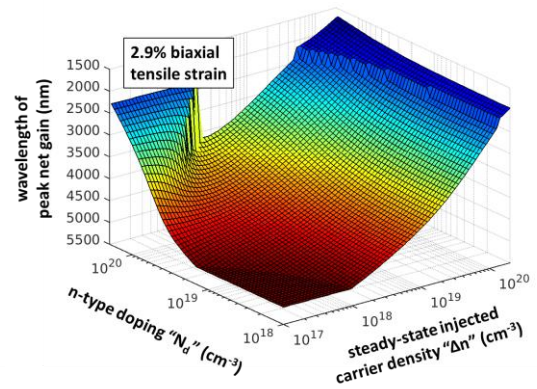
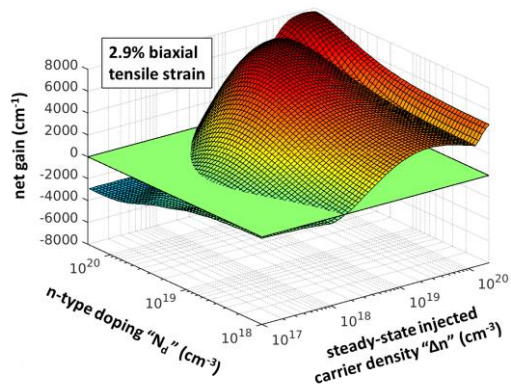
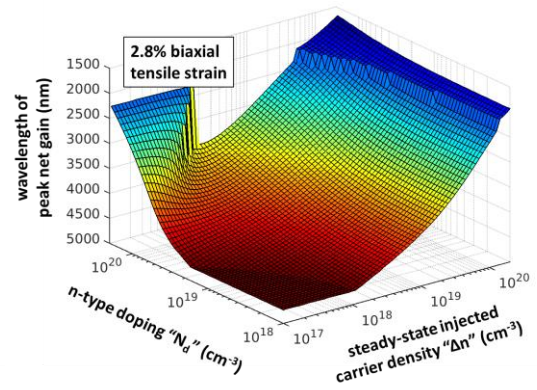
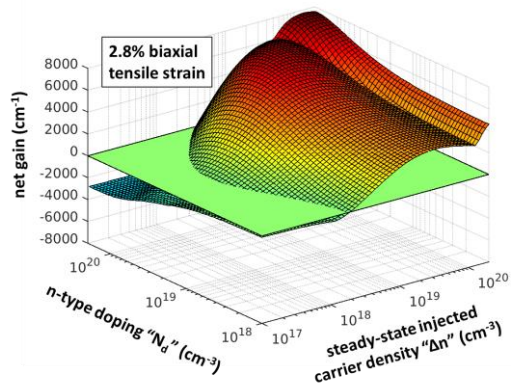
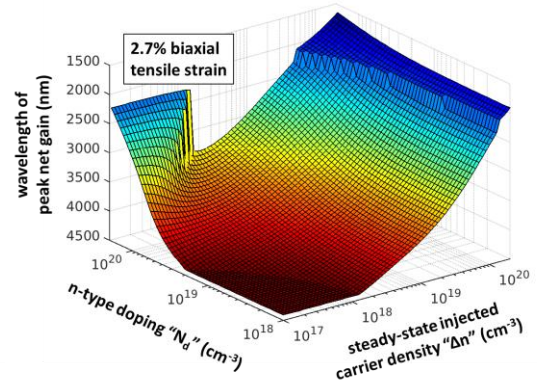
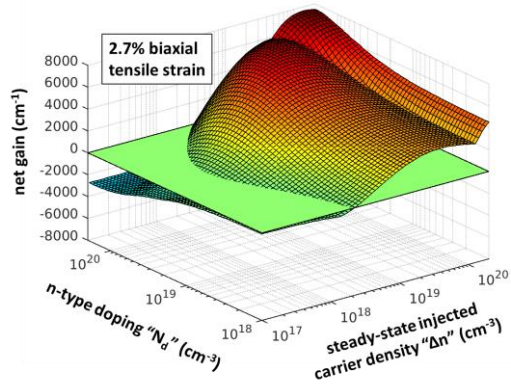












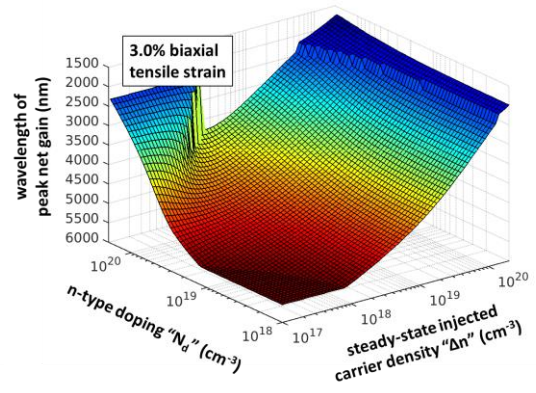
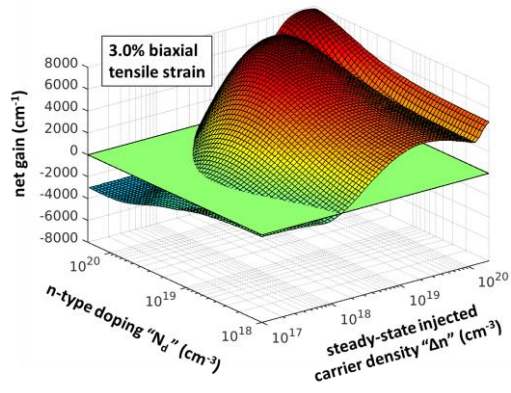
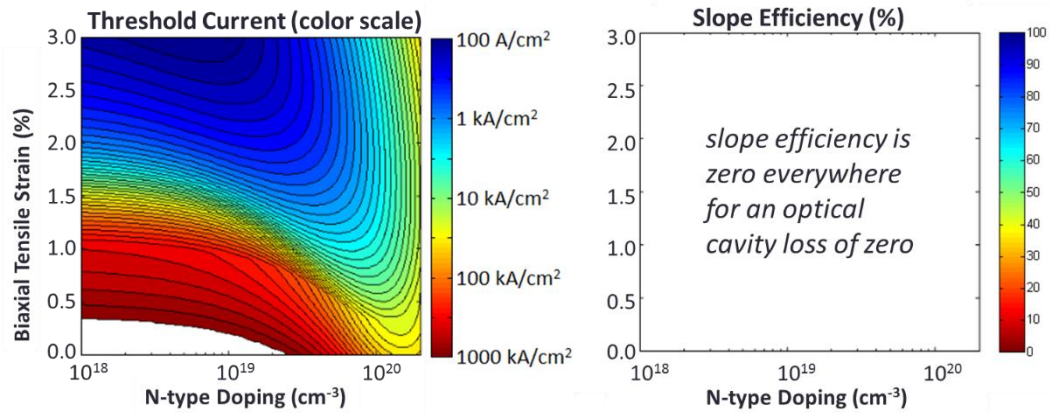
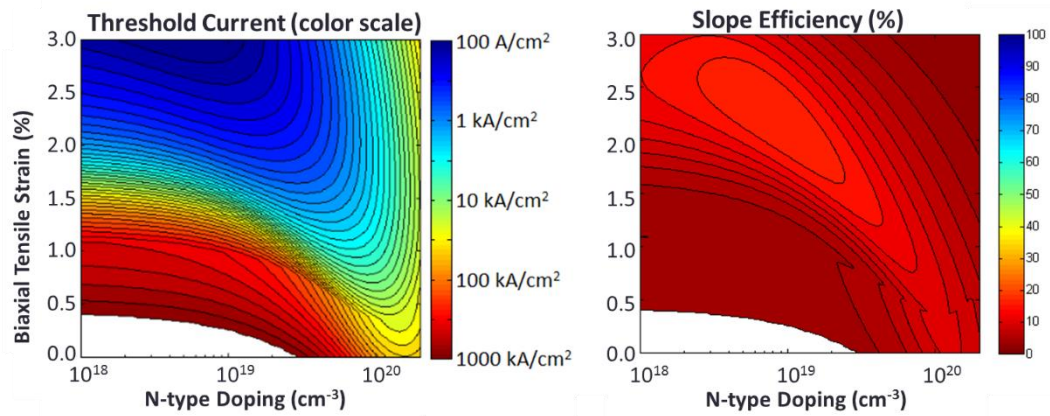


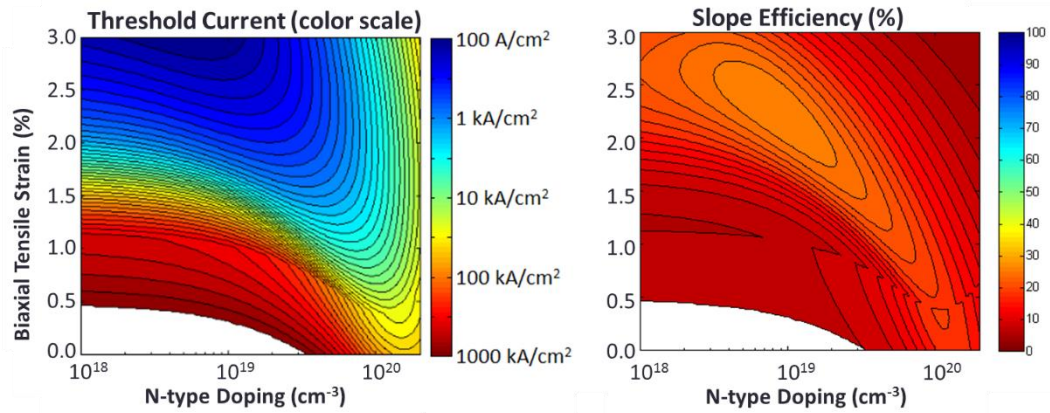
Figure A-3. Threshold current density (left) and slope efficiency (right) vs. biaxial tensile strain (<100> orientation) and n-type doping, shown for an extended range of optical cavity loss values.



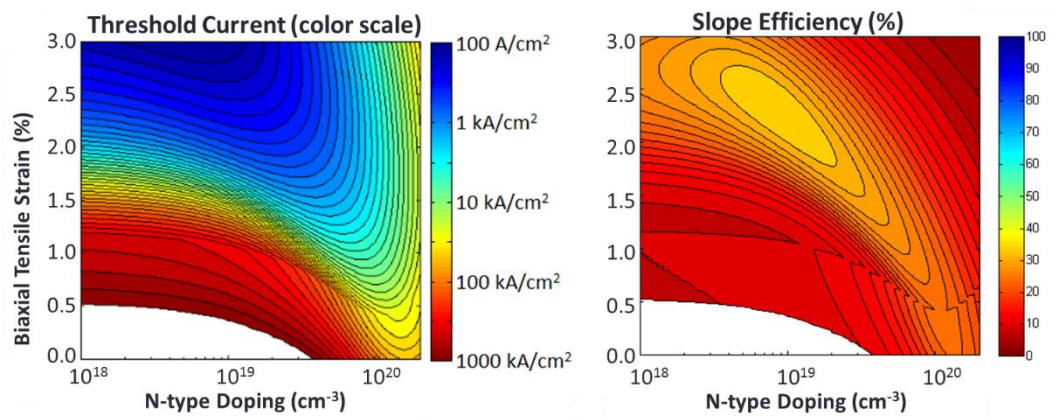
optical cavity out-coupling "loss" = 0 cm⁻¹



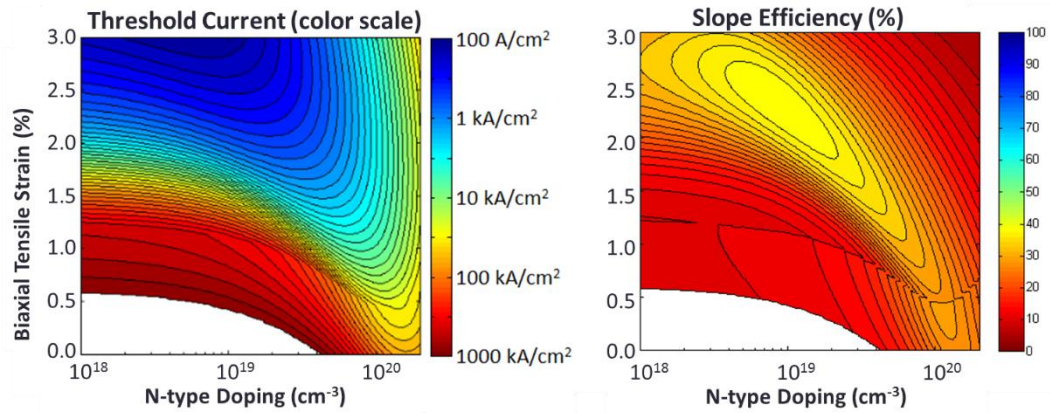
optical cavity out-coupling "loss" = 100 cm⁻¹



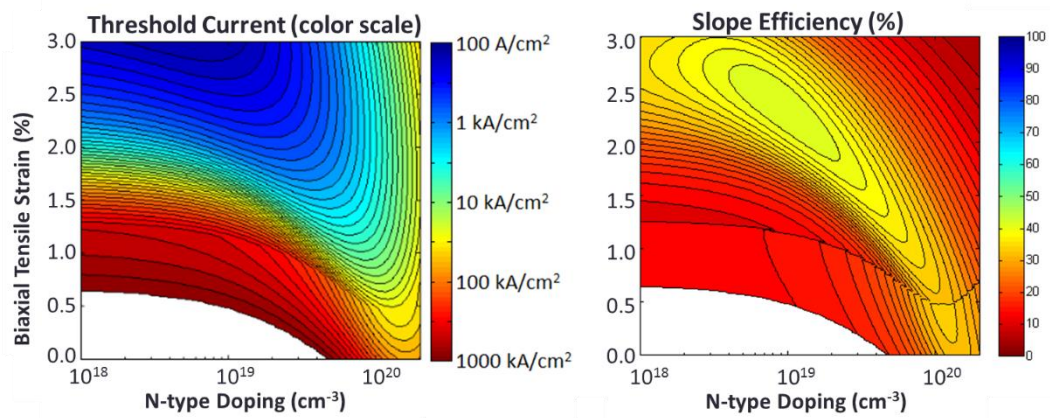
optical cavity out-coupling "loss" = 200 cm^{-1}



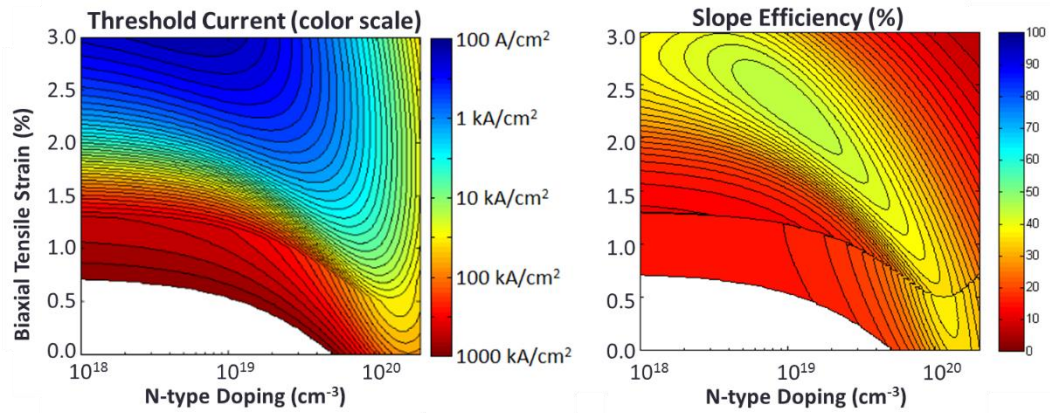
optical cavity out-coupling "loss" = 300 cm^{-1}



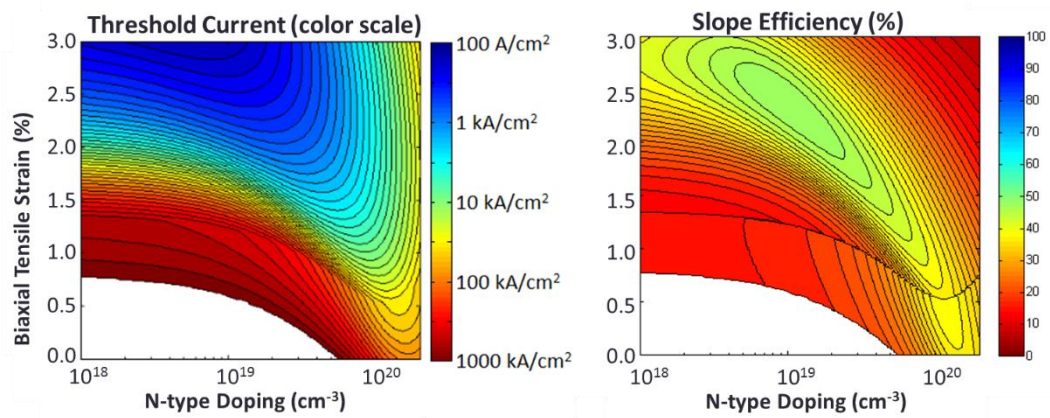
optical cavity out-coupling "loss" = 400 cm^{-1}



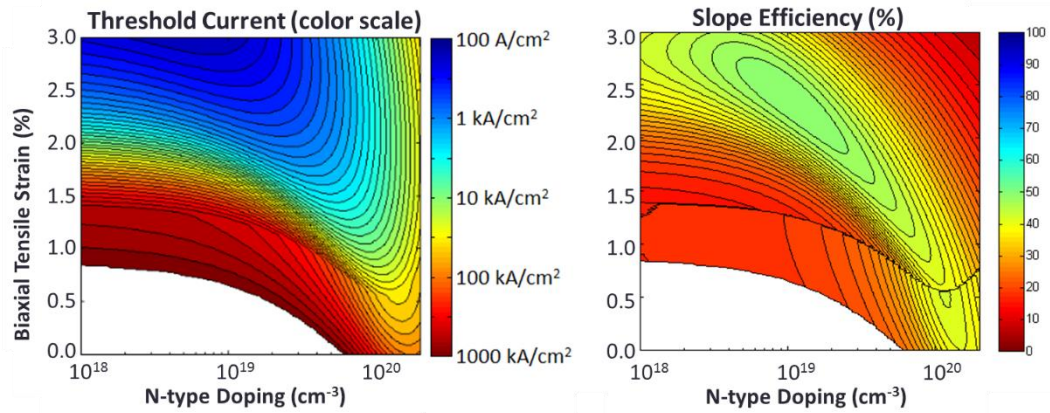
optical cavity out-coupling "loss" = 500 cm^{-1}



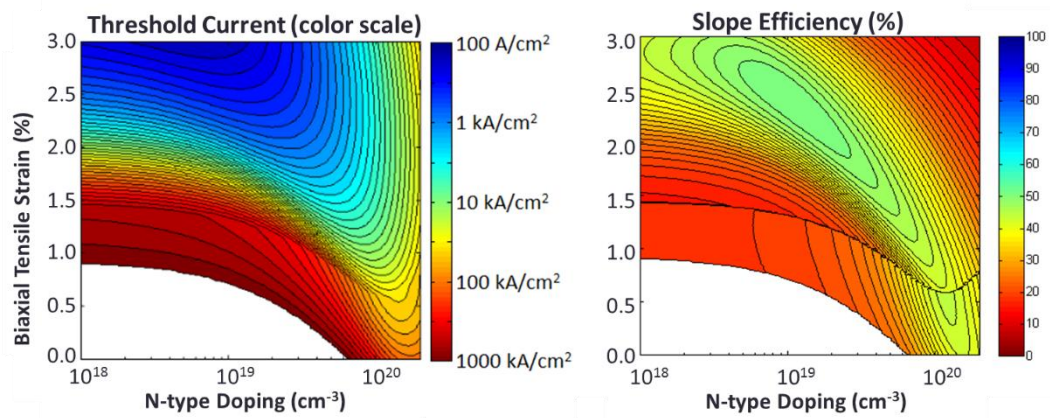
optical cavity out-coupling "loss" = 600 cm^{-1}



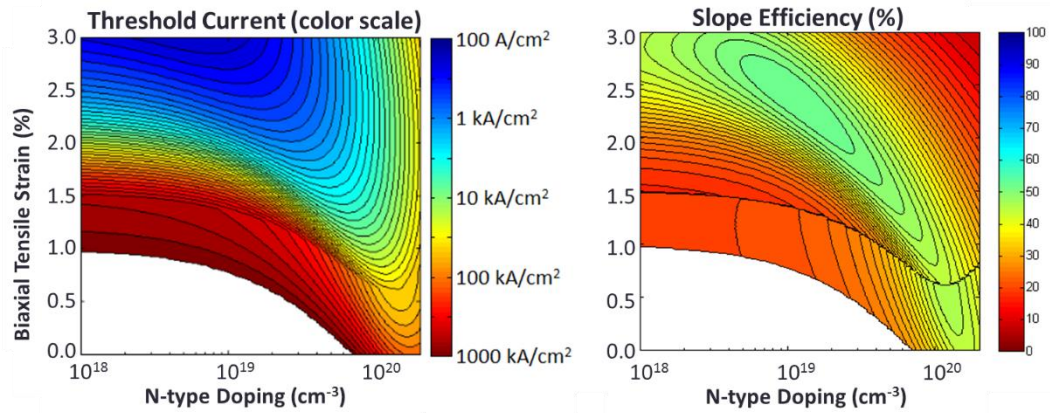
optical cavity out-coupling "loss" = 700 cm^{-1}



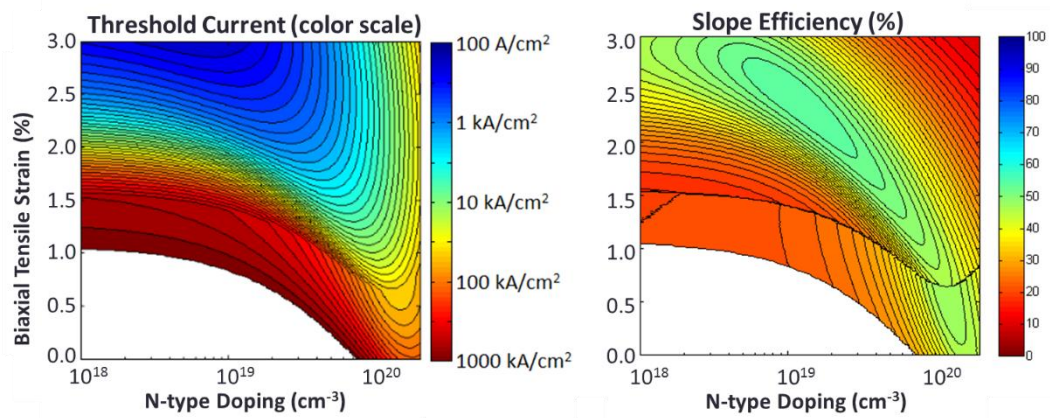
optical cavity out-coupling "loss" = 800 cm^{-1}



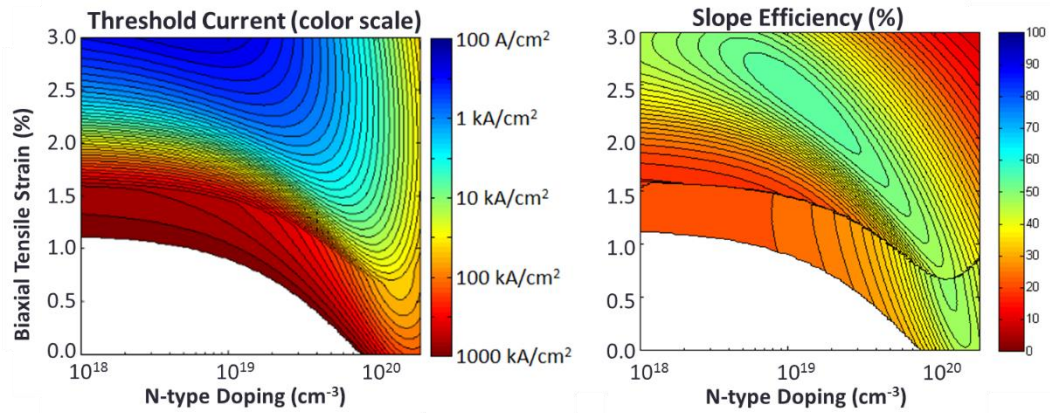
optical cavity out-coupling "loss" = 900 cm^{-1}



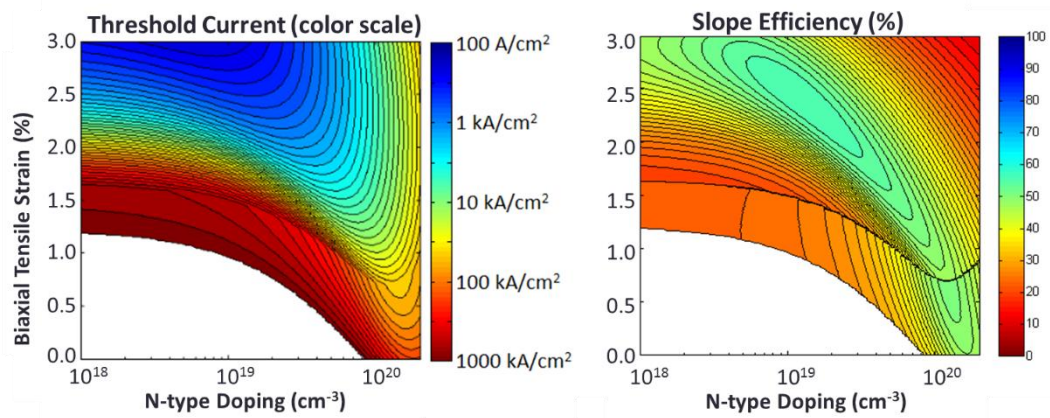
optical cavity out-coupling "loss" = 1000 cm^{-1}



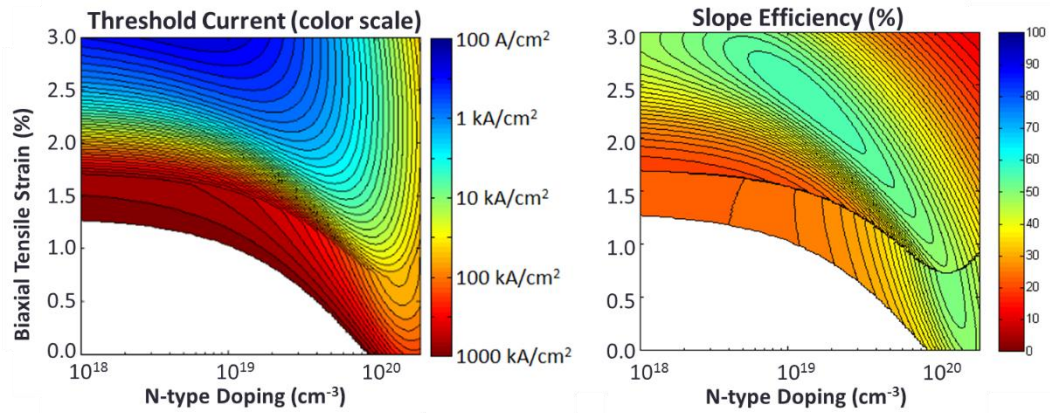
optical cavity out-coupling "loss" = 1100 cm^{-1}



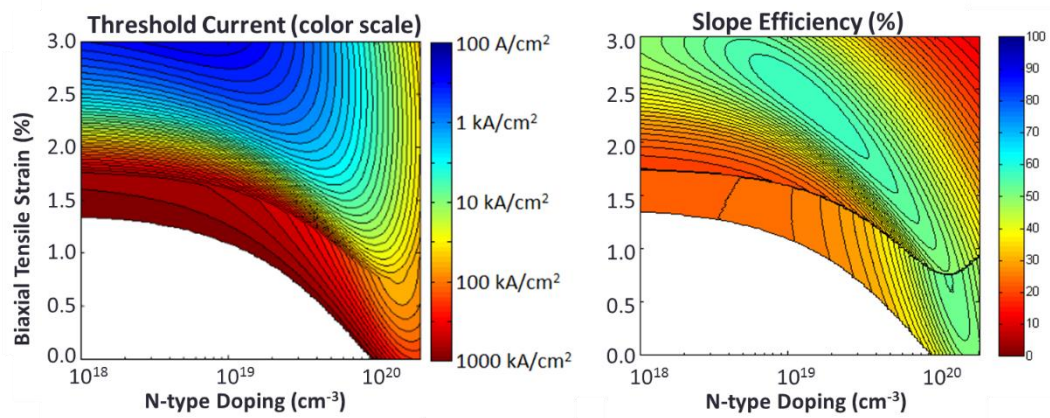
optical cavity out-coupling "loss" = 1200 cm^{-1}



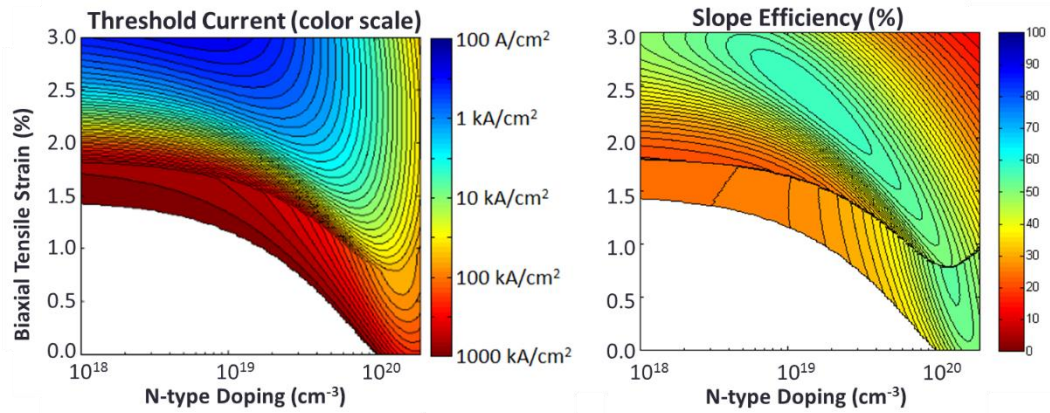
optical cavity out-coupling "loss" = 1300 cm^{-1}



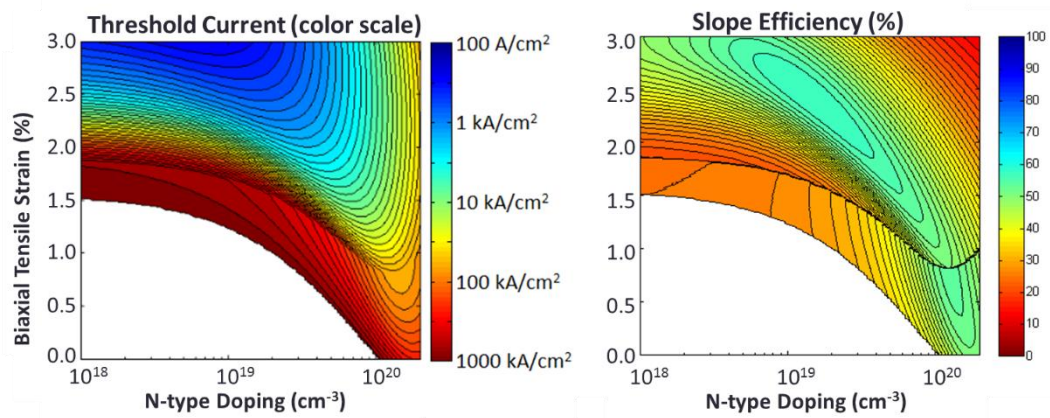
optical cavity out-coupling "loss" = 1400 cm^{-1}



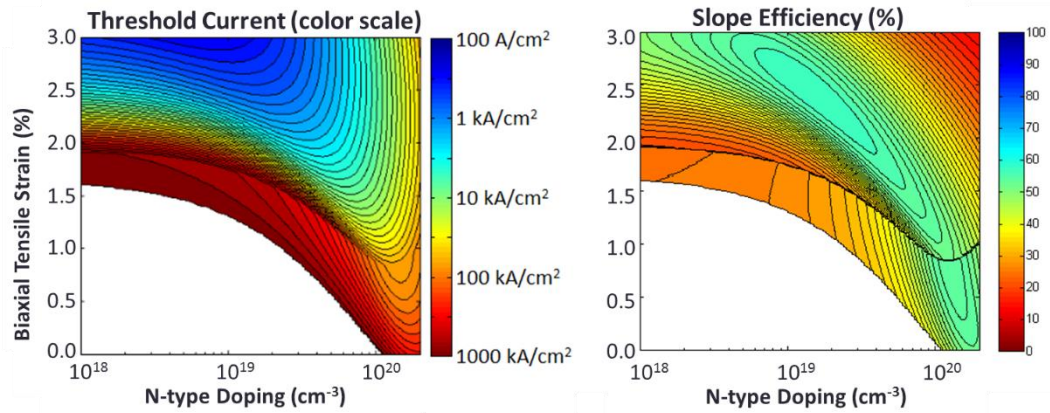
optical cavity out-coupling "loss" = 1500 cm^{-1}



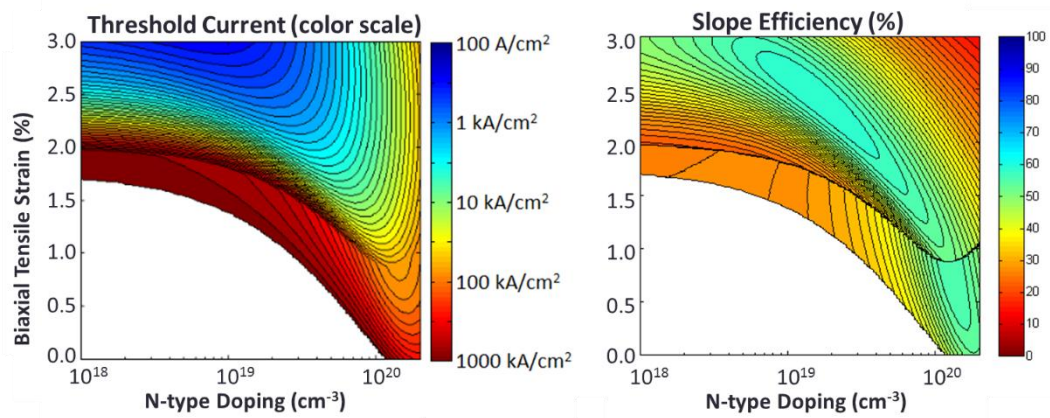
optical cavity out-coupling "loss" = 1600 cm^{-1}



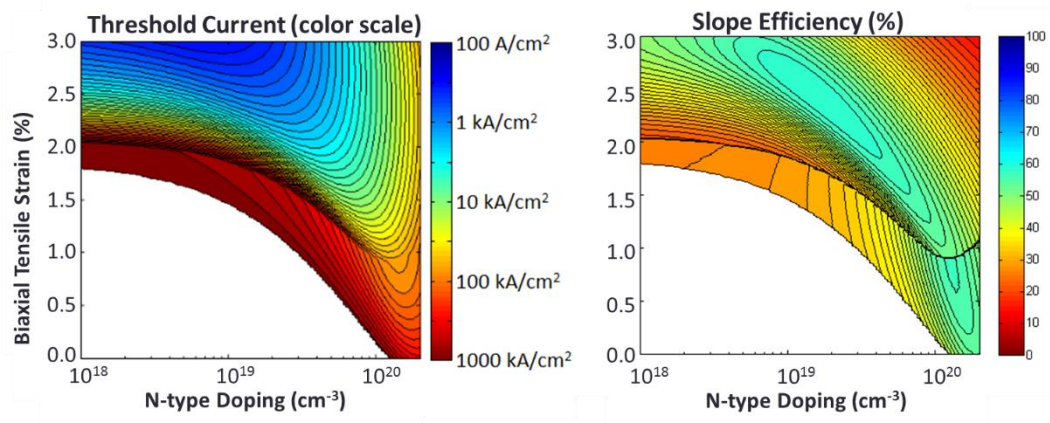
optical cavity out-coupling "loss" = 1700 cm^{-1}



optical cavity out-coupling "loss" = 1800 cm^{-1}

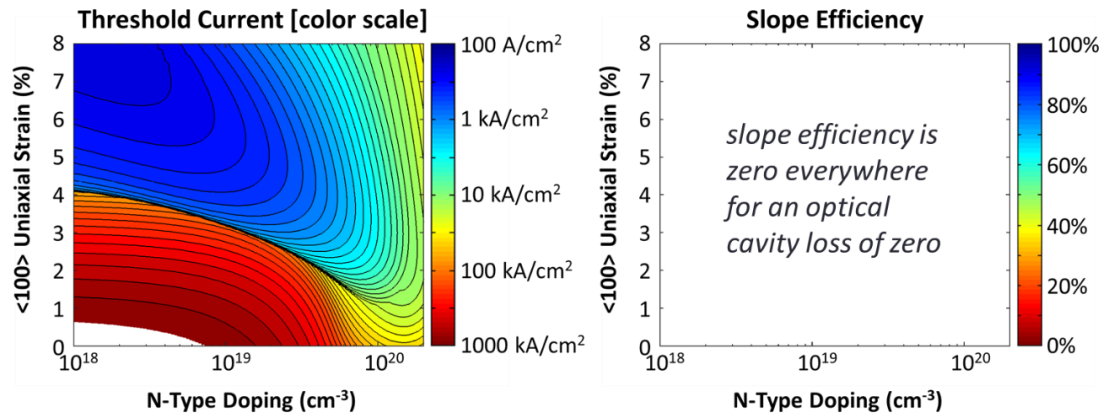


optical cavity out-coupling "loss" = 1900 cm^{-1}

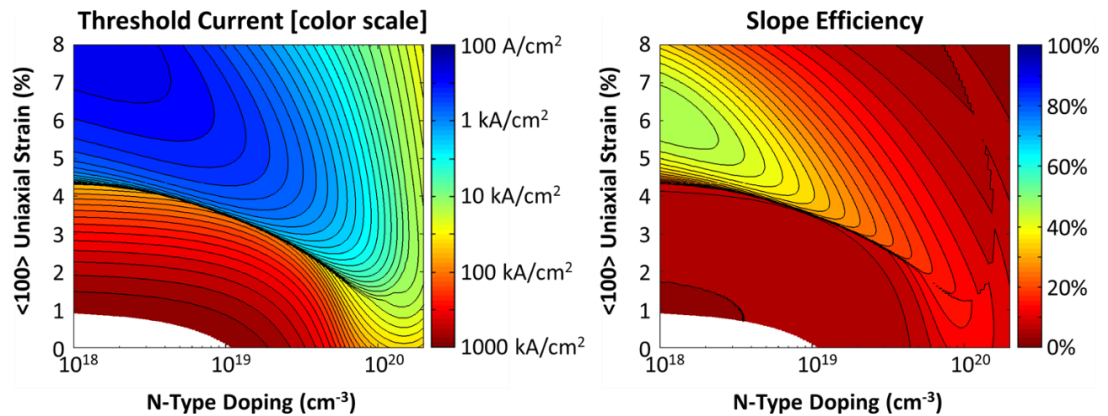


optical cavity out-coupling "loss" = 2000 cm⁻¹

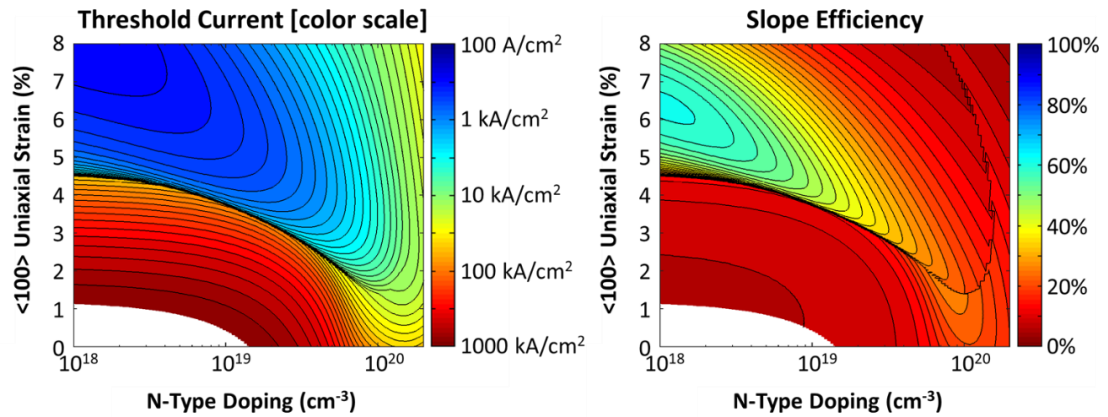
Figure A-4. Threshold current density (left) and slope efficiency (right) vs. uniaxial tensile strain (<100> orientation) and n-type doping, shown for an extended range of optical cavity loss values.



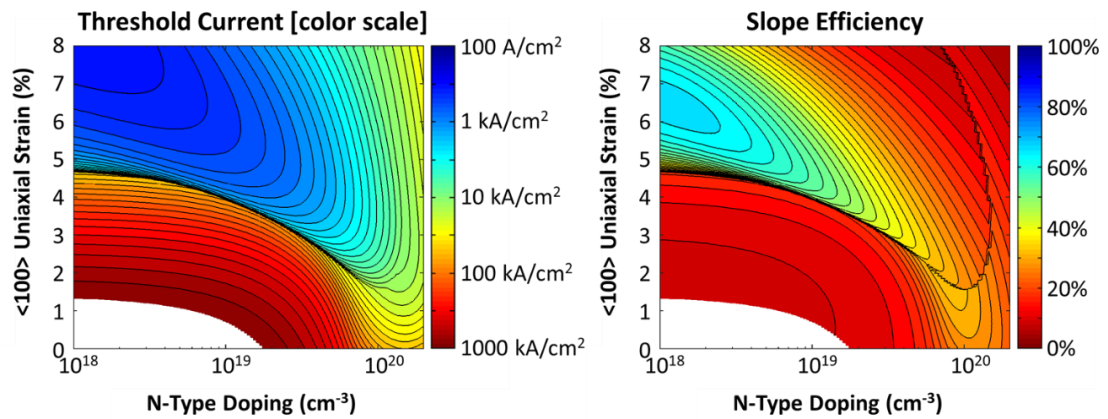
optical cavity out-coupling "loss" = 0 cm⁻¹



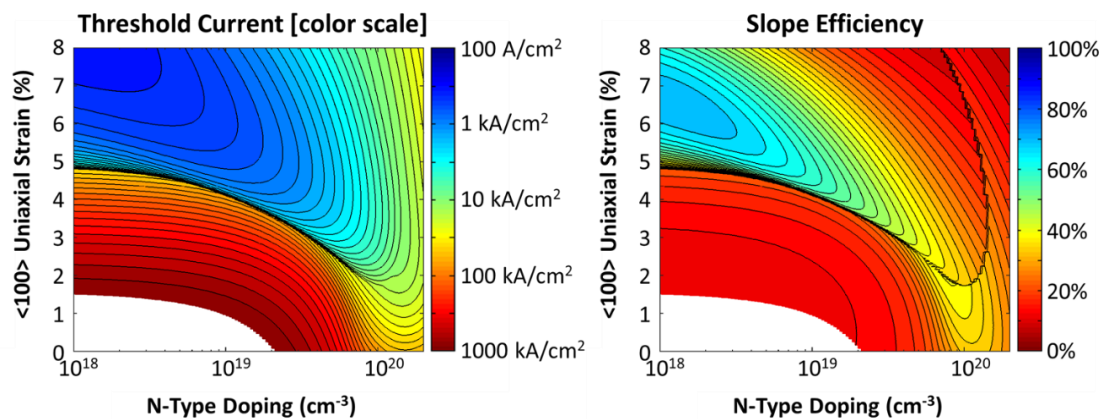
optical cavity out-coupling "loss" = 100 cm⁻¹



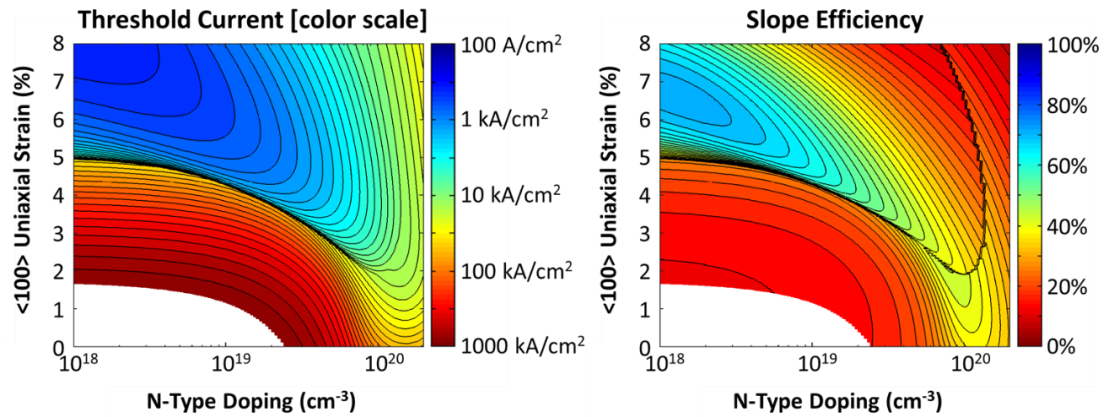
optical cavity out-coupling “loss” = 200 cm⁻¹



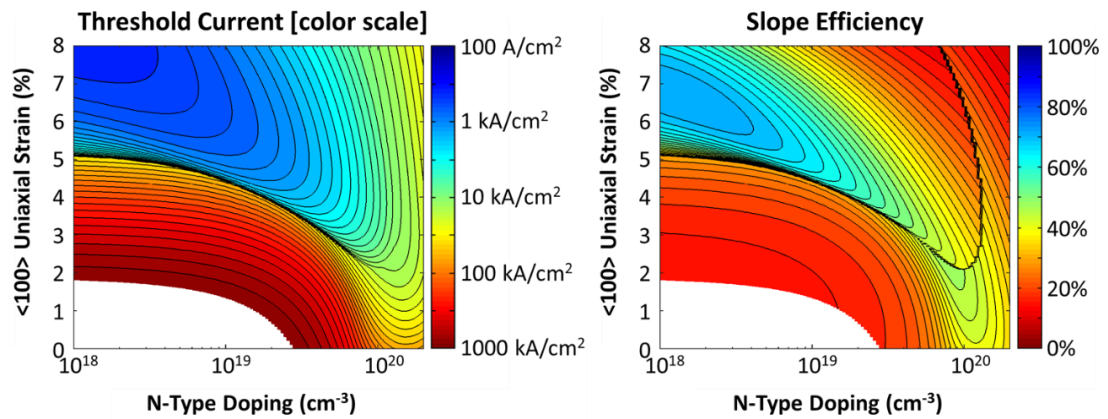
optical cavity out-coupling “loss” = 300 cm⁻¹



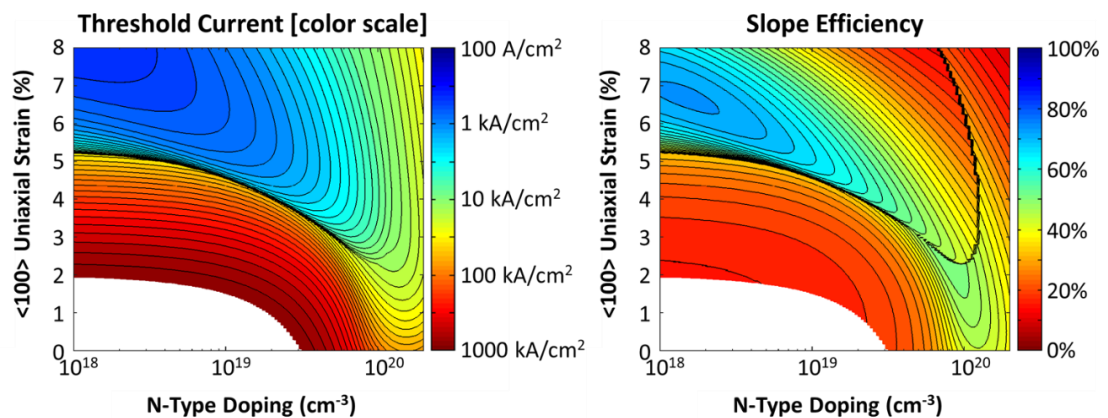
optical cavity out-coupling “loss” = 400 cm⁻¹



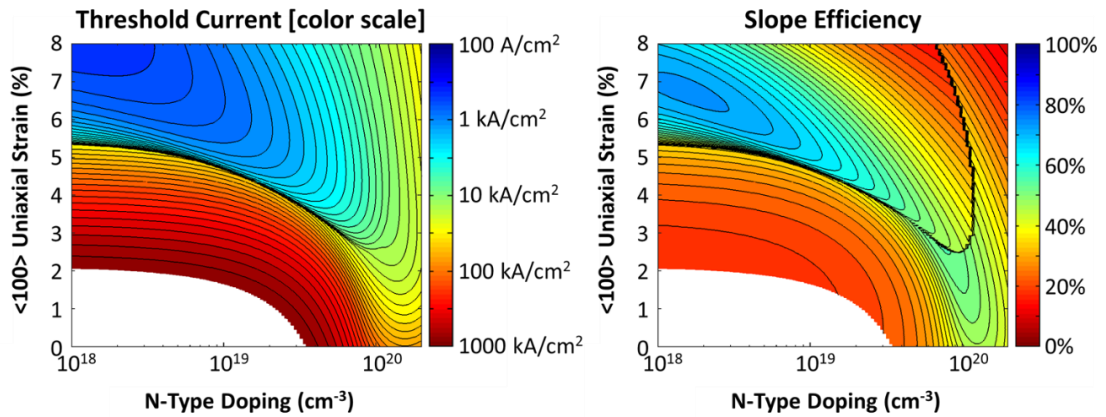
optical cavity out-coupling “loss” = 500 cm^{-1}



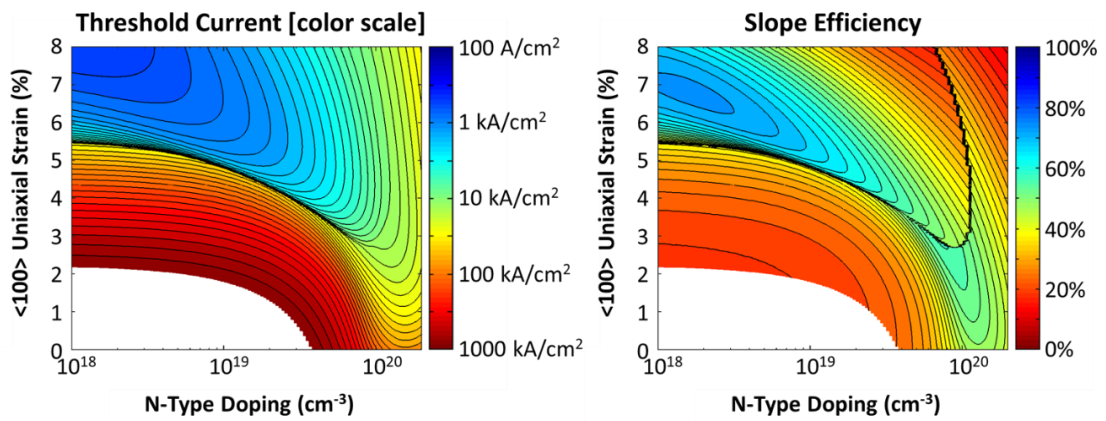
optical cavity out-coupling “loss” = 600 cm^{-1}



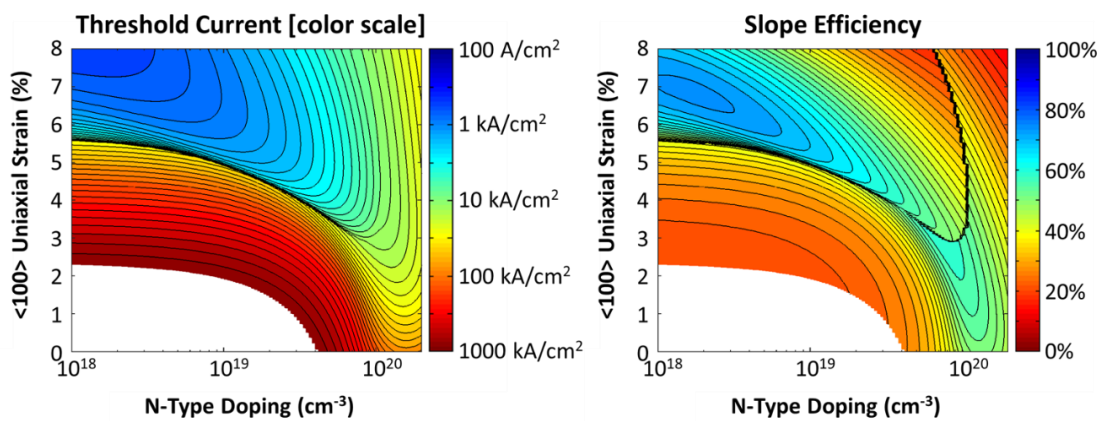
optical cavity out-coupling “loss” = 700 cm^{-1}



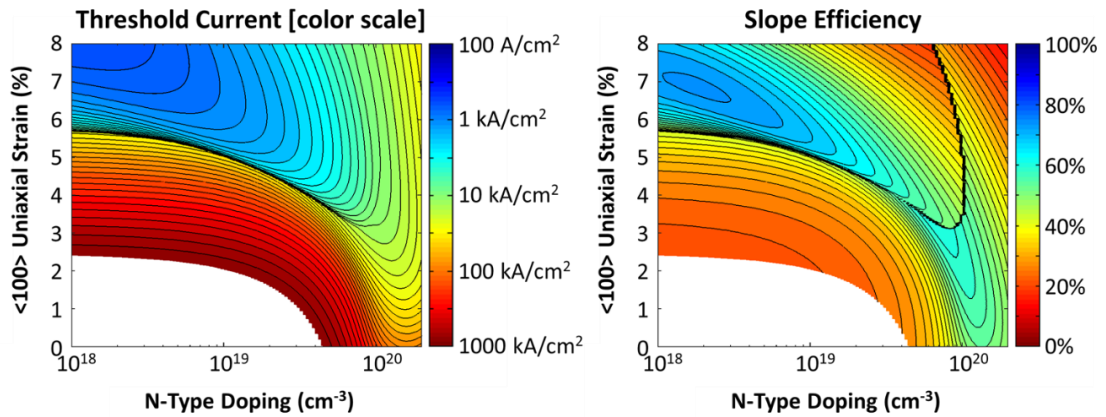
optical cavity out-coupling “loss” = 800 cm^{-1}



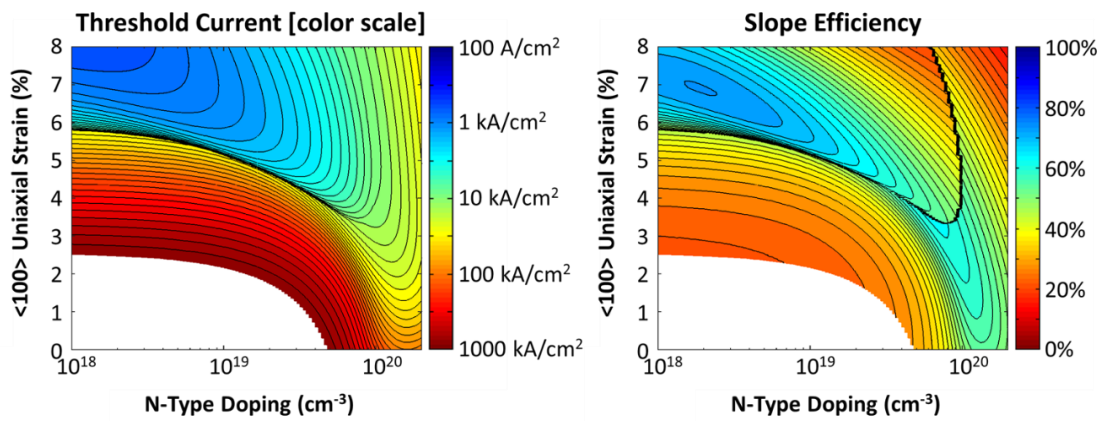
optical cavity out-coupling “loss” = 900 cm^{-1}



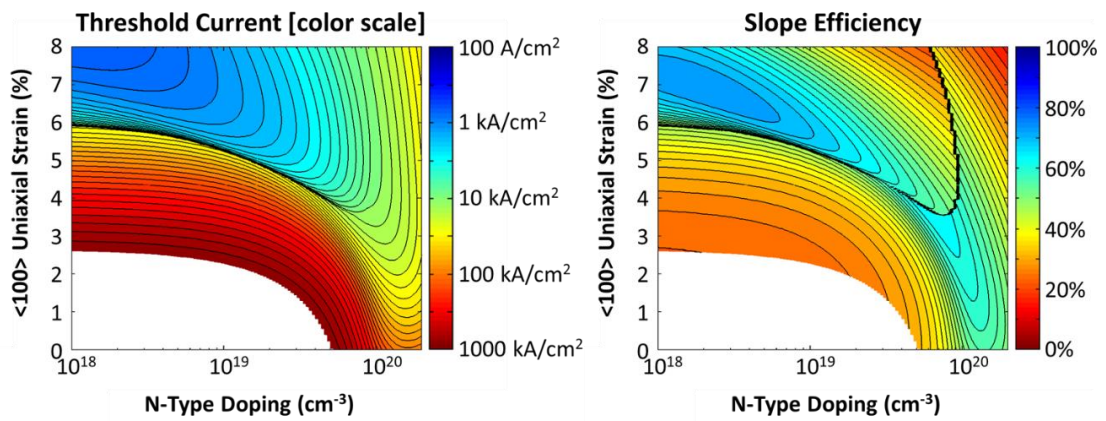
optical cavity out-coupling “loss” = 1000 cm^{-1}



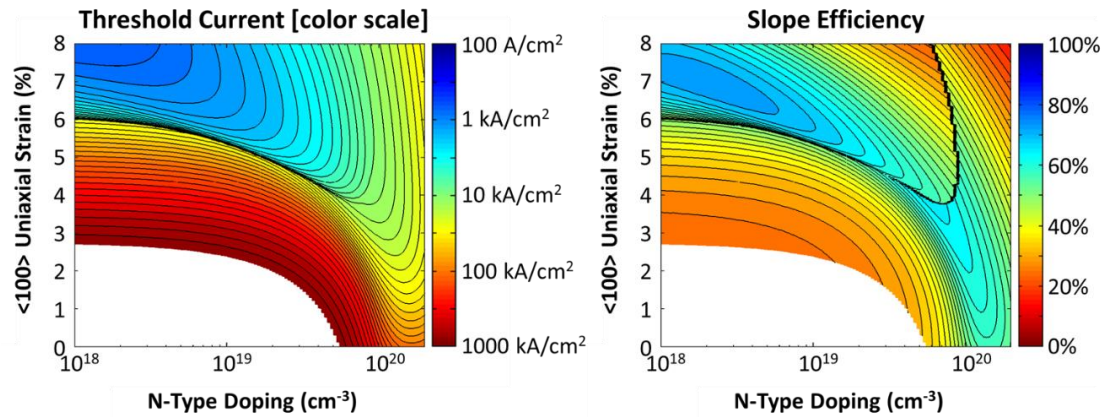
optical cavity out-coupling “loss” = 1100 cm^{-1}



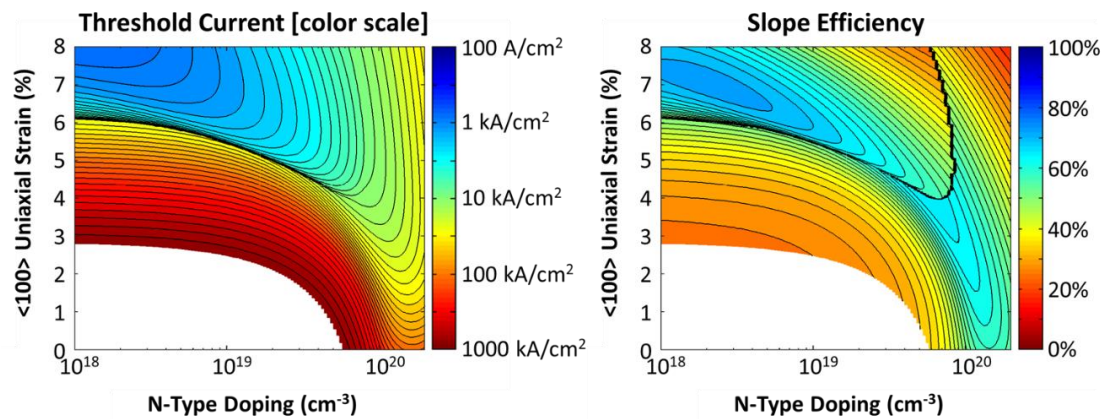
optical cavity out-coupling “loss” = 1200 cm^{-1}



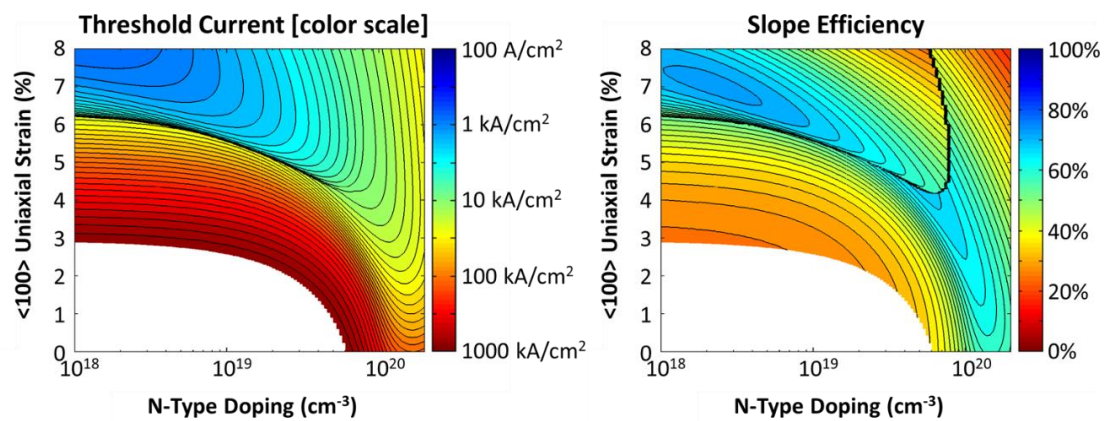
optical cavity out-coupling “loss” = 1300 cm^{-1}



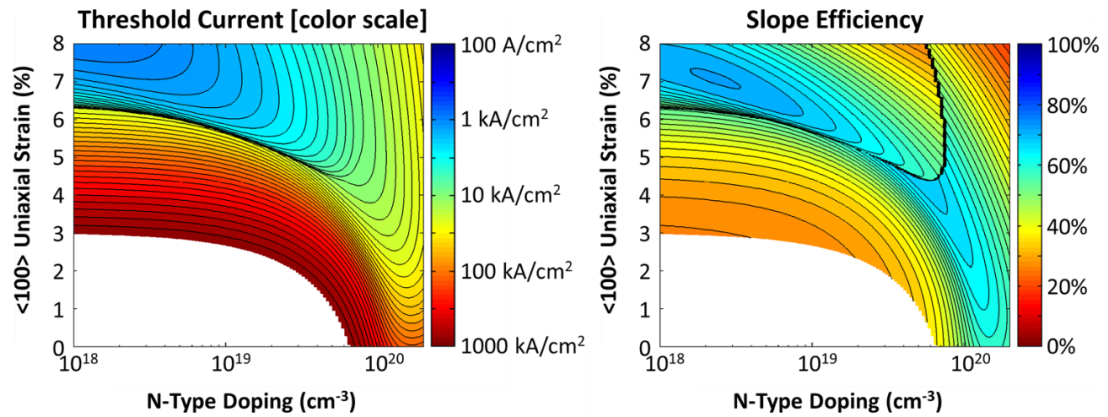
optical cavity out-coupling "loss" = 1400 cm^{-1}



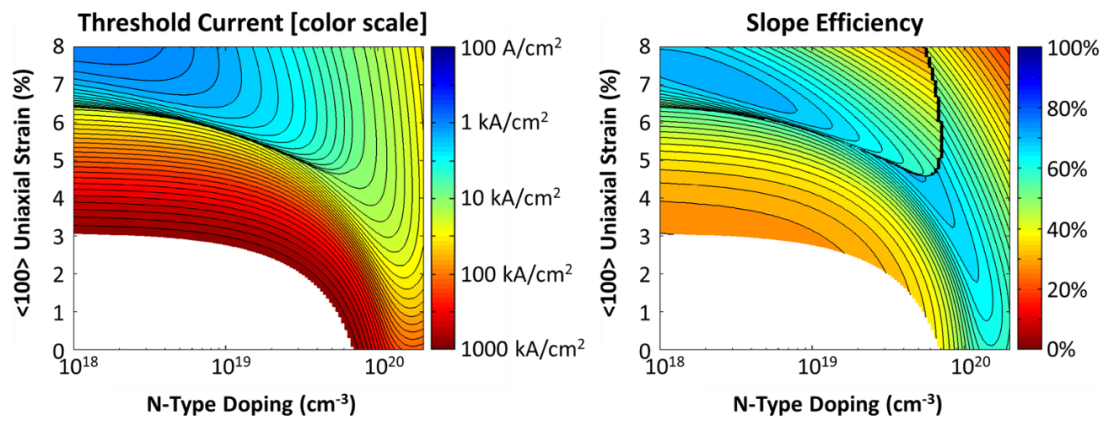
optical cavity out-coupling "loss" = 1500 cm^{-1}



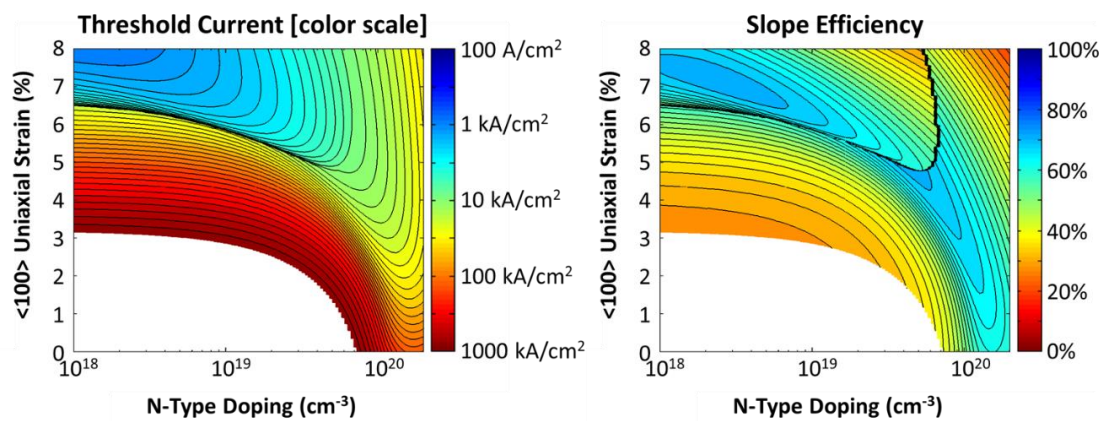
optical cavity out-coupling "loss" = 1600 cm^{-1}



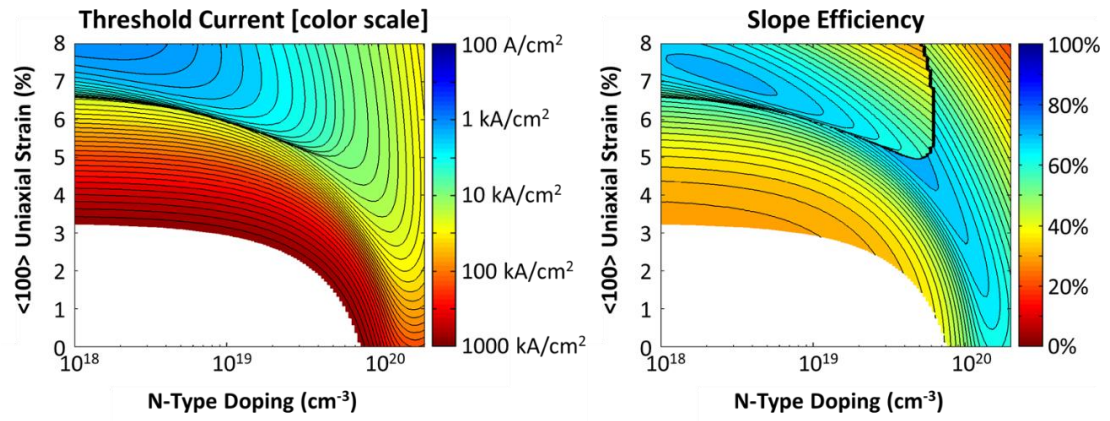
optical cavity out-coupling “loss” = 1700 cm^{-1}



optical cavity out-coupling “loss” = 1800 cm^{-1}

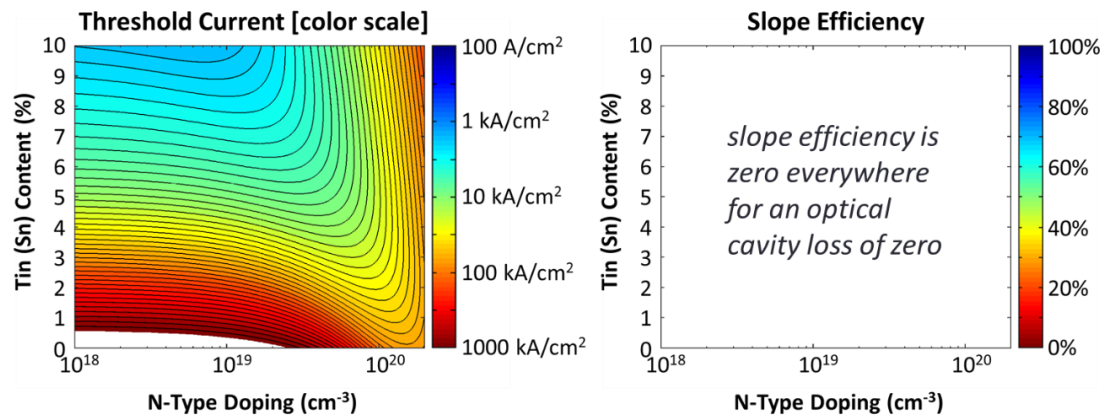


optical cavity out-coupling “loss” = 1900 cm^{-1}

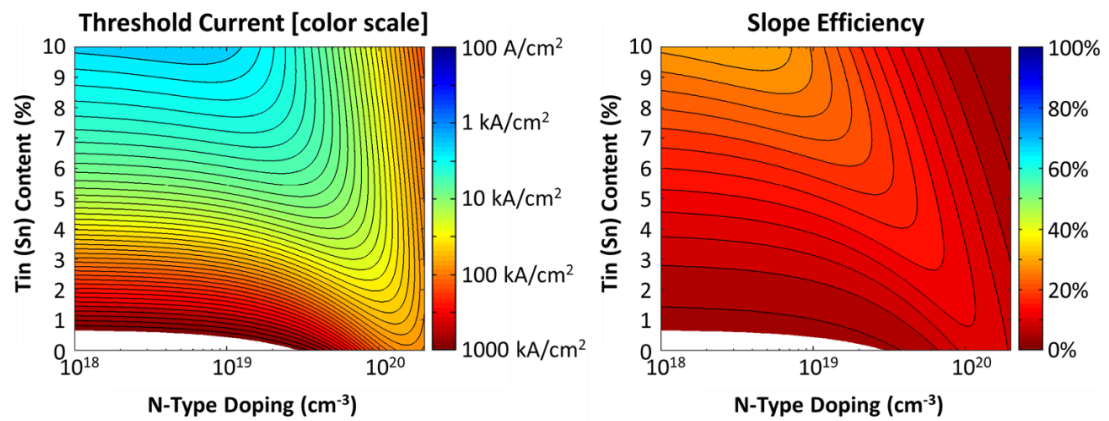


optical cavity out-coupling "loss" = 2000 cm⁻¹

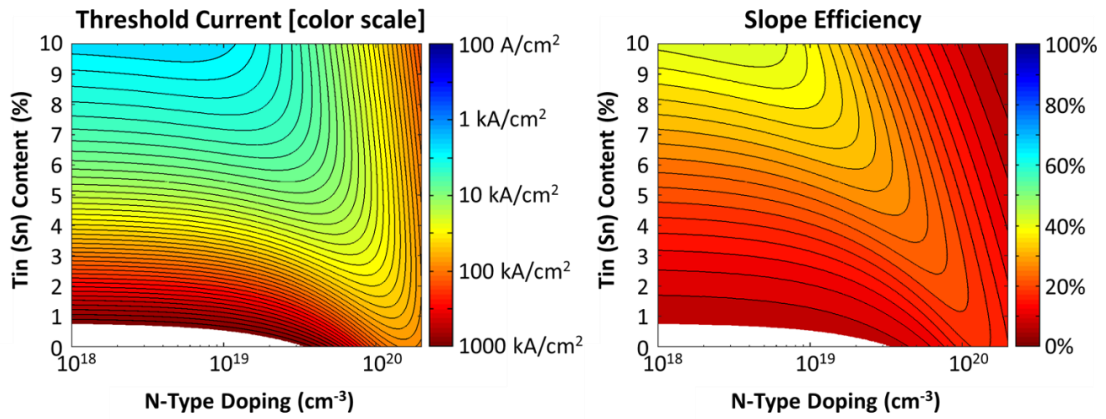
Figure A-5. Threshold current density (left) and slope efficiency (right) of an unstrained germanium-tin laser vs. tin concentration and n-type doping, shown for an extended range of optical cavity loss values.



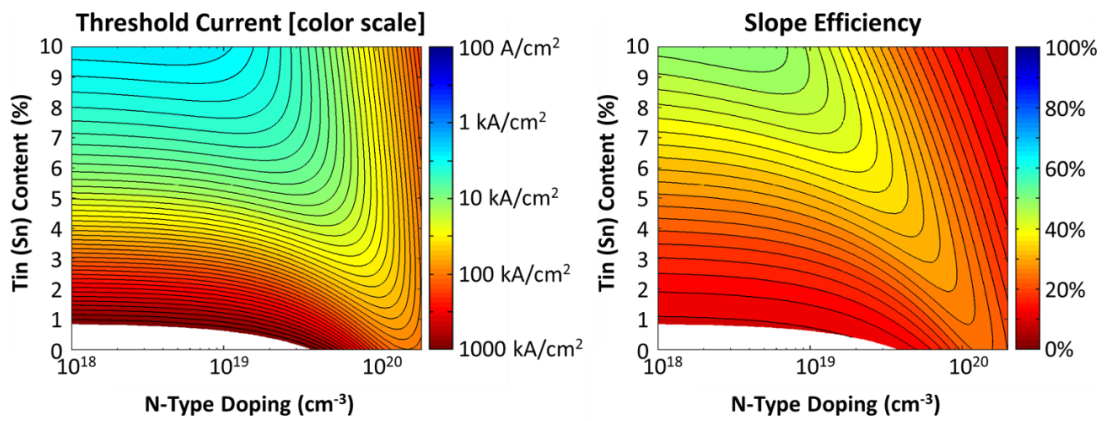
optical cavity out-coupling "loss" = 0 cm⁻¹



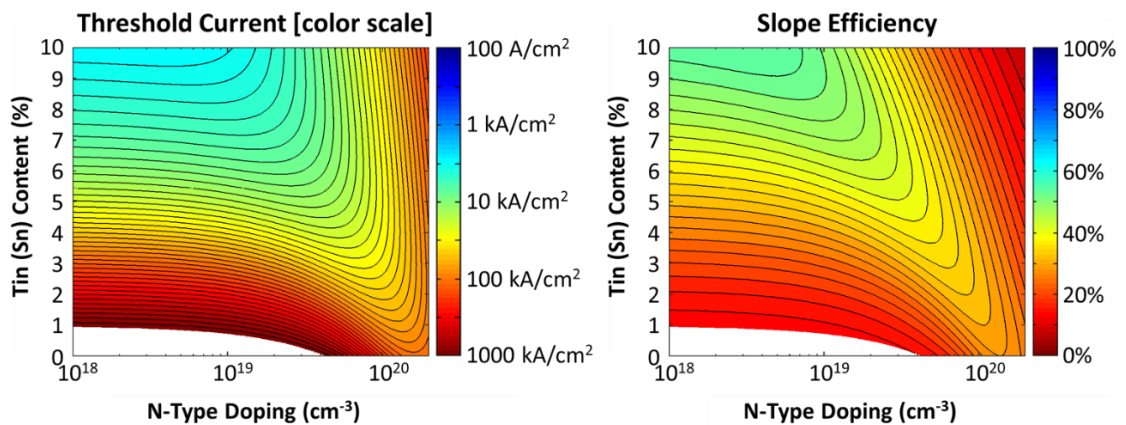
optical cavity out-coupling "loss" = 100 cm⁻¹



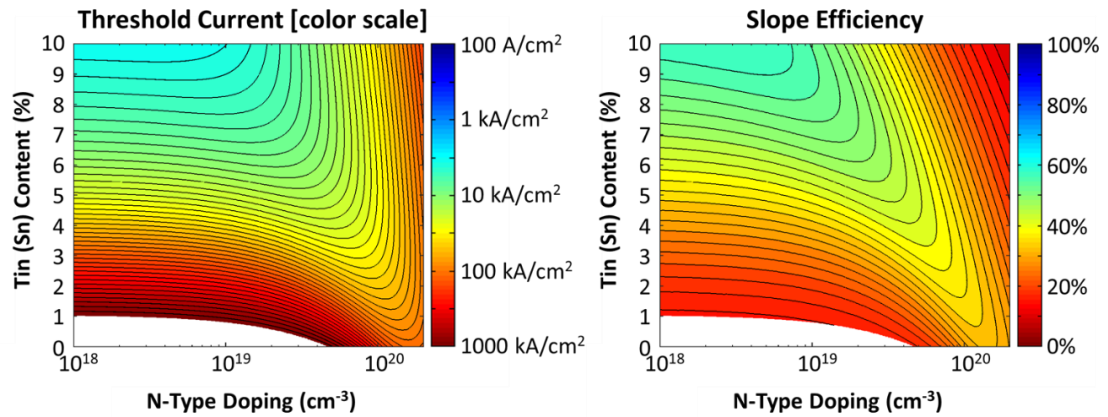
optical cavity out-coupling “loss” = 200 cm^{-1}



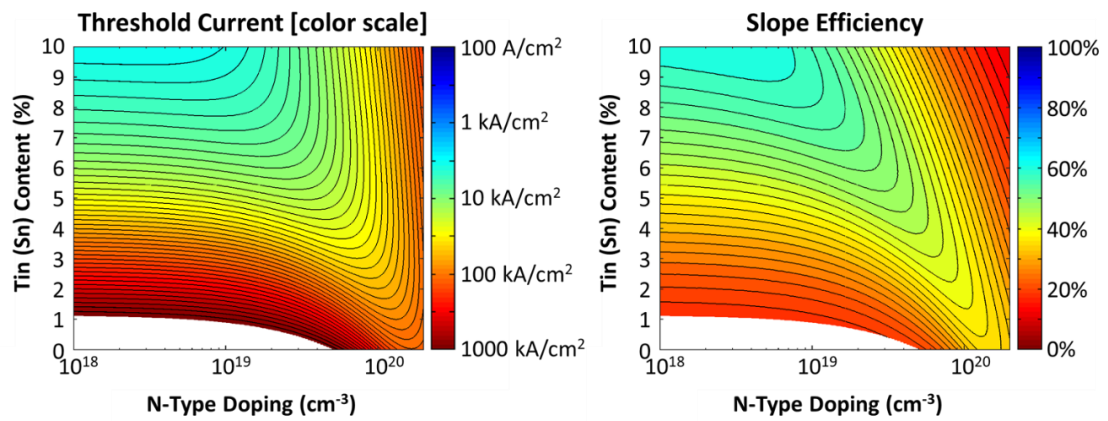
optical cavity out-coupling “loss” = 300 cm^{-1}



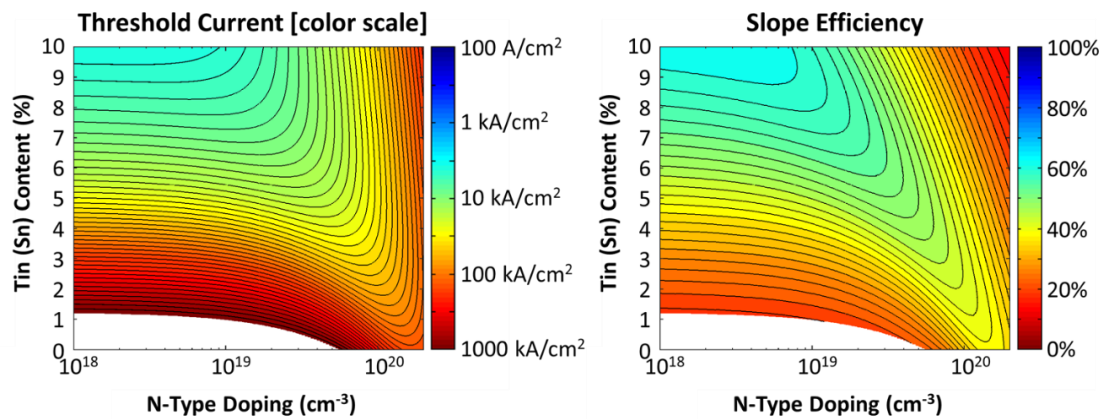
optical cavity out-coupling “loss” = 400 cm^{-1}



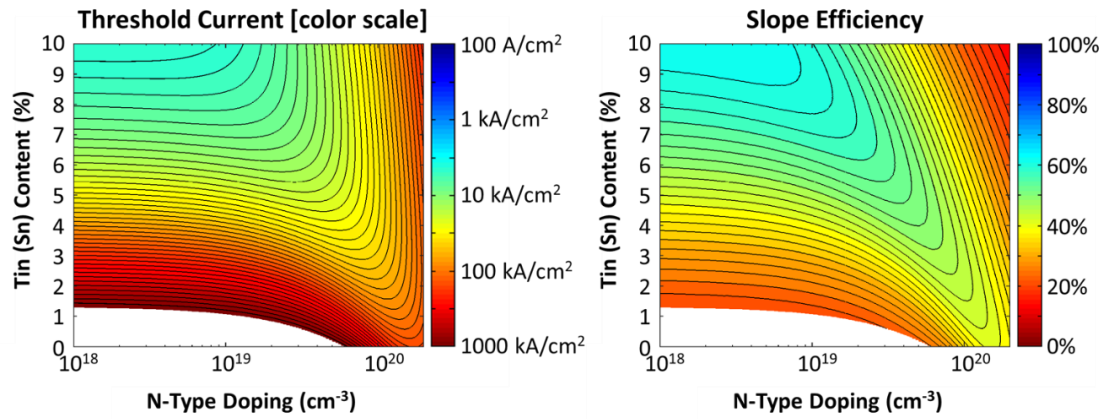
optical cavity out-coupling “loss” = 500 cm^{-1}



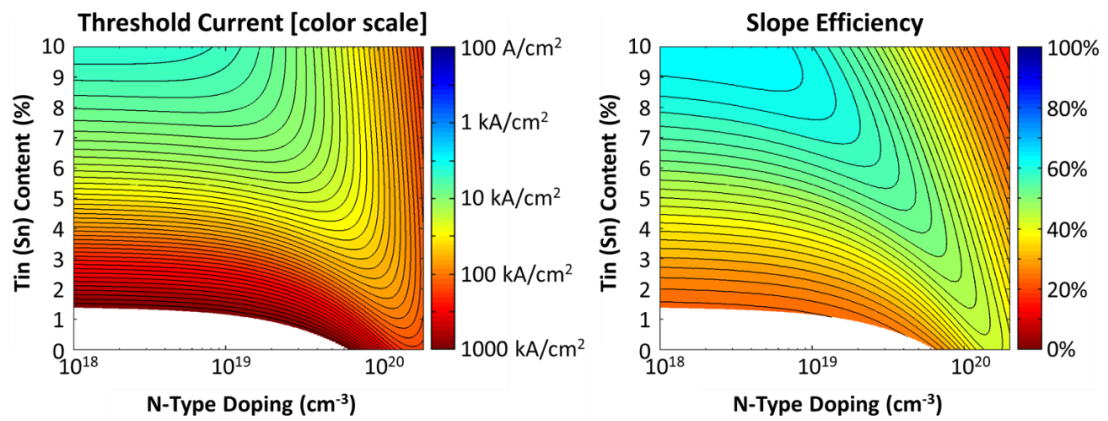
optical cavity out-coupling “loss” = 600 cm^{-1}



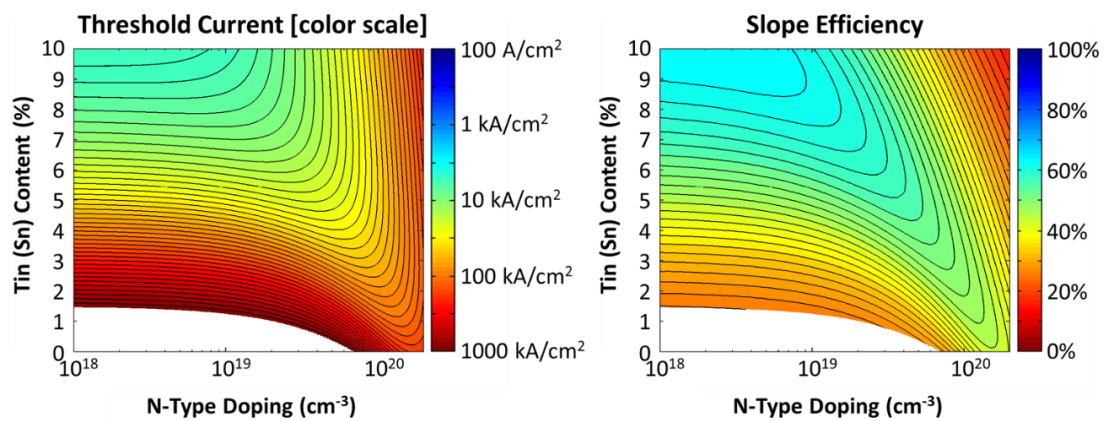
optical cavity out-coupling “loss” = 700 cm^{-1}



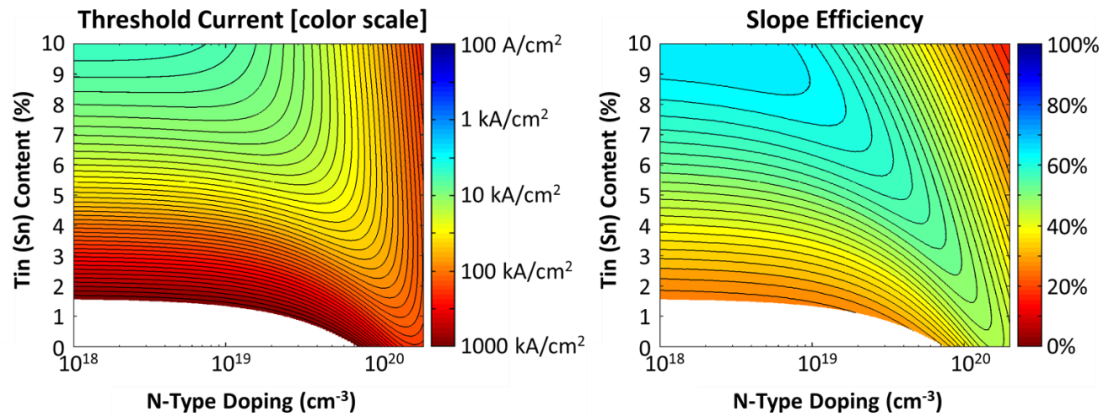
optical cavity out-coupling “loss” = 800 cm^{-1}



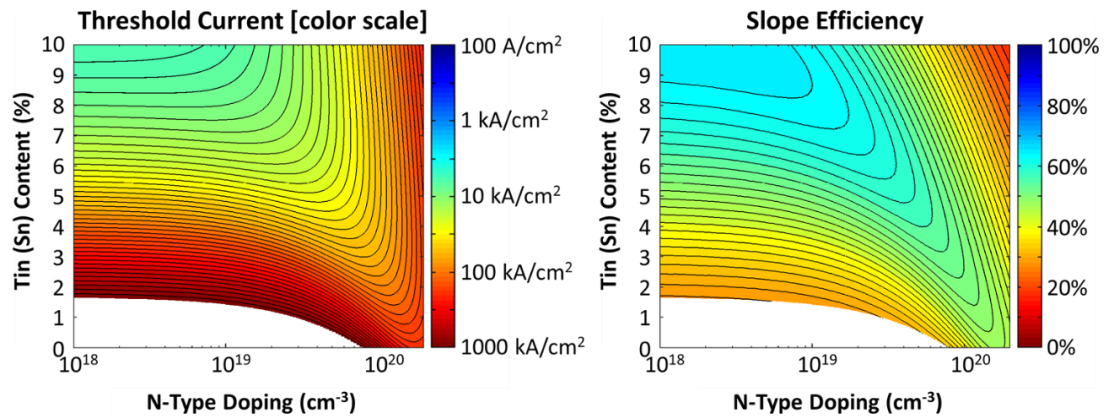
optical cavity out-coupling “loss” = 900 cm^{-1}



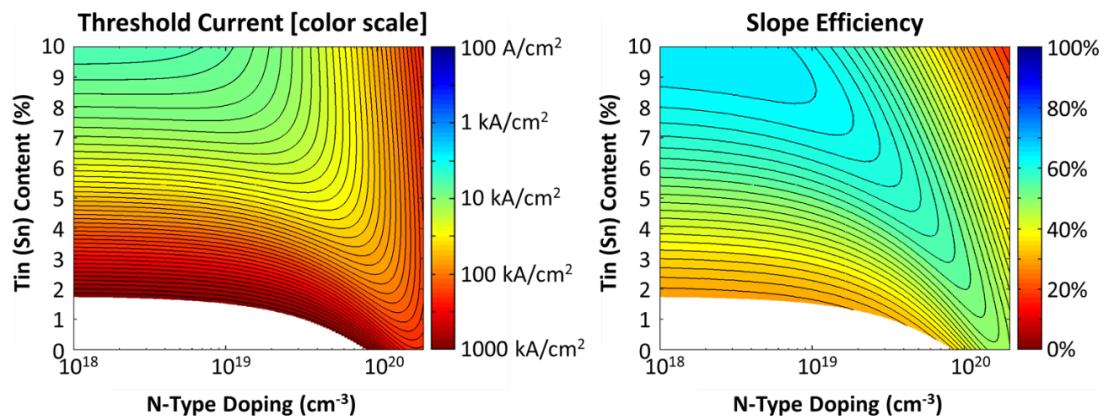
optical cavity out-coupling “loss” = 1000 cm^{-1}



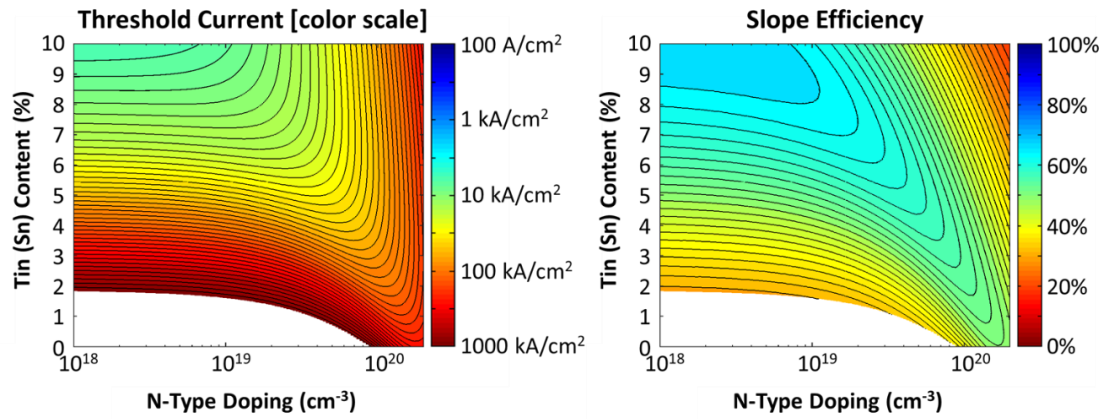
optical cavity out-coupling “loss” = 1100 cm^{-1}



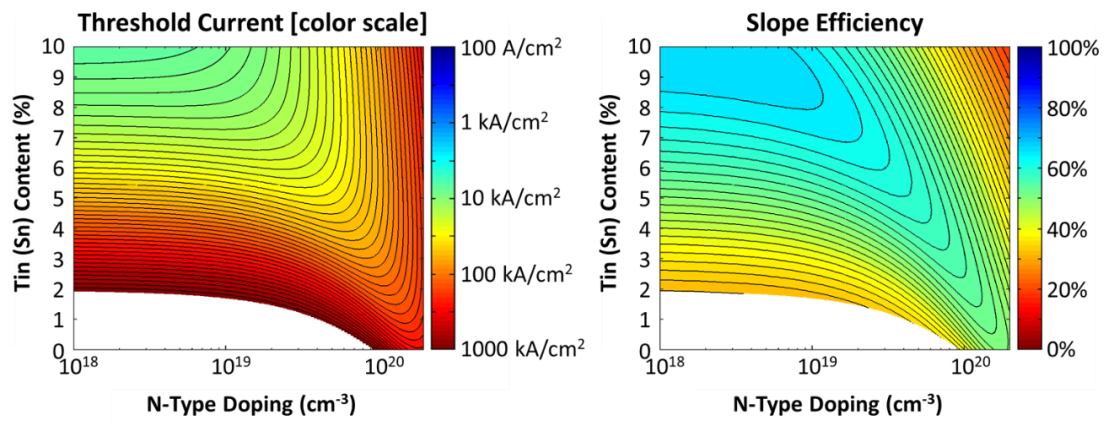
optical cavity out-coupling “loss” = 1200 cm^{-1}



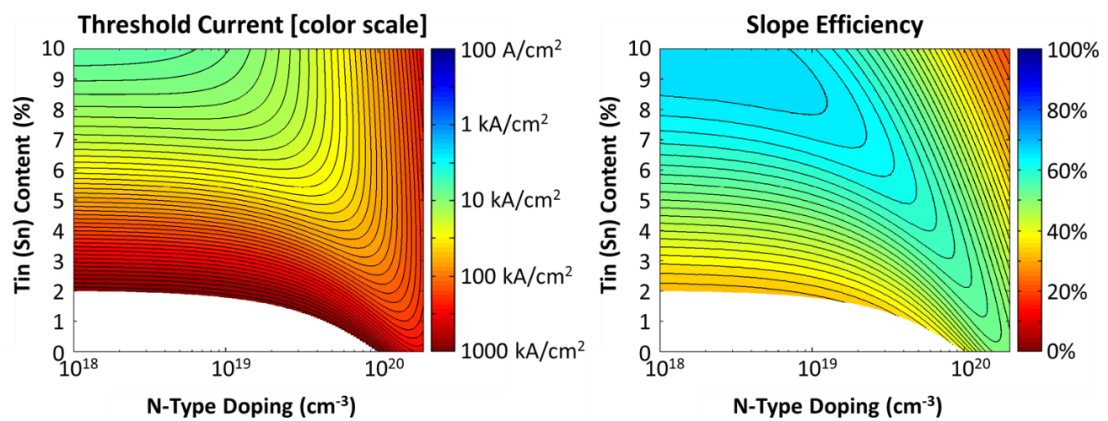
optical cavity out-coupling “loss” = 1300 cm^{-1}



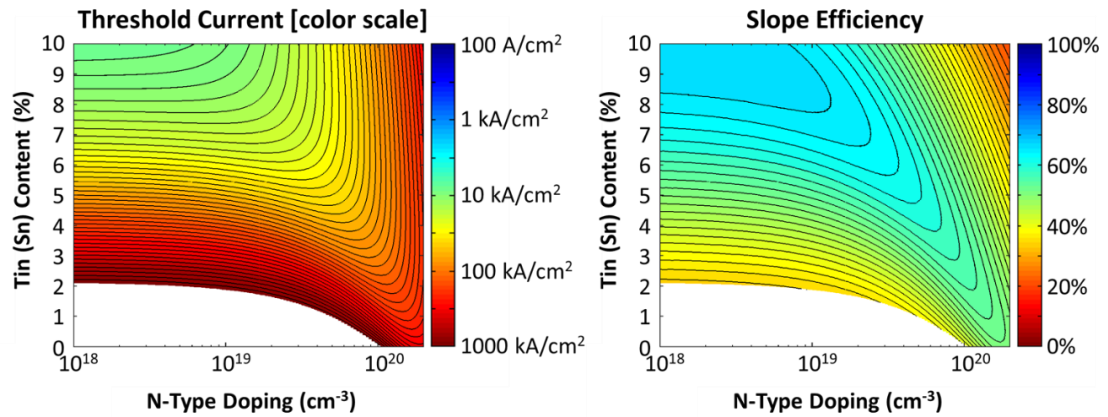
optical cavity out-coupling “loss” = 1400 cm^{-1}



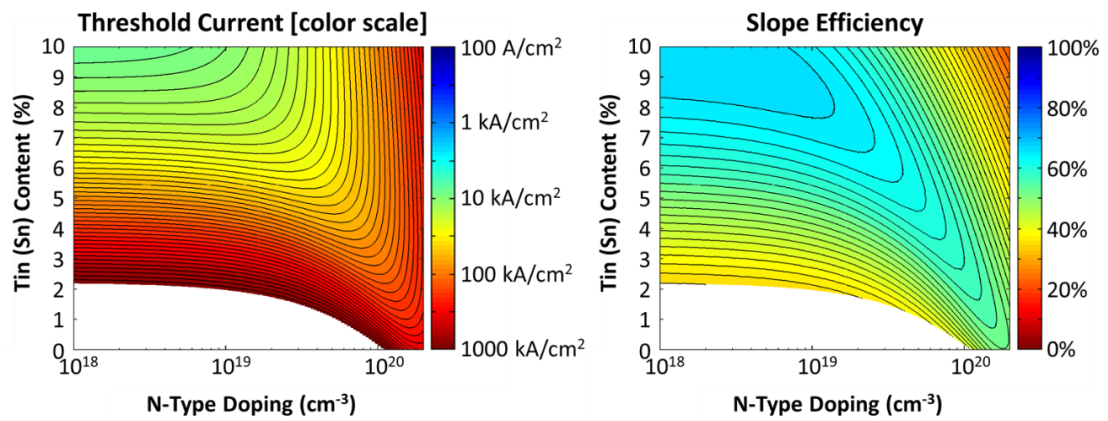
optical cavity out-coupling “loss” = 1500 cm^{-1}



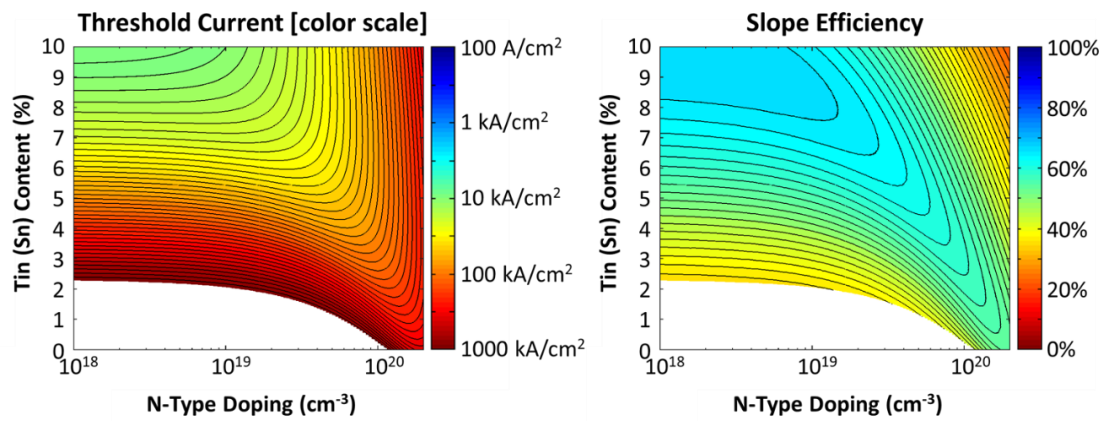
optical cavity out-coupling “loss” = 1600 cm^{-1}



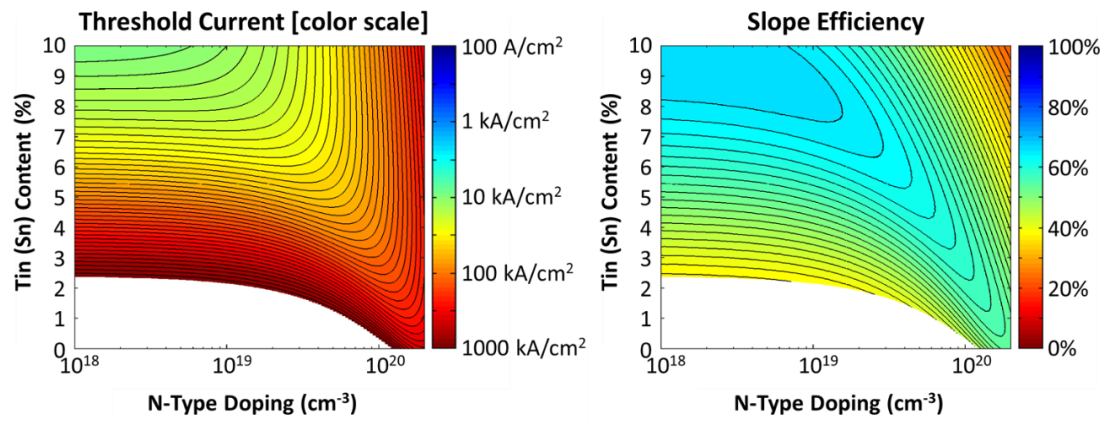
optical cavity out-coupling “loss” = 1700 cm^{-1}



optical cavity out-coupling “loss” = 1800 cm^{-1}

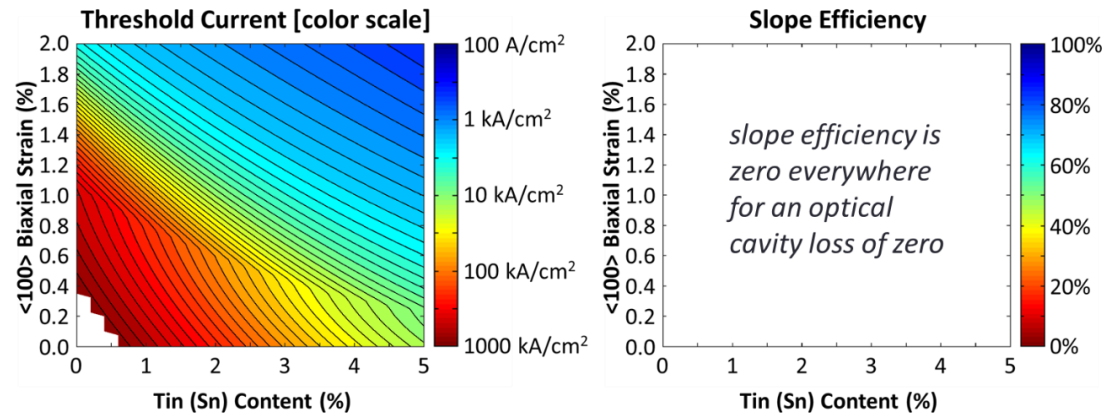


optical cavity out-coupling “loss” = 1900 cm^{-1}

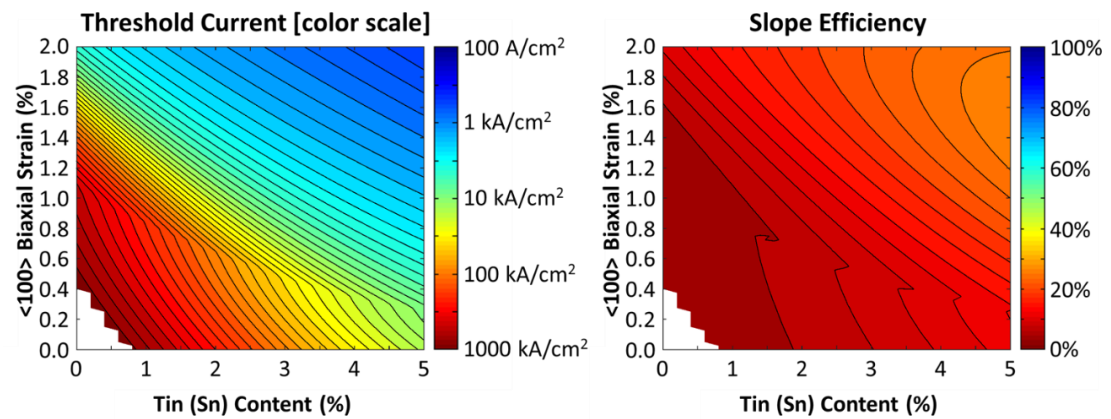


optical cavity out-coupling "loss" = 2000 cm⁻¹

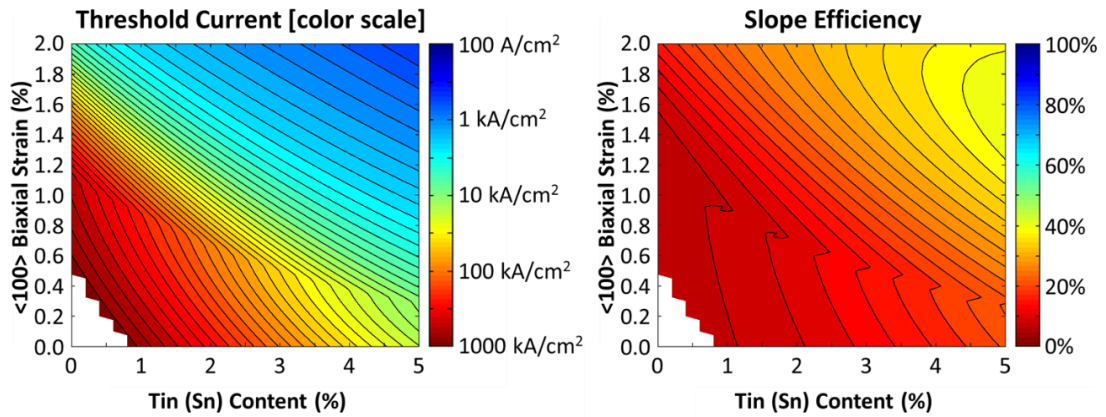
Figure A-6. Threshold current density (left) and slope efficiency (right) of a biaxially strained ($\langle 100 \rangle$ orientation) germanium-tin laser as a function of strain and tin content, shown for an extended range of optical cavity loss values. A double heterostructure design with a 300nm thick germanium tin ($\text{Ge}_x\text{Sn}_{1-x}$) active region, $1 \times 10^{18} \text{ cm}^{-3}$ n-type doping and $\tau_{\text{SRH}} = 100 \text{ ns}$ are assumed.



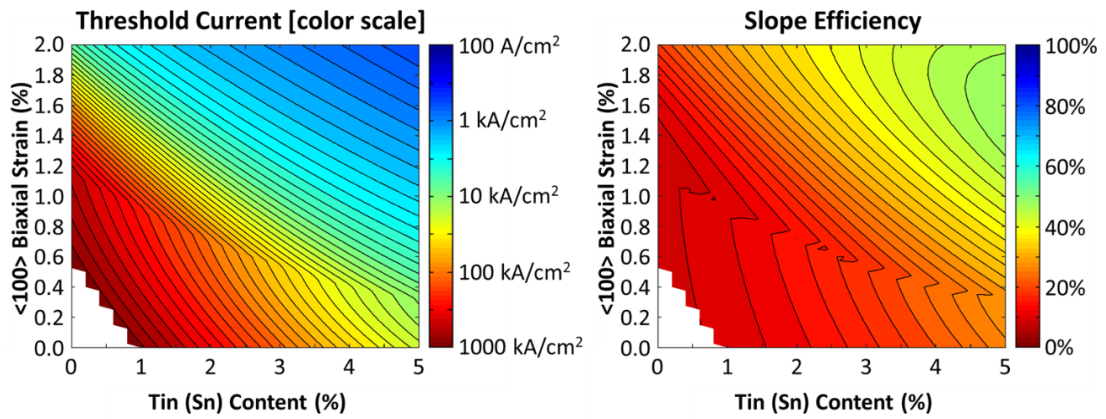
optical cavity out-coupling "loss" = 0 cm⁻¹



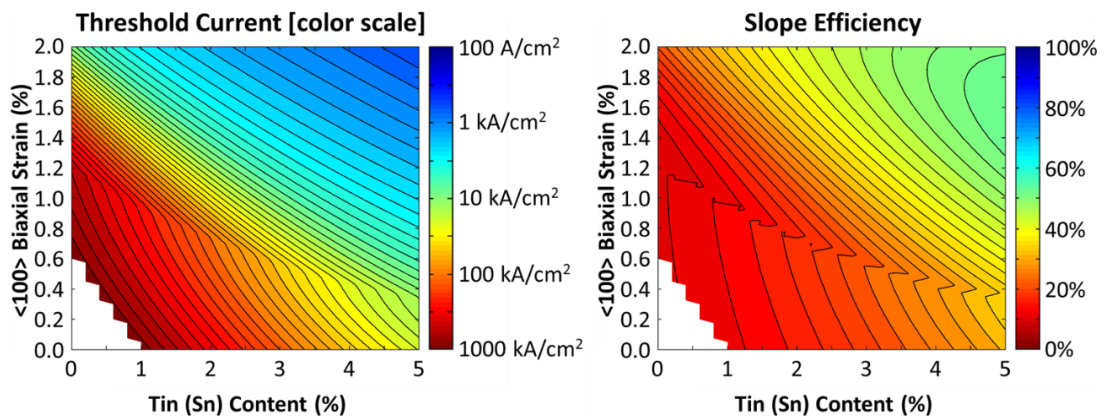
optical cavity out-coupling "loss" = 100 cm⁻¹



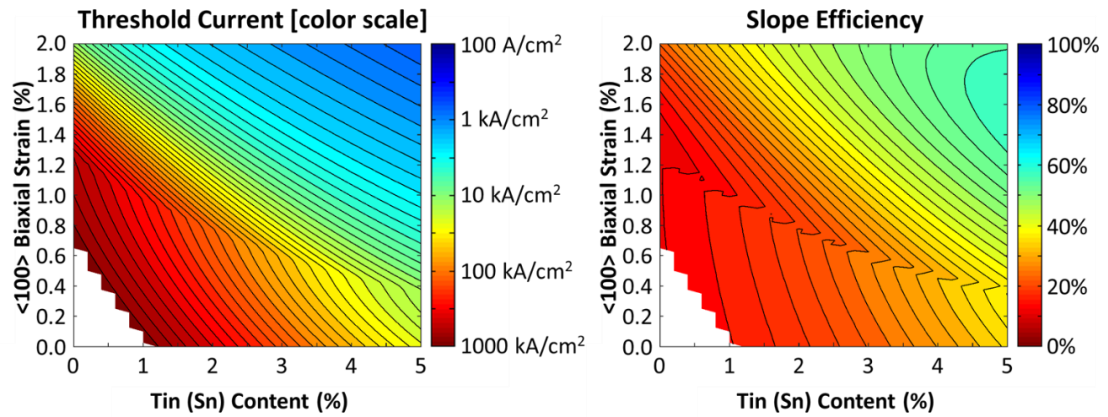
optical cavity out-coupling "loss" = 200 cm⁻¹



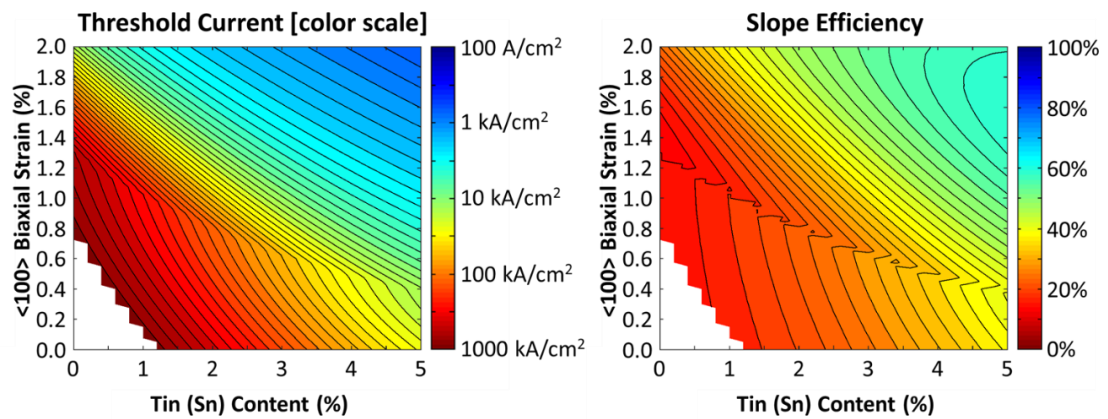
optical cavity out-coupling "loss" = 300 cm⁻¹



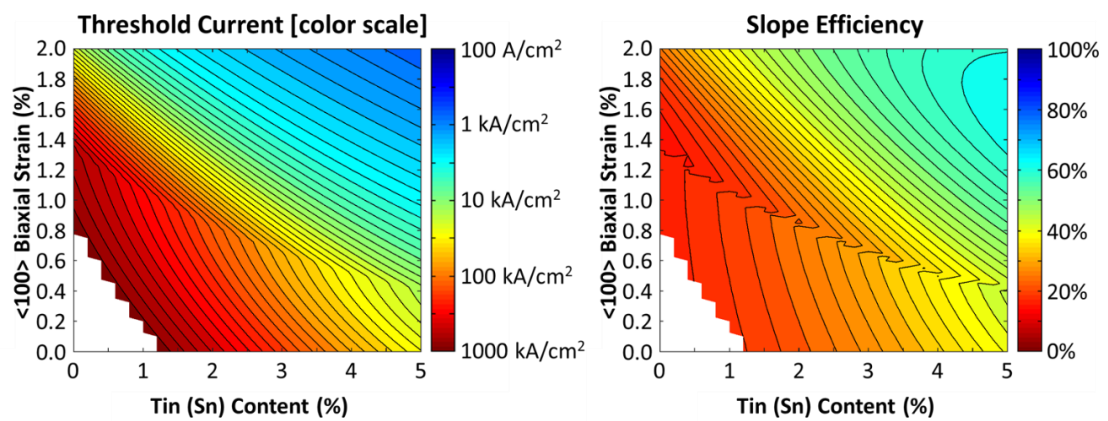
optical cavity out-coupling "loss" = 400 cm⁻¹



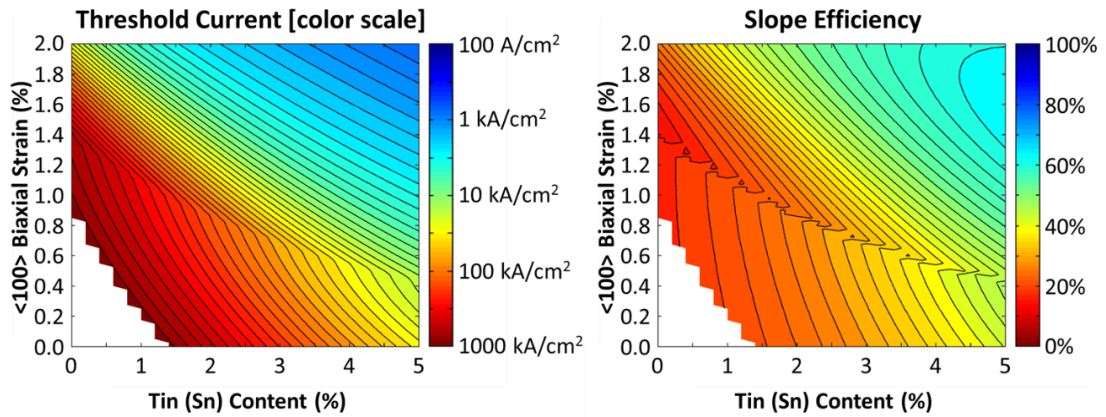
optical cavity out-coupling "loss" = 500 cm⁻¹



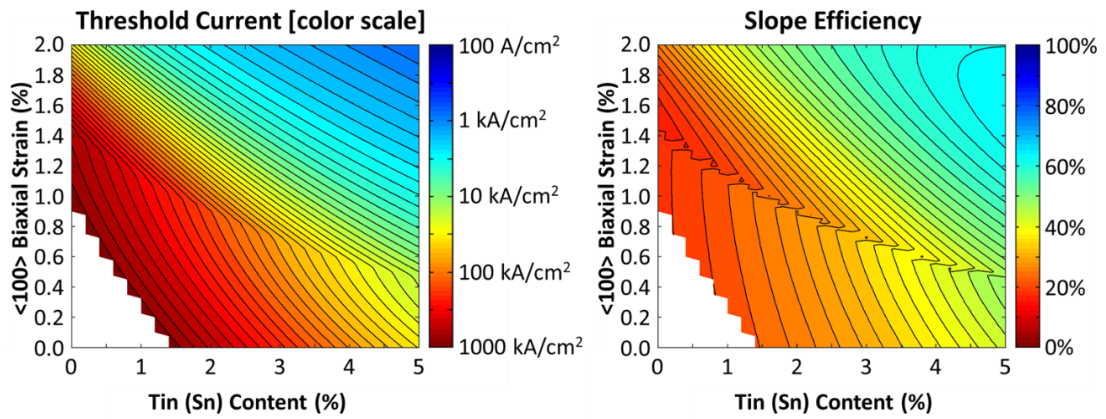
optical cavity out-coupling "loss" = 600 cm⁻¹



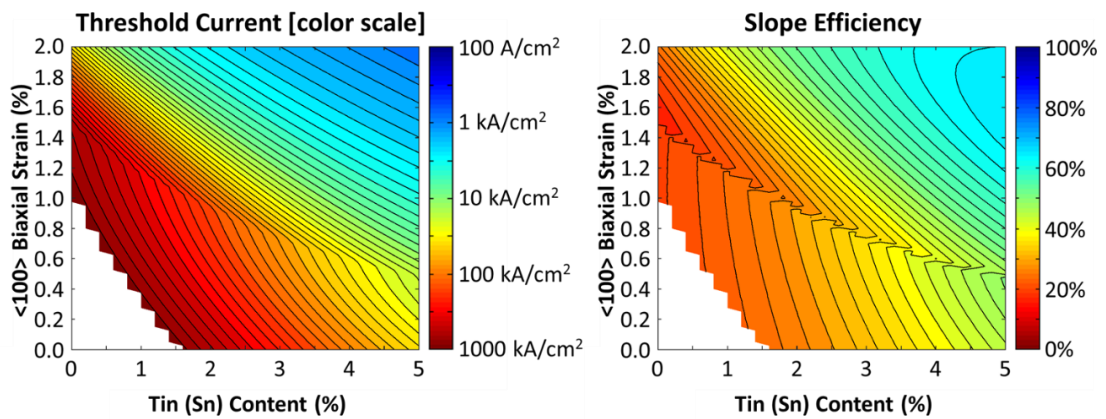
optical cavity out-coupling "loss" = 700 cm⁻¹



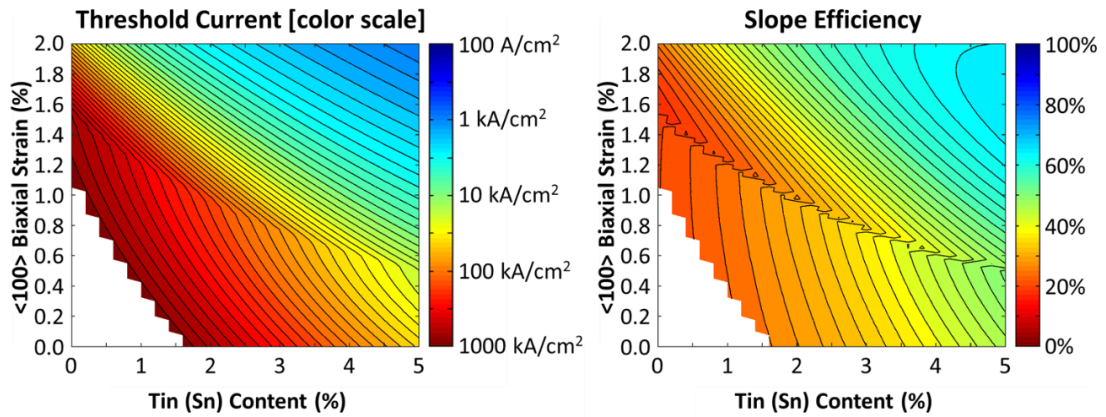
optical cavity out-coupling “loss” = 800 cm⁻¹



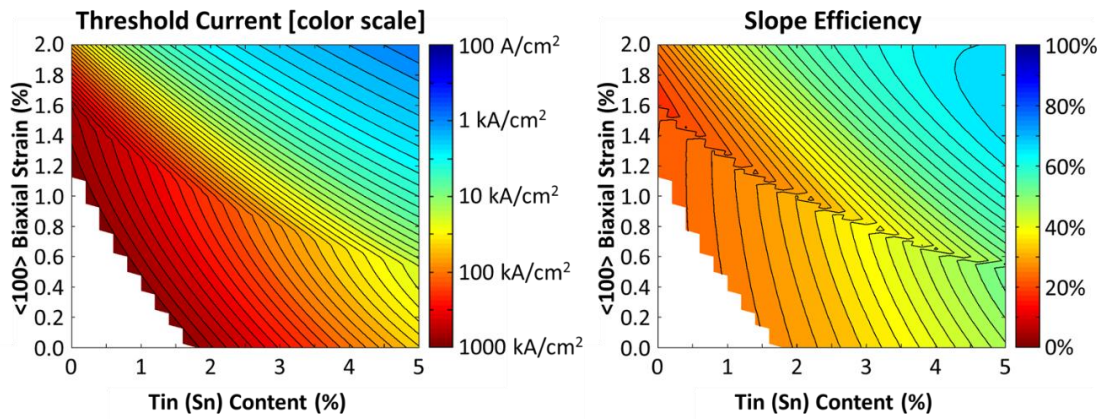
optical cavity out-coupling “loss” = 900 cm⁻¹



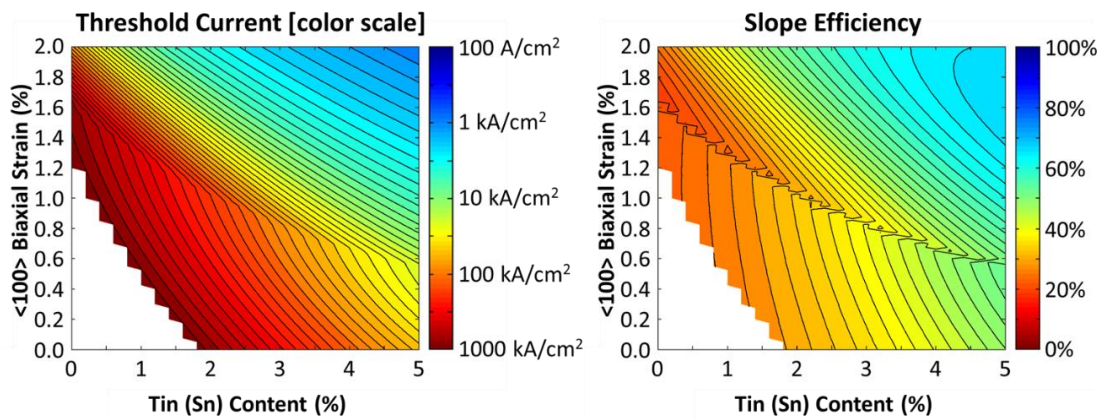
optical cavity out-coupling “loss” = 1000 cm⁻¹



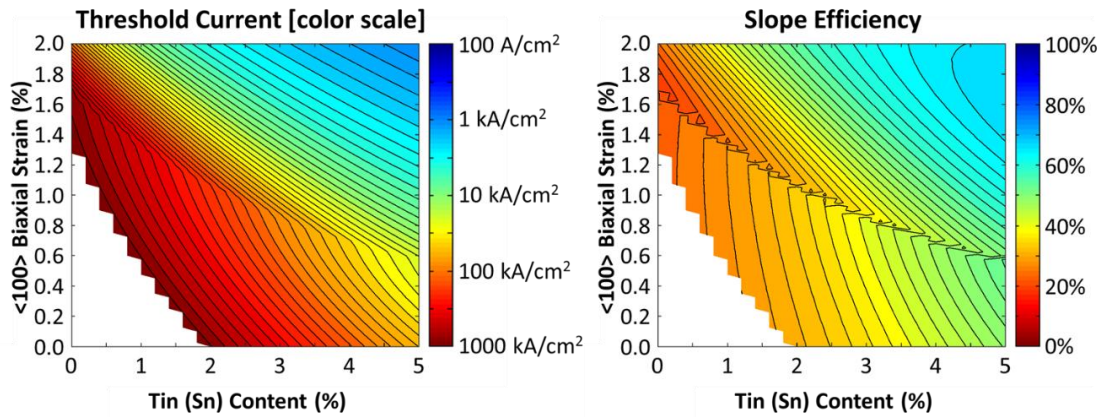
optical cavity out-coupling “loss” = 1100 cm⁻¹



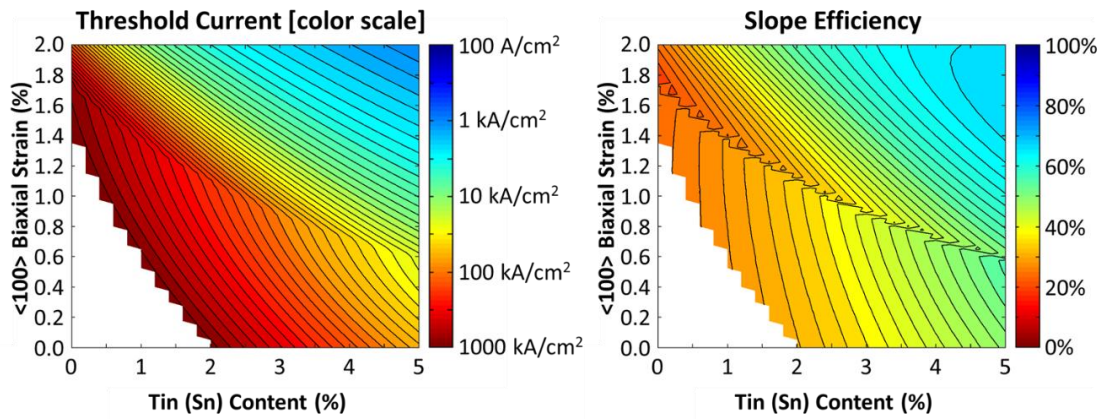
optical cavity out-coupling “loss” = 1200 cm⁻¹



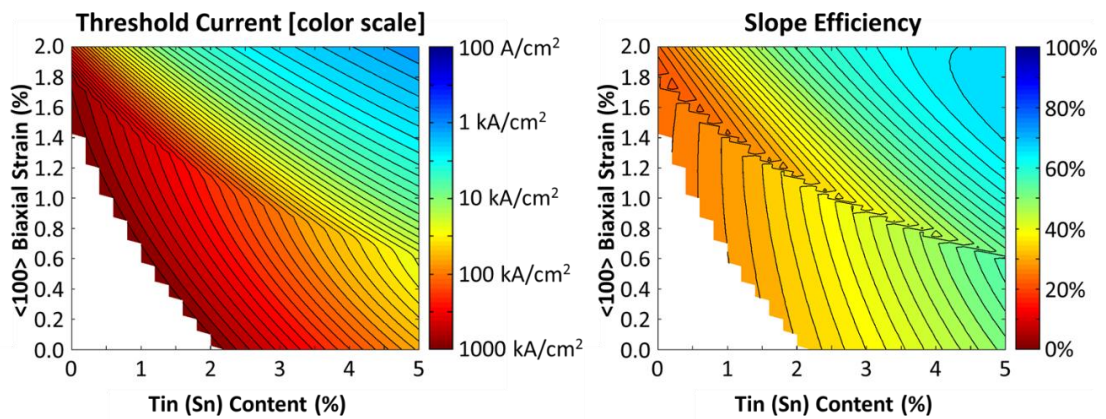
optical cavity out-coupling “loss” = 1300 cm⁻¹



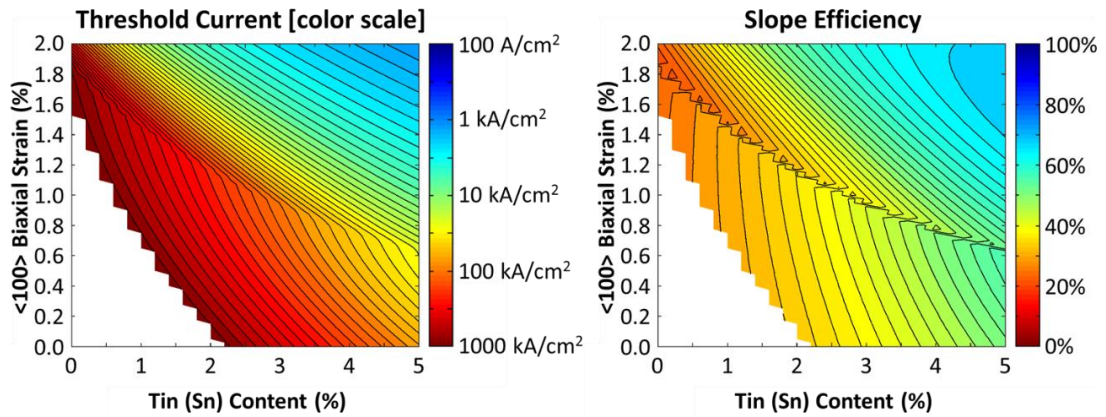
optical cavity out-coupling “loss” = 1400 cm^{-1}



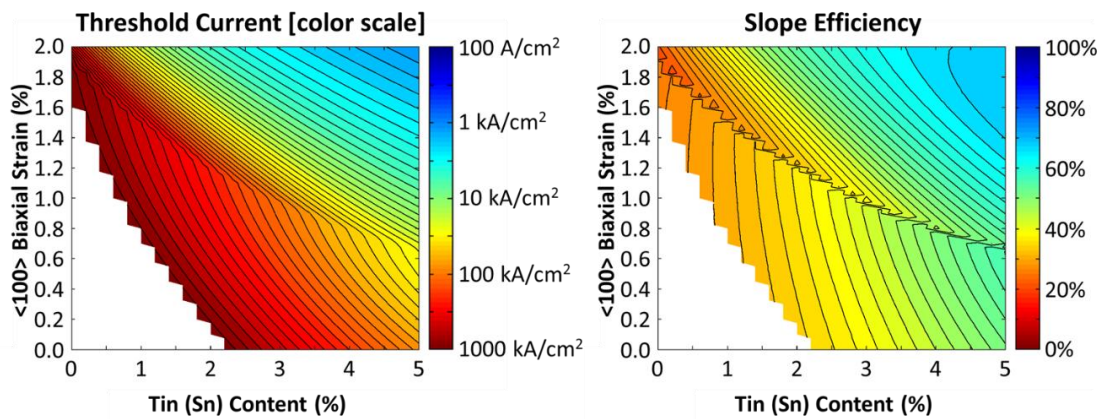
optical cavity out-coupling “loss” = 1500 cm^{-1}



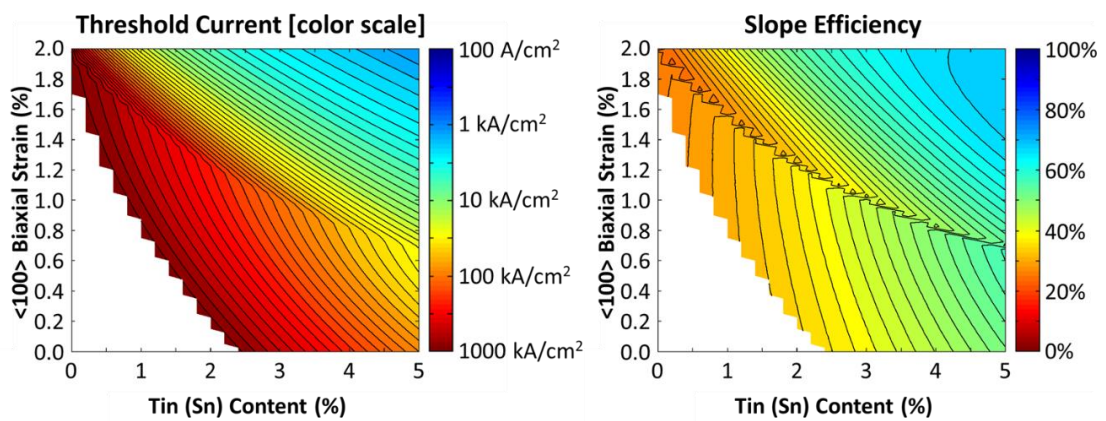
optical cavity out-coupling “loss” = 1600 cm^{-1}



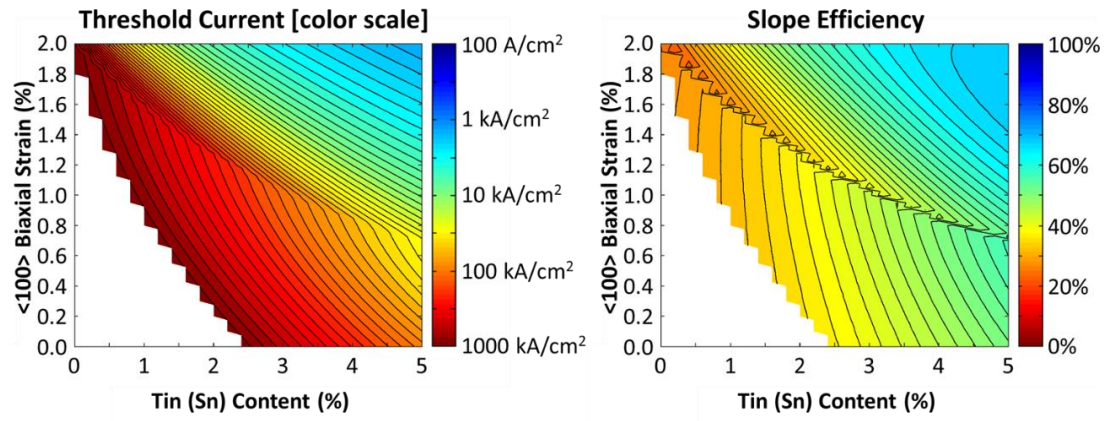
optical cavity out-coupling “loss” = 1700 cm⁻¹



optical cavity out-coupling “loss” = 1800 cm⁻¹



optical cavity out-coupling “loss” = 1900 cm⁻¹



optical cavity out-coupling "loss" = 2000 cm⁻¹

Bibliography

- [1] J. Bardeen and W. Brattain, "The transistor, a semi-conductor triode," *Phys. Rev.*, vol. 74, no. 2, pp. 230–231, 1948.
- [2] R. R. Schaller, "Moore's law: past, present and future," *IEEE Spectr.*, vol. 34, no. 6, pp. 52–59, 1997.
- [3] C. A. Mack, "Fifty Years of Moore's Law," *IEEE Trans. Semicond. Manuf.*, vol. 24, no. 2, pp. 202–207, May 2011.
- [4] K. J. Kuhn, "CMOS transistor scaling past 32nm and implications on variation," in *IEEE/SEMI Advanced Semiconductor Manufacturing Conference (ASMC)*, 2010, vol. 97124, pp. 241–246.
- [5] S. Borkar, "Design challenges of technology scaling," *IEEE Micro*, vol. 19, no. 4, pp. 23–29, 1999.
- [6] D. A. B. Miller, "Rationale and challenges for optical interconnects to electronic chips," *Proc. IEEE*, vol. 88, no. 6, pp. 728–749, Jun. 2000.
- [7] K.-H. Koo, H. Cho, P. Kapur, and K. C. Saraswat, "Performance comparisons between carbon nanotubes, optical, and Cu for future high-performance on-chip interconnect applications," *IEEE Trans. Electron Devices*, vol. 54, no. 12, pp. 3206–3215, 2007.
- [8] P. Kapur, G. Chandra, J. P. McVittie, and K. C. Saraswat, "Technology and reliability constrained future copper interconnects. II. Performance implications," *IEEE Trans. Electron Devices*, vol. 49, no. 4, pp. 598–604, 2002.
- [9] P. V. Andrews, M. B. West, and C. R. Robeson, "The effect of grain boundaries on the electrical resistivity of polycrystalline copper and aluminium," *Philos. Mag.*, vol. 19, no. 161, pp. 887–898, May 1969.
- [10] W. Wu, S. H. Brongersma, M. Van Hove, and K. Maex, "Influence of surface and grain-boundary scattering on the resistivity of copper in reduced dimensions," *Appl. Phys. Lett.*, vol. 84, no. 15, p. 2838, 2004.
- [11] W. Steinhögl, G. Schindler, G. Steinlesberger, M. Traving, and M. Engelhardt, "Comprehensive study of the resistivity of copper wires with lateral dimensions of 100 nm and smaller," *J. Appl. Phys.*, vol. 97, no. 2, p. 023706, 2005.

- [12] K.-H. Koo and K. C. Saraswat, "Study of Performances of Low-k Cu, CNTs, and Optical Interconnects," in *Nanoelectronic Circuit Design*, N. K. Jha and D. Chen, Eds. New York, NY: Springer New York, 2011, pp. 377–407.
- [13] W. Steinhögl, G. Schindler, G. Steinlesberger, and M. Engelhardt, "Size-dependent resistivity of metallic wires in the mesoscopic range," *Phys. Rev. B*, vol. 66, no. 7, p. 075414, Aug. 2002.
- [14] K.-H. Koo, P. Kapur, and K. C. Saraswat, "Compact Performance Models and Comparisons for Gigascale On-Chip Global Interconnect Technologies," *IEEE Trans. Electron Devices*, vol. 56, no. 9, pp. 1787–1798, Sep. 2009.
- [15] G. Chandra, P. Kapur, and K. C. Saraswat, "Scaling trends for the on chip power dissipation," in *Proceedings of the IEEE 2002 International Interconnect Technology Conference*, 2002, pp. 170–172.
- [16] P. Kapur and K. C. Saraswat, "Optical interconnects for future high performance integrated circuits," *Phys. E Low-dimensional Syst. Nanostructures*, vol. 16, no. 3–4, pp. 620–627, Mar. 2003.
- [17] D. Huang, T. Sze, A. Landin, R. Lytel, and H. L. Davidson, "Optical Interconnects : Out of the Box Forever?," *IEEE J. Sel. Top. Quantum Electron.*, vol. 9, no. 2, pp. 614–623, 2003.
- [18] A. Hadke, T. Benavides, R. Amirtharajah, M. Farrens, and V. Akella, "Design and evaluation of an optical CPU-DRAM interconnect," *2008 IEEE Int. Conf. Comput. Des.*, pp. 492–497, Oct. 2008.
- [19] R. Soref, "Mid-infrared photonics in silicon and germanium," *Nat. Photonics*, vol. 4, no. 8, pp. 495–497, Aug. 2010.
- [20] R. Soref, "Group IV photonics for the mid infrared," in *Proc. SPIE Silicon Photonics VIII*, 2013, vol. 8629, p. 862902.
- [21] X. Sun, "Germanium-on-Silicon for Integrated Silicon Photonics," in *Advanced Photonic Sciences*, M. Fadali, Ed. InTech, 2012, pp. 3–40.
- [22] M. J. Süess, R. Geiger, R. A. Minamisawa, G. Schiefler, J. Frigerio, D. Chrastina, G. Isella, R. Spolenak, J. Faist, and H. Sigg, "Analysis of enhanced light emission from highly strained germanium microbridges," *Nat. Photonics*, vol. 7, pp. 466–472, 2013.
- [23] D. S. Sukhdeo, D. Nam, J.-H. Kang, M. L. Brongersma, and K. C. Saraswat, "Direct bandgap germanium-on-silicon inferred from 5.7% <100> uniaxial tensile strain," *Photonics Res.*, vol. 2, no. 3, pp. A8–A13, 2014.
- [24] D. Nam, D. S. Sukhdeo, J.-H. Kang, J. Petykiewicz, J. H. Lee, W. S. Jung, J. Vučković, M. L. Brongersma, and K. C. Saraswat, "Strain-induced

pseudoheterostructure nanowires confining carriers at room temperature with nanoscale-tunable band profiles.,” *Nano Lett.*, vol. 13, no. 7, pp. 3118–3123, Jun. 2013.

- [25] D. S. Sukhdeo, D. Nam, J.-H. Kang, M. L. Brongersma, and K. C. Saraswat, “A Nanomembrane-Based Bandgap-Tunable Germanium Microdisk Using Lithographically-Customizable Biaxial Strain for Silicon-Compatible Optoelectronics,” *ArXiv*, 2014.
- [26] Y. Ishikawa and K. Wada, “Germanium for silicon photonics,” *Thin Solid Films*, vol. 518, no. 6, pp. S83–S87, Jan. 2010.
- [27] D. Liang and J. E. Bowers, “Recent progress in lasers on silicon,” *Nat. Photonics*, vol. 4, no. 8, pp. 511–517, Jul. 2010.
- [28] M. J. R. Heck, J. F. Bauters, M. L. Davenport, J. K. Doyland, S. Jain, G. Kurczveil, S. Srinivasan, Y. Tang, and J. E. Bowers, “Hybrid silicon photonic integrated circuit technology,” *IEEE J. Sel. Top. Quantum Electron.*, vol. 19, no. 4, p. 6100117, Jul. 2013.
- [29] G. Roelkens, L. Liu, D. Liang, R. Jones, a. Fang, B. Koch, and J. Bowers, “III-V/silicon photonics for on-chip and intra-chip optical interconnects,” *Laser Photon. Rev.*, vol. 4, no. 6, pp. 751–779, Nov. 2010.
- [30] S. J. Koester, S. Member, J. D. Schaub, G. Dehlinger, and J. O. Chu, “Germanium-on-SOI Infrared Detectors for Integrated Photonic Applications,” *IEEE J. Quantum Electron.*, vol. 12, no. 6, pp. 1489–1502, 2006.
- [31] S. Famà, L. Colace, G. Masini, G. Assanto, and H.-C. Luan, “High performance germanium-on-silicon detectors for optical communications,” *Appl. Phys. Lett.*, vol. 81, no. 4, p. 586, 2002.
- [32] L. Colace, P. Ferrara, G. Assanto, S. Member, D. Fulgoni, and L. Nash, “Low Dark-Current Germanium-on-Silicon Near-Infrared Detectors,” vol. 19, no. 22, pp. 1813–1815, 2007.
- [33] L. Colace, G. Masini, and G. Assanto, “Ge-on-Si approaches to the detection of near-infrared light,” *Quantum Electron. IEEE ...*, vol. 35, no. 12, pp. 1843–1852, 1999.
- [34] J. E. Roth, O. Fidaner, R. K. Schaevitz, Y.-H. Kuo, T. I. Kamins, J. S. Harris, and D. A. B. Miller, “Optical modulator on silicon employing germanium quantum wells,” *Opt. Express*, vol. 15, no. 9, pp. 5851–5859, Apr. 2007.
- [35] A. Nayfeh, C. O. Chui, K. C. Saraswat, and T. Yonehara, “Effects of hydrogen annealing on heteroepitaxial-Ge layers on Si: Surface roughness and electrical quality,” *Appl. Phys. Lett.*, vol. 85, no. 14, p. 2815, 2004.
- [36] A. K. Okyay, A. M. Nayfeh, K. C. Saraswat, T. Yonehara, A. Marshall, and P. C. McIntyre, “High-efficiency metal-semiconductor-metal photodetectors on

heteroepitaxially grown Ge on Si.,” *Opt. Lett.*, vol. 31, no. 17, pp. 2565–2567, Sep. 2006.

- [37] M. Caymax, G. Eneman, F. Bellenger, C. Merckling, A. Delabie, G. Wang, R. Loo, E. Simoen, J. Mitard, B. De Jaeger, G. Hellings, K. De Meyer, M. Meuris, and M. Heyns, “Germanium for advanced CMOS anno 2009: a SWOT analysis,” in *2009 IEEE International Electron Devices Meeting (IEDM)*, 2009, pp. 1–4.
- [38] M. L. Lee, E. a. Fitzgerald, M. T. Bulsara, M. T. Currie, and A. Lochtefeld, “Strained Si, SiGe, and Ge channels for high-mobility metal-oxide-semiconductor field-effect transistors,” *J. Appl. Phys.*, vol. 97, no. 1, p. 011101, 2005.
- [39] C. G. Van de Walle, “Band lineups and deformation potentials in the model-solid theory,” *Phys. Rev. B*, vol. 39, no. 3, p. 1871, 1989.
- [40] S. A. Claussen, E. Tasyurek, J. E. Roth, and D. A. B. Miller, “Measurement and modeling of ultrafast carrier dynamics and transport in germanium/silicon-germanium quantum wells,” *Opt. Express*, vol. 18, no. 25, pp. 25596–25607, Dec. 2010.
- [41] J. Liu, X. Sun, D. Pan, X. Wang, L. C. Kimerling, T. L. Koch, and J. Michel, “Tensile-strained, n-type Ge as a gain medium for monolithic laser integration on Si,” *Opt. Express*, vol. 15, no. 18, pp. 11272–11277, Sep. 2007.
- [42] A. Rogalski, “Comparison of the performance of quantum well and conventional bulk infrared photodetectors,” *Infrared Phys. Technol.*, vol. 38, no. 5, pp. 295–310, Aug. 1997.
- [43] D. S. Sukhdeo, D. Nam, S.-L. Cheng, Z. Yuan, A. Roy, K. C.-Y. Huang, M. Brongersma, Y. Nishi, and K. Saraswat, “Highly-Strained Germanium as a Gain Medium for Silicon-Compatible Lasers,” in *CLEO: Science and Innovations*, 2012, p. CTh3D.6.
- [44] M. J. Chen, C. S. Tsai, and M. K. Wu, “Optical Gain and Co-Stimulated Emissions of Photons and Phonons in Indirect Bandgap Semiconductors,” *Jpn. J. Appl. Phys.*, vol. 45, no. 8B, pp. 6576–6588, Aug. 2006.
- [45] P. Boucaud, M. El Kurdi, A. Ghrib, M. Prost, M. de Kersauson, S. Sauvage, F. Aniel, X. Checoury, G. Beaudoin, L. Largeau, I. Sagnes, G. Ndong, M. Chaigneau, and R. Ossikovski, “Recent advances in germanium emission,” *Photonics Res.*, vol. 1, no. 3, pp. 102–109, Aug. 2013.
- [46] D. L. Mathine, “The integration of III-V optoelectronics with silicon circuitry,” *IEEE J. Sel. Top. Quantum Electron.*, vol. 3, no. 3, pp. 952–959, Jun. 1997.
- [47] A. W. Fang, H. Park, O. Cohen, R. Jones, M. J. Paniccia, and J. E. Bowers, “Electrically pumped hybrid AlGaInAs-silicon evanescent laser,” *Opt. Express*, vol. 14, no. 20, p. 9203, 2006.

- [48] K. Tanabe, K. Watanabe, and Y. Arakawa, "III-V/Si hybrid photonic devices by direct fusion bonding.," *Sci. Rep.*, vol. 2, p. 349, Jan. 2012.
- [49] C. T. Santis, S. T. Steger, Y. Vilenchik, A. Vasilyev, and A. Yariv, "High-coherence semiconductor lasers based on integral high-Q resonators in hybrid Si/III-V platforms.," *Proc. Natl. Acad. Sci. U. S. A.*, vol. 111, no. 8, pp. 2879–84, Feb. 2014.
- [50] X. Sun, J. Liu, L. C. Kimerling, and J. Michel, "Toward a Germanium Laser for Integrated Silicon Photonics," *IEEE J. Sel. Top. Quantum Electron.*, vol. 16, no. 1, pp. 124–131, 2010.
- [51] G.-E. Chang, S.-W. Chang, and S. L. Chuang, "Theory for n-type doped, tensile-strained Ge – Si(x)Ge(y)Sn(1-x-y) quantum-well lasers at telecom wavelength," *Opt. Express*, vol. 17, no. 14, pp. 11246–11258, 2009.
- [52] M. V. Fischetti and S. E. Laux, "Band structure, deformation potentials, and carrier mobility in strained Si, Ge, and SiGe alloys," *J. Appl. Phys.*, vol. 80, no. 4, pp. 2234–2252, 1996.
- [53] B. Dutt, D. S. Sukhdeo, D. Nam, B. M. Vulovic, Z. Yuan, and K. C. Saraswat, "Roadmap to an Efficient Germanium-on-Silicon Laser: Strain vs. n-Type Doping," *IEEE Photonics J.*, vol. 4, no. 5, pp. 2002–2009, Oct. 2012.
- [54] R. A. Soref and J. P. Lorenzo, "All silicon active and passive guided wave components for $\lambda=1.3$ and $\lambda=1.6$ μm ," *IEEE J. Quantum Electron.*, vol. 22, no. 6, pp. 873–879, 1986.
- [55] L. Carroll, P. Friedli, S. Neuenschwander, H. Sigg, S. Cecchi, F. Isa, D. Chrastina, G. Isella, Y. Fedoryshyn, and J. Faist, "Direct-Gap Gain and Optical Absorption in Germanium Correlated to the Density of Photoexcited Carriers, Doping, and Strain," *Phys. Rev. Lett.*, vol. 109, no. 5, pp. 1–5, Aug. 2012.
- [56] J. Greil, A. Lugstein, C. Zeiner, G. Strasser, and E. Bertagnolli, "Tuning the electro-optical properties of germanium nanowires by tensile strain," *Nano Lett.*, vol. 12, no. 12, pp. 6230–6234, Dec. 2012.
- [57] G. Capellini, C. Reich, S. Guha, Y. Yamamoto, M. Lisker, M. Virgilio, A. Ghrib, M. El Kurdi, P. Boucaud, B. Tillack, and T. Schroeder, "Tensile Ge microstructures for lasing fabricated by means of a silicon complementary metal-oxide-semiconductor process," *Opt. Express*, vol. 22, no. 1, pp. 399–410, 2014.
- [58] J. R. Jain, A. Hryciw, T. M. Baer, D. A. B. Miller, M. L. Brongersma, and R. T. Howe, "A micromachining-based technology for enhancing germanium light emission via tensile strain," *Nat. Photonics*, vol. 6, no. 6, pp. 398–405, 2012.
- [59] P. Boucaud, M. El Kurdi, S. Sauvage, M. de Kersauson, A. Ghrib, and X. Checoury, "Light emission from strained germanium," *Nat. Photonics*, vol. 7, no. 3, p. 162, 2013.

- [60] D. Nam, D. S. Sukhdeo, S. Gupta, J.-H. Kang, M. L. Brongersma, and K. C. Saraswat, "Study of Carrier Statistics in Uniaxially Strained Ge for a Low-Threshold Ge Laser," *IEEE J. Sel. Top. Quantum Electron.*, vol. 20, no. 4, p. 1500107, 2014.
- [61] D. Nam, "Strained Germanium Technology for On-chip Optical Interconnects," Stanford University PhD Thesis, December 2013.
- [62] Y. Huo, H. Lin, R. Chen, M. Makarova, Y. Rong, M. Li, T. I. Kamins, J. Vuckovic, and J. S. Harris, "Strong enhancement of direct transition photoluminescence with highly tensile-strained Ge grown by molecular beam epitaxy," *Appl. Phys. Lett.*, vol. 98, no. 1, p. 011111, 2011.
- [63] J. R. Sánchez-Pérez, C. Boztug, F. Chen, F. F. Sudradjat, D. M. Paskiewicz, R. B. Jacobson, M. G. Lagally, and R. Paiella, "Direct-bandgap light-emitting germanium in tensilely strained nanomembranes," *Proc. Natl. Acad. Sci. U. S. A.*, vol. 108, no. 47, pp. 18893–18898, Nov. 2011.
- [64] A. Ghrib, M. El Kurdi, M. Prost, S. Sauvage, X. Checoury, G. Beaudoin, M. Chaigneau, R. Ossikovski, I. Sagnes, and P. Boucaud, "All-Around SiN Stressor for High and Homogeneous Tensile Strain in Germanium Microdisk Cavities," *Adv. Opt. Mater.*, p. Early Access Online, Dec. 2015.
- [65] Y. Ishikawa, K. Wada, J. Liu, D. D. Cannon, H.-C. Luan, J. Michel, and L. C. Kimerling, "Strain-induced enhancement of near-infrared absorption in Ge epitaxial layers grown on Si substrate," *J. Appl. Phys.*, vol. 98, no. 1, p. 013501, 2005.
- [66] V. V Zhdanova and T. A. Kontorova, "Thermal expansion of doped germanium," *Sov. Phys. – Solid State*, vol. 7, no. 11, pp. 2685–2689, 1966.
- [67] X. Sun, J. Liu, L. C. Kimerling, and J. Michel, "Direct gap photoluminescence of n-type tensile-strained Ge-on-Si," *Appl. Phys. Lett.*, vol. 95, no. 1, p. 011911, 2009.
- [68] H. Ibach, "Thermal expansion of silicon and zinc oxide (II)," *Phys. status solidi*, vol. 33, pp. 257–265, 1969.
- [69] J. Hall, "Electronic effects in the elastic constants of n-type silicon," *Phys. Rev.*, vol. 161, no. 3, pp. 756–761, 1967.
- [70] R. W. Keyes, "The electronic contribution to the elastic properties of germanium," *IBM J. Res. Dev.*, vol. 5, no. 4, pp. 266–278, 1961.
- [71] D. Nam, D. Sukhdeo, A. Roy, K. Balram, S.-L. Cheng, K. C.-Y. Huang, Z. Yuan, M. Brongersma, Y. Nishi, D. Miller, and K. Saraswat, "Strained germanium thin film membrane on silicon substrate for optoelectronics," *Opt. Express*, vol. 19, no. 27, pp. 25866–25872, Dec. 2011.
- [72] D. Nam, D. Sukhdeo, S.-L. Cheng, A. Roy, K. C.-Y. Huang, M. Brongersma, Y. Nishi, and K. Saraswat, "Electroluminescence from strained germanium membranes and

- implications for an efficient Si-compatible laser,” *Appl. Phys. Lett.*, vol. 100, no. 13, p. 131112, 2012.
- [73] R. A. Soref and L. Friedman, “Direct-gap Ge/GeSn/Si and GeSn/Ge/Si heterostructures,” *Superlattices Microstruct.*, vol. 14, no. 2–3, pp. 189–193, 1993.
- [74] G. Sun, R. a. Soref, and H. H. Cheng, “Design of an electrically pumped SiGeSn/GeSn/SiGeSn double-heterostructure midinfrared laser,” *J. Appl. Phys.*, vol. 108, no. 3, p. 033107, 2010.
- [75] G. He and H. a. Atwater, “Synthesis of epitaxial Sn_xGe_{1-x} alloy films by ion-assisted molecular beam epitaxy,” *Appl. Phys. Lett.*, vol. 68, no. 5, p. 664, 1996.
- [76] M. Bauer, J. Taraci, J. Tolle, A. V. G. Chizmeshya, S. Zollner, D. J. Smith, J. Menendez, C. Hu, and J. Kouvetakis, “Ge–Sn semiconductors for band-gap and lattice engineering,” *Appl. Phys. Lett.*, vol. 81, no. 16, pp. 2992–2994, 2002.
- [77] W.-J. Yin, X.-G. Gong, and S.-H. Wei, “Origin of the unusually large band-gap bowing and the breakdown of the band-edge distribution rule in the Sn_xGe_{1-x} alloys,” *Phys. Rev. B*, vol. 78, no. 16, p. 161203, Oct. 2008.
- [78] H. Pérez Ladrón de Guevara, A. G. Rodríguez, H. Navarro-Contreras, and M. A. Vidal, “Nonlinear behavior of the energy gap in Ge_[sub 1-x]Sn_[sub x] alloys at 4 K,” *Appl. Phys. Lett.*, vol. 91, no. 16, p. 161909, 2007.
- [79] Y. Nakamura, N. Fujinoki, and M. Ichikawa, “Luminescence at 1.5 μm from Si/GeSn nanodot/Si structures,” *J. Phys. D: Appl. Phys.*, vol. 45, no. 3, p. 035304, Jan. 2012.
- [80] B. Vincent, F. Gencarelli, A. Kumar, A. Vantomme, C. Merckling, D. Lin, V. Afanasiev, G. Eneman, T. Clarysse, A. Firrincieli, A. Gassenq, W. Vandervorst, J. Dekoster, R. Loo, and M. Caymax, “CVD Epitaxial Growth of GeSn Opens a New Route for Advanced Sn-Based Logic and Photonics Devices,” *2012 Int. Silicon-Germanium Technol. Device Meet.*, pp. 1–2, Jun. 2012.
- [81] R. Chen, Y.-C. Huang, S. Gupta, A. C. Lin, E. Sanchez, Y. Kim, K. C. Saraswat, T. I. Kamins, and J. S. Harris, “Material characterization of high Sn-content, compressively-strained GeSn epitaxial films after rapid thermal processing,” *J. Cryst. Growth*, vol. 365, pp. 29–34, Feb. 2013.
- [82] H. Lin, R. Chen, W. Lu, Y. Huo, T. I. Kamins, and J. S. Harris, “Investigation of the direct band gaps in Ge_(1-x)Sn_(x) alloys with strain control by photoreflectance spectroscopy,” *Appl. Phys. Lett.*, vol. 100, no. 10, p. 102109, 2012.
- [83] T. Asano, Y. Shimura, N. Taoka, O. Nakatsuka, and S. Zaima, “Epitaxial Growth and Anisotropic Strain Relaxation of Ge_{1-x}Sn_x Layers on Ge (110) Substrates,” no. 110, pp. 12–13, 2012.

- [84] R. Chen, H. Lin, Y. Huo, C. Hitzman, T. I. Kamins, and J. S. Harris, "Increased photoluminescence of strain-reduced, high-Sn composition Ge_{1-x}Sn_x alloys grown by molecular beam epitaxy," *Appl. Phys. Lett.*, vol. 99, no. 18, p. 181125, 2011.
- [85] S. Takeuchi, A. Sakai, K. Yamamoto, O. Nakatsuka, M. Ogawa, and S. Zaima, "Growth and structure evaluation of strain-relaxed Ge_{1-x}Sn_x buffer layers grown on various types of substrates," *Semicond. Sci. Technol.*, vol. 22, no. 1, pp. S231–S235, Jan. 2007.
- [86] S. Gupta, B. Magyari-Köpe, Y. Nishi, and K. C. Saraswat, "Achieving direct band gap in germanium through integration of Sn alloying and external strain," *J. Appl. Phys.*, vol. 113, no. 7, p. 073707, 2013.
- [87] S. Wirths, R. Geiger, N. von den Driesch, G. Mussler, T. Stoica, S. Mantl, Z. Ikonc, M. Luysberg, S. Chiussi, J. M. Hartmann, H. Sigg, J. Faist, D. Buca, and D. Grützmacher, "Lasing in direct-bandgap GeSn alloy grown on Si," *Nat. Photonics*, vol. 9, no. 2, pp. 88–92, Jan. 2015.
- [88] K. P. Homewood and M. A. Lourenço, "Optoelectronics: The rise of the GeSn laser," *Nat. Photonics*, vol. 9, no. 2, pp. 78–79, Feb. 2015.
- [89] J. Liu, R. Camacho-Aguilera, J. T. Bessette, X. Sun, X. Wang, Y. Cai, L. C. Kimerling, and J. Michel, "Ge-on-Si optoelectronics," *Thin Solid Films*, vol. 520, no. 8, pp. 3354–3360, Feb. 2012.
- [90] J. Liu, X. Sun, R. Camacho-Aguilera, L. C. Kimerling, and J. Michel, "Ge-on-Si laser operating at room temperature," *Opt. Lett.*, vol. 35, no. 5, pp. 679–81, Mar. 2010.
- [91] J. Liu, X. Sun, L. C. Kimerling, and J. Michel, "Direct-gap optical gain of Ge on Si at room temperature," *Opt. Lett.*, vol. 34, no. 11, pp. 1738–40, Jun. 2009.
- [92] R. Camacho-Aguilera, Z. Han, Y. Cai, L. C. Kimerling, and J. Michel, "Direct band gap narrowing in highly doped Ge," *Appl. Phys. Lett.*, vol. 102, no. 15, p. 152106, 2013.
- [93] Y. Cai, R. Camacho-Aguilera, J. T. Bessette, L. C. Kimerling, and J. Michel, "High phosphorous doped germanium: Dopant diffusion and modeling," *J. Appl. Phys.*, vol. 112, no. 3, p. 034509, 2012.
- [94] G. Thareja, S. Chopra, and B. Adams, "High n-Type Antimony Dopant Activation in Germanium Using Laser Annealing for n+/p Junction Diode," *Electron Device Lett.*, vol. 32, no. 7, pp. 838–840, 2011.
- [95] J. Kim, S. W. Bedell, and D. K. Sadana, "Improved germanium n+/p junction diodes formed by coimplantation of antimony and phosphorus," *Appl. Phys. Lett.*, vol. 98, no. 8, p. 082112, 2011.

- [96] M. de Kersauson, R. Jakomin, M. El Kurdi, G. Beaudoin, N. Zerounian, F. Aniel, S. Sauvage, I. Sagnes, and P. Boucaud, "Direct and indirect band gap room temperature electroluminescence of Ge diodes," *J. Appl. Phys.*, vol. 108, no. 2, p. 023105, 2010.
- [97] P. Velha and K. Gallacher, "Direct band-gap electroluminescence from strained n-doped germanium diode," *CLEO Sci. Innov.*, p. CW1L.7, 2012.
- [98] R. Camacho-Aguilera, J. Bessette, Y. Cai, L. C. Kimerling, and J. Michel, "Electroluminescence of highly doped Ge pnn diodes for Si integrated lasers," *8th IEEE Int. Conf. Gr. IV Photonics*, pp. 190–192, Sep. 2011.
- [99] S.-L. Cheng, G. Shambat, J. Lu, H.-Y. Yu, K. Saraswat, T. I. Kamins, J. Vuckovic, and Y. Nishi, "Cavity-enhanced direct band electroluminescence near 1550 nm from germanium microdisk resonator diode on silicon," *Appl. Phys. Lett.*, vol. 98, no. 21, p. 211101, 2011.
- [100] E. Kasper, M. Oehme, T. Arguirov, J. Werner, M. Kittler, and J. Schulze, "Room Temperature Direct Band Gap Emission from Ge p-i-n Heterojunction Photodiodes," *Adv. Optoelectron.*, vol. 2012, no. 100, pp. 1–4, 2012.
- [101] R. E. Camacho-Aguilera, Y. Cai, N. Patel, J. T. Bessette, M. Romagnoli, L. C. Kimerling, and J. Michel, "An electrically pumped germanium laser," *Opt. Express*, vol. 20, no. 10, pp. 11316–11320, May 2012.
- [102] M. de Kersauson, M. El Kurdi, S. David, X. Checoury, G. Fishman, S. Sauvage, R. Jakomin, G. Beaudoin, I. Sagnes, and P. Boucaud, "Optical gain in single tensile-strained germanium photonic wire.," *Opt. Express*, vol. 19, no. 19, pp. 17925–34, Sep. 2011.
- [103] D. Kim, "Theoretical Performance Evaluations of NMOS Double Gate FETs with High Mobility Materials : Strained III-V, Ge and Si," Stanford University PhD Thesis, November 2009.
- [104] K. C. Saraswat, D. Kim, T. Krishnamohan, D. Kuzum, A. K. Okyay, A. Pethe, and H.-Y. Yu, "Germanium for High Performance MOSFETs and Optical Interconnects," *ECS Trans.*, vol. 16, no. 10, pp. 3–12, 2008.
- [105] T. Boykin, G. Klimeck, R. Bowen, and F. Oyafuso, "Diagonal parameter shifts due to nearest-neighbor displacements in empirical tight-binding theory," *Phys. Rev. B*, vol. 66, no. 12, p. 125207, Sep. 2002.
- [106] T. Boykin, N. Kharche, and G. Klimeck, "Brillouin-zone unfolding of perfect supercells having nonequivalent primitive cells illustrated with a Si/Ge tight-binding parameterization," *Phys. Rev. B*, vol. 76, no. 3, p. 035310, Jul. 2007.
- [107] M. El Kurdi, G. Fishman, S. Sauvage, and P. Boucaud, "Band structure and optical gain of tensile-strained germanium based on a 30 band k·p formalism," *J. Appl. Phys.*, vol. 107, no. 1, p. 013710, 2010.

- [108] O. Madelung, *Semiconductors: data handbook*. Springer Science & Business Media, 2004.
- [109] E. Gaubas and J. Vanhellefont, “Comparative Study of Carrier Lifetime Dependence on Dopant Concentration in Silicon and Germanium,” *J. Electrochem. Soc.*, vol. 154, no. 3, p. H231, 2007.
- [110] R. Conradt and J. Aengenheister, “Minority carrier lifetime in highly doped Ge,” *Solid State Commun.*, vol. 10, no. 3, pp. 321–323, 1972.
- [111] R. Geiger, J. Frigerio, M. J. Suess, R. a. Minamisawa, D. Chrastina, G. Isella, R. Spolenak, J. Faist, and H. Sigg, “Excess carrier lifetimes in Ge layers on Si,” in *IEEE International Conference on Group IV Photonics*, 2013, pp. 103–104.
- [112] D. Nam, J.-H. Kang, M. L. Brongersma, and K. C. Saraswat, “Observation of improved minority carrier lifetimes in high-quality Ge-on-insulator using time-resolved photoluminescence,” *Opt. Lett.*, vol. 39, no. 21, p. 6205, Oct. 2014.
- [113] E. Gaubas and J. Vanhellefont, “Dependence of carrier lifetime in germanium on resistivity and carrier injection level,” *Appl. Phys. Lett.*, vol. 89, no. 14, p. 142106, 2006.
- [114] W.-S. Jung, J.-H. Park, A. Nainani, D. Nam, and K. C. Saraswat, “Fluorine passivation of vacancy defects in bulk germanium for Ge metal-oxide-semiconductor field-effect transistor application,” *Appl. Phys. Lett.*, vol. 101, no. 7, p. 072104, Aug. 2012.
- [115] D. Nam, D. S. Sukhdeo, B. R. Dutt, and K. C. Saraswat, “(Invited) Light Emission from Highly-Strained Germanium for on-Chip Optical Interconnects,” *ECS Trans.*, vol. 64, no. 6, pp. 371–381, 2014.
- [116] J. Liu, L. C. Kimerling, and J. Michel, “Monolithic Ge-on-Si lasers for large-scale electronic–photonic integration,” *Semicond. Sci. Technol.*, vol. 27, no. 9, p. 094006, Sep. 2012.
- [117] W. G. Spitzer, F. a. Trumbore, and R. a. Logan, “Properties of Heavily Doped n-Type Germanium,” *J. Appl. Phys.*, vol. 32, no. 10, p. 1822, 1961.
- [118] R. Newman and W. W. Tyler, “Effect of Impurities on Free-Hole Infrared Absorption in p-type Germanium,” *Phys. Rev.*, vol. 105, no. 3, pp. 885–886, 1957.
- [119] J. Liu, D. D. Cannon, K. Wada, Y. Ishikawa, S. Jongthammanurak, D. T. Danielson, J. Michel, and L. C. Kimerling, “Tensile strained Ge p-i-n photodetectors on Si platform for C and L band telecommunications,” *Appl. Phys. Lett.*, vol. 87, no. 1, p. 011110, 2005.
- [120] B. Mizaikoff, “Mid-IR Fiber-Optic Sensors,” *Anal. Chem.*, vol. 75, no. 11, p. 258A–267A, 2003.

- [121] R. Geiger, J. Frigerio, M. J. Süess, D. Chrastina, G. Isella, R. Spolenak, J. Faist, and H. Sigg, “Excess carrier lifetimes in Ge layers on Si,” *Appl. Phys. Lett.*, vol. 104, no. 6, p. 062106, Feb. 2014.
- [122] T. Taira, W. M. Tulloch, and R. L. Byer, “Modeling of quasi-three-level lasers and operation of cw Yb: YAG lasers,” *Appl. Opt.*, vol. 36, no. 9, pp. 12–14, 1997.
- [123] J. Harrison, A. Finch, D. M. Rines, G. A. Rines, and P. F. Moulton, “Low-threshold, cw, all-solid-state Ti:Al₂O₃ laser,” *Opt. Lett.*, vol. 16, no. 8, pp. 581–583, 1991.
- [124] D. Sukhdeo, D. Nam, Z. Yuan, B. R. Dutt, and K. C. Saraswat, “Toward an efficient germanium-on-silicon laser: ultimate limits of tensile strain and n-type doping,” in *CLEO: QELS_Fundamental Science*, 2013, p. JTh2A.109.
- [125] A. Haug, “Auger recombination in direct-gap semiconductors: band-structure effects,” *J. Phys. C Solid State Phys.*, vol. 16, pp. 4159–4172, 1983.
- [126] C. Haas, “Infrared absorption in heavily doped n-type germanium,” *Phys. Rev.*, vol. 125, no. 1960, pp. 1965–1971, 1962.
- [127] Y. Cai, Z. Han, X. Wang, R. E. Camacho-Aguilera, L. C. Kimerling, J. Michel, and J. Liu, “Analysis of Threshold Current Behavior for Bulk and Quantum-Well Germanium Laser Structures,” *IEEE J. Sel. Top. Quantum Electron.*, vol. 19, no. 4, p. 1901009, Jul. 2013.
- [128] Z. Alferov, “Double heterostructure lasers: early days and future perspectives,” *IEEE J. Sel. Top. Quantum Electron.*, vol. 6, no. 6, pp. 832–840, 2000.
- [129] G. Pizzi, M. Virgilio, and G. Grosso, “Tight-binding calculation of optical gain in tensile strained [001]-Ge/SiGe quantum wells,” *Nanotechnology*, vol. 21, no. 5, p. 055202, Feb. 2010.
- [130] M. Virgilio, M. Bonfanti, D. Chrastina, and A. Neels, “Polarization-dependent absorption in Ge/SiGe multiple quantum wells: Theory and experiment,” *Phys. Rev. B*, vol. 79, no. 7, p. 075323, 2009.
- [131] E. Yablonovitch and E. O. Kane, “Band structure engineering of semiconductor lasers for optical communications,” *J. Light. Technol.*, vol. 6, no. 8, pp. 1292–1299, 1988.
- [132] K. T. Delaney, P. Rinke, and C. G. Van de Walle, “Auger recombination rates in nitrides from first principles,” *Appl. Phys. Lett.*, vol. 94, no. 19, p. 191109, 2009.
- [133] L. Huldt, “Auger recombination in germanium,” *Phys. Status Solidi*, vol. 24, no. 1, pp. 221–229, Jul. 1974.
- [134] L. Huldt, “Phonon-assisted Auger recombination in germanium,” *Phys. Status Solidi*, vol. 33, no. 2, pp. 607–614, Feb. 1976.

- [135] W. Lochmann, “Phonon-assisted auger recombination in indirect gap semiconductors,” *Phys. Status Solidi*, vol. 45, no. 2, pp. 423–432, 1978.
- [136] G. Fuchs, C. Schiedel, a. Hangleiter, V. Härle, and F. Scholz, “Auger recombination in strained and unstrained InGaAs/InGaAsP multiple quantum-well lasers,” *Appl. Phys. Lett.*, vol. 62, no. 4, p. 396, 1993.
- [137] S. Mukherjee, A. Paul, N. Neophytou, R. Kim, J. Geng, Povolotskyi, T. C. Kubis, A. Ajoy, B. Novakovic, J. Fonseca, S. Steiger, M. McLennan, M. Lundstrom, and G. Klimeck, “Band Structure Lab.” Nanohub, 2014.
- [138] G. Klimeck, F. Oyafuso, T. B. Boykin, R. C. Bowen, and P. von Allmen, “Development of a Nanoelectronic 3-D (NEMO 3-D) Simulator for Multimillion Atom Simulations and Its Application to Alloyed Quantum Dots,” *Comput. Model. Eng. Sci.*, vol. 3, no. 5, pp. 601–642, 2002.
- [139] H. Tahini, a Chroneos, R. W. Grimes, U. Schwingenschlögl, and a Dimoulas, “Strain-induced changes to the electronic structure of germanium,” *J. Phys. Condens. Matter*, vol. 24, no. 19, p. 195802, May 2012.
- [140] J. J. Wortman and R. A. Evans, “Young’s Modulus, Shear Modulus, and Poisson’s Ratio in Silicon and Germanium,” *J. Appl. Phys.*, vol. 36, no. 1, p. 153, 1965.
- [141] B. Dutt, H. Lin, D. S. Sukhdeo, B. M. Vulovic, S. Gupta, D. Nam, K. C. Saraswat, and J. S. Harris, “Theoretical Analysis of GeSn Alloys as a Gain Medium for a Si-compatible Laser,” *IEEE J. Sel. Top. Quantum Electron.*, vol. 19, no. 5, p. 1502706, 2013.
- [142] D. Jenkins and J. Dow, “Electronic properties of metastable Ge x Sn 1-x alloys,” *Phys. Rev. B*, vol. 36, no. 15, pp. 7994–8000, 1987.
- [143] V. Fiorentini and A. Baldereschi, “Dielectric scaling of the self-energy scissor operator in semiconductors and insulators,” *Phys. Rev. B*, vol. 51, no. 23, pp. 17196–17198, 1995.
- [144] H. Lin, “Growth and Characterization of GeSn and SiGeSn Alloys for Optical Interconnects,” Stanford University PhD Thesis, May 2012.
- [145] S. Gupta, R. Chen, B. Magyari-Kope, H. Lin, A. Nainani, Y. Nishi, J. S. Harris, and K. C. Saraswat, “GeSn technology: Extending the Ge electronics roadmap,” *2011 Int. Electron Devices Meet.*, pp. 16.6.1–16.6.4, Dec. 2011.
- [146] G. He and H. A. Atwater, “Interband transitions in Sn x Ge 1-x alloys,” *Phys. Rev. Lett.*, vol. 79, no. 10, pp. 1937–1940, 1997.
- [147] N. Amrane, S. Ait Abderrahmane, and H. Aourag, “Band structure calculation of GeSn and SiSn,” *Infrared Phys. Technol.*, vol. 36, no. 5, pp. 843–848, Aug. 1995.

- [148] D. S. Sukhdeo, H. Lin, D. Nam, Z. Yuan, B. M. Vulovic, S. Gupta, J. S. Harris, B. R. Dutt, and K. C. Saraswat, "Approaches for a viable Germanium laser: tensile strain, GeSn alloys, and n-type doping," *2013 Opt. Interconnects Conf.*, vol. 5, pp. 112–113, May 2013.
- [149] Y. Cai and R. Camacho-Aguilera, "High n-type doped germanium for electrically pumped Ge laser," in *Integrated Photonics Research, Silicon and Nanophotonics (IPRSN)*, 2012, pp. 5–7.
- [150] R. A. Minamisawa, M. J. Süess, R. Spolenak, J. Faist, C. David, J. Gobrecht, K. K. Bourdelle, and H. Sigg, "Top-down fabricated silicon nanowires under tensile elastic strain up to 4.5%," *Nat. Commun.*, vol. 3, p. 1096, Jan. 2012.
- [151] D. S. Sukhdeo, D. Nam, J.-H. Kang, J. Petykiewicz, J. H. Lee, W. S. Jung, J. Vučković, M. L. Brongersma, and K. C. Saraswat, "Mimicking Heterostructure Behavior Within a Single Material at Room Temperature Using Strain," in *CLEO: Science and Innovations*, 2014, no. c, p. SM1H.2.
- [152] J. R. Jain, D. Ly-Gagnon, K. C. Balram, J. S. White, M. L. Brongersma, D. A. B. Miller, and R. T. Howe, "Tensile-strained germanium-on-insulator substrate fabrication for silicon-compatible optoelectronics," *Opt. Mater. Express*, vol. 1, no. 6, pp. 1121–1126, 2011.
- [153] A. K. Okyay, A. M. Nayfeh, K. C. Saraswat, A. Marshall, P. C. McIntyre, and T. Yonehara, "Ge on Si by novel heteroepitaxy for high efficiency near infrared photodetection," in *Conference on Lasers and Electro-Optics (CLEO)*, 2006, vol. 2, no. c, pp. 1–2.
- [154] T. Yi, L. Li, and C. Kim, "Microscale material testing of single crystalline silicon: process effects on surface morphology and tensile strength," *Sensors Actuators A Phys.*, vol. 83, no. 1–3, pp. 172–178, May 2000.
- [155] A. Nayfeh, C. O. Chui, T. Yonehara, and K. C. Saraswat, "Fabrication of high-quality p-MOSFET in Ge grown heteroepitaxially on Si," *IEEE Electron Device Lett.*, vol. 26, no. 5, pp. 311–313, May 2005.
- [156] D. S. Sukhdeo, D. Nam, J.-H. Kang, J. Petykiewicz, J. H. Lee, W. S. Jung, J. Vu, M. L. Brongersma, and K. C. Saraswat, "Direct bandgap germanium nanowires inferred from 5.0% uniaxial tensile strain," in *2013 IEEE 10th International Conference on Group IV Photonics (GFP)*, 2013, vol. 4, pp. 73–74.
- [157] M. J. Süess, "Private Communication." 2013.
- [158] H. Kroemer, "Band offsets and chemical bonding: the basis for heterostructure applications," *Phys. Scr.*, vol. T68, pp. 10–16, Jan. 1996.

- [159] W. T. Tsang, "A graded-index waveguide separate-confinement laser with very low threshold and a narrow Gaussian beam," *Appl. Phys. Lett.*, vol. 39, no. 2, pp. 134–137, 1981.
- [160] M. El Kurdi, H. Bertin, E. Martincic, M. de Kersauson, G. Fishman, S. Sauvage, a. Bosseboeuf, and P. Boucaud, "Control of direct band gap emission of bulk germanium by mechanical tensile strain," *Appl. Phys. Lett.*, vol. 96, no. 4, p. 041909, 2010.
- [161] D. Nam, A. Roy, K. C.-Y. Huang, M. L. Brongersma, and K. C. Saraswat, "Strained Germanium Membrane using Thin Film Stressor for High Efficiency Laser," in *CLEO: QELS_Fundamental Science*, 2011, p. JTU185.
- [162] G. Capellini, G. Kozlowski, Y. Yamamoto, M. Lisker, C. Wenger, G. Niu, P. Zaumseil, B. Tillack, a. Ghrib, M. de Kersauson, M. El Kurdi, P. Boucaud, and T. Schroeder, "Strain analysis in SiN/Ge microstructures obtained via Si-complementary metal oxide semiconductor compatible approach," *J. Appl. Phys.*, vol. 113, no. 1, p. 013513, 2013.
- [163] L. Nataraj, F. Xu, and S. G. Cloutier, "Direct-bandgap luminescence at room-temperature from highly-strained Germanium nanocrystals," *Opt. Express*, vol. 18, no. 7, pp. 7085–7091, Mar. 2010.
- [164] C. Boztug, J. R. Sánchez-Pérez, F. F. Sudradjat, R. B. Jacobson, D. M. Paskiewicz, M. G. Lagally, and R. Paiella, "Tensilely strained germanium nanomembranes as infrared optical gain media.," *Small*, vol. 9, no. 4, pp. 622–30, Feb. 2013.
- [165] R. Perez and P. Gumbsch, "Directional anisotropy in the cleavage fracture of silicon," *Phys. Rev. Lett.*, vol. 84, no. 23, pp. 5347–5350, Jun. 2000.
- [166] P. H. Lim, S. Park, Y. Ishikawa, and K. Wada, "Enhanced direct bandgap emission in germanium by micromechanical strain engineering," *Opt. Express*, vol. 17, no. 18, pp. 16358–65, Aug. 2009.
- [167] J. Wales, G. Lovitt, and R. Hill, "Optical properties of germanium films in the 1-5 μ range," *Thin Solid Films*, vol. 1, no. 2, pp. 137–150, 1967.
- [168] M. Prost, M. El Kurdi, a. Ghrib, S. Sauvage, X. Checoury, N. Zerounian, F. Aniel, G. Beaudoin, I. Sagnes, F. Boeuf, and P. Boucaud, "Tensile-strained germanium microdisk electroluminescence," *Opt. Express*, vol. 23, no. 5, p. 6722, Mar. 2015.